THE UNIVERSITY OF MICHIGAN

INDUSTRY PROGRAM OF THE COLLEGE OF ENGINEERING

PRINCIPLES AND APPLICATIONS OF THE HODOGRAPH METHOD IN SPACE MECHANICS

Fang T. Sun

A dissertation submitted in partial fulfillment
of the requirements for the degree of
Doctor of Philosophy in the
University of Michigan
Department of Aerospace Engineering
1966

May, 1966

IP-737

PREFACE

This dissertation is an outgrowth of the author's major work done in the past seven years on the hodograph method in space mechanics. The main text is arranged in three parts: Part I deals with the fundamentals of the hodograph method, illustrated with a number of elementary examples; Part II presents the application of the hodograph method to the analysis of the ballistic trajectories between two terminal points in space; and Part III is an extension of Part II to the optimization of these trajectories. The materials in Part I are based on the author's three earlier papers published in the years 1960 - 61 when the author was in Taiwan, China. Those in Part II are based on the author's recent work done at the University of Michigan, which has been first published by the University as a technical report in September 1964, and then issued by the National Aeronautics and Space Administration as a NASA contractor's report in January 1965. Part III consists of the author's most recent and unpublished work on this subject done at this University.

The author wishes to express his appreciation and thanks to Professors Harm Buning, Donald T. Greenwood, Arnold M. Kuethe, Alfred C. Robinson, and C. J. Titus for their careful preliminary review of the draft of this dissertation. Special thanks are due to Professor Buning, whose keen interest in the author's work, whose many stimulating discussions with the author, and whose close follow of the development from the early stages up to the present presentation have been most inspiring and helpful; and to Professor Greenwood, whose thorough reading of the manuscript and constructive suggestions were of great value in the final preparation of this dissertation. The author feels particularly indebted

to Professor Arnold M. Kuethe and Dr. David T. Williams, my former teacher and Professor at this University, for their personal encouragement, without which the compilation of this work as a doctoral dissertation would have never been attempted.

Acknowledgement is also due to the National Long-range Science Development Commission, Republic of China, for its support of the author's early work in Taiwan; and to the National Aeronautics and Space Administration, U. S. A. for its grant which enabled the author to continue his work in this country. Finally the kind assistance and genial cooperation of the Industry Program of the College of Engineering of this University in preparing the final copy of this dissertation is also appreciated.

TABLE OF CONTENTS

	Page
PREFACE	ii
LIST OF TABLES	viii
LIST OF ILLUSTRATIONS	x
NOMENCLATURE	xiii
INTRODUCTION	1
PART I: FUNDAMENTALS OF THE HODOGRAPH METHOD	6
1. PRELIMINARIES ON KEPLERIAN MOTION	7
1.1 Fundamental Assumptions	7
1.2 Some Basic Formulas and General Remarks	8
2. THE HODOGRAPH EQUATIONS	11
2.1 The Polar Hodograph Equation	11
2.2 The Hamiltonian Hodograph Equation	13
3. CORRELATION BETWEEN THE ORBITAL PLANE AND THE HODOGRAPH PLANE	16
3.1 General Correlations	16
3.2 The Elliptic Orbit	23
3.3 The Hyperbolic Orbit	27
3.4 The Parabolic Orbit	29
4. SOME ELEMENTARY APPLICATIONS OF THE ORBITAL HODOGRAPH	32
4.1 The Exploration of Orbital Characteristics	32
4.2 Derivation of Orbital Relations	35
5. THE DIMENSIONLESS HODOGRAPHS AND THEIR APPLICATIONS	38
5.1 The Dimensionless Hodographs	38
5.2 The Eccentric Anomalies in the Dimensionless Hodographs	40
5.3 Determination of the Time of Orbital Flight from the Dimensionless Hodographs	45
5.4 Derivation of the Dimensionless Orbital Relations	48

TABLE OF CONTENTS (CONT'D)

		Page
6.	SOME GENERAL REMARKS ON THE HODOGRAPH METHOD.....	50
	6.1 The Construction of the Orbital Hodograph.....	50
	6.2 The Basic Advantages and Main Applications of the Hodograph Method.....	52
	6.3 The Hamiltonian Hodograph versus the Polar Hodograph.....	54
PART II.	HODOGRAPH ANALYSIS OF THE BALLISTIC TRAJECTORIES BETWEEN TWO TERMINAL POINTS IN SPACE.....	56
7.	INTRODUCTORY REMARKS.....	57
8.	THE HODOGRAPHIC REPRESENTATION AND A GENERAL SURVEY OF THE SYSTEM OF TWO-TERMINAL TRAJECTORIES....	58
	8.1 General Considerations.....	58
	8.2 The Hodographic Representation.....	60
	8.3 A General Survey.....	64
	8.4 Limits of Variation of the Trajectory Elements..	68
9.	CHARACTERISTICS OF THE CONJUGATE TRAJECTORIES.....	75
	9.1 The Chordal and Radial Components of the Terminal Velocities.....	75
	9.2 The Conjugate Relations.....	77
	9.3 The Principal Elements of the Conjugate Trajectories.....	85
10.	ANALYSIS OF SOME PARTICULAR TRAJECTORIES.....	90
	10.1 The Minimum Energy Trajectory.....	90
	10.2 The Least Eccentric Trajectory and Its Conjugate.....	95
	10.3 Other Trajectories.....	97
11.	THE CASE OF 180 DEGREE RANGE.....	99
	11.1 The Hodographic Representation and a General Survey.....	99
	11.2 The Characteristics of the Conjugate Trajectories and Their Principal Elements.....	102
	11.3 The Minimum Energy Trajectory and the Least Eccentric Trajectory.....	107

TABLE OF CONTENTS (CONT'D)

		Page
12.	SUMMARY OF FINDINGS	118
12.1	General Conclusions on the Two-Terminal Trajectory System	118
12.2	On the Conjugate Trajectories	119
12.3	On the Minimum Energy Trajectory	120
12.4	On the Least Eccentric Trajectory	120
12.5	On the Case of 180° Range	120
12.6	On the Hohmann Ellipse	121
PART III.	HODOGRAPH ANALYSIS OF THE OPTIMIZATION OF THE TRANSFER TRAJECTORIES BETWEEN TWO TERMINAL POINTS FOR MINIMUM INITIAL IMPULSE	122
13.	INTRODUCTORY REMARKS	123
14.	TWO-DIMENSIONAL ANALYSIS OF THE PROBLEM	124
14.1	Formulation of the Problem	124
14.2	The Constraining Hyperbola and the Orthogonality Condition	126
14.3	Criterion of the Nature of the Real Solutions and the Boundary Evolute	133
15.	DETERMINATION OF THE OPTIMUM SOLUTION	139
15.1	The Absolute Minimum Solution and Its Determination	139
15.2	Lines of Constant Optimum Trajectory and Lines of Constant Velocity Increment	147
15.3	The Critical Condition and the Unrealistic Trajectories	151
15.4	Choice of the Realistic Optimum Transfer Trajectory	158
15.5	Effects of the Initial Velocity Vector on the Optimum Solution: Summary of Findings	163
16.	HODOGRAPHIC REPRESENTATION OF THE TWO-DIMENSIONAL OPTIMUM TRANSFER	168
16.1	The Orthogonal Net in the Hodograph Plane and the Optimization Chart	168
16.2	The Construction of the Transfer Hodograph	170
16.3	The Hodograph of Optimum Transfer Trajectories in the $\bar{v}$-Plane	172

TABLE OF CONTENTS (CONT'D)

Page

17. ANALYSIS OF SOME PARTICULAR CASES 178

17.1 The Case $\psi = 0$ 178
17.2 The Case $\psi = \pi$ 183
17.3 The Case $r_2 \to \infty$ $(n \to \infty)$ 190
17.4 The Case $r_1 \to \infty$ $(n \to 0)$ 195

18. SOME GENERALIZATIONS 202

18.1 The Orthogonality Principle and the Impulsive Change of Orbit 202
18.2 The Three Dimensional Case of Terminal-to-Terminal Transfer 203
18.3 Impulsive Orbital Change Problems with Hyperbolic Constraint 206

FINAL REMARKS AND DISCUSSION 208

BIBLIOGRAPHY AND REFERENCES 215

APPENDICES 218

A. INTER-RELATIONS BETWEEN THE GEOMETRIC PARAMETERS AND THE DYNAMIC PARAMETERS OF THE KEPLERIAN ORBIT 219

B. PROOFS OF SOME OF THE CORRELATION FORMULAS 221

C. THE INTERSECTING PROPERTY OF THE NORMALS OF A HYPERBOLA 226

LIST OF TABLES

Table		Page
I-1	General Correlations Between the Orbital Plane and the Hodograph Planes	19
I-2	Correlations Between the Orbital Plane and the Hodograph Planes for the Three Types of the Keplerian Orbit	26
I-3	Determination of the Dimensionless Time of Orbital Flight (t/T) from the Dimensionless Hodographs	46
I-4	Some Expressions for the Hodograph Parameters: the Radius and the Origin-to-center Distance of the Circular Hodograph	51
II-1	Location of the Hodograph Origin and the Nature of the Two-Terminal Trajectory	67
II-2	Possible and Forbidden Regions of Departure and Approach	72
II-3	Regions for the Apsidal Axes (Positive Portions)	74
II-4	Summary of Conjugate Relations	84
II-5	Formulas for the Principal Elements of the Conjugate Trajectories	87
II-6	Hodographic Criteria for the Occurrence of Apses on the Trajectory $(\psi < \pi)$	89
II-7	Possible and Forbidden Regions of Departure and Approach, $(\psi = \pi)$	101
III-1	Principal Formulas in the Nondimensional Form for the Terminal-to-terminal Optimum Transfer	129
III-2	Principal Geometrical Elements of the Constraining Hyperbola	130
III-3	Nature of the Real Roots (ν_{C*} or ν_{R*}) of the Orthogonality Quartic and the Number of Real Solutions	134
III-4	The Real Roots of the ν_{C*}-equation and the Nature of the Stationary Points on the $\lvert\Delta\nu\rvert$ - curve	141
III-5	Regions in the Hodograph Plane and the Nature of the Optimum Transfer Trajectories	164

LIST OF TABLES (CONT'D)

Table		Page
III-6	Optimum Solutions for Vertical Transfer ($\psi = 0$)	181
III-7	Optimum Solutions for 180° Transfer ($\psi = \pi$)	186
A-1	Conversion of Geometric Parameters into Dynamic Parameters (Keplerian Orbit) (Appendix A)	219
A-2	Conversion of Dynamic Parameters into Geometric Parameters (Keplerian Orbit) (Appendix A)	220

LIST OF ILLUSTRATIONS

Figure		Page
I-1	The Keplerian Orbits and Their Hodograph Images	14
I-2	General Correlation Between the Orbital Plane and the Hodograph Planes	18
I-3	The Elliptic Orbit and Its Hodograph Images	24
I-4	The Hyperbolic Orbit and Its Hodograph Images	28
I-5	The Parabolic Orbit and Its Hodograph Images	30
I-6	Change of Orbital Velocity along a Keplerian Orbit	33
I-7	The Dimensionless Hodographs for Keplerian Orbits	39
I-8	The Elliptic Eccentric Anomaly in the Dimensionless Hodographs	41
I-9	The Hyperbolic Eccentric Anomaly in the Dimensionless Hodographs	43
I-10	Determination of the Time of Orbital Flight from the Dimensionless Hodographs	47
II-1	System of Two-terminal Trajectories and Its Hodographic Representation (Range $\neq 180°$)	59
II-2	Linear Distribution of the Hodograph Origins in the Dimensionless Hodograph Plane	62
II-3	General Survey of the System of Two-Terminal Trajectories	71
II-4	Terminal Velocities and Their Chordal and Radial Components	76
II-5	The Conjugate Elliptic Trajectories, Range $< 180°$	80
II-6	The Conjugate Hyperbolic Trajectories, Range $< 180°$	81
II-7	The Conjugate Parabolic Trajectories, Range $< 180°$	82
II-8	The Minimum Energy Trajectory and Its Relation with a Pair of Conjugate Trajectories, Range $< 180°$	91
II-9	The Least Eccentric Trajectory and Its Conjugate, Range $< 180°$	96

LIST OF ILLUSTRATIONS (CONT'D)

Figure		Page
II-10	System of Two-terminal Trajectories and Its Hodographic Representation, 180° Range	100
II-11	The Conjugate Elliptic Trajectories, 180° Range	103
II-12	The Conjugate Hyperbolic Trajectories, 180° Range	104
II-13	The Minimum Energy and Least Eccentric Trajectory, 180° Range	108
II-14	Variation of the Range-Constrained Path Angle With Distance Ratio and Initial Speed: a. $\psi = 60°$ b. $\psi = 90°$ c. $\psi = 120°$ d. $\psi = 180°$	110-113
II-15	Variation of the Range-Constrained Trajectory Eccentricity With Distance Ratio and Initial Speed: a. $\psi = 60°$ b. $\psi = 90°$ c. $\psi = 120°$ d. $\psi = 180°$	114-117
III-1	The Transfer Trajectory and the Constraining Hyperbola in the Hodograph Plane	125
III-2	Quadrants in the Hodograph Plane	132
III-3	Geometry of the Constraining Hyperbola and the Boundary Lamé	136
III-4	Variation of $\lvert\Delta v\rvert$ and the Corresponding Geometry in the Hodograph Plane	140
III-5	Lines of Constant Optimum Transfer Trajectory and Lines of Constant Optimum Velocity-Increment	148
III-6	Geometry of the Parallel Curves	150
III-7	Regions in the Hodograph Plane and the Nature of the Optimum Transfer Trajectory	152
III-8	Choice of the Realistic Optimum Trajectory: Initial Velocity Vector in the Unrealistic Region	160
III-9	Determination of the Boundary Point, $\lvert\Delta v\rvert_3 = \lvert\Delta v\rvert^*$	162
III-10	The Optimization Chart for Minimum Initial Impulse Terminal-to-Terminal Transfer ($\psi = 60°$, $\phi_1 = 75°$)	169
III-11	Construction of the Transfer Hodograph in the $\vec{V}$-Plane	171

LIST OF ILLUSTRATIONS (CONT'D)

Figure		Page
III-12	Hodograph of Optimum Transfer Trajectories in the $\vec{v}$ - Plane (ψ = Const.)	174
III-13	Optimization of Vertical Transfer ($\psi = 0$)	179
III-14	Optimization of 180° Transfer ($\psi = \pi$)	184
III-15	The Optimum Trajectory Hodograph for 180° Transfer	188
III-16	Optimization of Transfer to Infinity ($r_2 \rightarrow \infty$)	192
III-17	The Optimum Trajectory Hodograph for Transfer to Infinity	193
III-18	Optimization of Transfer from Infinity ($r_1 \rightarrow \infty$)	196
III-19	Geometry of 3-Dimensional Terminal-to-Terminal Transfer	205
C-1	Intersection of the Normal Lines to a Hyperbola	227

NOMENCLATURE

A	semitransversal axis, the constraining hyperbola (Figure III-1c).
a	semimajor axis, elliptic orbit; or semitransversal axis, hyperbolic orbit.
B	semiconjugate axis, the constraining hyperbola (Figure III-1c).
b	semiminor axis, elliptic orbit; or semiconjugate axis, hyperbolic orbit.
C	focus-to-center distance, the constraining hyperbola (Figure III-1c).
c	focus-to-center distance, the Keplerian conic.
C_1 , C_2	parameters defined by Equations (15.12).
d	base altitude or the perpendicular distance from the field center to the chord Q_1 Q_2 of the base triangle (Figure II-1a).
e	eccentricity, the constraining hyperbola.
F	hyperbolic anomaly (Equation (5.11)).
f	constraining function
G	Newtonian gravitational constant (Equation (1.1)).
h	angular momentum per unit reduced mass.
I	an invariant of the orthogonality quartic, defined by Equation (14.18).
J	an invariant of the orthogonality quartic, defined by Equation (14.18).
K	Godal's compatibility constant.
k	orbital energy per unit reduced mass.
ℓ	chord length.
M	gravitating mass of the field.
M	orthogonal projection of the orbital velocity vector on the local radial axis (Part III).
m	mass of the space vehicle.
m	ℓ/r_1 (Part II).

$\mathcal{m}$ dimensionless orthogonal radial projection = M/V_{S1}.

$\dot{\mathcal{m}}$ dimensionless orthogonal radial projection = M/V_{S2}.

N orthogonal projection of the orbital velocity vector on the local chordal axis.

n distance ratio = r_2/r_1.

$\mathcal{n}$ dimensionless orthogonal chordal projection = N/V_{S1}.

$\dot{\mathcal{n}}$ dimensionless orthogonal chordal projection = N/V_{S2}.

r radial distance from the field center.

$\dot{r}$ dr/dt.

$\bar{r}$ semilatus rectum.

$\mathcal{R}$ rh/μ.

$\dot{\mathcal{R}}$ rh/μ.

s semi-perimeter of the base triangle = $\frac{1}{2}(r_1 + r_2 + \ell)$.

t time of orbital flight from the pericenter to any orbital point.

T $\sqrt{a^3/\mu}$ for elliptic or hyperbolic orbit; $\sqrt{\bar{r}^3/\mu}$ for parabolic orbit.

U potential function.

V speed.

$\vec{V}$ velocity vector.

V^* escape speed = $\sqrt{2\mu/r}$.

V_s circular speed = $\sqrt{\mu/r}$.

V_∞ residual speed.

υ dimensionless speed = Vh/μ.

$\vec{\upsilon}$ dimensionless velocity vector = $\vec{V}h/\mu$.

X^*, Y^* critical coordinates, defined by Equations (15.5).

x,y displacement coordinates defined in Figure I-2a; or general rectangular coordinates (Appendix C).

$\dot{x},\dot{y}$ velocity coordinates, inertial frame, = dx/dt, dy/dt.

$\dot{x}, \dot{y}$ dimensionless velocity coordinates = $\dot{x}h/\mu$, $\dot{y}h/\mu$.

α eccentric anomaly, elliptic or hyperbolic.

β inclination of the orbital velocity vector with the x-axis.

γ half-angle between the asymptotes, hyperbolic orbit (Figure I-4a).

Δ discriminant of the orthogonality quartic (Equation (14.17)).

$\Delta\vec{V}$ change of velocity between two orbital points.

$\Delta\vec{V}$ impulsive change of velocity at a point.

$\Delta\vec{v}$ nondimensional impulsive change of velocity = $\Delta\vec{V}/V_{S1}$.

$\Delta\vec{v}$ nondimensional impulsive change of velocity = $\Delta\vec{V}/V_{S2}$.

δ inclination of the line of origins (Figure II-1).

ϵ orbital eccentricity.

ζ, χ parameters, defined by Equation (9.20)

η parameter, defined by Equation (10.11).

θ true anomaly.

$\dot{\theta}$ $d\theta/dt$.

κ dimensionless Godal's compatibility constant = K/V_{S1}.

$\acute{\kappa}$ dimensionless Godal's compatibility constant = K/V_{S2}.

λ speed parameter = V/V^*

μ $G(M+m)$.

ν dimensionless speed = V/V_{S1}.

$\vec{\nu}$ dimensionless velocity vector = $\vec{V}/V_{S1}$.

$\bar{\nu}$ value of ν on the boundary Lamé (Equation (14.22)).

$\acute{\nu}$ dimensionless speed = V/V_{S1}.

$\vec{\acute{\nu}}$ dimensionless velocity vector = $\vec{V}/V_{S2}$.

ρ distance of the optimum origin from the radical center (T) in the $\acute{\upsilon}$ -plane (Figure III-12).

ρ' distance of the optimum origin from the initial terminal in the $\vec{\upsilon}$ -plane (Figure III-15b).

σ included angle between the local radial and chordal axes, or the exterior angle of the base triangle (Figure III-1).

τ period, elliptic motion.

Φ auxiliary angle defined in Figures (II-5), (II-6), and (II-7).

Φ path angle with respect to the minimum energy direction (Figure III-1c).

$\not\phi$ path angle with respect to the local horizon.

φ base angle, the interior angle of the base triangle at the terminal point (Figure II-1a).

ψ angle of separation, or the vertex angle, the interior angle of the base triangle at the field center (= range angle, normal trajectory).

ψ $2\pi - \psi$ (= range angle, complementary trajectory).

ω auxiliary angle defined in Figure II-3 (Part II).

ω the inclination of the initial velocity vector to the plane of the transfer trajectory (Figure III-19).

ω a parametric angle defined by Equations(C-1), Appendix C.

Superscripts

$*$ critical condition.

$'$ complementary trajectory (Part II).

$'$ nondimensionalization with reference to the final terminal (Q_2) (Part III).

$'$ point symmetrical with the orbital point with respect to the apsidal axis (Figures I-3, I-4, I-5).

$''$ point symmetrical with the orbital point with respect to the minor axis (elliptic orbit) or the conjugate axis (hyperbolic orbit) (Figures I-3 and I-4).

$'''$ point symmetrical with the orbital point with respect to the center of the conic (Figures I-3 and I-4).

Subscripts

A apocenter

H pertaining to high half-plane (defined in Figure III-2), or high trajectory.

I, I'	points at infinity, hyperbolic orbit.
L	pertaining to low half-plane (defined in Figure III-2) or low trajectory.
LL	lower limit.
M, M'	end points of the latus rectum.
N, N'	end points of the minor axis, elliptic orbit.
P	pericenter.
UL	UPPER LIMIT.
d	direction of the base altitude (Figure III-3).
i	index.
opt	optimum condition.
Δ	pertaining to $\vec{\Delta V}$ (or $\vec{\Delta v}$).
C, R	chordal and radial pair of directions (Figure II-4).
P, N	in-plane and out-plane components (Figure III-19).
r, θ	radial and transversal pair of directions (Figure I-2a).
ξ, η	general oblique coordinate directions.
χ, ζ	outward directions of the interior and exterior angle bisectors of the base triangle (Figure III-3).
o	initial condition.
1	initial terminal.
2	final terminal.
I	low trajectory (Part II).
II	high trajectory (Part II).
+	positive half-plane defined in Figure III-2.
-	negative half-plane defined in Figure III-2.
∞	condition at infinity.
*	minimum energy (Part II only).
*	ortho-point, or orthogonal solution in Chapters 14 and 15 and optimum condition elsewhere in Part III.
**	absolute minimum distance solution (Chapter 15).

INTRODUCTION

Historical Sketch

The hodograph, as Sir Williams R. Hamilton[2] put it, is the locus of the end of the velocity vector of a moving body drawn from a common origin. In modern language a hodograph is the path of a moving point in the velocity space. The idea of hodograph was originated by Mobius[1] in 1840, and the fact that the hodograph for the motion in a Newtonian gravity field is a perfect circle was discovered by Hamilton[2] in 1846. Several theorems concerning the characteristics of the motion in a central force field were deduced from this Law of Circular Hodograph, as he called it, and contained in his brilliant papers presented at the Royal Irish Academy during the years 1846-47.[2,3,4] An analytical treatment of this subject is also found in his classical work on quaternions published later.[5] However, it is strange to see that, despite its elegance and simplicity, Hamilton's Hodograph Theory has not been followed up since then either in classical mechanics or in celestial mechanics until very recently. During this period, while the hodograph transformation had found its application in gas dynamics through the efforts of Busemann, Chaplygin, von Karman etc. and played an important role in the treatment of the compressible flow, problems in the mechanics of a central force field were still dealt with almost exclusively in the physical space while Hamilton's Hodograph Theory remained in obscurity.

The recent interest in the hodograph method in the field of space mechanics, it seems, did not begin until after Russia's Sputnik had gone into orbit. With the opening of the new space era new problems

in space flight have been arising continually, providing new challenges to the old problem of Kepler, and the classical orbital hodograph began to receive the due attention from current workers in this field. The polar hodograph of orbital motion[1] was introduced by Sun in 1960 at the Second International Symposium on Rockets and Astronautics in Tokyo in an article(7) in which he extended Hamilton's Law of Circular Hodograph to a non-inertial frame, and worked out the hodograph analysis for the three main types of the Keplerian orbit, the elliptic, the parabolic, and the hyperbolic. From then on he has been continually developing this polar hodograph as well as the Hamiltonian version, their fundamentals and their applications, resulting in several published papers(7, 9, 12, 19) which form a part of this dissertation. During about the same period articles on the same subject written by a number of contemporary authors also appeared in the technical literature, notably the work of Altman, Pistiner, and Paul of the United States of America and Pesĕk of Czechoslovakia (see e.g., References 8, 11, 13-18, 20, and 21). Paul's work(8) is essentially of the graphical nature, and Pesek's published work on this subject (like Reference 17) is rather scarce. The major work in this country on the same subject was done mainly by Altman and Pistiner. Their pioneer work on the hodograph for elliptic orbit appeared in a series of papers, notably References 10, 11, 13 published in 1961, and later a broader treatment of the hodograph mapping of the orbital conics was found in Reference 14. Recent publications indicate that Altman's work(20,21)

---

[1] Unaware of the connection between the classical circular hodograph and Hamilton, it was referred to as the "conventional hodograph," while the polar version was called the "special hodograph" in Sun's early writings, like References 7 and 8, etc.

has well advanced into the realm of Hodographic Transformation Theory which might open a new era in the analytical study of orbital mechanics. Finally, it is to be mentioned that Boksenbom's short article on graphical trajectory analysis[6] which was published in December, 1959, contained actually some elements of the hodograph mapping although no particular reference to it was stated.

Purpose and Scope of the Present Study

As implied in Hamilton's pioneering writing[2] the entire Keplerian Mechanics may well be developed from hodograph analysis. In fact he succeeded in deducing that the Keplerian orbit is a conic directly from his Law of Circular Hodograph. However, the present study will be aimed at the solution of current problems in space flight by using the hodograph method.

It is generally known that Kepler's problem has been well solved analytically ever since Newton's time; even the subsequent application of the Hamilton-Jacobi equation to Kepler's problem in space added only some elegance to the method of solution, but not much to its contents. However, the importance of further exploration of the characteristics of such a motion cannot be overlooked. First, despite its inadequacy in describing the motion of a space vehicle in the presence of various perturbing forces, the Keplerian orbit is the reference orbit or trajectory in almost all the problems of unpowered, or ballistic flight, on which all approximations or refinements are based. Second, despite the fact that the Keplerian motion is amenable to complete

analysis the present knowledge of the dynamic characteristics of such a motion is not as adequate as generally believed. This situation is more evident when special constraining conditions are involved as in the new problems in present space flight, which are usually not in the realm of Celestial Mechanics. For example, the simple and interesting orbital characteristics manifested in Godal's terminal compatibility condition,[37] which forms an analytical basis for most orbital transfer problems, is rather a recent contribution. In view of these facts the further exploration of the characteristic of the basic orbit as represented by the Keplerian model with particular reference to the various constraining conditions appearing in current problems like the terminal constraints, the optimization requirement, and so on, will constitute an essential step toward the analytical solution of such problems. And to this end the hodograph method which offers a geometric approach to the problem by transforming all the Keplerian orbits into circles is obviously an efficient tool to use. It is with this in mind that the present study has been motivated. More specifically the main study has been as follows:

(1) To develop adequate correlations between the orbital plane and the hodograph plane in an inertial as well as a non-inertial frame so that problems may be analyzed in a suitable hodograph plane instead of the physical plane.

(2) To apply the hodograph analysis to current problems so as to have an insight of the situation to find its solution or to obtain some conclusions on the solution through the geometrical approach.

In the following, Part I will be devoted to the fundamentals concerning the hodograph geometry and its kinematic significance for both the Hamiltonian version and the polar version, which will form the background for any hodograph analysis within the realm of Keplerian motion; and, in Parts II and III the application of the hodograph method to two specific problems will be given. The first application is the hodograph analysis of the family of trajectories which pass through two fixed but arbitrary terminal points in space. The second one is the optimization of such trajectories for minimum initial impulse when an arbitrary initial velocity vector is prescribed. The first is one of the basic problems encountered in space flight, and in this example the use of the dimensionless hodograph for the treatment of a family of infinite number of trajectories will be fully illustrated. The second one is an immediate extension of the first.

Within the limited scope of this dissertation the material will be confined to the velocity hodograph (as defined in the preceding section) for the Keplerian motion only. The extension of the present development to the acceleration hodograph, and the potentialities of the hodograph approach to the analysis of the non-Keplerian motions will be briefly discussed in the final chapter.

PART I

FUNDAMENTALS OF THE HODOGRAPH METHOD

1. PRELIMINARIES ON KEPLERIAN MOTION

1.1 Fundamental Assumptions

Throughout this paper, the motion of the space vehicle will be regarded as Keplerian. The fundamental assumptions underlying a Keplerian Motion may be listed as follows:

(1) The gravity field is central and Newtonian, that is, its field potential is given by

$$U(r) = \frac{GMm}{r} \tag{1.1}$$

where

M = the gravitating mass of the field

m = the mass of the vehicle

r = the separation distance

G = the Newtonian gravitation constant

(2) The vehicle is at such a tremendous distance from the center of the field as compared with its own dimensions, that it may be regarded as a point-mass.

(3) No disturbing forces present.

(4) The impulse applied to the vehicle is instantaneous if any.

(5) The vehicle speed relative to the field center may be much higher than the escape speed but is far below the speed of light, so that the relativistic effect may be neglected.

1.2 Some Basic Formulas and General Remarks

Since the analytical solution of Kepler's problem is well-known, only a recapitulation of a few basic formulas and definitions with some brief remarks will suffice here. By placing the origin of the coordinate system at the field center, and considering the motion of the vehicle relative to this center, the equation of motion is

$$\ddot{\vec{r}} = -\frac{\mu}{r^3}\vec{r} \tag{1.2}$$

where

$$\mu \equiv G(M+m) \tag{1.3}$$

Such a motion will take place in a plane determined by the field center and the initial position and velocity of the vehicle; and the path of the vehicle in the plane of motion is a conic given by

$$\frac{\bar{r}}{r} = 1 + \epsilon \cos\theta \tag{1.4}$$

where θ is the true anomaly, ϵ and $\bar{r}$ are the eccentricity and the semilatus rectum of the conic respectively given by

$$\epsilon = \sqrt{1 + 2k\left(\frac{h}{\mu}\right)^2} \tag{1.5}$$

$$\bar{r} = h^2/\mu \tag{1.6}$$

with h and k being the angular momentum and the orbital energy of the motion respectively, both referring to a unit reduced mass of the 2-body system.[1.1] In the following, such a path of motion will generally be called the Keplerian orbit. Whenever specific terminal points are to be emphasized, it will be referred to as the Keplerian trajectory. In any case it may

---

[1.1] Reduced mass $\equiv mM/(M+m)$.

be called simply the Keplerian conic. The plane of motion will be called the orbital plane or the trajectory plane. The relations between the geometric elements of a Keplerian conic and the orbital velocity at any orbital point have been given in References 35 and 36 and they are summarized in Appendix A for reference.

A Keplerian conic is usually classified according to its eccentricity as follows:

$\epsilon < 1$ ellipse

$\epsilon = 1$ parabola

$\epsilon > 1$ hyperbola

In particular, when $\epsilon = 0$, the conic becomes a circle, a special case of ellipse. In any case one of the foci of a Keplerian conic coincides with the field center. The second focus of a parabola is being considered as at infinity; while the two foci coincide in the case a circle. Besides, a Keplerian hyperbola refers only to the concave branch of a geometrical hyperbola, since this is the only branch that can be realized in a central gravity field.

It is to be noted that the usual practice of classifying a Keplerian conic according to its eccentricity as outlined above may run into difficulties when the conic degenerates. For example, a Keplerian ellipse may degenerate into a line segment, and a Keplerian parabola or hyperbola may degenerate into a straight line, and they will all have their eccentricities equal to unity. This is the case encountered in a vertical shoot. A better way of classification is to use either the orbital energy k, or the speed parameter, λ, which, as introduced in References 35 and 36 is defined as

$$\lambda \equiv \frac{V}{V^*} = \frac{V}{\sqrt{2}V_s} \tag{1.7}$$

where V^* and V_s are the local escape speed and the local circular speed respectively, given by

$$V^* = \sqrt{2}\, V_s = \sqrt{\frac{2\mu}{r}} \tag{1.8}$$

These two parameters λ and k are related through the energy integral,

$$\lambda^2 - 1 = \frac{rk}{\mu} \tag{1.9}$$

By using λ or k, a Keplerian conic may be classified as follows:

$\lambda < 1 \quad (k < 0)$ ellipse

$\lambda = 1 \quad (k = 0)$ parabola

$\lambda > 1 \quad (k > 0)$ hyperbola

In particular,

$\lambda = \frac{1}{\sqrt{2}} \left(k = -\frac{V_s^2}{2}\right)$ circle

There is no ambiguity in such a classification even when the conic degenerates. The dimensionless parameter λ is especially convenient in formulating nondimensional equations, and it will be extensively used in such formulations in the subsequent development.

2. THE HODOGRAPH EQUATIONS

In Reference 2, Hamilton proved his Law of Circular Hodograph without referring to a particular coordinate system except it is understood to be an inertial one. In the following a formal derivation of the hodograph equation for the polar version will be given first, and then the transformation to the Hamiltonian version will follow.

2.1 The Polar Hodograph Equation

Consider the velocity components in the local radial and transversal directions respectively:

$$V_r = \dot{r} \tag{2.1}$$

$$V_\theta = r\dot{\theta}$$

The momentum integral gives

$$rV_\theta = h \tag{2.2}$$

and the vis viva integral gives

$$\frac{1}{2} V^2 - \frac{\mu}{r} = k \tag{2.3}$$

where

$$V^2 = V_r^2 + V_\theta^2 \tag{2.4}$$

and h and k are the angular momentum and orbital energy respectively, which are the constants of the motion. Eliminating r from Equations (2.2) and (2.3) and using Equation (2.4) yields the hodograph equation,

$$V_r^2 + \left(V_\theta - \frac{\mu}{h}\right)^2 = \left(\frac{\mu}{h}\right)^2 + 2k \tag{2.5}$$

which may be put in the alternate form,

$$V_r^2 + \left(V_\theta - \frac{\mu}{h}\right)^2 = \left(\epsilon \frac{\mu}{h}\right)^2 \qquad (2.5a)$$

through the orbital relation (1.5)

Thus the hodograph in the V_r, V_θ plane is a circle regardless of the magnitude of ϵ or the type of the orbit. As seen from Equation (2.5a) such a polar hodograph circle has its center on the V_θ-axis, and is characterized by the two parameters,

$$\begin{aligned} \text{Origin-to-center distance} &= \frac{\mu}{h} \\ \text{Radius} &= \epsilon \frac{\mu}{h} \end{aligned} \qquad (2.6)$$

the ratio of which gives the orbital eccentricity. Consequently the hodograph origin will be outside the hodograph circle if the orbit is elliptic, inside the circle if it is hyperbolic, and on the circumference if it is parabolic. The geometry of the polar hodograph for the three types of the Keplerian orbit is shown in Figure I-1. In the particular case of a circular orbit ($\epsilon = 0$) the polar hodograph circle shrinks to its centerpoint.

It is to be noted that the velocity-coordinate system employed here is a local system attached to the orbiting mass instead of being fixed in an inertial frame like that in the Hamiltonian hodograph. The foregoing derivation shows that Hamilton's Law of Circular Hodograph for an inertial frame may well be extended to such a non-inertial frame. It is in fact a direct consequence of the two first integrals of the equation of motion, the momentum integral and the vis viva integral.

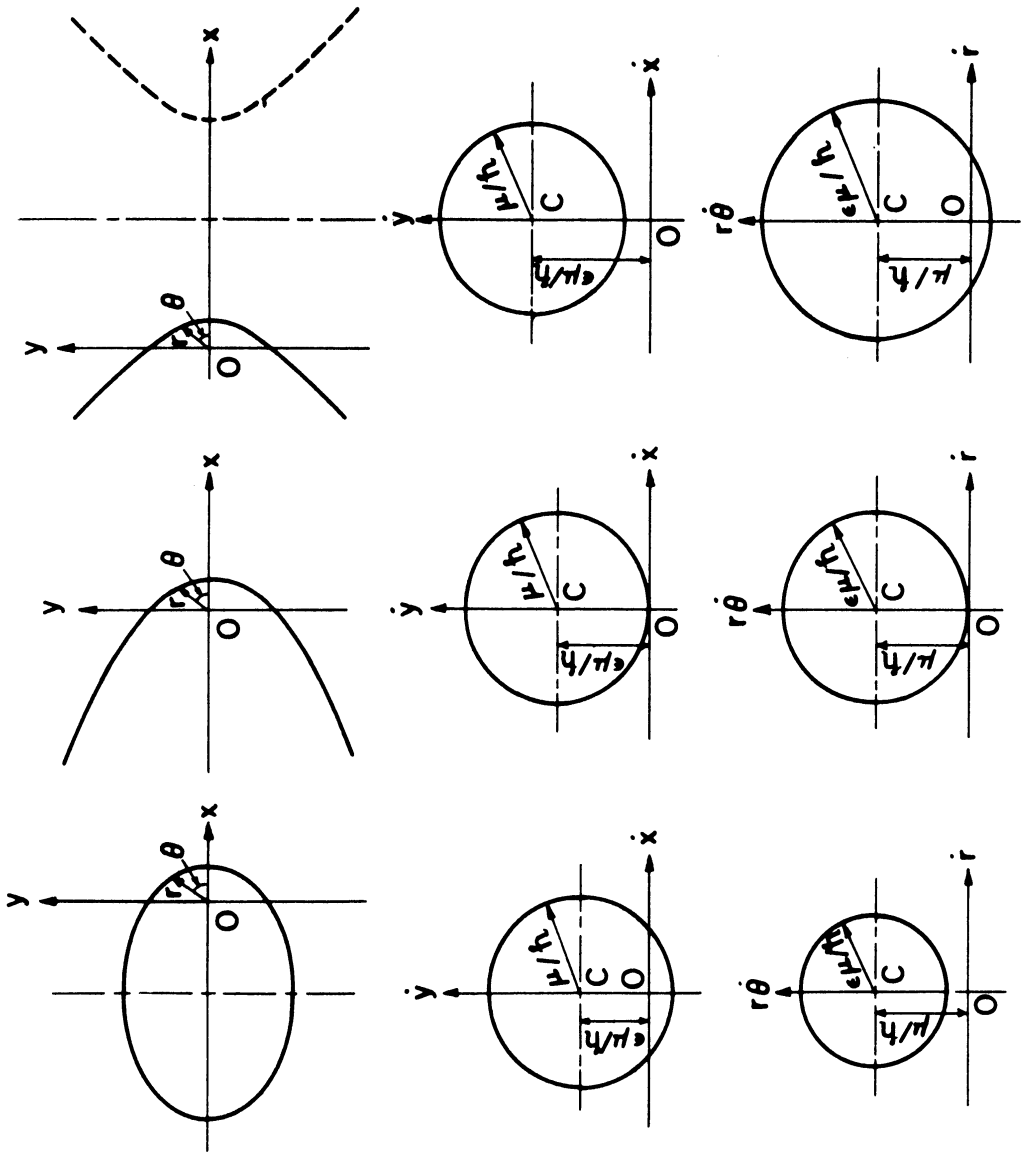

Figure I-1 The Keplerian Orbits and Their Hodograph Images.

Finally some sign convention in connection with the polar hodograph should be mentioned. For convenience V_θ will be taken positive in the direction of motion, and so is h,[2.1] while V_r will be taken positive if it directs away from the field center, and negative if towards it. It is to be noted that, in deriving Equation (2.5) we have virtually assumed $h \neq 0$. Such a condition will be generally assumed throughout the following analysis. When $h = 0$, V_θ will vanish at every orbital point according to the momentum integral (2.2), and we have a straight orbit. Special treatment will be given to such degenerate cases when they arise later in particular problems.

2.2 The Hamiltonian Hodograph Equation

As mentioned earlier, the Hamiltonian hodograph refers to an inertial frame. For convenience let us choose a righthand rectangular coordinate system (x,y) fixed in the orbit plane with its origin at the field center and its x-axis coinciding with the apsidal axis of the orbit and pointing toward the pericenter, so that its y-axis is along the latus rectum. Then proceeding from the polar hodograph equation (2.5a) and using the transformation

$$\begin{aligned} V_r &= \dot{x}\cos\theta + \dot{y}\sin\theta \\ V_\theta &= -\dot{x}\sin\theta + \dot{y}\cos\theta \end{aligned} \tag{2.7}$$

we obtain

$$\dot{x}^2 + \left(\dot{y} - \epsilon\frac{\mu}{h}\right)^2 = \left(\frac{\mu}{h}\right)^2 \tag{2.8}$$

2.1 Such a convention is possible only when only one orbit is being considered. If two or more coplanar orbits are under consideration, V_θ and hence h may be positive or negative.

which is the equation for the Hamiltonian hodograph in rectangular coordinates. It is evident that it is a circle in the $\dot{x},\dot{y}$-plane with its center on the $\dot{y}$-axis , and characterized by the parameters

$$\begin{aligned} \text{Origin-to-center distance} &= \epsilon \frac{\mu}{h} \\ \text{Radius} &= \frac{\mu}{h} \end{aligned} \tag{2.9}$$

the ratio of which is again the orbital eccentricity. It is interesting to see that, by merely interchanging the origin-to-center distance and the radius of the circle we may transform the polar hodograph to Hamiltonian hodograph and vice versa. Evidently the hodograph origin will be inside the Hamiltonian hodograph circle if the orbit is elliptic, outside the circle if it is hyperbolic, and on the circumference if it is parabolic. Thus the Hamiltonian hodograph and the polar hodograph are identical in the case of a parabolic orbit ($\epsilon = 1$). For a circular orbit ($\epsilon = 0$) the Hamiltonian circle is centered at the origin. The geometry of the Hamiltonian hodograph for the three principal types of the Keplerian orbit is shown in Figure I-1.

3. CORRELATION BETWEEN THE ORBITAL PLANE AND THE HODOGRAPH PLANE

As a basic characteristic of the Keplerian motion there is an unique velocity vector at each orbital point on a given orbit, and vice versa. It follows that there is a one-to-one correspondence between the position vector $\vec{r}$ in the physical space and the velocity vector $\vec{V}$ in the velocity space. Thus the hodographic representation of a Keplerian orbit may be regarded as a mapping of the orbit in the orbital plane onto the hodograph plane. Every orbital point Q has an unique hodograph image (which is the tip of the corresponding velocity vector and will also be designated as Q so long as no confusion arises) in the hodograph plane, and vice versa. Consequently, to each geometrical element in the hodograph some physical significance concerning the orbit can be attached; and conversely, each orbital element, geometric or dynamic, can be represented by a geometrical element or a combination of the geometrical elements of the hodograph. The establishment of such correlations between the orbital plane and the hodograph plane is thus a pre-requisite for the use of the orbital hodographs as means for the solution of orbital problems. In the following, such correlation will be first established for a Keplerian orbit in general, and then for each of the three principal types of the orbit, the elliptic, the parabolic, and the hyperbolic.

3.1 General Correlations

The correlations between the orbital elements and the geometrical elements in the circular hodograph in either the $\dot{x},\dot{y}$- or the $\dot{r}$, $r\dot{\theta}$-plane can be easily established from the geometrical construction of the hodograph and the definition of these orbital elements with the aid of a few

basic orbital relations. These principal correlations for a general Keplerian orbit are depicted in Figure I-2.[3.1] A few essential correlation rules for each version of the hodograph will be given below.

On the Hamiltonian Hodograph (see Figure I-2b)

(H-1) Directly from the hodograph construction the orbital velocity and its x, y-components are given by

$$\begin{aligned} \vec{V} &= \overrightarrow{OQ} \\ \vec{V}_x &= \overrightarrow{OX} \\ \vec{V}_y &= \overrightarrow{OY} \end{aligned} \tag{3.1}$$

with its inclination to the apsidal axis,

$$\beta = \sphericalangle \dot{x}OQ \tag{3.2}$$

where the point Q on the hodograph circle is the image of the orbital point Q in the physical plane.

(H-2) For the radial and transversal velocity components, we observe from the definition of a hodograph (see Introduction, p. 1) that the tangential direction at any point on a hodograph is in the direction of the local acceleration, and in a central field this must be the local radial direction. This is, in fact, the basis on which Hamilton proved his Law of the Circular Hodograph,(2) and constitutes the fundamental characteristic of the Hamiltonian hodograph. It enables us to establish immediately that the radius CQ of the hodograph circle at the point Q is in the local transversal direction, and consequently by completing the right triangle OSQ in the hodograph plane we find

$$\vec{V}_r = \overrightarrow{OS} \ , \quad \vec{V}_\Theta = \overrightarrow{SQ} \tag{3.3}$$

3.1 The auxiliary circle in each hodograph plane is drawn to facilitate the geometrical constructions.

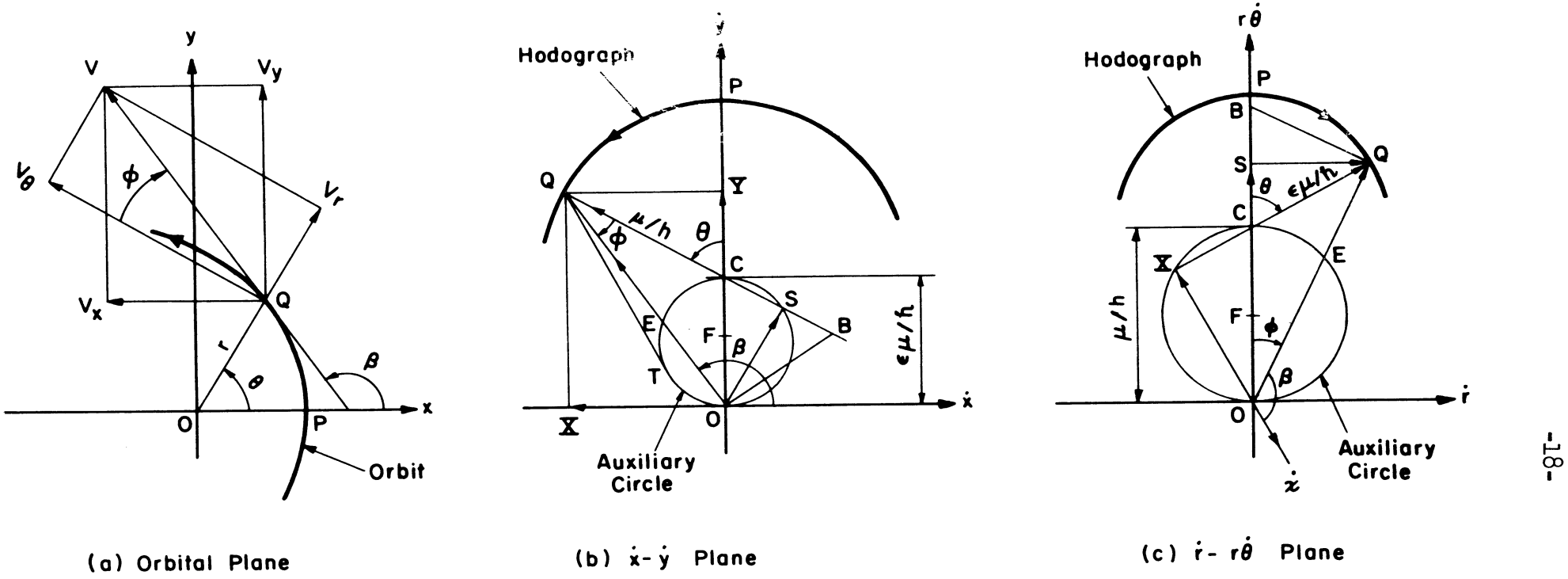

(a) Orbital Plane

(b) $\dot{x}$-$\dot{y}$ Plane

(c) $\dot{r}$- $r\dot{\theta}$ Plane

Figure I-2. General Correlation Between the Orbital Plane and the Hodograph Planes

TABLE I-1

GENERAL CORRELATIONS BETWEEN THE ORBITAL PLANE AND THE HODOGRAPH PLANES

	Orbital Element		$\dot{x}$-$\dot{y}$ Plane	$\dot{r}$-$\dot{r\theta}$ Plane	Remark
1	Orbital Velocity	$\vec{V}$	$\vec{OQ}$	$\vec{OQ}$	
2	x-component	$\vec{V}_x$	$\vec{OX}$	$\vec{OX}$	
3	y-component	$\vec{V}_y$	$\vec{OY} = \vec{XQ}$	$\vec{XQ}$	
4	r-component	$\vec{V}_r$	$\vec{OS}$	$\vec{SQ}$	$\overline{SQ} \perp r\dot{\theta}$-axis
5	θ-component	$\vec{V}_\theta$	$\vec{SQ}$	$\vec{OS}$	
6	Inclination Angle	β	$\sphericalangle \dot{x}OQ$	$\sphericalangle \dot{x}OQ$	
7	True Anomaly	θ	$\sphericalangle PCQ$	$\sphericalangle PCQ$	
8	Path Angle	ϕ	$\sphericalangle CQO$	$\sphericalangle COQ$	
9	Eccentricity	ϵ	$\overline{OC}/\overline{CQ}$	$\overline{CQ}/\overline{OC}$	
10	Local Circular Speed	V_S^2	$\overline{OQ}\cdot\overline{OE} = \overline{QT}^2$	$\overline{OQ}\cdot\overline{OE} = \overline{OC}\cdot\overline{OS}$	$\overline{QT}$ tangent to auxiliary circle at T
11	Local Speed Ratio	λ^2	$\overline{BQ}/2\ \overline{CO}$	$\overline{OB}/2\ \overline{OC}$	$\overline{OB} \perp \overline{OQ}$ ($\dot{x}$-$\dot{y}$) $\overline{BQ} \perp \overline{OQ}$ ($\dot{r}$-$r\dot{\theta}$)
12	Radial Distance	r	$\frac{\mu}{\overline{OQ}\cdot\overline{EQ}} = \frac{\mu}{\overline{QT}^2}$	$\frac{\mu}{\overline{OQ}\cdot\overline{OE}} = \frac{\mu}{\overline{OC}\cdot\overline{OS}}$	
13	Angular Momentum	J	$\mu/\overline{CQ}$	$\mu/\overline{OC}$	

Notes: 1) For the symbols, see Figure I-2.
2) The positive directions of the angular measurements in the orbital plane are arbitrarily chosen as indicated in Figure I-2 (a) and the corresponding directions in the hodograph plane are shown in Figure I-2 (b) and (c).

(H-3) It follows directly from the rules (H-1) and (H-2) that the true anomaly is given by the central angle made by the radius CQ with the y-axis, i.e.,

$$\theta = \sphericalangle PCQ \tag{3.4}$$

and the path angle with reference to the transversal direction or the local horizon is given by the angle included between CQ and OQ, i.e.,

$$\phi = \sphericalangle CQO \tag{3.5}$$

The positive direction of each of these angular measurements including that of β has been indicated in Figure I-2 (a) and (b) in consistence with the sign conventions of the various velocity components.

(H-4) The orbital eccentricity has already been shown by the ratio of the origin-to-center distance to the radius of the hodograph circle, i.e.,

$$\epsilon = \overline{OC}/\overline{CQ} \tag{3.6}$$

(H-5) The local circular speed at any orbital point Q can be obtained from the hodograph by simply drawing a tangent from its image point Q on the hodograph circle to the auxiliary circle at T, giving

$$V_S = \overline{QT} \tag{3.7}$$

A proof is given in Appendix B.

(H-6) With V_S thus determined the speed parameter λ is also determined since according to definition $\lambda = V/V^* = V/\sqrt{2}V_S$. However, since usually it is λ^2 which occurs frequently in orbit analysis, a direct method for its graphical determination is to drop a line OB from the hodograph origin perpendicular to the velocity $\overrightarrow{OQ}$, meeting CQ or its extension at B, then we have

$$\lambda^2 = \frac{1}{2}\frac{\overline{BQ}}{\overline{CQ}} \tag{3.8}$$

A proof is also given in Appendix B.

(H-7) Since the circular speed is uniquely related to the radial distance of the orbital point from the center of the field through the formula $V_s^2 = \mu/r$, the latter can be determined once the former is found. Thus, with the field constant μ known, the value of r may be determined from

$$r = \frac{\mu}{QT^2} \tag{3.9}$$

(H-8) Directly from the hodograph equation, the angular momentum of the orbital motion is given by the radius of the Hamiltonian hodograph circle according to

$$h = \frac{\mu}{CQ} \tag{3.10}$$

All these rules are summarized in Table I-1.

On the Polar Hodograph (see Figure I-2c)

(P-1) By its construction the polar hodograph gives directly the orbital velocity and its radial and transversal components,

$$\begin{aligned} \vec{V} &= \vec{OQ} \\ \vec{V}_r &= \vec{SQ} \\ \vec{V}_\Theta &= \vec{OS} \end{aligned} \tag{3.11}$$

as viewed from the local reference frame. Its path angle is given by

$$\phi = \sphericalangle\, COQ \tag{3.12}$$

(P-2) Similar to the Hamiltonian hodograph the true anamoly is given by the central angle made by the radius CQ with the $r\dot{\Theta}$ - axis, i.e.,

$$\Theta = \sphericalangle\, PCQ \tag{3.13}$$

A proof is given in Appendix B.

(P-3) It follows from rule (P-2) that the x, y-components of the orbital velocity can be obtained from the polar hodograph by completing the right

triangle OXQ, giving

$$\vec{V}_x = \vec{OX} \,, \quad \vec{V}_y = \vec{XQ} \tag{3.14}$$

Thus while the tangential direction along a Hamiltonian hodograph points in the local radial direction; that along a **polar** hodograph points in the constant direction (in the inertial space) - the direction of the apsidal axis.

(P-4) Directly from rule (P-3) we see that the inclination of the orbital velocity vector to the apsidal axis of the orbit is given by the angle between the vector $\vec{OQ}$ and the tangent to the polar hodograph circle at Q, or we may write

$$\beta = \measuredangle \dot{x}OQ \tag{3.15}$$

(P-5) The orbital eccentricity, as mentioned before, is given by the ratio

$$\epsilon = \overline{CQ}/\overline{OC} \tag{3.16}$$

(P-6) The local circular speed at any orbital point is given by the geometrical mean of the origin-to-center distance and the Θ-component of the orbital velocity at that point, that is,[3.2]

$$V_s^2 = \overline{OC} \cdot \overline{OS} \tag{3.17}$$

(P-7) The speed parameter λ at any orbital point Q may be found from the polar hodograph by drawing a line from the image point Q on the hodograph circle perpendicular to the velocity vector OQ, meeting the $r\dot{\Theta}$-axis at B, giving[3.2]

$$\lambda^2 = \frac{1}{2} \frac{\overline{OB}}{\overline{OC}} \tag{3.18}$$

(P-8) Following Rule (P-6) the radial distance at any orbital point Q may be found from the polar hodograph according to

$$r = \frac{\mu}{\overline{OC} \cdot \overline{OS}} \tag{3.19}$$

[3.2] The proofs of Rules (P-6) and (P-7) are similar to those of the Rules (H-5) and (H-6) respectively as shown in Appendix B, and are therefore omitted.

(P-9) In contrast with the Hamiltonian hodograph the angular momentum of the orbital motion is now given by the origin-to-center distance in the polar hodograph according to

$$h = \frac{\mu}{\overline{OC}} \tag{3.20}$$

All these rules are also summarized in Table I-1.

Finally it is well to note that the hodograph circle is symmetrical with respect to the $\dot{y}$-axis in the $\dot{x}$-$\dot{y}$ plane, or the $r\dot{\theta}$ -axis in the $\dot{r}$-$r\dot{\theta}$ plane. Consequently, at the orbital points symmetrically situated with respect to the apsidal axis, the magnitudes of the orbital velocities, and their $\dot{y}$-components and θ-components are identical respectively, while their $\dot{x}$-components and $\dot{r}$-components are equal in magnitudes but opposite in sign.

3.2 The Elliptic Orbit (see Figure I-3)

The hodograph circle for an elliptic orbit encloses the origin in the $\dot{x}$-$\dot{y}$ plane, cutting each axis at two distinct points. The intersection points on $\dot{y}$-axis, P and A, give the images of the pericenter and apocenter of the orbit respectively; while those on $\dot{x}$-axis give the images of the ends of the minor axis, N and N'. However, in $\dot{r}$-$r\dot{\theta}$ plane, the hodograph circle lies entirely above the $\dot{r}$-axis, meeting it at no real points. While the intersection points on $r\dot{\theta}$ -axis give the images of the two apses, the points where the radial lines from the origin touch the hodograph circle (which are also the intersection points of the auxiliary circle and the hodograph circle) give the images of the ends of the minor axis. In both hodograph planes, the image of the ends of the latus rectum are located midway between P and A. A glance at either hodograph shows clearly

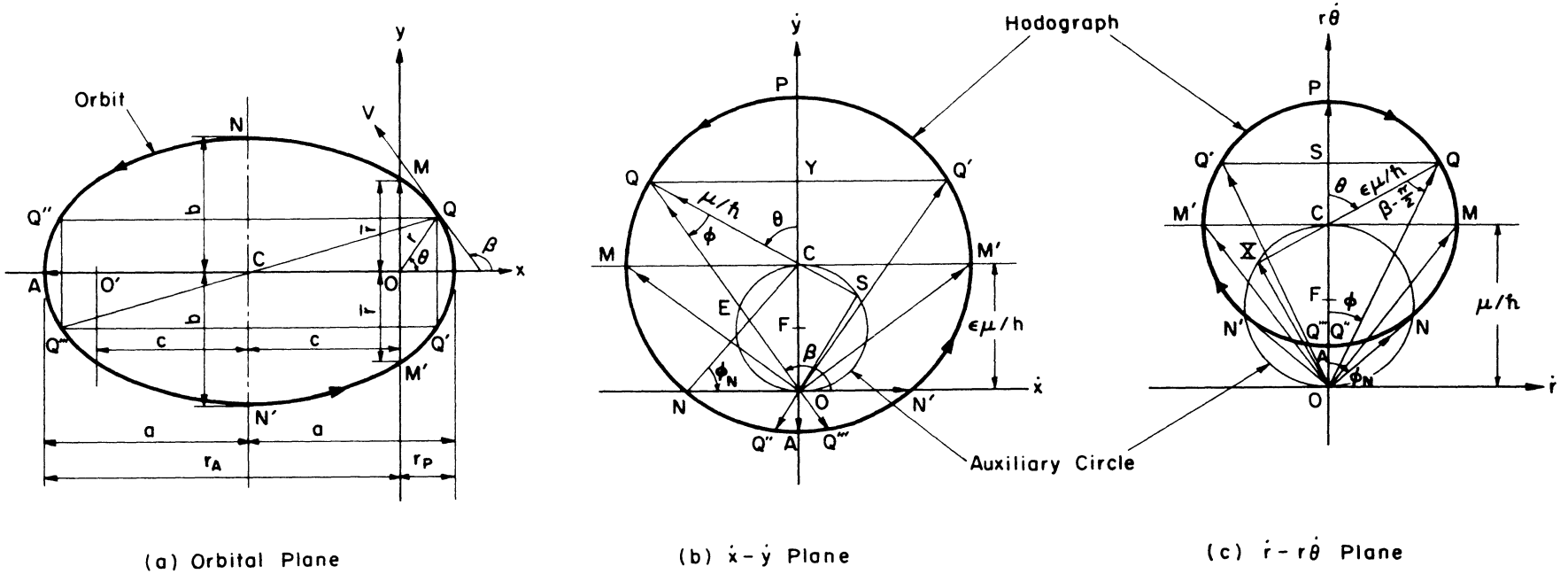

Figure I-3. The Elliptic Orbit and Its Hodograph Images

that

$$V_P = \overline{OP} = V_{max} \tag{3.21}$$

$$V_A = \overline{OA} = V_{min} \tag{3.22}$$

$$|\phi_{N,N'}| = \measuredangle CNO = |\phi|_{max} \tag{3.23}$$

Besides the particular points mentioned above, it is to be noted that each radial line from the origin may cut the hodograph in two distinct points, which, in the x-y plane correspond to the extremities of a diameter of the ellipse; and, in the $\dot{r}$-$r\dot{\theta}$ plane, the orbital points symmetrically situated with respect to the minor axis. Let Q', Q" and Q'" be the points symmetrical with the orbital point Q with respect to the major axis, the minor axis, and the center of the ellipse respectively (Figure I-3a), the corresponding images in each hodograph plane are shown in Figure I-3b and c.

The principal geometrical elements of the orbit, such as the semi-axes a and b, the semi-latus rectum $\bar{r}$, the peri-and-apo-radii r_P and r_A, may be found from the hodograph by applying the general correlation formula (3.9 or 3.19), and recalling their definitions. The results are given in Table I-2.

Finally, with the semi-major axis, a, found from the hodograph, the orbital energy k for a unit orbiting mass is also determined since

$$k = -\frac{\mu}{2a} = -\frac{1}{2}\overline{ON}^2 \tag{3.24}$$

The graphical determination of the eccentric anomaly for an elliptic orbit, will be given in Chapter 5.

TABLE I-2

CORRELATIONS BETWEEN THE ORBIT PLANE AND THE HODOGRAPH PLANES
FOR THE THREE TYPES OF THE KEPLERIAN ORBITS

			Elliptic Orbit		Hyperbolic Orbit		Parabolic Orbit
			$\dot{x}$-$\dot{y}$ Plane	$\dot{r}$-$r\dot{\theta}$ Plane	$\dot{x}$-$\dot{y}$ Plane	$\dot{r}$-$r\dot{\theta}$ Plane	$\dot{x}$-$\dot{y}$ Plane $\dot{r}$-$r\dot{\theta}$
1	Velocity at Pericenter	$\vec{V}_P$	$\vec{OP}$	$\vec{OP}$	$\vec{OP}$	$\vec{OP}$	$\vec{OP}$
2	Velocity at Apocenter	$\vec{V}_A$	$\vec{OA}$	$\vec{OA}$	--	--	--
3	Velocity at End of Latus Rectum	$\vec{V}_{M,M'}$	$\vec{OM}$, $\vec{OM'}$	$\vec{OM}$, $\vec{OM'}$	$\vec{OM}$, $\vec{OM'}$	$\vec{OM}$, $\vec{OM'}$	$\vec{OM}$, $\vec{OM'}$
4	Velocity at End of Minor-Axis	$\vec{V}_{N,N'}$	$\vec{ON}$, $\vec{ON'}$	$\vec{ON}$, $\vec{ON'}$	--	--	--
5	Velocity at Infinity	$\vec{V}_{I,I'}$	--	--	$\vec{OI}$, $\vec{OI'}$	$\vec{OI}$, $\vec{OI'}$	0
6	Path Angle at End of Minor-Axis	$\phi_{N,N'}$	$\sphericalangle$ CNO, $\sphericalangle$ CN'O	$\sphericalangle$ CON, $\sphericalangle$ CON'	--	--	--
7	Direction Angle of Asymptote	γ	--	--	$\sphericalangle$ OCI, $<$ OCI'	$\sphericalangle$ OCI, $\sphericalangle$ OCI'	--
8	Eccentric Anomaly	α	$\sphericalangle$ PCD	$\sphericalangle$ PCD	$\sphericalangle$ PCD	$\sphericalangle$ PCD	--
9	Semilatus Rectum	$\bar{r}$	$\mu/\overline{CQ}^2$	$\mu/\overline{OC}^2$	$\mu/\overline{CQ}^2$	$\mu/\overline{OC}^2$	$\mu/\overline{OC}^2$
10	Pericenter Distance	r_P	$\mu/\overline{OP} \cdot \overline{CP}$	$\mu/\overline{OP} \cdot \overline{OC}$	$\mu/\overline{OP} \cdot \overline{CP}$	$\mu/\overline{OP} \cdot \overline{OC}$	$\mu/2\overline{OC}^2$
11	Apocenter Distance	r_A	$\mu/\overline{OA} \cdot \overline{CA}$	$\mu/\overline{OA} \cdot \overline{OC}$	$\mu/\overline{OA} \cdot \overline{AC}$	$\mu/\overline{AO} \cdot \overline{OC}$	--
12	Semimajor Axis	a	$\mu/\overline{ON}^2$	$\mu/\overline{ON}^2$	$\mu/\overline{OI}^2$	$\mu/\overline{OI}^2$	∞
13	Semiminor Axis	b	$\mu/\overline{ON} \cdot \overline{CN}$	$\mu/\overline{ON} \cdot \overline{OC}$	$\mu/\overline{OI} \cdot \overline{CI}$	$\mu/\overline{OI} \cdot \overline{OC}$	--
14	Orbital Energy	k	$-\frac{1}{2}\overline{ON}^2$	$-\frac{1}{2}\overline{ON}^2$	$\frac{1}{2}\overline{OI}^2$	$\frac{1}{2}\overline{OI}^2$	0

(For the symbols, see Figures I-3, 4 and 5)

3.3 The Hyperbolic Orbit (See Figure I-4)

The hodograph circle in $\dot{x}$-$\dot{y}$ plane for an hyperbolic orbit lies entirely above the $\dot{x}$-axis; while that in the $\dot{r}$-$r\dot{\theta}$ plane encloses the origin. However, as mentioned in Section 1.2, in a central gravity field, only the concave branch of the hyperbola can be realized, consequently, only a part of the hodograph circle gives the image of the physical orbit. As shown in Figure I-4, while a mass particle moves along an hyperbolic orbit from negative infinity to positive infinity via the pericenter, the velocity vector describes a circular arc from I' to I via P (full line in Figure I-4), where P is the image of the pericenter of the hyperbola, and I and I', the images of the points at infinity. In $\dot{x}$-$\dot{y}$ plane, I and I' are the points where the radial lines from the origin touch the hodograph circle (which are also the intersection points of the auxiliary circle and the hodograph circle); and, in the $\dot{r}$-$\dot{r}\theta$ plane, they are the points where the hodograph circle cuts the $\dot{r}$-axis. The circular arc I'AI in either hodograph plane (dotted line) corresponds to the image of the convex branch of the hyperbola (dotted line), which has physical meaning in a central repulsive field but not a gravity field. A discussion of this branch is found in Reference 12 (Section X).

With our attention fixed on the full line part either hodograph shows clearly that

$$V_P = \overline{OP} = V_{max} \tag{3.25}$$

$$V_{I,I'} = \overline{OI} = V_{min} \tag{3.26}$$

$$|\phi_{I,I'}| = \frac{\pi}{2} = |\phi|_{max} \tag{3.27}$$

$$\beta_I = \pi - \gamma = \beta_{max} \tag{3.28}$$

$$\beta_{I'} = \gamma = \beta_{min} \tag{3.29}$$

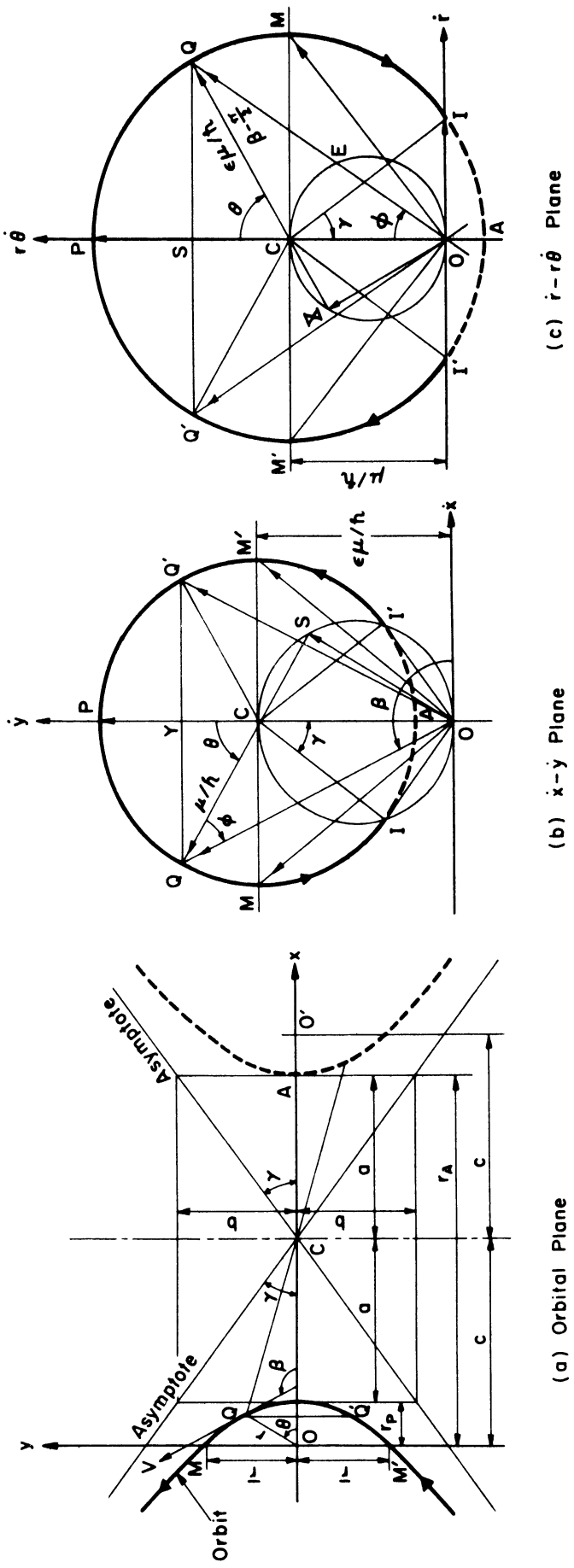

Figure I-4. The Hyperbolic Orbit and Its Hodograph Images

Furthermore, in analogy with the elliptic orbit, all the principal orbital elements of the hyperbolic orbit may be found from the hodograph, and the results for both orbits are quite similar, with the point I (or I') on the hyperbolic orbit plays the counter-part of the point N (or N') on an elliptic orbit. For example, the corresponding formula for the orbital energy of an hyperbolic orbit is

$$k = \frac{1}{2} \overline{OI}^2 \tag{3.30}$$

Finally it is to be noted here that, although the apocenter A lies now on the fictitious branch of the hyperbola, the quantity "apocenter radius" still plays an important role as a geometrical parameter of the orbit, and the part of the hodograph circle which corresponds to this branch may be employed to develop the orbital relations if needed since it satisfies the hodograph equations (2.5, 2.8) just as well if r is taken as negative. All these results are listed in Table I-2. For the eccentric anomaly of a hyperbolic orbit, see Chapter 5.

3.4 The Parabolic Orbit (see Figure I-5)

The hodograph for a parabolic orbit is the simplest of all three. It is a circle tangent to the $\dot{x}$-axis at the origin in $\dot{x}$-$\dot{y}$ plane, and tangent to the $\dot{r}$-axis at the origin in $\dot{r}$-$r\dot{\theta}$ plane. In fact, the hodograph circles are identical in both planes, with the direct consequence

$$V_x = -V_r \ , \quad V_y = V_\theta \tag{3.31}$$

As shown in Figure 5, the pericenter of the orbit is mapped into the point P on $\dot{y}$- or $r\dot{\theta}$-axis, and the points at infinity are

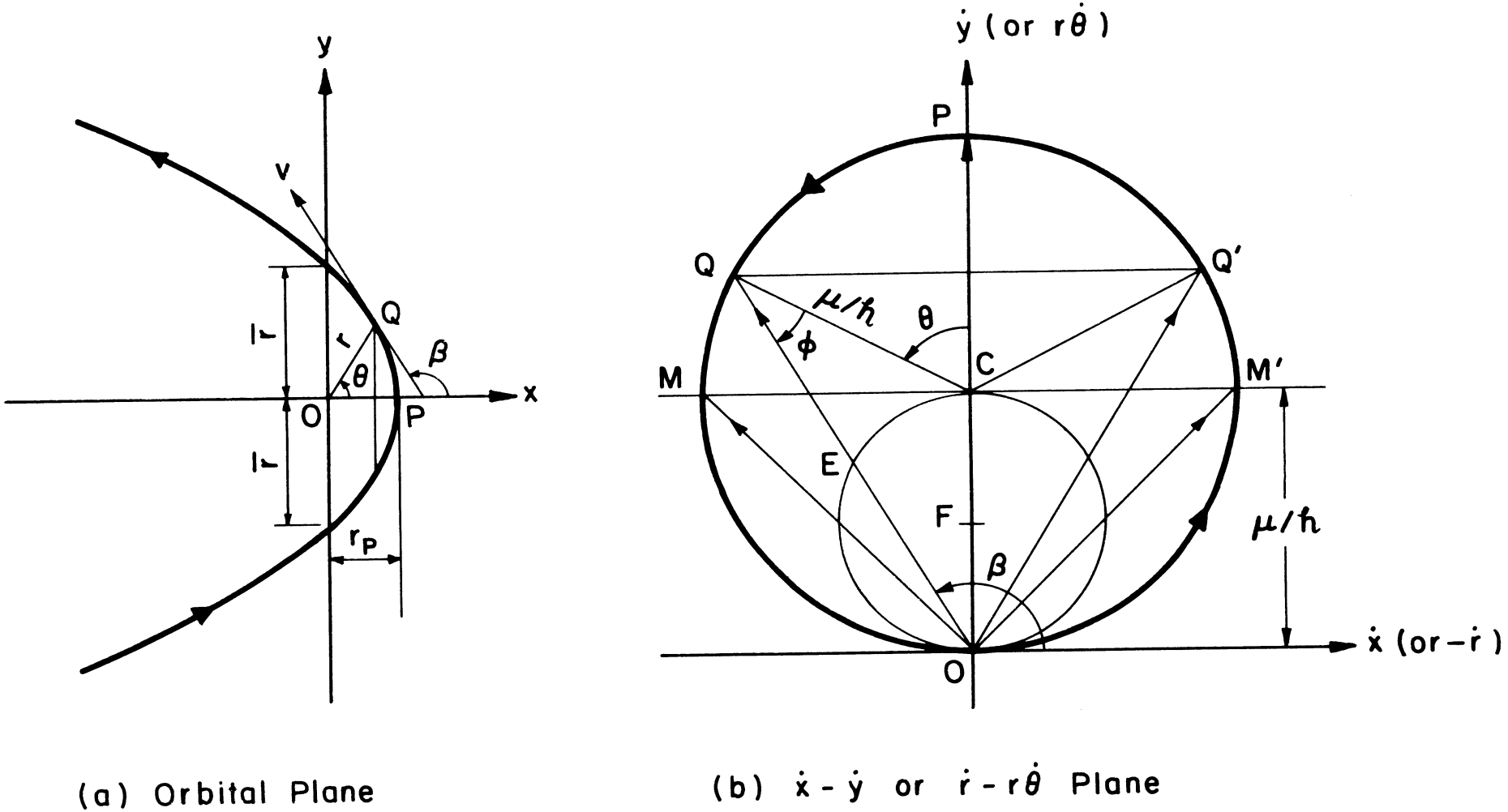

(a) Orbital Plane

(b) $\dot{x}$ - $\dot{y}$ or $\dot{r}$ - $r\dot{\theta}$ Plane

Figure I-5. The Parabolic Orbit and Its Hodograph Images

mapped into the single point, the origin. A glance of the hodograph shows that

$$V_P = \overline{OP} = V_{max} \tag{3.32}$$

$$V_\infty = 0 \quad = V_{min} \tag{3.33}$$

It also shows that, at every point,

$$\phi = \frac{1}{2}\theta \tag{3.34}$$

which is a peculiar feature of the parabolic orbit; and in particular, at either end of the latus rectum, we have

$$|\phi_{M,M'}| = \frac{\pi}{4} \tag{3.35}$$

As the parabolic orbit is the limiting case of an elliptic or hyperbolic orbit as its major axis approaches infinity, all formulas previously deduced for either one may be applied to parabolic orbit. The results are also summarized in Table I-2.

4. SOME ELEMENTARY APPLICATIONS OF THE ORBITAL HODOGRAPH

4.1 The Exploration of Orbital Characteristics

As seen in the preceding chapter the characteristics of the Keplerian motion exhibit themselves quite naturally following the development of the orbital hodographs. To mention a few more, the hodograph in either plane shows that there is a maximum path angle (magnitude) for each elliptic orbit, and it occurs at either end of the minor axis. It also shows that, at every orbital point

$$\lambda \begin{matrix} < \\ = \\ > \end{matrix} 1, \quad \phi \begin{matrix} < \\ = \\ > \end{matrix} \frac{1}{2}\theta \qquad \text{if the orbit is} \begin{cases} \text{elliptic} \\ \text{parabolic} \\ \text{hyperbolic} \end{cases}$$

Such a manifestation of the orbital characteristics through the geometry of the hodograph is probably the most fundamental asset of the orbital hodograph as means of studying such motions. In fact it was with this in mind Hamilton introduced his circular hodograph. Probably one of the best examples is provided by the "invariant two-body velocity components theorem" which has been proved in classical mechanics (see for example, Reference 29) but brought to attention only very recently.[43,45] As demonstrated in Pesek's short note[16] it is so self-evident in the hodograph plane that its proof is almost trivial. To further illustrate such applications an additional example is given below.

Consider a Hamiltonian hodograph as shown in Figure I-6a, the change of velocity between two orbital points Q_1 and Q_2 is given by $\overrightarrow{Q_1Q_2}$. Let us draw CH perpendicular to Q_1Q_2, then by elementary geometry the central angle Q_1CQ_2 is bisected by CH. Now if we turn the lines CQ_1, CQ_2 and CH each through 90°, then CQ_1 and CQ_2

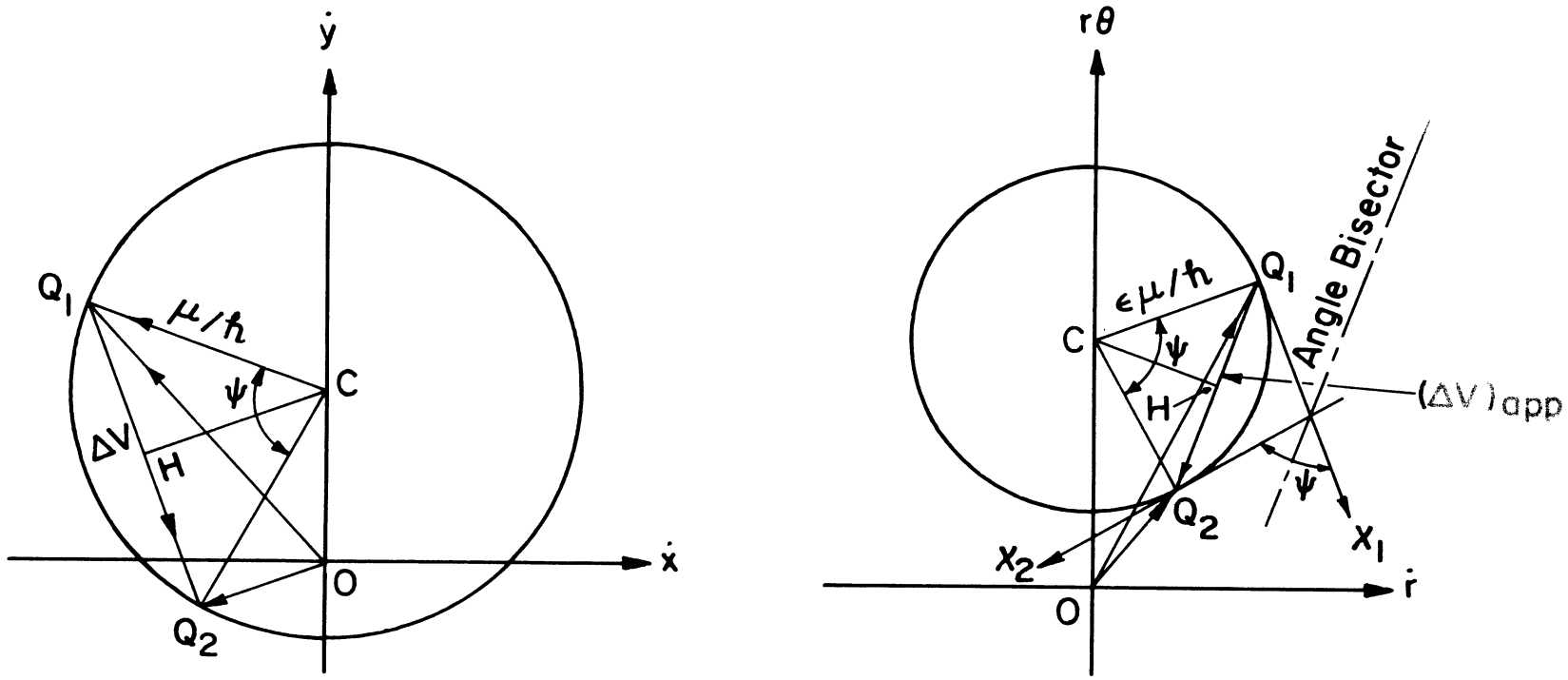

(a) Hamiltonian Hodograph

(b) Polar Hodograph

Figure I-6. Change of Orbital Velocity Along a Keplerian Orbit

will point in the radial directions of r_1 and r_2 respectively, while the line CH coincides with Q_1Q_2. Thus we may draw the conclusion that the vector change between the velocities at any two orbital points on a Keplerian orbit is parallel to the bisector of the angle between the radius vectors at these two points, a theorem proved analytically in Reference 37. This is true regardless of the type of the Keplerian orbit. Furthermore, the geometry of the hodograph shows that along a given Keplerian orbit the magnitude of the velocity change depends only on the angle of separation (ψ) of the two orbital points, or the change of the true anomaly, but not the position of these two points respectively. Such a velocity change is given directly by the hodograph as

$$\Delta V = 2 \frac{\mu}{h} \sin \frac{\psi}{2} \tag{4.1}$$

It is interesting to note that the same geometry is retained in the polar hodograph as shown in Figure I-6b; however, a different interpretation is needed. The vector $\overrightarrow{Q_1Q_2}$ now is not the true change of orbital velocity, but the apparent velocity change observed in the local frame, or the vehicle frame. The hodograph geometry shows that its direction is parallel to the bisector of the two apparent directions of the apsidal axis (or any other reference axis fixed in the inertial frame) as observed in this local frame at the orbital points Q_1 and Q_2 respectively. The magnitude of this apparent velocity change also depends on the angle of separation only, and the ratio of this apparent change to its absolute change is evidently same as the ratio of the radius of the polar hodograph circle to that of the Hamiltonian hodograph circle, that is

$$(\Delta V)_{app.} : (\Delta V)_{abs.} = \epsilon : 1 \tag{4.2}$$

where ϵ is the orbital eccentricity. From this equation we observe that, for the same angle of separation, the magnitude of the absolute change of velocity is greater than that of the apparent change on an elliptic orbit, but smaller than that on a hyperbolic orbit, while on a parabolic orbit they are equal.

More observations on the orbital characteristics from the hodograph geometry will be found in the later development in this dissertation. Also many more illustrations are found in References 7, 9, and 12.

4.2 Derivation of Orbital Relations

As pointed out in the beginning of Chapter 3, to each geometrical element in the hodograph plane we may attach some dynamic significance; consequently, to each geometrical relation in the hodograph plane there is a corresponding dynamic relation for the motion. By applying this principle of duality many orbital relations can be readily found from the hodograph. A few examples will be given below.

Consider the triangle OCQ in the $\dot{x}\dot{y}$-plane (Figure I-2b), and apply the Law of Cosines, giving

$$\overline{OQ}^2 = \overline{CQ}^2 + \overline{OC}^2 + 2\overline{CQ} \cdot \overline{OC} \cos\theta \qquad (4.3)$$

Writing

$$\overline{CQ} = \sqrt{\frac{\mu}{\bar{r}}}, \quad \overline{OC} = \epsilon \sqrt{\frac{\mu}{\bar{r}}} \qquad (4.4)$$

in accordance with Equations (1.6, 2.9), the foregoing equation gives immediately

$$V^2 = \frac{\mu}{\bar{r}} (1 + \epsilon^2 + 2\epsilon \cos\theta) \qquad (4.5)$$

which expresses the speed at any orbital point in terms of the true anomaly and the orbital constants ϵ and $\bar{r}$. This holds for a

Keplerian orbit in general. Now if we write, in $\dot{x}$-$\dot{y}$ plane, for an elliptic orbit

$$\overline{CQ} = \frac{1}{2}(V_P + V_A), \quad \overline{OC} = \frac{1}{2}(V_P - V_A) \tag{4.6}$$

the application of the same Cosine Law to the same triangle OCQ will lead to

$$V^2 = \frac{1}{2}[V_P^2 + V_A^2 + (V_P^2 - V_A^2)\cos\theta] \tag{4.7}$$

which expresses the orbital velocity in terms of the true anomaly and the maximum and minimum orbital speeds. The corresponding expression for an hyperbolic orbit may be obtained in the same way by writing

$$\overline{CQ} = \frac{V_P^2 - V_\infty^2}{2V_P}, \quad \overline{OC} = \frac{V_P^2 + V_\infty^2}{2V_P} \tag{4.8}$$

giving

$$V^2 = \frac{1}{2V_P^2}[V_P^4 + V_\infty^4 + (V_P^4 - V_\infty^4)\cos\theta] \tag{4.9}$$

All Equations (4.5), (4.7), and (4.9) can be obtained from the polar hodograph just as well, since the triangles OCQ in both hodograph planes are in fact identical.

In many simple cases the derivations are so trivial that the orbital relations can almost be written down immediately from a glance of the hodograph. For example, the geometry of the Hamiltonian hodograph (Figure I-2b) enables one to write readily

$$\begin{aligned} V_x &= \overline{YQ} = -\frac{\mu}{h}\sin\theta \\ V_y &= \overline{OC} + \overline{CY} = \frac{\mu}{h}(\epsilon + \cos\theta) \end{aligned} \tag{4.10}$$

while the polar hodograph (Figure I-2c) gives

$$\begin{aligned} V_r &= \overline{SQ} = \epsilon\frac{\mu}{h}\sin\theta \\ V_\theta &= \overline{OC} + \overline{CS} = \frac{\mu}{h}(1 + \epsilon\cos\theta) \end{aligned} \tag{4.11}$$

In fact many such simple relations have been written down in the previous analysis of the orbital hodographs in Chapter 3. Few more examples will be given in the next chapter, and still more are found in References 7, 9, and 12.

5. THE DIMENSIONLESS HODOGRAPHS AND THEIR APPLICATIONS

5.1 The Dimensionless Hodographs

The hodographs may be rendered dimensionless by using the non-dimensional velocity coordinates defined as

$$\mathring{x} = \frac{h}{\mu}\,\dot{x}\,, \qquad \mathring{y} = \frac{h}{\mu}\,\dot{y} \tag{5.1}$$

$$\mathring{R} = \frac{h}{\mu}\,\dot{r}\,, \qquad R\mathring{\theta} = \frac{h}{\mu}\,r\dot{\theta} \tag{5.2}$$

This amounts to changing the scale of the hodograph by a factor h/μ without altering its configuration. By introducing these new velocity coordinates into Equations (2.5a) and (2.8) we obtain the hodograph equations in the dimensionless form,

Hamiltonian version:

$$\mathring{x}^2 + (\mathring{y} - \epsilon)^2 = 1 \tag{5.3}$$

Polar version:

$$\mathring{R}^2 + (R\dot{\theta} - 1)^2 = \epsilon^2 \tag{5.4}$$

Consequently, the hodograph in the $\mathring{x}\mathring{y}$-plane is invariably a unit circle with its center-to-origin distance equal to ϵ; while in the $\mathring{R}, R\mathring{\theta}$-plane it is a circle of radius ϵ with its center-to-origin distance invariably equal to unity. The dimensionless hodographs, Hamiltonian and polar, for each of the three types of orbits are depicted in Figure I-7. It is to be noted that, in such dimensionless hodographs, while the angles still have the same physical significance as those in the ordinary hodographs, the line elements represent no longer the velocities, but the ratios of various orbital elements as indicated in Figure I-7. As these ratios follow directly from the previous correlation rules and the

Orbit	$\dot{x}$-$\dot{y}$ Plane	$\dot{\mathcal{R}}$-$\mathcal{R}\dot{\theta}$ Plane
Elliptic	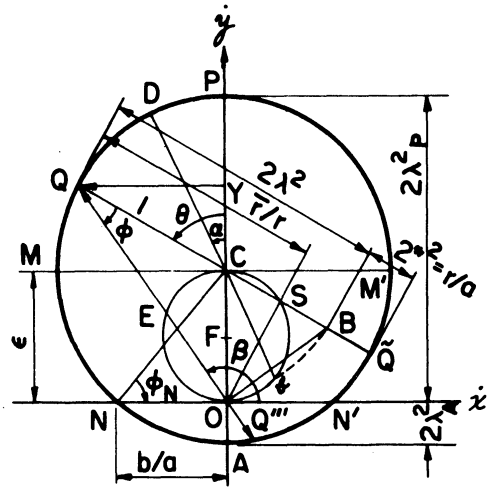	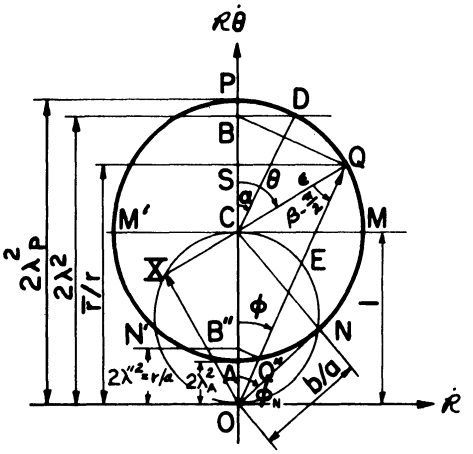
Hyperbolic	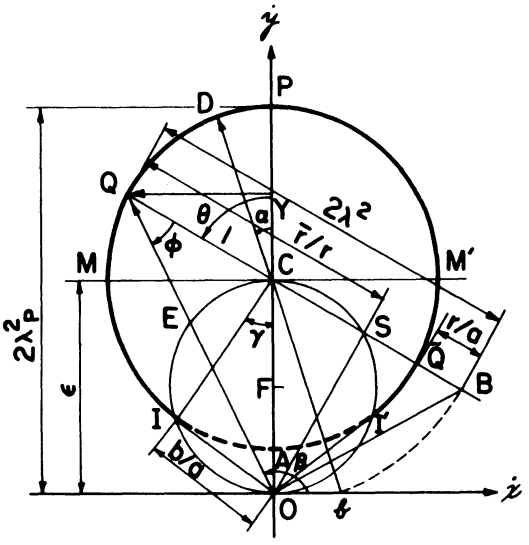	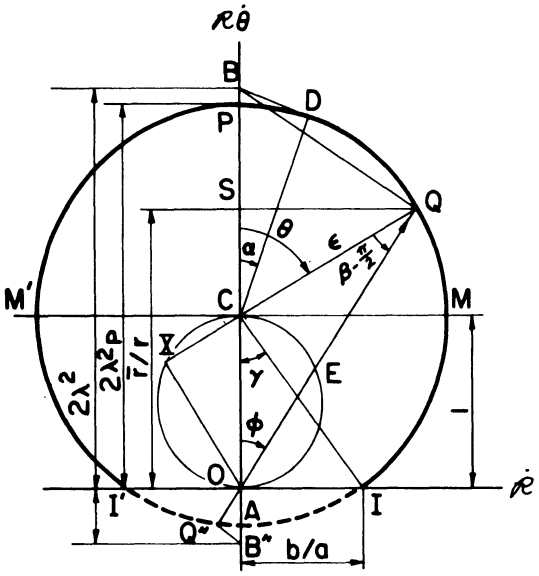
Parabolic	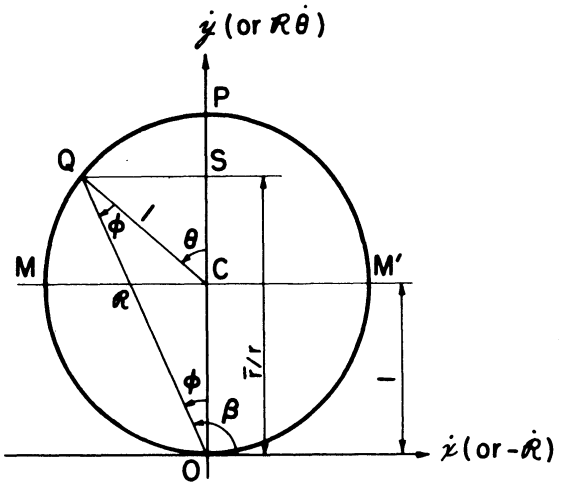	

Figure I-7. The Dimensionless Hodographs for the Keplerian Orbits $\left(\begin{matrix}\dot{x}\equiv\frac{h}{\mu}\dot{x} & \dot{\mathcal{R}}\equiv\frac{h}{\mu}\dot{r}\\ \dot{y}\equiv\frac{h}{\mu}\dot{y} & \mathcal{R}\dot{\theta}\equiv\frac{h}{\mu}r\dot{\theta}\end{matrix}\right)$

usual orbital relations, their derivations will be omitted. Such dimensionless hodographs are simple in construction, and especially useful in showing the nondimensional elements (geometric or dynamic) of the orbit and their mutual relations. The uses of the dimensionless hodographs in determining the eccentric anomalies, time of flight, etc. will be illustrated in the following sections.

5.2 The Eccentric Anomalies in the Dimensionless Hodographs

A. The Elliptic Eccentric Anomaly

The eccentric anomaly α at a point Q on an elliptic orbit may be defined analytically by the equation,

$$\epsilon \cos \alpha = 1 - \frac{r}{a} \tag{5.5}$$

where a is the semimajor axis of the orbit. A geometrical construction for α in the physical plane is depicted in Figure I-8a.

In a dimensionless polar hodograph we may obtain the angle α corresponding to any arbitrary orbital point Q as follows: draw from the image point Q on the hodograph circle in the $\mathcal{R}\dot{R}$, $\mathcal{R}\dot{\theta}$-plane the line QB perpendicular to OQ and intersecting the $\mathcal{R}\dot{\theta}$-axis at B, and then erect the line BD, meeting the hodograph circle at D, giving (see Figure I-8b)

$$\alpha = \sphericalangle BCD \tag{5.6P}$$

It is to be noted that such a construction is always possible since the point B cannot be outside the hodograph circle in the case of an elliptic orbit. Furthermore, of the two points, where the line BD meets the hodograph circle, the point on the same side of the $\mathcal{R}\dot{\theta}$-axis with the point Q should be chosen consistent with the definition of α in the physical plane. A proof of formula (5.6P) is given in Appendix B.

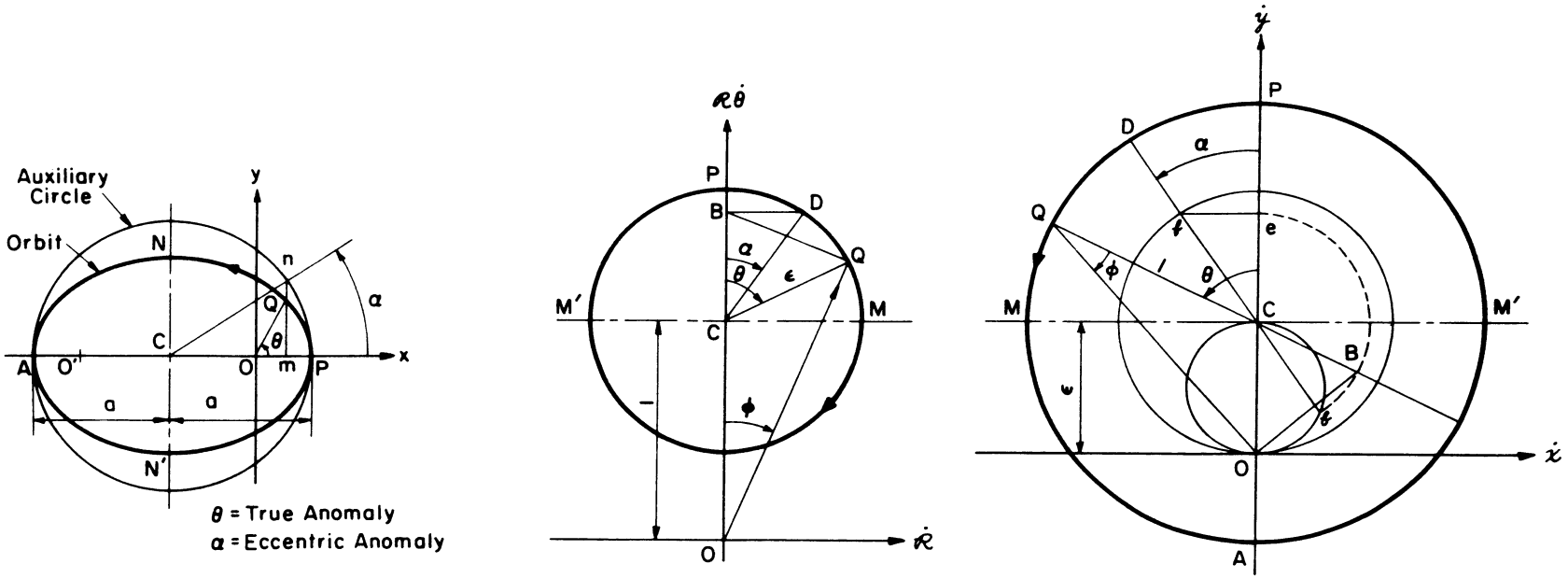

(a) The Elliptic Orbit (b) The Dimensionless Polar Hodograph (c) The Dimensionless Hamiltonian Hodograph

Figure I-8. The Elliptic Eccentric Anomaly in the Dimensionless Hodographs

A little different geometric construction will enable one to find the eccentric anomaly in a dimensionless Hamiltonian hodograph as follows: draw first the line QB from the point Q in the $\dot{x},\dot{y}$-plane perpendicular to OQ as usual, and then describe a circular arc Bb with C as center, intersecting the auxiliary circle at b, and finally joining b and C, meeting the hodograph circle at D, giving (Figure I-8c)

$$\alpha = \sphericalangle \text{ PCD} \tag{5.6H}$$

Alternately, α may be found by drawing in the $\dot{x},\dot{y}$-plane another auxiliary circle of radius ϵ and center C, and rotating CB in the direction of Θ (counterclockwise on arc PMA, and clockwise on arc PM'A) until it meets the $\dot{y}$-axis at e, and then erecting $\overline{ef}$ perpendicular to $\dot{y}$-axis, intersecting the second auxiliary circle at f, giving

$$\alpha = \sphericalangle \text{ eCf} \tag{5.6'H}$$

The proof of the formulas (5.6H) and (5.6'H) are given in Appendix B. In fact, this second method of construction brings the same geometry in the polar hodograph to the Hamiltonian hodograph. This alternate method of construction is preferable though a little more involved, as no confusion will arise if we remember the rule that the arm CB is always rotated in the direction of Θ, and that the points f (or D) and Q are always on the same side of the $\dot{y}$-axis consistent with the definition of α. It will be seen later that the second auxiliary circle drawn is also helpful in the determination of the time of flight.

B. <u>The Hyperbolic Eccentric Anomaly</u>

In analogy with an elliptic orbit an eccentric anomaly α for a hyperbolic orbit may be defined by

$$\epsilon \sec \alpha = 1 + \frac{r}{a} \tag{5.7}$$

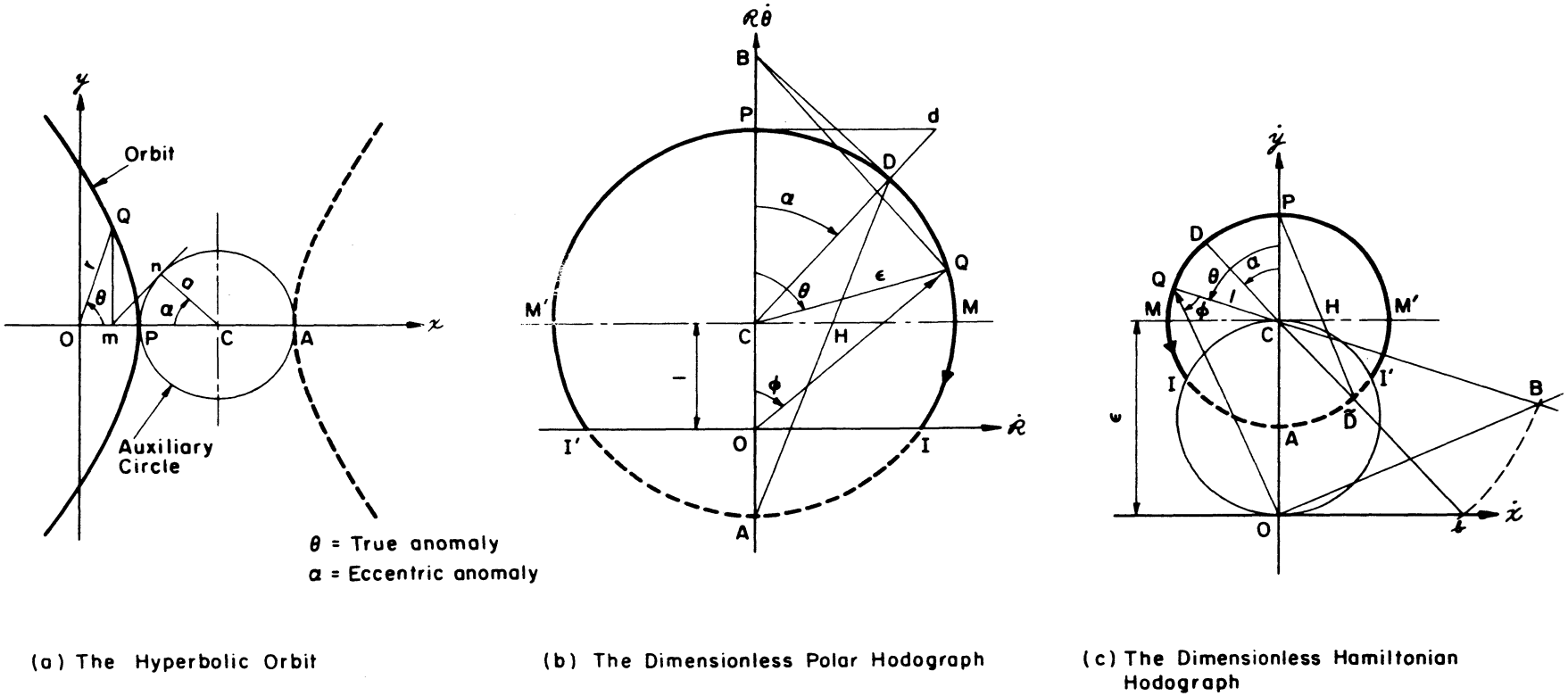

Figure I-9. The Hyperbolic Eccentric Anomaly in the Dimensionless Hodographs

where a is the semitransversal axis of the hyperbola. This real angle is called by Deutsch the hyperbolic anomaly in Reference 42 and will be referred to here as the hyperbolic eccentric anomaly or the eccentric anomaly for an hyperbolic orbit, and will be denoted by the same symbol α. Its geometrical construction in the physical plane is depicted in Figure I-9a.

To obtain α from the dimensionless polar hodograph we draw the line QB perpendicular to OQ as before (note here the point B cannot be inside the hodograph circle since the orbit is hyperbolic), and from B draw the line tangent to the hodograph circle at D, giving again (see Figure I-9b)

$$\alpha = \sphericalangle BCD \tag{5.8P}$$

where D is the point of tangency on the same side of the $\dot{r}$-axis with the point Q consistent with the definition of α in the physical plane. A proof of formula (5.8P) is given in Appendix B.

Similarly, we may obtain α for a hyperbolic orbit from the dimensionless Hamiltonian hodograph by describing in the $\dot{x},\dot{y}$-plane a circular arc Bb with C as center, intersecting the $\dot{x}$-axis at b, and then joining b and C, meeting the hodograph circle at D, giving (Figure I-9c)

$$\alpha = \sphericalangle PCD \tag{5.8H}$$

The proof is also given in Appendix B. To avoid confusion, it is well to remember that the points Q and b (or B) are always on the opposite side of $\dot{y}$-axis, and that Q and D, on the same side in accordance with the definition of α.

5.3 Determination of the Time of Orbital Flight from the Dimensionless Hodographs

The time of flight from the pericenter to an arbitrary orbital point along an elliptic orbit is given by Kepler's equation,

$$\frac{t}{T} = \alpha - \epsilon \sin \alpha \tag{5.9}$$

where

$$T \equiv \sqrt{\frac{a^3}{\mu}} \tag{5.10}$$

The corresponding equation for the hyperbolic flight is usually given in celestial mechanics by the standard form,

$$\frac{t}{T} = \epsilon \sinh F - F \tag{5.11}$$

where T is defined by the same Equation (5.9) and F is an orbital variable comparable to the eccentric anomaly for elliptic motion. However, to facilitate the graphical determination of the time of flight the hyperbolic eccentric anomaly α will be used instead of F, and Equation (5.11) takes the alternate form

$$\frac{t}{T} = \epsilon \tan \alpha - \ln \tan \left(\frac{\alpha}{2} + \frac{\pi}{4}\right) \tag{5.12}$$

For parabolic flight the corresponding equation may be written

$$\frac{t}{T} = \frac{1}{2} \tan \frac{\Theta}{2} \left(1 + \frac{1}{3} \tan^2 \frac{\Theta}{2}\right) \tag{5.13}$$

where Θ is the true anomaly, and T is defined in analogy with Equation (5.10) by

$$T = \sqrt{\frac{\bar{r}^3}{\mu}} \tag{5.10a}$$

With α and Θ determined from the hodograph, the dimensionless time of flight t/T can be easily expressed in terms of the geometrical elements of the dimensionless hodograph, Hamiltonian or polar.

The results are summarized below:

TABLE I-3

DETERMINATION OF THE DIMENSIONLESS TIME OF ORBITAL FLIGHT, t/T FROM THE DIMENSIONLESS HODOGRAPHS

Orbit	Formula	Conversion to Hodograph Elements	
		$\dot{R}, R\dot{\theta}$-Hodograph	$\dot{x}, \dot{y}$-Hodograph
Elliptic	$\alpha - \epsilon \sin\alpha$	$\frac{1}{4}$PCD-$\overline{BD}$ (5.14P)	$\frac{1}{4}$PCD-$\overline{fe}$ (5.14H)
Hyperbolic	$\epsilon \tan\alpha - \ln \tan\left(\frac{\alpha}{2} + \frac{\pi}{4}\right)$	$\overline{Pd} - \ln \frac{\overline{M'H}}{\overline{HM}}$ (5.15P)	$\overline{Ob} - \ln \frac{\overline{MH}}{\overline{HM'}}$ (5.15H)
Parabolic	$\frac{1}{2} \tan \frac{\theta}{2}\left(1 + \frac{1}{3} \tan^2 \frac{\theta}{2}\right)$	$\frac{1}{2} \overline{CR}\left(1 + \frac{1}{3} \overline{CR}^2\right)$ (5.16)	

(See Figures I-8, 9 for elliptic and hyperbolic orbit, Figure 7 for parabolic orbit.)

All conversion formulas listed here follow from the correlation formulas in the previous section, and the general correlations in Section 3.1. A proof for the formulas for hyperbolic flight is given in Appendix B; while the rest are self-evident.

The dimensionless time of orbital flight between two arbitrary points on a Keplerian orbit with a separation angle not greater than 2π follows directly from Table I-3. Such a graphical determination with the accompanying correlation formulas are depicted in Figure I-10.

If absolute time is required, the dimensionless time thus obtained is to be multiplied by the constant T, which may also be determined from the hodograph according to Table I-2:

Hodograph Plane \ Orbit	Elliptic	Hyperbolic	Parabolic
$\mathcal{R}$-$\mathcal{R}\dot{\theta}$	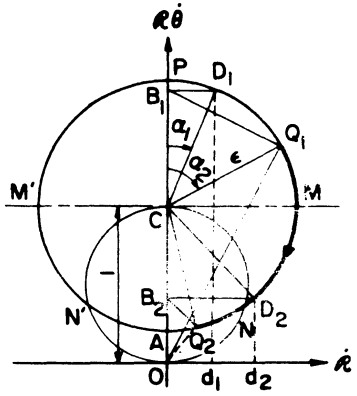	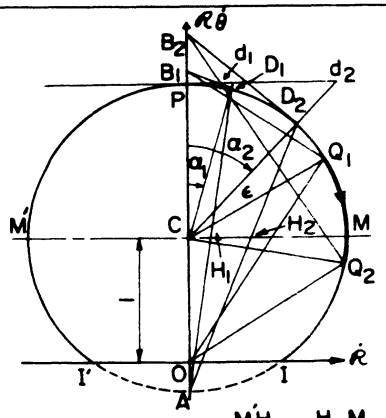	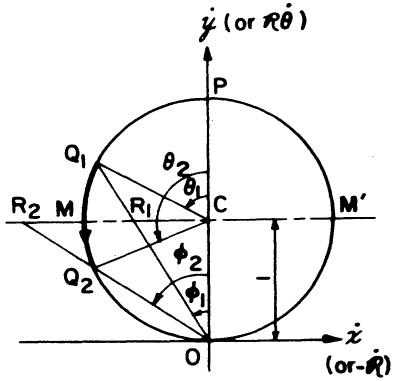
$\dot{x}$-$\dot{y}$	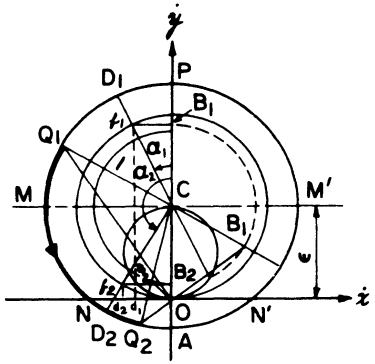	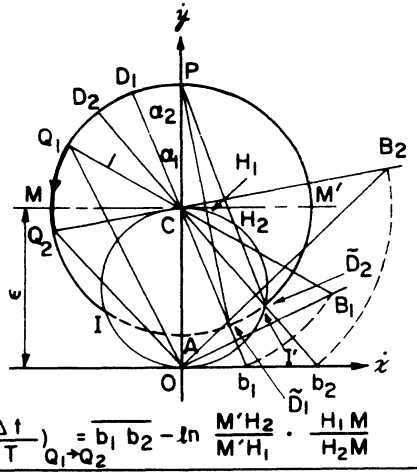	

$$\left(\frac{\Delta t}{T}\right)_{Q_1 \to Q_2} = \angle D_1 C D_2 - \overline{d_1 d_2}$$

$$\left(\frac{\Delta t}{T}\right)_{Q_1 \to Q_2} = \overline{d_1 d_2} - \ln \frac{M'H_2}{M'H_1} \cdot \frac{H_1 M}{H_2 M}$$

$$\left(\frac{\Delta t}{T}\right)_{Q_1 \to Q_2} = \frac{1}{2} \overline{R_2 R_1} \left[1 + \overline{R_1 C} \cdot \overline{R_2 C} + \frac{1}{3} \overline{R_2 R_1}^2\right]$$

$$\left(\frac{\Delta t}{T}\right)_{Q_1 \to Q_2} = \angle D_1 C D_2 - \overline{d_2 d_1}$$

$$\left(\frac{\Delta t}{T}\right)_{Q_1 \to Q_2} = \overline{b_1 b_2} - \ln \frac{M'H_2}{M'H_1} \cdot \frac{H_1 M}{H_2 M}$$

Figure I-10. Determination of the Time of Orbital Flight from the Dimensionless Hodographs

$$T = \begin{cases} \mu/\overline{ON}^3 & \text{(Elliptic)} \\ \mu/\overline{OI}^3 & \text{(Hyperbolic)} \\ \mu/\overline{OC}^3 & \text{(Parabolic)} \end{cases} \qquad (5.17)$$

where the quantities $\overline{ON}$, $\overline{OI}$, and $\overline{OC}$ are to be measured in the true velocity scale.

5.4 Derivation of the Dimensionless Orbital Relations

The dimensionless hodographs are especially convenient for the derivation of the orbital relations in the nondimensional form. For example, a glance at the geometry of triangle OCQ in either the $\mathring{x}, \mathring{y}$-hodograph or the $\mathring{R}, R\mathring{\Theta}$-hodograph (Figure I-7) enables one to write readily the following relations among the three principal angles Θ, ϕ, and β :

$$\tan\phi = \left(\frac{\overline{SQ}}{\overline{OS}}\right)_{\mathring{R},R\mathring{\Theta}} = \frac{\epsilon \sin\Theta}{1 + \epsilon\cos\Theta} \qquad (5.18)$$

$$\tan\beta = \left(\frac{\overline{OY}}{\overline{YQ}}\right)_{\mathring{x},\mathring{y}} = -\frac{\epsilon + \cos\Theta}{\sin\Theta} \qquad (5.19)$$

$$\sin\phi = (\overline{CE})_{\text{either}} = -\epsilon\cos\beta \qquad (5.20)$$

which hold for the Keplerian orbit in general. Furthermore, remember that the line OQ now represents the dimensionless quantity hV/μ which may also be written as

$$\overline{OQ} = 2\lambda^2\cos\phi$$

as shown by the hodograph (either plane), the application of the Cosine Law to the triangle OCQ again now yields for a Keplerian orbit

$$\epsilon^2 = 1 - 4\lambda^2(1-\lambda^2)\cos^2\phi \qquad (5.21)$$

which is an important formula in determining the orbital eccentricity from the burnout condition defined by λ and ϕ.

Dimensionless relations involving the eccentric anomalies may also be easily obtained from the dimensionless hodographs. For example, consider an elliptic orbit and note from the dimensionless polar hodograph (Figure I-7) that $\overline{CB}:\overline{OC} = \overline{EQ}:\overline{OE}$, and that

$$\overline{CB} = \epsilon \cos \alpha, \quad \overline{OC} = 1, \quad \overline{OE} = \cos \phi, \text{ and } \quad \overline{EQ} = \sqrt{\epsilon^2 - \sin^2 \phi}$$

It follows immediately that

$$\cos \alpha = \frac{\sqrt{\epsilon^2 - \sin^2 \phi}}{\epsilon \cos \phi} \quad \text{or} \quad \sin \alpha = \frac{\sqrt{1-\epsilon^2}}{\epsilon} \tan \phi \qquad (5.22)$$

Furthermore by noting from the diagram that

$$\overline{CB} = \overline{OB} - \overline{OC} \quad \text{and} \quad \overline{OB} = \overline{OQ}^2/\overline{OS} = \overline{OS} + \overline{SQ}^2/\overline{OS}$$

a relation between the anomalies θ and α is found to be

$$\cos \alpha = \frac{\epsilon + \cos\theta}{1 + \epsilon \cos\theta} \qquad (5.23)$$

Same procedures applied to the hyperbolic orbit will lead to similar results.

In fact many interesting orbital characteristics can also be obtained from the dimensionless hodographs, and even the purely geometrical relations for a conic can be obtained from the hodograph in a rather simple way. However, no comprehensive presentation of such derivations is attempted in this dissertation. Numerous such examples are found in References 7, 9, 12, and in particular, a vast collection of the orbital relations in the nondimensional form with brief indications of their geometrical derivations is available in Reference 9 (Appendix D).

6. SOME GENERAL REMARKS ON THE HODOGRAPH METHOD

6.1 The Construction of the Orbital Hodograph

A polar hodograph circle can be drawn if two points on the circle are known, since its center is invariably on the $r\dot{\theta}$-axis. Thus two observations on the velocity vector in the vehicle frame will enable one to draw the orbital hodograph. Of course these two points should not be situated symmetrically with respect to the local horizontal axis. The same is true for the Hamiltonian hodograph if the orientation of the apsidal axis of the orbit in the inertial space is given. However, as this orientation is in general not known a priori, three observations on the velocity vectors in an inertial frame are needed to draw the Hamiltonian hodograph since it takes three points to determine a circle. It is interesting to note that once a polar hodograph is drawn, the corresponding Hamiltonian hodograph is determined, and vice versa, since by merely interchanging the hodograph circle and its origin-to-center distance, one form of the hodograph is transformed into another, a fact mentioned earlier in Section 2.2.

Alternately the hodograph circle can be drawn if its radius and its origin-to-center distance are known. These two hodographic parameters can be expressed in various ways, some of which are shown in Table I-4 for reference. It is important to note, among these various expressions, there are only two independent orbital elements (geometric and/or dynamic) are involved in a given Newtonian field. Thus two such elements are suffice to determine the hodograph, consistent with the well-known fact that a Keplerian motion is completely determined by two of its orbital elements independent of each other. The construction of the dimensionless hodograph is even simpler since only one orbital element, ϵ is involved.

TABLE I-4

SOME EXPRESSIONS FOR THE HODOGRAPHIC PARAMETERS: THE RADIUS AND THE ORIGIN-TO-CENTER DISTANCE OF THE CIRCULAR HODOGRAPH

Orbit / Hamiltonian Hodograph $(\dot{x},\dot{y})$	Keplerian Orbit in General			Elliptic	Hyperbolic	Parabolic	Orbit / Polar Hodograph $(\dot{r},r\dot{\theta})$
Radius	$\frac{\mu}{h}$	$\frac{\mu}{h}$	$\sqrt{\frac{\mu}{r}}$	$\frac{1}{2}(V_P + V_A)$	$\frac{V_P^2 - V_\infty^2}{2V_P}$	$\frac{1}{2} V_P$	Origin-to-Center Distance
Origin-to-Center Distance	$(\frac{\mu}{h})^2 + 2k$	$\epsilon \frac{\mu}{h}$	$\epsilon\sqrt{\frac{\mu}{r}}$	$\frac{1}{2}(V_P - V_a)$	$\frac{V_P^2 + V_\infty^2}{2V_P}$	$\frac{1}{2} V_P$	Radius

6.2 The Basic Advantages and Main Applications of the Hodograph Method

The basic advantage of the hodograph method stems from the circularity of the orbital hodograph, the Hamiltonian version or the polar version. As discussed in the previous section, such a hodograph circle can be easily determined from the observations or known conditions, and once the hodograph circle is drawn, the Keplerian motion is completely determined, and all the principal orbital elements, constants as well as variables, can be found by geometrical constructions or simple calculations through the application of the proper correlation formulas presented in Chapters 3 and 5. Thus as a first application the hodograph method serves as simple graphical means for the determination of orbital or trajectory elements. However, what is more important is its use as an analytical tool. More specifically such uses are as follows:

(1) The orbital hodograph exhibits clearly and naturally the particular features of the motion through its circular geometry. This makes it the best tool for exploring the orbital characteristics and derivation of many orbital relations, as illustrated in Chapters 4 and 5. In this connection the highly suggestive nature of the orbital hodograph by its simple geometry is worth special appreciation as it may easily lead to the discovery of new characteristics or new orbital relations which are not likely to be unmasked when viewed in the physical space. A few such examples are scattered in References 7, 9, 12 and a few more will be found in the later part of this dissertation.

(2) By mapping a Keplerian orbit in the physical space into a circle in the hodograph space, it virtually transforms a dynamic problem to a geometric problem involving essentially circles, and thus it offers

a geometric approach to every such problem it deals with. Owing to the simplicity of the circular geometry, problems which are complicated in the physical space is usually simpler in the hodograph space, and those which are simple in the physical space often become so obvious in the hodograph space that their solutions can be readily found by elementary means. Many examples illustrating the use of the orbital hodographs, Hamiltonian and polar, for the solution of some elementary orbit and trajectory problems have been given in author's early writings.[7, 9, 12] More detailed hodograph analysis for the specific problems will be illustrated by two examples given in the subsequent parts II and III respectively.

(3) It offers a unified treatment of the three types of the Keplerian orbit or trajectory encountered in space flight, the elliptic, the parabolic, and the hyperbolic, since the difference among these three types are no more than the positions of their hodograph circles relative to the hodograph origin. Thus the hodograph method is especially useful when

a. General theorems on the Keplerian motion are to be developed.

b. Characteristics of different types of the Keplerian orbit are to be compared.

c. Various types of the Keplerian orbits or trajectories are involved in the same problem.

As shown in Chapters 3 to 5 many results derived from the hodograph are valid for a Keplerian orbit in general without the necessity of a separate proof for each of the three types of the orbit; and whenever they exhibit some apparently different characters, their analogy can easily be made and their corresponding formulas be established without difficulty by simply observing

the differences in their hodograph geometry. All these illustrate the advantages of the hodograph method regarding items a and b. The advantage regarding item c will be seen in Parts I and II when specific problems are being analyzed.

6.3 The Hamiltonian Hodograph versus the Polar Hodograph

Basically, the Hamiltonian hodograph describes the motion in an inertia frame, while the polar hodograph, the motion in a non-inertial frame, the vehicle frame. For example, a polar hodograph yields directly the radial and transversal velocity components of the motion which are the local vertical and horizontal components observed in the vehicle frame. The fact that these are usually the velocity components of interest in space flight makes the polar hodograph very useful. However, this same information can also be obtained from the Hamiltonian hodograph by simple geometrical construction according to the correlation rules. Similarly, the velocity components in an inertial frame like V_x and V_y can also be obtained from the polar hodograph. Thus, whenever only one orbital point is concerned, the use of either type of the hodograph is optional, depending on the particular problem at hand. However, when two or more orbital points are concerned then the Hamiltonian hodograph is preferable when the absolute motion is concerned: and the polar version is preferable if the apparent motion is of interest. It is worthy to note that even in such cases the essential features of the geometry in one version are usually preserved in the other; only the physical interpretations are different. A typical example of this sort has been given in Section 4.1 concerning the velocity change between two orbital points. As indicated by this example, to each relation concerning the absolute motion in a

Hamiltonian hodograph there is a corresponding relation in the polar hodograph concerning the apparent motion. This may also be regarded as a principle of duality relating the absolute Keplerian motion to the apparent Keplerian motion of a space vehicle.

Finally with the dimensionless velocity coordinates introduced in Section 5.1 the Hamiltonian hodographic transformation maps all Keplerian orbits into a unit circle, while the polar hodographic transformation maps all such orbits into a family of concentric circles. Such a nondimensional mapping is of special help in dealing with a number of Keplerian orbits or trajectories at the same time. The use of the dimensionless polar hodograph for trajectory analysis has been given in Reference 9 (pp. 386-396), and the use of the dimensionless Hamiltonian hodograph for such analysis will be fully illustrated in Part II.

PART II

HODOGRAPH ANALYSIS OF THE BALLISTIC TRAJECTORIES BETWEEN TWO TERMINAL POINTS IN SPACE

7. INTRODUCTORY REMARKS

The science of exterior ballistics has been one of the well-developed old subjects of applied mechanics. However, the extension from the artillery trajectory over a flat earth to the space trajectory in a central gravity field is rather a recent advance. Some pioneering work in this direction appeared in Cranz's work in the 1920's like Reference 26, in which he introduced the elements of the Keplerian motion into his trajectory analysis, and thus marked the beginning of linking the celestial mechanics to the subject of ballistics. It seems that Cranz's early work had not been further developed along this line until the late 1940's when the long-range ballistic missiles were under development. From then on numerous articles and books on this subject appeared frequently in the technical literature, from the early fragmentary treatment by Barker, Blitzer, Hart etc. (see e.g. References 31, 32) to the later authoritative work by Wheelon[34], Ehricke[42] and so on. In almost all of this literature one common feature is that the elliptic trajectory was the center of attention, and another is that the treatment was mostly given to the symmetrical case in which the initial and the final terminals were assumed to be equi-distant, from the field center. In 1961 the author did the similar analysis[9] by using the polar hodograph in the non-dimensional form instead of the usual Wheelon's hit equation;[34] and later, by using the dimensionless hodograph of the Hamiltonian version, it was extended to the unsymmetrical case and to all three types of Keplerian trajectories.[19] The essential part of this later analysis will be presented in the following as the first example of applying the hodograph method to the analysis of a specific problem in space flight. It will also pave the way for the further analysis of the optimization problem to be presented in Part III.

8. THE HODOGRAPHIC REPRESENTATION AND A GENERAL SURVEY OF THE SYSTEM OF TWO-TERMINAL TRAJECTORIES

8.1 General Considerations

In a central force field all free-flight trajectories passing through two fixed terminal points, Q_1 and Q_2 will lie in the same plane determined by the three points Q_1, Q_2, and the field center O. The triangle OQ_1Q_2 will be called the base triangle; the line Q_1Q_2, the chord; and the interior angle at O, the vertex angle, or the angle of separation. The departure velocity vector to achieve such a trajectory will necessarily be coplanar with the base triangle, while either its magnitude or its direction in the trajectory plane may be arbitrary. Thus in a given force field the geometry of the base triangle together with the departure speed or the departure path angle completely determine the trajectory.[8.0]

To insure that the base triangle does not degenerate, the vertex angle ψ here is assumed to be between zero and π. A typical base triangle and several such Keplerian trajectories are depicted in Figure II-1a. The geometry of such a trajectory system in the physical plane has been analyzed to some details by Battin.(33) The purpose of this section is to represent such a system in the hodograph plane so as to form the basis for subsequent analysis.

It is to be noted that, with two given terminals, a vehicle starting from one terminal may reach the other in either direction around the field center. Thus the system of two-terminal trajectories may be divided into two groups: the one with a common range angle equal to the vertex angle ψ which is less than π, and the other with a common range angle $\psi' = 2\pi-\psi$ which is greater than π. The first group is usually

---

[8.0] The solution may not be unique, see Section 8.3.

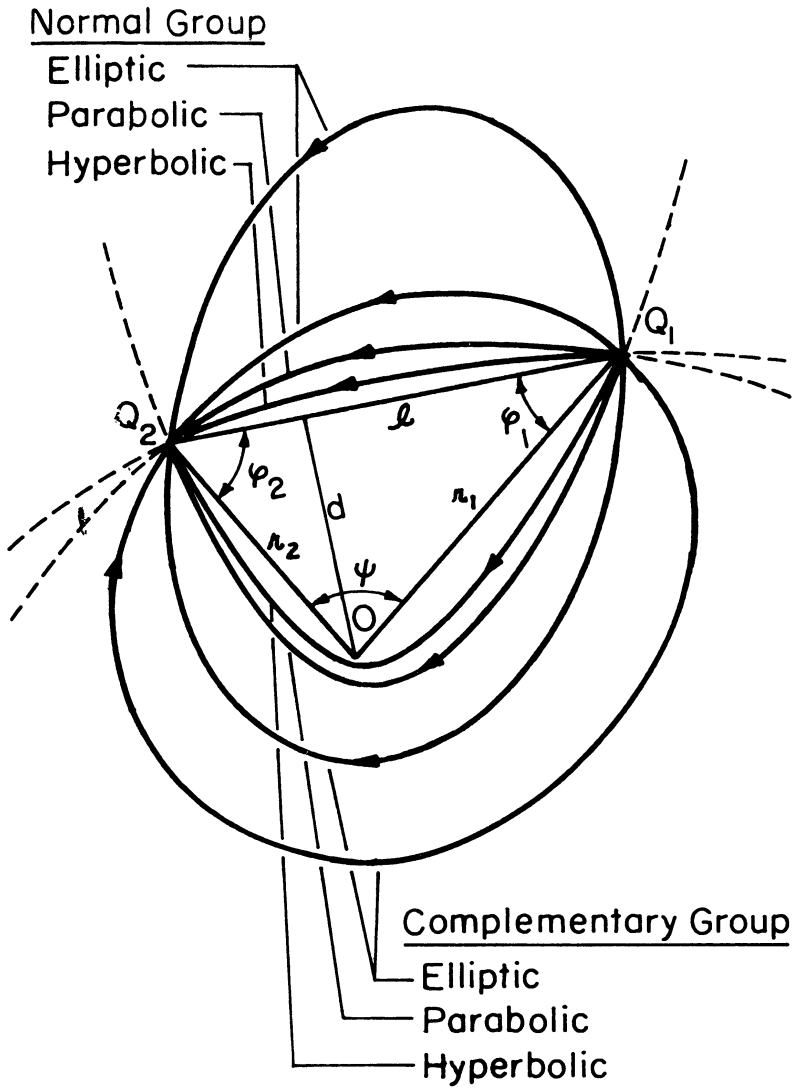

(a) Physical Plane

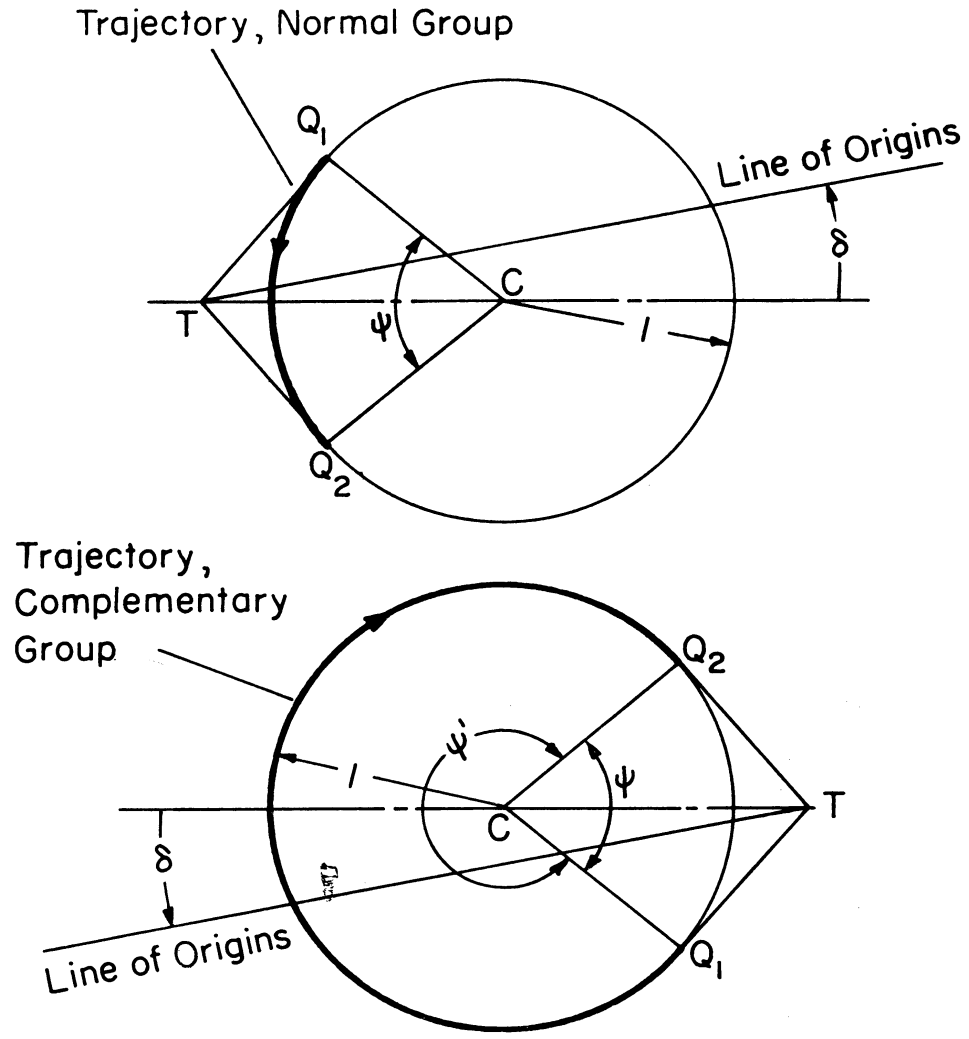

(b) Dimensionless Hodograph Plane

Figure II-1. System of Two-terminal Trajectories and Its Hodographic Representation (Range $\neq$ 180°).

the one of interest in most practical problems, and will be called the normal group, while the second, its complement. In fact each member of one group will find its complement in the other, the two forming a complete Keplerian conic. However, if the trajectory is parabolic or hyperbolic, then its complement, being open between the terminals, can hardly be regarded as a trajectory in the ordinary sense, and will be referred to as an unrealistic trajectory for convenience. In the following the main analysis will be concerned with the trajectory system of the normal group with its range angle equal to $\psi < \pi$. However, as we will see, the information so obtained may be easily adapted to its complementary group if needed. The boundary case of $\psi = \pi$ will be treated separately later.

8.2 The Hodographic Representation

Based on the principle of the dimensionless hodographic mapping given in Section 5.1 it is clear that all Keplerian conics are represented in the dimensionless $\mathring{x}, \mathring{y}$-plane by a unit circle, and the images of all the two-terminal trajectories of a common range angle ψ are given by the same arc of this circle, subtending a central angle ψ between the radii CQ_1 and CQ_2 which are 90° in advance (in the direction of motion) to the radius vector OQ_1 and OQ_2 in the physical plane respectively (Figure I-1b); the points Q_1 and Q_2 on the circle are therefore the images of the terminal points. To complete the construction of such a hodograph one merely needs to locate the origin of the hodograph for each particular trajectory under consideration.

At first sight it seems there might be a wide scattering of such possible origins in the hodograph plane corresponding to the

infinitely many possible Keplerian trajectories leading from Q_1 to Q_2 through the same range angle ψ. However, a careful analysis shows that the distribution of such origins is linear. The proof is as follows:

With reference to Figure II-2 and the general correlations given in Section 3.1 (see Rule H-6), the hodograph origin of the trajectory with an arbitrary departure speed parameter λ_1, and the corresponding approach speed parameter λ_2 will lie on both auxiliary circles (called speed circles) with radii λ_1^2 and λ_2^2, tangent internally to the unit hodograph circle at Q_1 and Q_2 respectively, and therefore it is at their intersection O_I or O_{II}. The two speed parameters λ_1 and λ_2 are connected by

$$\frac{1-\lambda_2^2}{1-\lambda_1^2} = \frac{r_2}{r_1} \equiv n \tag{8.1}$$

according to Equation (1.9). Now draw the lines tangent to the hodograph circle at Q_1 and Q_2 respectively, intersecting at T. Then the three lines O_IO_{II}, TQ_1 and TQ_2 are the radical axes of the two speed circles and the hodograph circle taken in pairs, therefore, they are concurrent with T as their radical center.[8.1] That is, the line O_IO_{II} also passes through the point T. Furthermore, from geometry the line O_IO_{II} is perpendicular to the line of centers G_1G_2. But, the line G_1G_2 is perpendicular to the chord Q_1Q_2 in the physical plane since the triangles CG_1G_2 (hodograph plane) and OQ_1Q_2 (physical plane) are similar. Consequently O_IO_{II} is parallel to the chord Q_1Q_2.

[8.1] See any standard text on Higher Geometry, e.g., Reference 28.

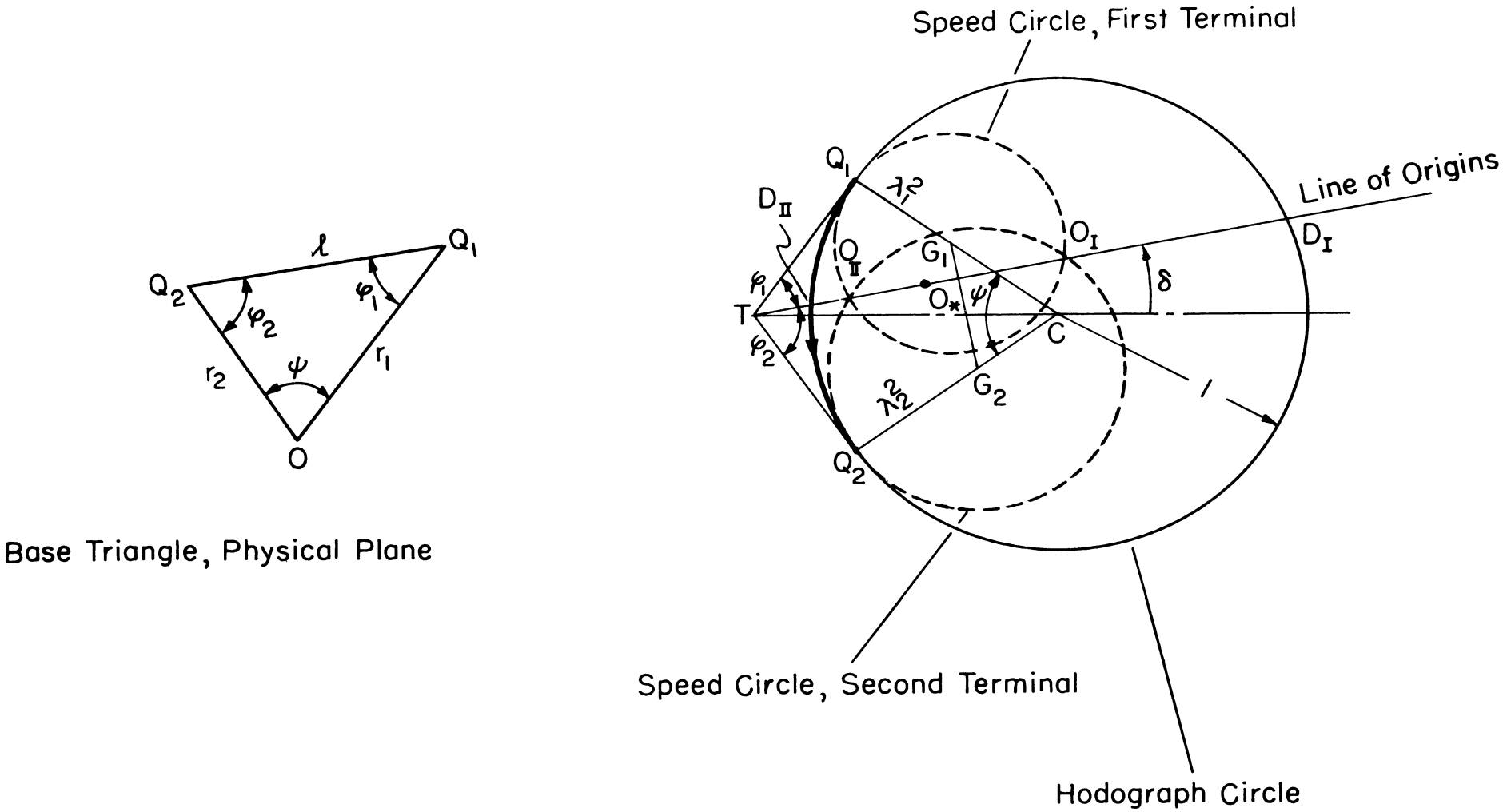

Figure II-2. Linear Distribution of the Hodograph Origins in the Dimensionless Hodograph Plane.

With terminals Q_1 and Q_2 given, T is a fixed point, and the chord Q_1Q_2 is in a fixed direction, thus the line through $O_I O_{II}$ is a fixed straight line, irrespective of the departure speed given by λ_1. In other words, the intersection of any pair of speed circles, and therefore all the possible hodograph origins will lie on this same line, which will be called the line of origins. This completes the proof. It evidently applies to either group.

Based on the foregoing analysis the hodograph images of all two-terminal trajectories of one group may be represented in the dimensionless hodograph plane by a unit circular arc together with the straight line which passes through the intersection of the tangents to the unit circle at Q_1 and Q_2, and is parallel to the chord Q_1Q_2 in the physical plane, as shown in Figure II-1b. Each particular point on this line corresponds to a particular trajectory in the physical plane, and the selection of a particular trajectory to suit some specific purpose is no more than the selection of a certain particular point on this line. Thus in comparison with the complexity of the trajectory geometry in the physical plane the situation in the hodograph plane is far simpler.

It is worth to note that, the hodograph for the complementary group may be obtained by turning that for the normal group through 180°. Thus information concerning the former may be obtained directly from the hodograph for the latter, and a separate construction for the complementary group is often unnecessary. Besides, as the geometry of the hodograph shows, the angles between the line of origins and the two tangents TQ_1 and TQ_2 are equal to the base angles φ_1 and φ_2 of the base triangle at Q_1 and Q_2 respectively, and the inclination of the

line of origins with the centerline CT is given by

$$\delta = \frac{1}{2}(\varphi_2 - \varphi_1) \tag{8.2}$$

whence $\delta \gtreqless 0$ according as $\varphi_1 \lesseqgtr \varphi_2$ (or $r_1 \gtreqless r_2$) .

8.3 A General Survey

Based on the foregoing hodographic representation we may now make a general survey on the nature of the system of the two-terminal Keplerian trajectories associated with an arbitrary base triangle. We will first consider the normal group.

As seen from the hodograph construction, for a given base triangle, there is a departure speed for which the speed circle will tangent to the line of origins. This is the minimum speed below which no such terminal-to-terminal trajectory is possible. The trajectory corresponding to the minimum speed is known as the minimum energy trajectory; its hodograph origin is given by the point of tangency O_* .

When the departure speed exceeds this minimum value, the speed circle will meet the line of origins in two distinct points such as O_I and O_{II} in Figure II-2, giving two distinct trajectories corresponding to the same departure speed. Such trajectories will be referred to as the conjugate trajectories for short, and the corresponding origins, O_I and O_{II} , the conjugate origins. As the hodograph shows, conjugate trajectories have different initial path angles: the one with the low path angle as that associated with O_I is known as the low trajectory; and the one with the high path angle as that associated with O_{II} , the high trajectory. More precisely, the one with its path angle below that for the minimum energy trajectory at the same terminal will be classified

as the low trajectory; and the one with its path angle over that, the high trajectory. For brevity the corresponding origins in the hodograph plane will also be called low and high accordingly.

With reference to Figure II-2, when the departure speed parameter is less than unity, the origin is within the hodograph circle, and the trajectory is elliptic. As the departure speed increases from its minimum value, the conjugate origins O_I and O_{II} move toward the points D_I and D_{II} respectively. At each of the points D_I and D_{II} the speed parameter is 1, both trajectories become parabolic. However, it is to be noted that, of this conjugate parabolic pair the high one with its hodograph origin at D_{II} will have its point at infinity (which has D_{II} as its hodograph image) interposed between the terminals Q_1 and Q_2 in the assumed direction of motion, indicating that such a trajectory is physically unrealistic. This is in fact the limiting trajectory which the high elliptic trajectories approach when the initial speed approaches that of escape. As the departure speed further increases, the conjugate origins move from D_I and D_{II} outward respectively, and the trajectories become hyperbolic. On the low trajectory side as the origin moves outward from D_I toward infinity, the eccentricity increases without bound, the trajectory approaches the chord line, and in the limit it degenerates into the chord Q_1Q_2. This is of course physically impossible since it requires an infinite departure speed. On the high side, as the origin moves outward from D_{II} toward the point T, the eccentricity increases toward CT as its limit, and the two asymptotes of the trajectory hyperbola approach the radii OQ_1 and OQ_2 in the physical plane respectively. However, just like the

parabolic case, these high hyperbolic trajectories are unrealistic since their points at infinity are interposed between the terminal points. In the limit when the origin is at T, the trajectory degenerates into the broken line segment Q_2OQ_1 implying again an infinite departure speed, and thus the trajectory is not only unrealistic but also physically impossible. If the origin moves beyond T, the trajectory will be the far branch of a hyperbola which can be realized in a central repulsion field,[8.2] but not in a gravity field. These various situations are summarized in Table II-1.

Thus in conclusion, for a given base triangle in a Newtonian gravity field the line of origins in the dimensionless hodograph plane starts from the point T and extends toward infinity in the direction of the chord line (Q_1Q_2) in the physical plane; and the origins of all realistic trajectories lie in the open interval from D_I via D_{II} to infinity. Furthermore, the conjugate origins are separated by the point O_* with all the low origins situated at its right side, and all the high origins, its left side (Figure II-2); thus the points in the interval O_*D_I and O_*D_{II} are the mutually conjugate elliptic origins; while those in the intervals D_I to infinity, and D_{II} to T are the mutually conjugate hyperbolic origins; and there is one and only one pair of conjugate parabolic origins, the points D_I and D_{II}.

All the foregoing findings for a normal group may be easily adapted to its complement if we note the following:

(1) The complement of a high trajectory in one group is a low trajectory in the other;

[8.2] See Reference 12, Section X, pp. 908-909.

TABLE II-1

LOCATION OF THE HODOGRAPH ORIGIN AND THE NATURE OF THE TWO-TERMINAL TRAJECTORY (RANGE = $\psi < \pi$)

Location of the Hodograph Origin	The Corresponding Trajectory	
	Type	Nature
Between O_* and D_I	elliptic	low, realistic
Between O_* and D_{II}	elliptic	high, realistic
At O_*	elliptic	minimum energy, realistic
At D_I	parabolic	low, realistic
At D_{II}	parabolic	high, unrealistic
D_I to infinity	hyperbolic	low, realistic
D_{II} to T	hyperbolic	high, unrealistic
At infinity	straight line (Q_1Q_2)	infinite speed, physically impossible
At T	broken line (Q_2OQ_1)	infinite speed, physically impossible
Beyond T	hyperbolic	realistic in a central repulsion field, but not in a gravity field

(2) An elliptic trajectory in one group and its complement in the other are both realistic; while the complement of a realistic parabolic or hyperbolic trajectory of one group is unrealistic in the other. Thus by interchanging the words "high" and "low," and, when a parabolic or a hyperbolic trajectory is concerned, interchanging the words realistic and unrealistic, a similar table for the complementary group may be constructed from Table II-1. For the benefit of later development it is also

worth to note the following additional relations between a trajectory (realistic or unrealistic) and its complement:

(3) All geometrical elements of the two are identical since they are of the same Keplerian conic;

(4) All terminal quantities which involve directions are equal in magnitude but opposite in sign, e.g.

$$\vec{V}_1 + \vec{V}_1' = 0, \qquad \phi_1 + \phi_1' = 0 \tag{8.3}$$

In the light of the foregoing analysis we see that in the physical plane (Figure II-3a) the elliptic trajectories of the normal group are all confined in the infinite region (A), while the realistic hyperbolic trajectories of the same group are all confined in the finite region (B). Similarly, elliptic trajectories and the realistic hyperbolic trajectories of the complementary group are all confined in the regions (A') and (B') respectively. The two conjugate parabolas and the three sides of the base triangle form the boundaries of these regions as shown in Figure II-3a. Consequently, the trajectories of both groups associated with a fixed base triangle all lie outside this triangle; and the boundary of this triangle form the limiting trajectories when the speed increases indefinitely.[8.3]

8.4 Limits of Variation of the Trajectory Elements

It is interesting to note that, of the infinitely many Keplerian trajectories associated with a given base triangle, there exist certain

---

8.3 It can be shown that the trajectories will all lie within the base triangle if the field is a central repulsive one.

limits for the possible variations of some of the trajectory elements. As generally known and pointed out earlier, there is a minimum value for the initial terminal speed below which no such a trajectory is possible. Consequently there are corresponding limits for the orbital energy, major axis, and the final terminal speed respectively. An examination of the hodograph shows that there exists also a least eccentricity which the trajectory can attain. It is given by the perpendicular distance $\overline{CE}$ in Figure II-3d since the eccentricity is always equal to the origin-to-center distance in the $\dot{x},\dot{y}$ -plane (see Section 5.1). Directly from the geometry of the hodograph one finds

$$\epsilon_{min} = \overline{CE} = \overline{CT}|\sin \delta| = \sec \frac{\psi}{2} \left|\sin \frac{1}{2} (\varphi_2 - \varphi_1)\right| \tag{8.4}$$

which, after some trigonometric simplifications, reduces to

$$\epsilon_{min} = \frac{|r_1 - r_2|}{\ell} = \frac{|1-n|}{m} \tag{8.4a}$$

where m is defined by

$$m \equiv \frac{\ell}{r_1} = \sqrt{1-2n \cos \psi + n^2} \tag{8.5}$$

Thus a circular trajectory is possible only when $r_1 = r_2$ and the greater the numerical difference between the terminal distances, the greater will be the least eccentricity, for a given chord length.

As observed earlier, when the initial speed increases indefinitely the eccentricity of the realistic trajectories of the normal group increases without bound while that of the complementary group approaches $\overline{CT}$ as limit. Thus for such a group there is an upper limit for the hyperbolic eccentricity

$$\epsilon_{UL} = \overline{CT} = \sec \frac{\psi}{2} \tag{8.6}$$

which depends only on the vertex angle of the base triangle, not on the terminal distances. This limiting value itself will approach infinity when ψ approaches π.

Furthermore, the hodograph shows that although the departure speed may increases indefinitely, the corresponding path angle can only vary within two definite limits. For the normal group the upper limit is given by the angle CQ_1D_{II} which the departure path angle of the high elliptic trajectory approaches when the departure speed approaches parabolic. From the hodograph geometry this angle is found to be

$$(\phi_1)_{UL} = \sphericalangle CQ_1D_{II} = \frac{1}{2}(\pi + \varphi_1 - \omega) \tag{8.7}$$

where,

$$\omega = \cos^{-1} \epsilon_{min} = \cos^{-1} \frac{|1-n|}{m} \tag{8.8}$$

The lower limit is the path angle for the straight line trajectory Q_1Q_2 which the hyperbolic trajectory approaches. Obviously it is

$$(\phi_1)_{LL} = \varphi_1 - \frac{\pi}{2} . \tag{8.9}$$

Consequently all possible directions of departure are confined in the angular region (a_1) as shown in Figure II-3b, with an included angle

$$\Delta \phi_1 = (\phi_1)_{UL} - (\phi_1)_{LL} = \pi - \frac{1}{2}(\varphi_1 + \omega) \tag{8.10}$$

The path angle at the final terminal is likewise limited, and all the possible directions of approach are confined in the angular regions (a_2) in Figure II-3b. Similar regions exist for the complementary group. Consequently, with a given configuration of the base triangle, there are certain forbidden regions for the direction of departure as those marked (b_1) and (c_1); and certain forbidden regions for the direction of approach as those marked (b_2) and (c_2). These limits of variation and the total

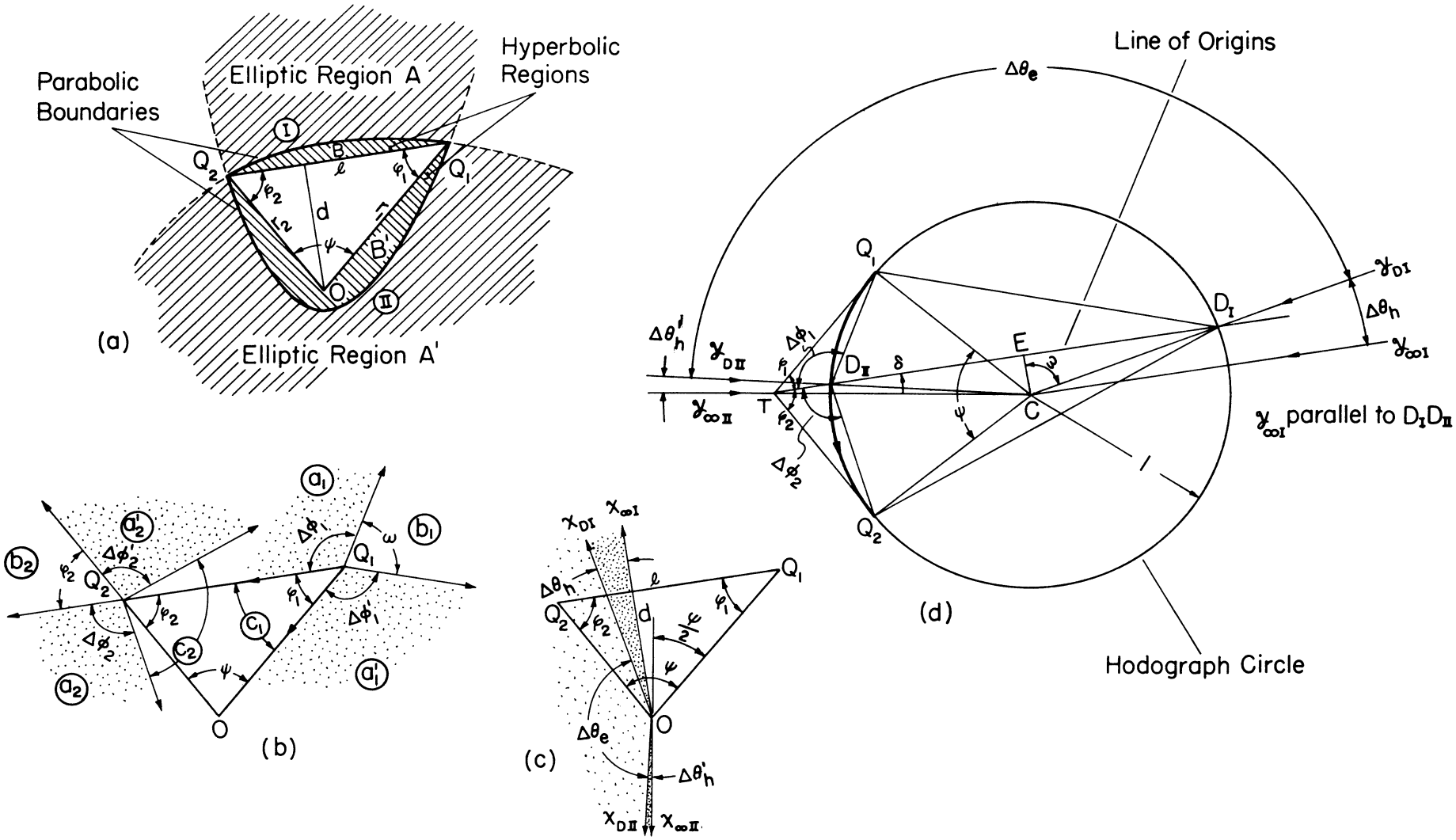

Figure II-3. General Survey of the System of Two-terminal Trajectories.

TABLE II-2

POSSIBLE AND FORBIDDEN REGIONS OF DEPARTURE AND APPROACH

	Initial Terminal		Final Terminal	
	Limiting Directions of Departure		Limiting Directions of Approach	
	Formula	Angle in Hodograph	Formula	Angle in Hodograph
Normal	$(\phi_1)_{UL} = \frac{1}{2}(\pi+\varphi_1-\omega)$	$\angle CQ_1D_{II}$	$(\phi_2)_{UL} = \frac{\pi}{2} - \varphi_2$	
	$(\phi_1)_{LL} = \varphi_1 - \frac{\pi}{2}$		$(\phi_2)_{LL} = -\frac{1}{2}(\varphi_2+\omega)$	$\angle CQ_2D_{II}$
Complementary	$(\phi_1')_{UL} = \frac{1}{2}(\pi-\varphi_1-\omega)$	$\angle CQ_1D_{I}$	$(\phi_2')_{UL} = \frac{\pi}{2}$	
	$(\phi_1')_{LL} = -\frac{\pi}{2}$		$(\phi_2')_{LL} = \frac{1}{2}(\varphi_2-\omega)$	$\angle CQ_2D_{I}$

	Possible Regions of Departure			Possible Regions of Approach		
	Region	Included Angle	Angle in Hodograph	Region	Included Angle	Angle in Hodograph
Normal	(a_1)	$\Delta\phi_1 = \pi - \frac{1}{2}(\varphi_1+\omega)$	$\angle Q_1D_{II}T$	(a_2)	$\Delta\phi_2 = \frac{1}{2}(\pi-\varphi_2+\omega)$	$\angle Q_2D_{II}T$
Complementary	(a_1')	$\Delta\phi_1' = \pi - \frac{1}{2}(\varphi_1+\omega)$	$\angle Q_1D_{II}T$	(a_2')	$\Delta\phi_2' = \frac{1}{2}(\pi-\varphi_2+\omega)$	$\angle Q_2D_{II}T$

	Forbidden Regions of Departure			Forbidden Regions of Entry		
	Region	Included Angle	Angle in Hodograph	Region	Included Angle	Angle in Hodograph
Inner	(c_1)	φ_1	$\angle Q_1TD_{II}$	(c_2)	$\pi - \omega$	
Outer	(b_1)	ω	$\angle ECD_{I}$	(b_2)	φ_2	$\angle Q_2TD_{II}$

included angle of each region are listed in Table II-2. It is to be noted that, as shown in the table, the regions for possible departure for the normal and the complementary groups have equal included angles, and it can also be verified from the hodograph that they are symmetrically oriented with respect to the bisector of the base angle at the initial terminal; the same is true for the regions of possible approach at the final terminal. Furthermore, the included angle of the inner forbidden region of departure (c_1) and that of the outer forbidden region of approach (b_2) are equal respectively to the base angles at the corresponding terminals; while the included angles of the outer forbidden region of departure (b_1) and the inner forbidden region of approach (c_2) are supplementary to each other. In view of Equation (8.4) and Table II-2, we may say that for a given vertex angle ψ, the smaller the difference between the base angles, the larger will be the outer forbidden region of departure and the smaller will be the inner forbidden region of approach. In the symmetrical case, $\varphi_1 = \varphi_2$, $r_1 = r_2$, the included angle of the outer forbidden region of departure reaches its maximum and that of the inner forbidden region of approach reaches its minimum, both equal to 90°.

Finally we observe that the apsidal axes of the present system of trajectories are also confined in certain regions as tabulated below (see also Figure 3c). Of the four boundary axes, OX_{DI} and OX_{DII} are the apsidal axes of the two parabolic trajectories respectively, while $OX_{\infty I}$ and $OX_{\infty II}$ are those of the limiting hyperbolic trajectories of infinite departure speed respectively. Their directions may be obtained directly from those of the corresponding $\dot{\mathcal{X}}$ -axes in the hodograph plane.

Evidently, $OX_{\infty I}$ is perpendicular to the chord Q_1Q_2, and OX_{DII} bisects the vertex angle ψ.

TABLE II-3

REGIONS FOR APSIDAL AXES (POSITIVE PORTIONS[8.4])

Trajectories	Boundary Axes	Included Angle
Elliptic	OX_{DI} and OX_{DII}	$\Delta\theta_e = 2\omega$
Hyperbolic Normal Group	OX_{DI} and $OX_{\infty I}$	$\Delta\theta_h = \frac{\pi}{2} - \omega$
Complementary Group	OX_{DII} and $OX_{\infty I}$	$\Delta\theta_h' = \frac{\psi}{2} + \varphi_1 - \omega$

8.4 Defined in Figure I-2a.

9. CHARACTERISTICS OF THE CONJUGATE TRAJECTORIES

9.1 The Chordal and Radial Components of the Terminal Velocities

The characteristics of the two-terminal trajectories can be best analyzed by using the chordal and radial components of the terminal velocities. As introduced by Godal in Reference 37 they are the components in the chordal and radial directions respectively as depicted in Figure II-4a. A method of determining such components in the hodograph will be introduced below.

As shown in Figure II-4b, if O is the origin of the hodograph, then from the proof given in Section 8.2, OT is in the chordal direction, while by construction TQ_1 and TQ_2 are in the radial directions at Q_1 and Q_2 respectively. Thus in the $\dot{x}\dot{y}$-plane, that is, if we take the radius of the hodograph circle as μ/h instead of unity, the hodograph gives the terminal velocities

$$\vec{V}_1 = \vec{OQ_1}\,, \quad \vec{V}_2 = \vec{OQ_2} \tag{9.1}$$

with their chordal and radial components

$$\begin{aligned} \vec{V_{C1}} &= \vec{OT}\,, \quad \vec{V_{R1}} = \vec{TQ_1} \\ \vec{V}_{C2} &= \vec{OT}\,, \quad \vec{V}_{R2} = \vec{TQ_2} \end{aligned} \tag{9.2}$$

from which we deduce immediately that

$$\vec{V}_{C1} = \vec{V}_{C2}\,, \quad V_{R1} = V_{R2} \tag{9.3}$$

The second relation stems from the fact that the two tangents $\overline{TQ_1}$ and $\overline{TQ_2}$ are equal in length. Thus along the same trajectory the chordal components of the terminal velocities are identical in magnitude and direction, while the radial components are equal in magnitude. Hence if we are dealing with their magnitudes only, the subscripts 1 and 2 are unnecessary and will be dropped hereafter.

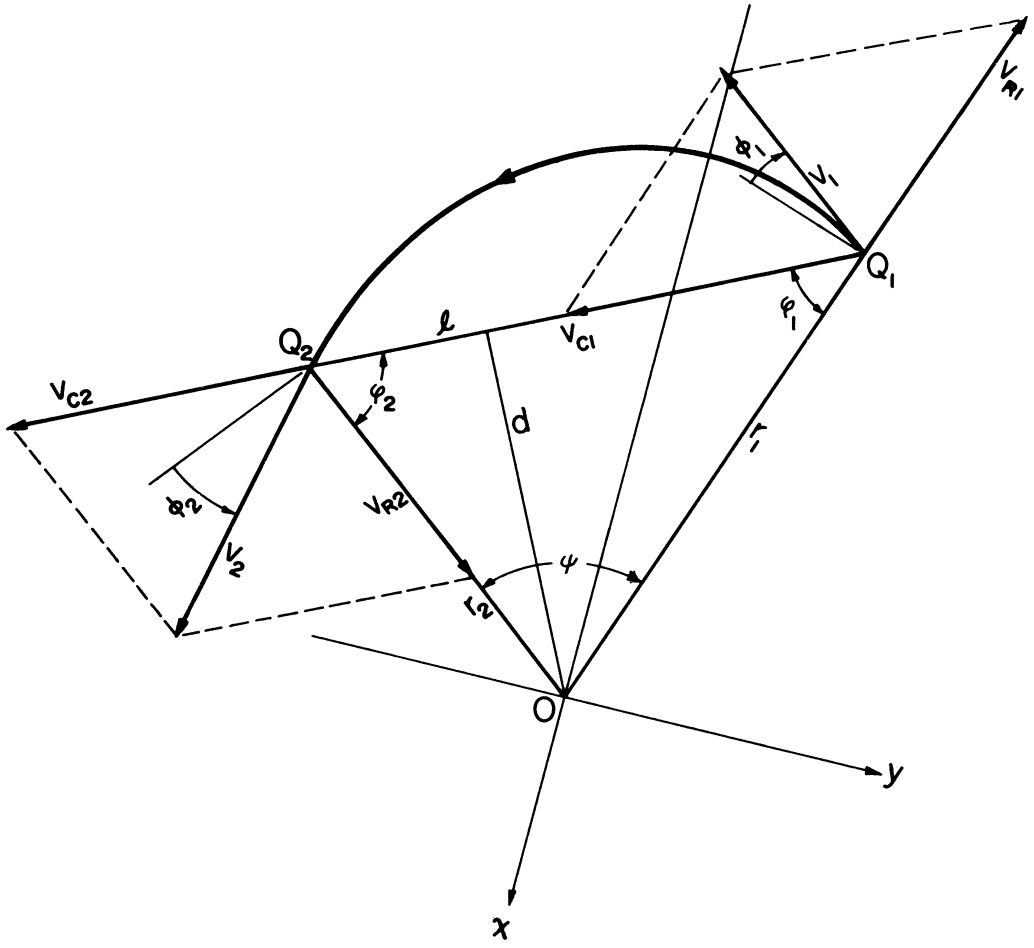

(a) Physical Plane

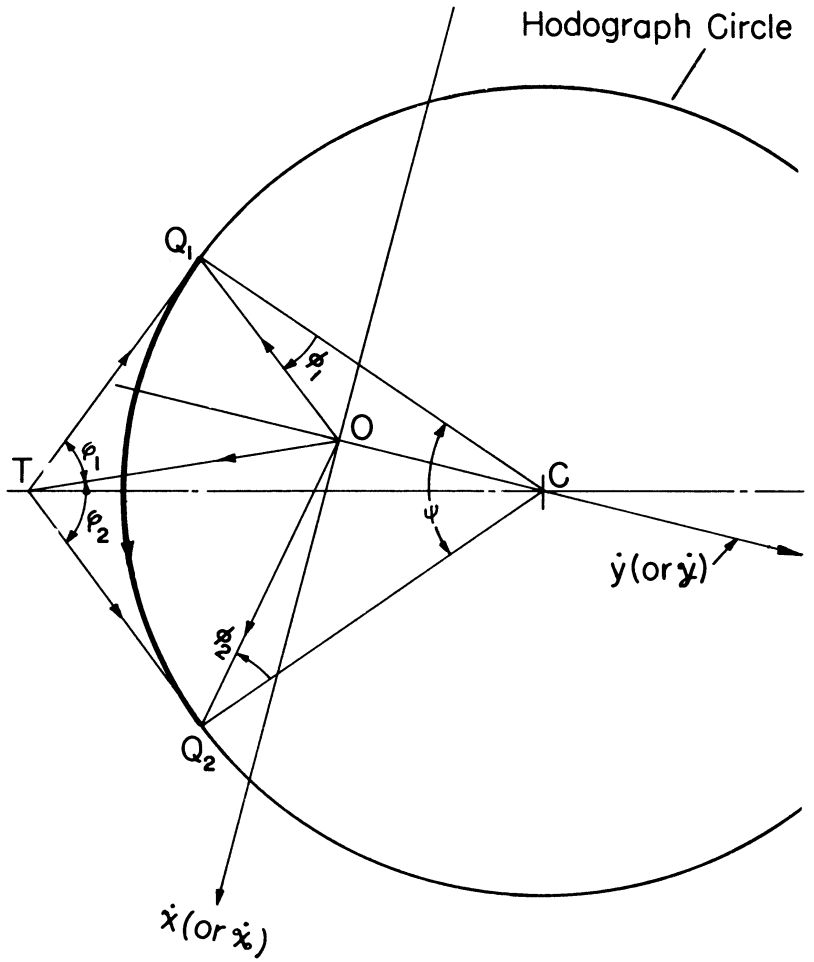

(b) Hodograph Plane

Figure II-4. Terminal Velocities and Their Chordal and Radial Components.

Furthermore, the hodograph geometry shows that

$$V_R = \overline{CQ} \tan \frac{\Psi}{2} = \frac{\mu}{h} \tan \frac{\Psi}{2} \tag{9.4}$$

With the angular momentum expressed as

$$h = V_C d \tag{9.5}$$

where d is the perpendicular distance from the field center to the chord Q_1Q_2 (to be called the base altitude for short), Equation (9.4) becomes

$$V_C V_R = \frac{\mu}{d} \tan \frac{\Psi}{2} \tag{9.6}$$

Thus the product of the chordal and radial components of either terminal velocity is constant for all trajectories passing through the given terminal points.

Equations (9.3) and (9.6) are known as Godal's compatibility conditions, which were analytically derived in Reference 37. They follow immediately from the present hodograph construction. These simple relations will be useful in the analyses that follow.

9.2 The Conjugate Relations

By definition, conjugate trajectories are those having the same initial and final terminal points, same departure speed, and the same range angle. (This implies that they are of the same group.) The proof of the existence of the line of origins has already revealed the existence of a pair of conjugate trajectories for a given base triangle and an arbitrary departure speed ($> V_*$), and lends itself a method of constructing such a conjugate pair in the hodograph plane by simply drawing the speed circle of radius λ_1^2 according to the given speed and finding its intersections with the line of origins, which are then the conjugate origins.

With the origins thus determined the elements of each of the conjugate pair may then be found in the usual manner according to the correlation rules in Chapters 3 and 5. The general geometry of such a hodograph is shown in Figure II-2; and a typical conjugate pair of each type of the Keplerian trajectories of a normal group and their hodograph images are shown in Figures II-5 to II-7.

Based on such hodographic representation we may now proceed to examine some of the essential features of the conjugate trajectories. With reference to Figure II-2 the geometry of the hodograph gives

$$\overline{TO}_I \cdot \overline{TO}_{II} = \overline{TQ}_1 \cdot \overline{TQ}_2 \tag{9.7}$$

However, in a dimensionless hodograph we have by definition

$$\begin{aligned} \overline{TO}_I &= \frac{h_I}{\mu} V_{CI} , \quad \overline{TO}_{II} = \frac{h_{II}}{\mu} V_{CII} \\ \overline{TQ}_1 &= \frac{h_I}{\mu} V_{RI} , \quad \overline{TQ}_2 = \frac{h_{II}}{\mu} V_{RII} \end{aligned} \tag{9.8}$$

and furthermore, from the hodograph geometry,

$$\overline{TQ}_1 = \overline{TQ}_2 = \tan \frac{\psi}{2} \tag{9.9}$$

Substituting Equations (9.8) and (9.9) into (9.7) and making use of Equation (9.5) yields

$$V_{CI} \cdot V_{CII} = V_{RI} \cdot V_{RII} = \frac{\mu}{d} \tan \frac{\psi}{2} \tag{9.10}$$

Thus for fixed terminal points the product of the conjugate chordal components of the terminal velocity and that of the conjugate radial components are identical, both equal to the same constant, determined by the geometry of the base triangle.

Furthermore, combining Equations (9.10) and (9.6) gives the reciprocal relations,

$$V_{CI} = V_{RII} , \quad V_{RI} = V_{CII} \tag{9.11}$$

That is, by merely interchanging the chordal and radial components of the velocity at either terminal we may change the trajectory to its conjugate.

Next, since the angular momentum is directly proportional to the terminal chordal component, it follows immediately from Equations (9.10) and (9.5) that the conjugate angular momenta are related by

$$h_I \cdot h_{II} = \mu d \tan \frac{\psi}{2} \tag{9.12}$$

Furthermore, as the latus rectum of the trajectory conic is determined by the angular momentum according to Equation (1.6), Equation (9.12) leads to

$$\bar{r}_I \cdot \bar{r}_{II} = d^2 \tan^2 \frac{\psi}{2} \tag{9.13}$$

The above equations show that in a given gravity field the product of each pair of the conjugate elements, V_C, V_R, h, and $\bar{r}$, is a constant, depending on the geometry of the base triangle, but independent of the initial terminal speed, and hence the choice of trajectory. In the case of the product of latus recta it is also independent of the field strength μ. Furthermore, as these products involve no other geometrical parameters than ψ and d, base triangles of different configurations will have the same values of these conjugate products as long as they have the same vertex angle and the same base altitude.

Finally as shown in Figure II-5, 6, and 7 the hodograph gives the conjugate path angles at the initial terminal Q_1 for either type of the trajectory,

$$\phi_{1I} = \sphericalangle CQ_1O_1 , \quad \phi_{1II} = \sphericalangle CQ_1O_{II} \tag{9.14}$$

Based on the sign convention for the angular measurement of ϕ defined in Figure I-2 and the geometry of the hodograph (Figure II-5) it is

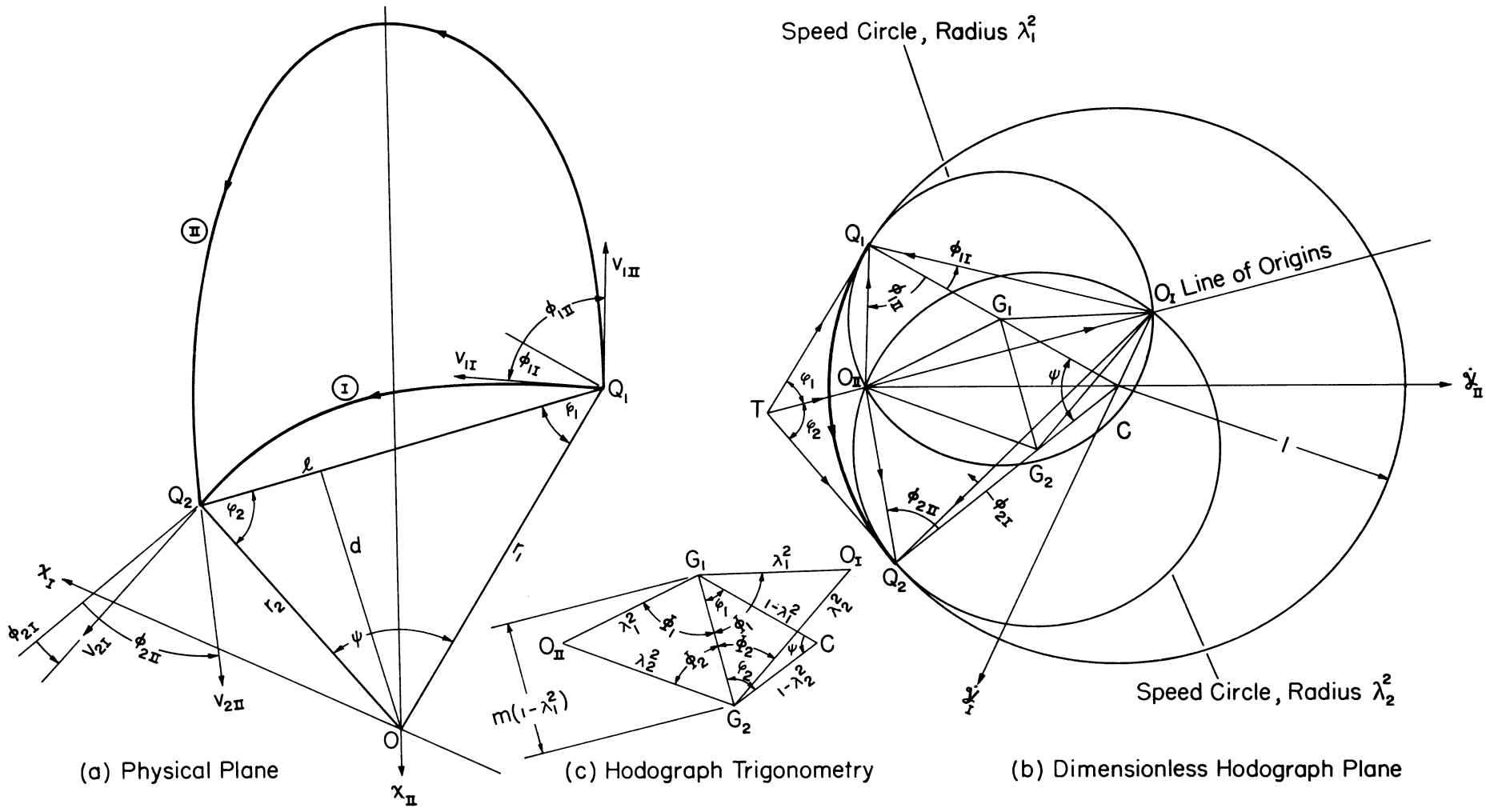

Figure II-5. The Conjugate Elliptic Trajectories, Range < 180°.

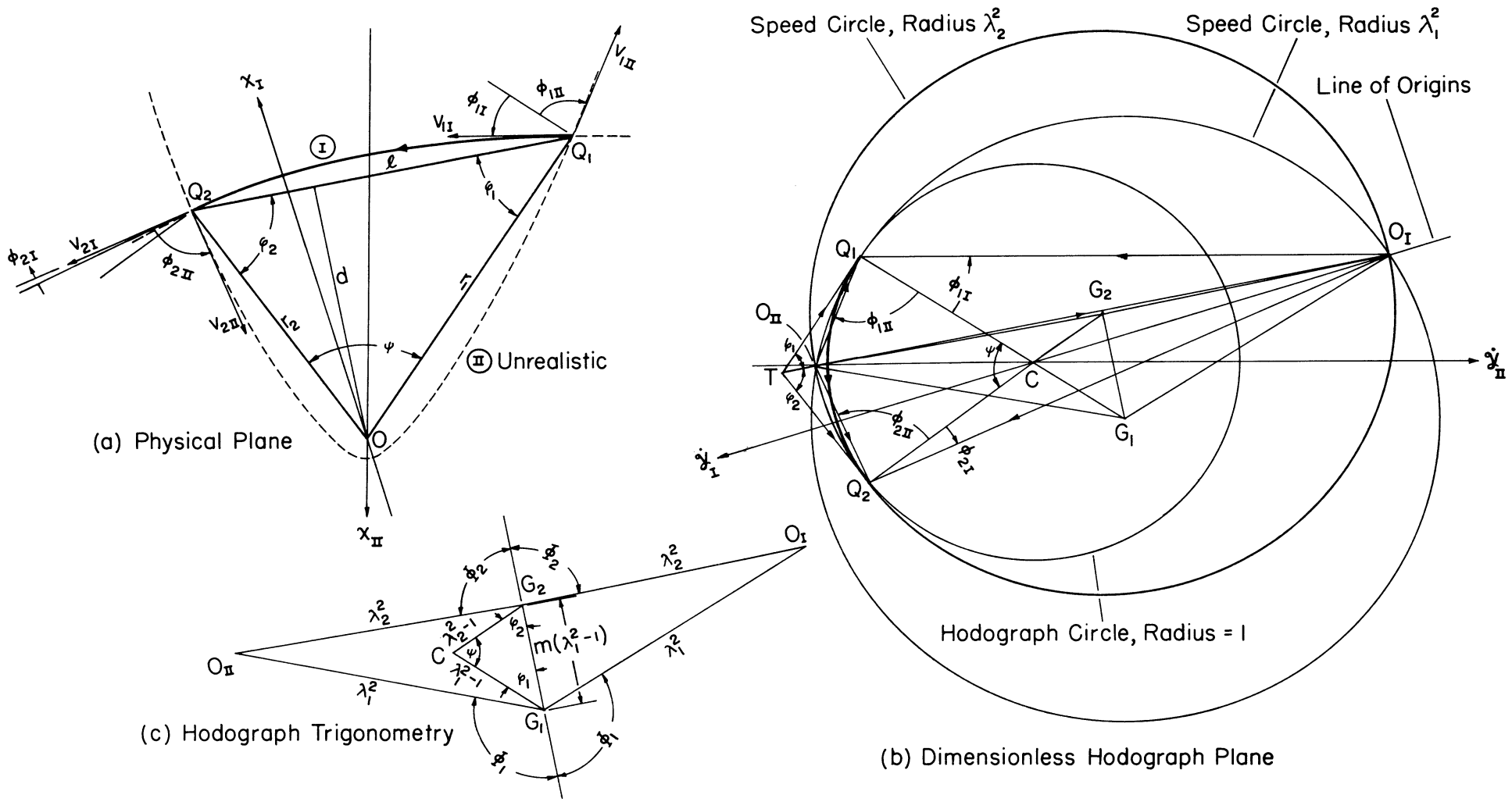

Figure II-6. The Conjugate Hyperbolic Trajectories, Range < 180°.

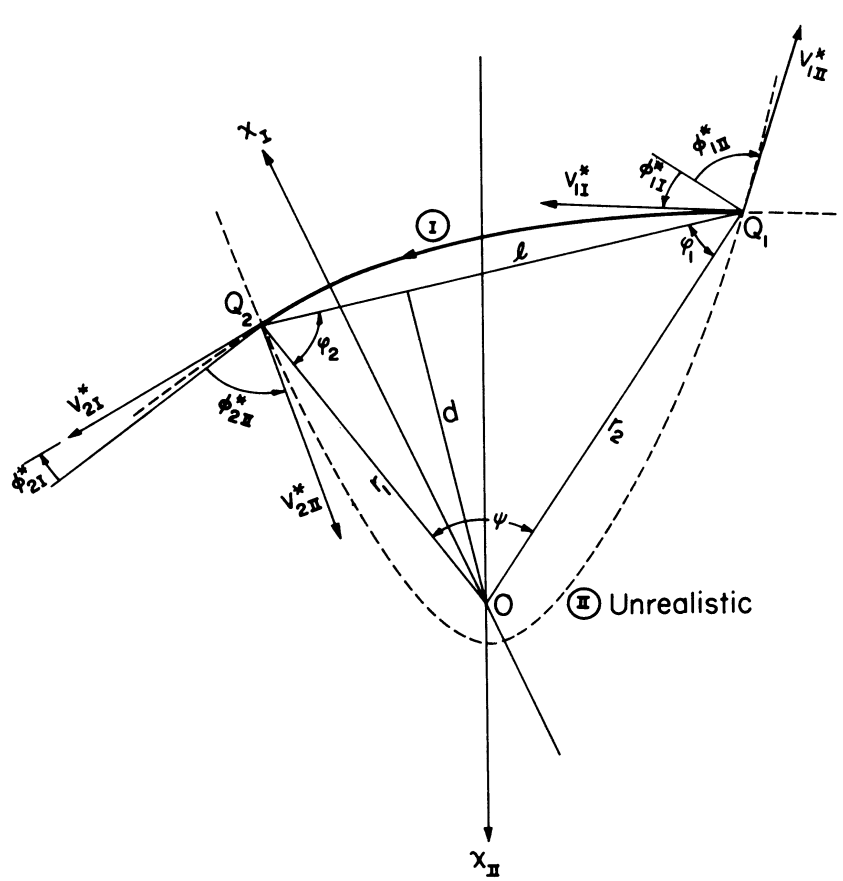

(a) Physical Plane

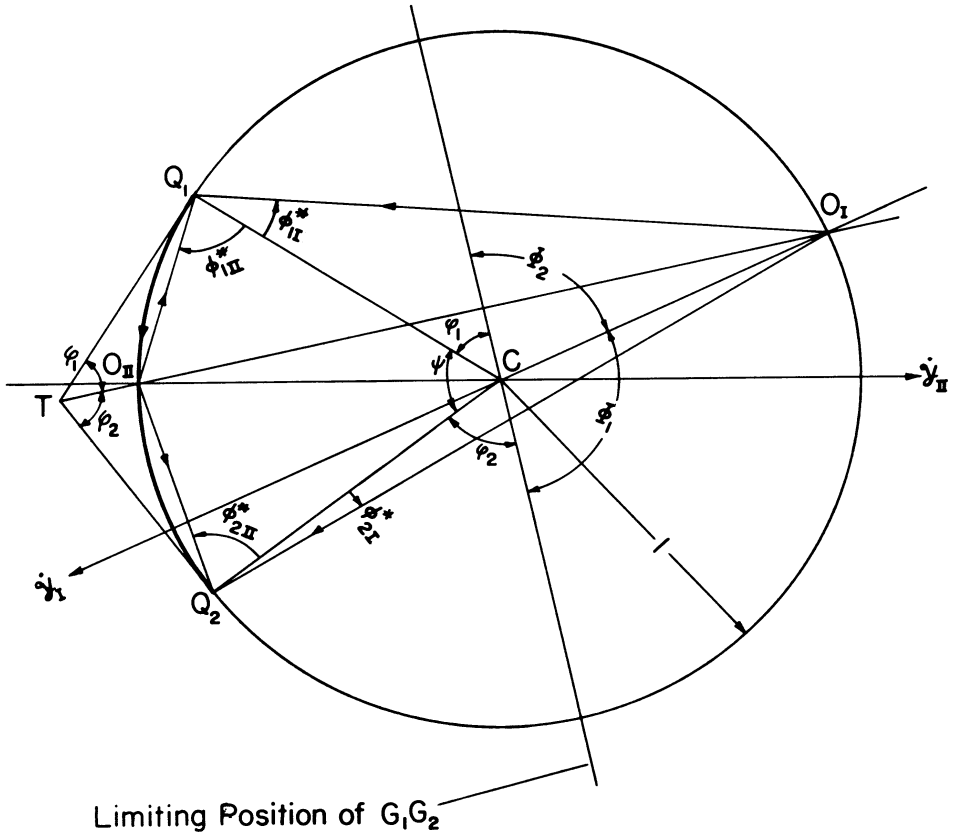

(b) Dimensionless Hodograph Plane

Figure II-7. The Conjugate Parabolic Trajectories, Range < 180°.

seen that, for an elliptic trajectory,

$$\sphericalangle CQ_1O_I = \frac{1}{2}\left(\sphericalangle CG_1G_2 - \sphericalangle O_IG_1G_2\right)$$

$$\sphericalangle CQ_1O_{II} = \frac{1}{2}\left(\sphericalangle CG_1G_2 + \sphericalangle O_{II}G_1G_2\right)$$

By the similarity of the triangles CG_1G_2 in the hodograph plane and OQ_1Q_2 in the physical plane, the angle CG_1G_2 may be identified as the base angle φ_1 ; and by hodograph construction the angles $O_IG_1G_2$ and $O_{II}G_1G_2$ are equal in magnitude, which will be denoted by Φ_1 . Thus the foregoing relations may be written as

$$\begin{aligned} \phi_{1I} &= \frac{1}{2}\left(\varphi_1 - \Phi_1\right) \\ \phi_{1II} &= \frac{1}{2}\left(\varphi_1 + \Phi_1\right) \end{aligned} \tag{9.15}$$

from which we deduce immediately

$$\phi_{1I} + \phi_{1II} = \varphi_1 \tag{9.16-1}$$

Evidently, similar relation holds at the final terminal Q_2 , that is

$$\phi_{2I} + \phi_{2II} = \varphi_2 \tag{9.16-2}$$

An examination of the hodograph geometry for the hyperbolic case (Figure II-6) shows that Equation (9.15) also holds if we define Φ_1 to be $\pi - \sphericalangle O_IG_1G_2$. Both definitions for Φ_1 become identical for the parabolic case (Figure II-7) in which the points G_1 and G_2 coincide with C (the center of the hodograph circle), and the limiting direction of G_1G_2 is given by the line through C and perpendicular to the line of origins. Consequently Equations (9.16) are also valid for the hyperbolic and parabolic cases. Thus in conclusion, the algebraic sum of the conjugate path angles at either terminal is equal to

the base angle of the base triangle at that terminal. Since for fixed terminal points, φ_1 and φ_2 are constants; we may say that algebraic sum of the conjugate path angles at either terminal is a constant, independent of the terminal speed, hence the choice of trajectory. This conclusion has been previously established in Reference 9 for the symmetric, elliptic case, the present analysis shows that it carries over to the general case not necessarily symmetric, and covering all three types of the Keplerian trajectories even though the high trajectory is not realistic in the hyperbolic or parabolic case.

Finally, it is obvious that the conjugate trajectories, being of the same departure speed, will have the same orbital energy, the same magnitude of the major-axis, and the same speed at the final terminal. All these conjugate relations are summarized in Table II-4.

TABLE II-4

SUMMARY OF CONJUGATE RELATIONS

	Formulas	
The Reciprocal Relations	$V_{CI} = V_{RII}$, $V_{CII} = V_{RI}$	(9.11)
The Constant Product Formulas	$V_{CI}V_{CII} = V_{RI}V_{RII} = \frac{\mu}{d}\tan\frac{\Psi}{2}$	(9.10)
	$h_I h_{II} = \mu d \tan\frac{\Psi}{2}$	(9.12)
	$\bar{r}_I \bar{r}_{II} = d^2 \tan^2\frac{\Psi}{2}$	(9.13)
The Constant Sum Formulas	$\phi_{1I} + \phi_{1II} = \varphi_1$ $\phi_{2I} + \phi_{2II} = \varphi_2$	(9.16)
Other Relations	$V_{1I} = V_{1II}$ (by definition) $V_{2I} = V_{2II}$ $k_I = k_{II}$ $a_I = a_{II}$	(9.17)

NOTE: All these relations hold for a conjugate pair of trajectories of either the normal group or the complementary group. Change of signs of the path angles in Equation (9.16) is needed for the complementary group.

9.3 The Principal Elements of the Conjugate Trajectories

In ballistic missile problems or problems of interplanetary flight it is usually desirable to determine the trajectory elements for an arbitrary departure speed V_1 when the range ψ and the terminal distances r_1 and r_2 are prescribed, that is when the base triangle is given. The hodograph construction described in Section 9.1 has already provided a simple graphical means for the determination of such elements. If analytical expressions are sought, we may easily proceed from the geometry of the hodograph.

A simple way for such derivation is again to start from the chordal and radial components of the terminal velocity. Let us first consider the trajectories of the normal group. As the hodograph shows (Figure II-4), for a given departure speed V_1 these two components are related by

$$V_C^2 + V_R^2 = V_1^2 + 2V_C V_R \cos \varphi_1 \tag{9.18}$$

Combining it with the compatibility condition (9.6) yields the pair of solutions

$$\begin{aligned} V_C &= \frac{1}{2}(\zeta \mp \chi) \\ V_R &= \frac{1}{2}(\zeta \pm \chi) \end{aligned} \tag{9.19}$$

where the upper sign corresponds to the high trajectory of the conjugate pair and the lower sign, the low trajectory (this double-sign convention will be followed through in Part II), and the parameters ζ and χ are defined by,

$$\begin{aligned} \zeta &= \sqrt{V_1^2 + \frac{4\mu}{d} \tan \frac{\psi}{2} \cos^2 \frac{\varphi_1}{2}} \\ \chi &= \sqrt{V_1^2 - \frac{4\mu}{d} \tan \frac{\psi}{2} \sin^2 \frac{\varphi_1}{2}} \end{aligned} \tag{9.20}$$

With these formulas as basis, other trajectory elements follow immediately from the general orbital relations. For example,

$$h = V_C d = \frac{d}{2}(\zeta \mp \chi) \tag{9.21}$$

$$V_{\theta 1} = \frac{h}{r_1} = \frac{d}{2r_1}(\zeta \mp \chi) \tag{9.22}$$

$$\cos \phi_1 = \frac{V_{\theta 1}}{V_1} = \frac{d}{2r_1 V_1}(\zeta \mp \chi) \tag{9.23}$$

$$\bar{r} = \frac{h^2}{\mu} = \frac{d^2}{4\mu}(\zeta \mp \chi)^2 \tag{9.24}$$

$$\epsilon = [1-4\lambda_1^2(1-\lambda_1^2) \cos^2 \phi_1]^{1/2} = \left[1 - \frac{d^2}{2\mu r_1}(1-\lambda_1^2)(\zeta \mp \chi)^2\right]^{1/2} \tag{9.25}$$

and so on. By using the trigonometric relations among the geometrical elements of the base triangle, the trajectory elements given by the foregoing formulas may all be expressed in terms of the three independent elements of the base triangle, ψ, φ_1, and r_1, together with the departure speed. The results are summarized in column 1, Table II-5. For convenience, all speeds have been expressed in the dimensionless form of speed parameters. The transition from the present set of independent variables to the more usual combination: ψ, n, r_1, and λ_1 is straightforward though tedious. To avoid long, cumbersome expressions, a redundant variable m defined by Equation (8.5) is introduced, and the results are given in column 2, Table II-5.

It is to be noted that, since Equations (9.6) and (9.18) on which the present derivation is based, are independent of the type of the trajectory, so are all the formulas shown in Table II-5. Finally in line with the observations in Chapter 8 although the formulas here stand for all three types of the Keplerian trajectory, they may or may not be realistic (see footnote, Table II-5).

TABLE II-5

FORMULAS FOR THE PRINCIPAL ELEMENTS OF THE CONJUGATE TRAJECTORIES

	Range Angle = $\psi < \pi$		Range Angle = π
	In terms of ψ, φ_1, r_1, and λ_1	In terms of ψ, m, n, r_1, and λ_1	
Initial Terminal Speed Parameter			
Chordal λ_{c1}	$\frac{1}{2}\left[\sqrt{\lambda_1^2+\tan\frac{\psi}{2}\cot\frac{\varphi_1}{2}} \mp \sqrt{\lambda_1^2-\tan\frac{\psi}{2}\tan\frac{\varphi_1}{2}}\right]$	$\frac{1}{2}\left[\sqrt{\lambda_1^2+\frac{m-n\cos\psi+1}{2n}\sec^2\frac{\psi}{2}} \mp \sqrt{\lambda_1^2-\frac{m+n\cos\psi-1}{2n}\sec^2\frac{\psi}{2}}\right]$	∞
Radial λ_{r1}	$\frac{1}{2}\left[\sqrt{\lambda_1^2+\tan\frac{\psi}{2}\cot\frac{\varphi_1}{2}} \pm \sqrt{\lambda_1^2-\tan\frac{\psi}{2}\tan\frac{\varphi_1}{2}}\right]$	$\frac{1}{2}\left[\sqrt{\lambda_1^2+\frac{m-n\cos\psi+1}{2n}\sec^2\frac{\psi}{2}} \pm \sqrt{\lambda_1^2-\frac{m+n\cos\psi-1}{2n}\sec^2\frac{\psi}{2}}\right]$	∞
Transverse λ_{t1}	$\sin\frac{\varphi_1}{2}\left[\sqrt{\lambda_1^2+\tan\frac{\psi}{2}\cot\frac{\varphi_1}{2}} \mp \sqrt{\lambda_1^2-\tan\frac{\psi}{2}\tan\frac{\varphi_1}{2}}\right]$	$\frac{1}{2}\frac{n}{m}\sin\psi\left[\sqrt{\lambda_1^2+\frac{m-n\cos\psi+1}{2n}\sec^2\frac{\psi}{2}} \mp \sqrt{\lambda_1^2-\frac{m+n\cos\psi-1}{2n}\sec^2\frac{\psi}{2}}\right]$	$\sqrt{\frac{n}{n+1}}$
Radial λ_{r1}	$\sin^2\frac{\varphi_1}{2}\sqrt{\lambda_1^2+\tan\frac{\psi}{2}\cot\frac{\varphi_1}{2}} \pm \cos^2\frac{\varphi_1}{2}\sqrt{\lambda_1^2-\tan\frac{\psi}{2}\tan\frac{\varphi_1}{2}}$	$\left[\frac{m+n\cos\psi-1}{2m}\sqrt{\lambda_1^2+\frac{m-n\cos\psi+1}{2n}\sec^2\frac{\psi}{2}} \pm \frac{m-n\cos\psi+1}{2m}\sqrt{\lambda_1^2-\frac{m+n\cos\psi-1}{2n}\sec^2\frac{\psi}{2}}\right]$	$\sqrt{\lambda_1^2-\frac{n}{n+1}}$
Initial Path Angle ϕ_1	$\frac{1}{2}\left[\varphi_1 \pm \cos^{-1}\left(\frac{1}{\lambda_1^2}\tan\frac{\psi}{2}\sin\varphi_1-\cos\varphi_1\right)\right]$ $= \cos^{-1}\left\{\frac{\sin\varphi_1}{2\lambda_1}\left[\sqrt{\lambda_1^2+\tan\frac{\psi}{2}\cot\frac{\varphi_1}{2}} \mp \sqrt{\lambda_1^2-\tan\frac{\psi}{2}\tan\frac{\varphi_1}{2}}\right]\right\}$	$\frac{1}{2}\left[\cos^{-1}\frac{1-n\cos\psi}{m} \pm \cos^{-1}\frac{n-1+(1-n\cos\psi)(1-2\lambda_1^2)}{m\lambda_1^2}\right]$ $= \cos^{-1}\left\{\frac{1}{2}\left(\frac{n}{m}\right)\frac{\sin\psi}{\lambda_1}\left[\sqrt{\lambda_1^2+\frac{m-n\cos\psi+1}{2n}\sec^2\frac{\psi}{2}} \mp \sqrt{\lambda_1^2-\frac{m+n\cos\psi-1}{2n}\sec^2\frac{\psi}{2}}\right]\right\}$	$\pm\cos^{-1}\frac{1}{\lambda_1}\sqrt{\frac{n}{n+1}}$
Angular Momentum h	$\sqrt{\frac{\mu r_1}{2}}\sin\varphi_1\left[\sqrt{\lambda_1^2+\tan\frac{\psi}{2}\cot\frac{\varphi_1}{2}} \mp \sqrt{\lambda_1^2-\tan\frac{\psi}{2}\tan\frac{\varphi_1}{2}}\right]$	$\sqrt{\frac{\mu r_1}{2}}\frac{n}{m}\sin\psi\left[\sqrt{\lambda_1^2+\frac{m+n\cos\psi+1}{2n}\sec^2\frac{\psi}{2}} \mp \sqrt{\lambda_1^2-\frac{m+n\cos\psi-1}{2n}\sec^2\frac{\psi}{2}}\right]$	$\sqrt{\frac{2\mu n r_1}{n+1}}$
Orbital Energy k	$\frac{\mu}{r_1}(\lambda_1^2-1)$	$\frac{\mu}{r_1}(\lambda_1^2-1)$	$\frac{\mu}{r_1}(\lambda_1^2-1)$
Semi-major Axis a (or Semi-transverse Axis)	$\frac{r_1}{2\lvert 1-\lambda_1^2\rvert}$	$\frac{r_1}{2\lvert 1-\lambda_1^2\rvert}$	$\frac{r_1}{2\lvert 1-\lambda_1^2\rvert}$
Semi-latus Rectum $\bar{h}$	$r_1\sin\varphi_1\left[\lambda_1^2+\tan\frac{\psi}{2}\cot\varphi_1 \mp \sqrt{\lambda_1^4+2\lambda_1^2\tan\frac{\psi}{2}\cot\varphi_1-\tan^2\frac{\psi}{2}}\right]$	$r_1\left(\frac{n}{m}\right)^2\sin^2\psi\left[\lambda_1^2+\frac{1-n\cos\psi}{2n}\sec^2\frac{\psi}{2} \mp \sqrt{\lambda_1^4+\lambda_1^2\frac{1-n\cos\psi}{n}\sec^2\frac{\psi}{2}-\tan^2\frac{\psi}{2}}\right]$	$\frac{2nr_1}{n+1}$
Eccentricity ϵ	$\left\{1-2(1-\lambda_1^2)\sin^2\varphi_1\left[\lambda_1^2+\tan\frac{\psi}{2}\cot\varphi_1 \mp \sqrt{\lambda_1^4+2\lambda_1^2\tan\frac{\psi}{2}\cot\varphi_1-\tan^2\frac{\psi}{2}}\right]\right\}^{\frac{1}{2}}$	$\left\{1-2(1-\lambda_1^2)\left(\frac{n}{m}\right)^2\sin^2\psi\left[\lambda_1^2+\frac{1-n\cos\psi}{2n}\sec^2\frac{\psi}{2} \mp \sqrt{\lambda_1^4+\lambda_1^2\frac{1-n\cos\psi}{n}\sec^2\frac{\psi}{2}-\tan^2\frac{\psi}{2}}\right]\right\}^{\frac{1}{2}}$	$\sqrt{\frac{4n\lambda_1^2-3n+1}{n+1}}$
Definitions: $n \equiv \frac{r_2}{r_1}$ $\quad m \equiv \frac{\ell_2}{\ell_1} = \sqrt{1-2n\cos\psi+n^2}$			

Note:
1. All formulas hold for all three types of the Keplerian trajectories, elliptic, parabolic, and hyperbolic.
2. Of the double sign, the upper one refers to the high trajectory, while the lower one, the lower trajectory. In the elliptic case, each sign is associated with a realistic trajectory; while in the hyperbolic or parabolic case, only the lower sign is associated with a realistic trajectory.
3. Quantities pertaining to the final terminal may be obtained from the corresponding formula for the initial terminal by replacing the subscript "1" by "2", and n by 1/n (m by m/n).
4. To obtain formulas for range angle $\psi' = 2\pi-\psi > \pi$, interchange the upper and lower sign and replace ϕ_1 by $-\phi_1'$.

Among these principal elements of the conjugate trajectories the path angle ϕ_1 deserves particular attention since it determines the correct direction of departure for an arbitrary speed. However, formula (9.23) may result in some ambiguity in finding the angle ϕ_1 from its cosine since ϕ_1 may be either positive or negative. An alternative formula for ϕ_1 obtained directly from Equation (9.15) with the aid of the hodograph geometry is

$$\phi_1 = \frac{1}{2}\left[\cos^{-1}\frac{1-n\cos\psi}{m} \pm \cos^{-1}\frac{n-1+(1-n\cos\psi)(1-\lambda_1^2)}{m\lambda_1^2}\right] \tag{9.26a}$$

$$= \frac{1}{2}\left[\varphi_1 \pm \cos^{-1}\left(\frac{1}{\lambda_1^2}\tan\frac{\psi}{2}\sin\varphi_1 - \cos\varphi_1\right)\right] \tag{9.26b}$$

Under the assumption $0 < \psi < \pi$ we have $0 < \varphi_1 < \pi$ and $0 < \Phi < \pi$. Thus either of the above expressions gives a unique value of ϕ_1 for each of the conjugate pair without ambiguity. Like Equation (9.23), expression (9.26a) or (9.26b) holds regardless of the type of the trajectory even though it may not be realistic.

Evidently all formulas of this section may apply to the complementary group with a change of sign for the path angle and interchange of the upper and lower signs in the double-sign convention. The dependence of the path angle and the trajectory eccentricity on the range angle, the distance ratio, and the departure speed are shown graphically in Figures II-14 and II-15.

Very often the maximum and minimum radial distances on the trajectory are of interest. One should be aware of the fact that, since the trajectory is only a part of the Keplerian conic, the two apses may or may not lie on the trajectory, and consequently the maximum and minimum radial distances may or may not be given by the apocenter and pericenter distances. In the hodograph plane this is indicated by whether

or not the $\dot{y}$-axis (the line through O and C) will cross the arc $\overset{\frown}{Q_1Q_2}$, the hodograph image of the trajectory; and this is in turn determined by the location of the hodograph origin relative to the two key points H_1 and H_2, the intersections of the line of origins with the radii OQ_1 and OQ_2 (or their extensions) respectively. An examination of the hodograph will help to clarify the situation and the criteria obtained are summarized in Table II-6. Thus in a normal group it is possible to have either the apocenter or the pericenter alone, or none of them, but never both lying on the trajectory. In case the apocenter or the pericenter does not lie on the trajectory, then the maximum or minimum distances, instead of being given by r_A or r_P will be either r_1 or r_2 itself. It is to be noted that same criteria of Table II-6 may apply to the complementary group if we interchange the letters A and P.

TABLE II-6

HODOGRAPHIC CRITERIA FOR THE OCCURRENCE OF THE APSES ON THE TRAJECTORY ($\psi < \pi$)

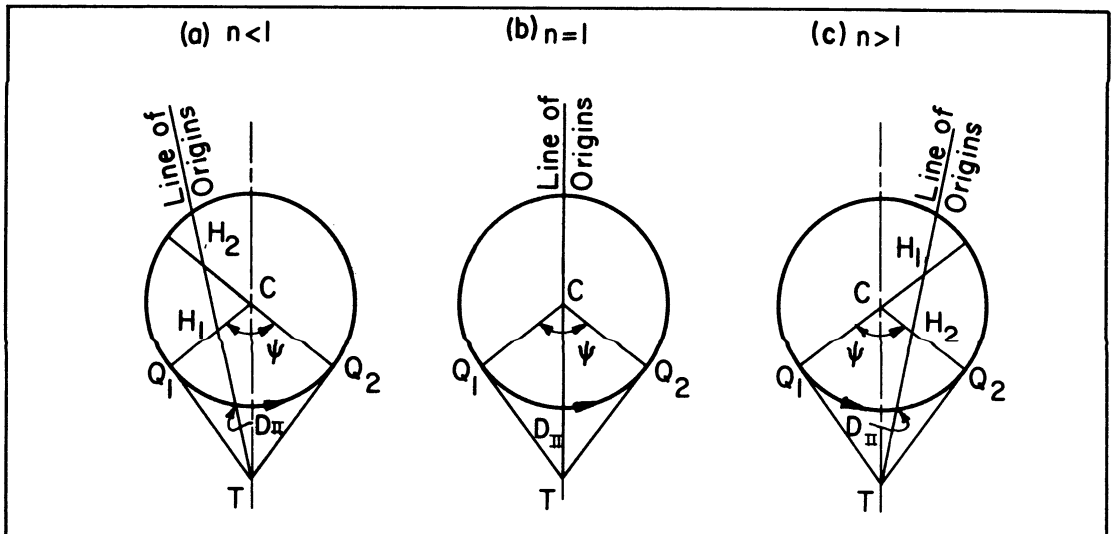

Occurrence of Apsis on the Trajectory	Location of the Hodograph Origin		
	$n < 1$	$n = 1$	$n > 1$
A, not P	Between D_{II} and H_1	Between D_{II} and C	Between D_{II} and H_2
P, not A	Beyond H_2	Beyond C	Beyond H_1
Neither A nor P	Between H_1 and H_2	---	Between H_1 and H_2

10. ANALYSIS OF SOME PARTICULAR TRAJECTORIES

The trajectory analysis made so far has been of a general nature, a brief analysis for some of the particular trajectories is now in order.

10.1 The Minimum Energy Trajectory

Since the minimum energy trajectory is fairly well-known,[10.1] only a few supplementary remarks will be sufficient.

In line with the concept of conjugate trajectories a minimum energy trajectory may be viewed as the one conjugate to itself. By using this concept all formulas for the minimum energy trajectory follow immediately from the previous conjugate relations. For example, setting $V_{CI} = V_{CII} = V_{C*}$, $V_{RI} = V_{RII} = V_{R*}$ in (9.10) we find

$$V_{C*} = V_{R*} = (V_{CI}V_{CII})^{1/2} = (V_{RI}V_{RII})^{1/2} = \left(\frac{\mu}{d}\tan\frac{\psi}{2}\right)^{1/2} \quad (10.1)$$

Thus the minimum energy trajectory is characterized by the fact that the chordal and radial components of either terminal velocity are identical in magnitude, both equal to the geometrical mean of any conjugate pair of either the chordal components or the radial components, with the same ψ and d. Formula (10.1) is in fact self-evident from the geometry of the hodograph since in the present case (see Figure II-8) the speed circle at Q_1 is tangent to both the line of origin and the line $T Q_1$ and the two tangents drawn from an exterior point to a circle are necessarily equal. This simple fact enables one to locate the optimum origin O_* in the hodograph plane for the minimum energy trajectory by simply laying off $TO_* = T Q_1$ on the line of origins.

10.1 See for example References 9, 12, 34, 42.

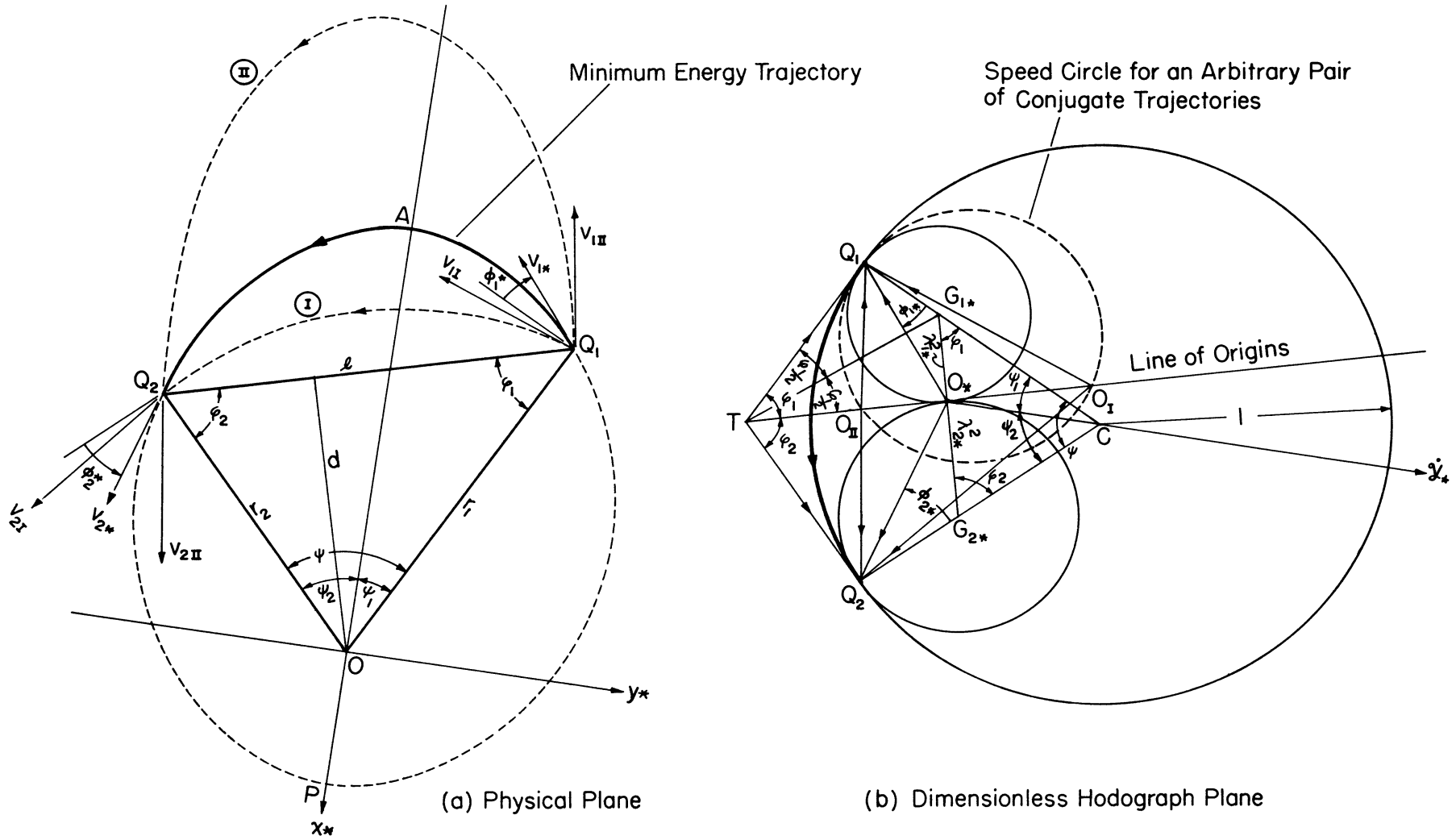

Figure II-8. The Minimum Energy Trajectory and Its Relation with a Pair of Conjugate Trajectories, Range < 180°.

Likewise by using the same concept we deduce

$$h_* = (h_I h_{II})^{1/2} = \left(\mu d \tan \frac{\psi}{2}\right)^{1/2} \tag{10.2}$$

$$\bar{r}_* = (\bar{r}_1 \bar{r}_2)^{1/2} = d \tan \frac{\psi}{2} \tag{10.3}$$

$$\begin{aligned} \phi_{1*} &= \frac{1}{2} (\phi_{1I} + \phi_{1II}) = \frac{1}{2} \varphi_1 \\ \phi_{2*} &= \frac{1}{2} (\phi_{2I} + \phi_{2II}) = \frac{1}{2} \varphi_2 \end{aligned} \tag{10.4}$$

Thus the optimum values of the angular momentum and latus rectum for minimum energy trajectory are the geometrical means of any conjugate pairs of the angular momenta and latus recta respectively for the same range angle ψ and the base altitude d ; while the optimum terminal path angle is the arithmetic mean of any conjugate pair of the terminal path angle for the same base angle at the terminal point, and is equal to one half of this base angle. The last statement on the path angle, in fact, amounts to saying: the optimum direction of departure for a minimum energy trajectory always bisects a pair of conjugate directions of departure and the same is true for the resulting direction of approach. In particular, the optimum direction bisects the external angle at the corresponding terminal since the chordal and radial directions at either terminal are such a conjugate pair; thus the optimum direction and the bisector of the base angle at the same terminal are perpendicular to each other. It is interesting to note here that the direction of optimum departure is determined by the initial base angle alone. Consequently

this direction will remain fixed if the final terminal moves along the chord line. This is in analogy with an artillery trajectory over a flat earth. Imagine a target point is in the same horizontal plane as the initial point, then $\varphi_1 = 90°$, and Equation (10.4) gives the optimum direction of departure at 45° with the local horizon just like the artillery case, although the force field considered here is central instead of uniform, and hence the trajectory here is elliptic instead of parabolic.

The optimum departure speed parameter for the minimum energy trajectory is given by the hodograph as the radius of the speed circle at Q_1 which is tangent to the line of origins, and the geometry of the hodograph (Figure II-8) shows that

$$\lambda_{1*}^2 = \tan \frac{\psi}{2} \tan \frac{\varphi_1}{2} \tag{10.5}$$

which simplifies to

$$\lambda_{1*}^2 = 1 - \frac{r_1}{s} \tag{10.6}$$

where s is the half-perimeter of the base triangle, defined by

$$s = \frac{1}{2} (r_1 + r_2 + \ell) \tag{10.7}$$

The minimum energy and the corresponding semimajor axis then found to be

$$k_* = \frac{\mu}{r_1} (\lambda_{1*}^2 - 1) = -\frac{\mu}{s} \tag{10.8}$$

and

$$a_* = -\frac{\mu}{2k_*} = \frac{1}{2} s \tag{10.9}$$

Thus, in a given gravity field, while the angular momentum and the latus rectum of a minimum energy trajectory are determined by ψ and d alone,

the orbital energy and the major axis depend only on the perimeter of the base triangle.

Following the foregoing formulas all other elements of a minimum energy trajectory may be easily obtained from the general orbital relations. Of course all formulas and conclusions in this section hold for a normal group or its complement as well except for a change of sign in the path angle, since the minimum energy trajectories of the two groups are of the same Keplerian ellipse.

In regard to the occurrence of the apses, it is to be noted that, for a normal group the apocenter of a minimum energy trajectory always lies on the trajectory while its pericenter does not, since the optimum origin O_* in such a case always lies between the points H_1 (or H_2) and D_{II} (see Table II-6). Thus for such a trajectory the apocenter is actually the trajectory peak while the point of closest approach on the trajectory is either Q_1 or Q_2 according as $r_1 < r_2$, or $r_1 > r_2$. A similar statement holds for a complementary group except that it is the pericenter which always lies on the trajectory, not the apocenter. Sometimes the location of such apses on the trajectory is of interest. By considering the similarities of the triangles OQ_1Q_2 (physical plane) and CG_1G_2 (hodograph plane) a little trigonometric manipulation yields

$$\tan \psi_I = \frac{\sin \psi}{\cos \psi + \eta}$$

$$\tan \psi_2 = \frac{\sin \psi}{\cos \psi + \frac{1}{\eta}} \qquad (10.10)$$

where the angles ψ_1 and ψ_2 are identified in Figure II-8, and

$$\eta \equiv \left(\sin \frac{\varphi_1}{2} \Big/ \sin \frac{\varphi_2}{2} \right)^2 \qquad (10.11)$$

which is a constant for a given base triangle. The above equations give the location of the apocenter for a normal minimum energy trajectory or the pericenter of its complement.

10.2 The Least Eccentric Trajectory and Its Conjugate

As shown in Section 8.4, there is a least eccentric trajectory for each fixed configuration of the base triangle. The hodograph origin for such a trajectory is given by the point E, the foot of the perpendicular drawn from the center of the hodograph circle to the line of origins, and the least eccentricity is given by Equations (8.4) or (8.4a). The dependence of ϵ_{min} on n and ψ is shown graphically in Figures 15a, b, c, d as the least eccentricity line which forms the lower envelope for all the eccentricity curves. Obviously with its hodograph origin located at E, a least eccentric trajectory will have its apsidal axis parallel to the chord lines Q_1Q_2 in the physical plane, and consequently its minor axis will pass through the middle point of the chord Q_1Q_2 (Figure II-9).

It can be shown that the trajectory conjugate to the least eccentric one is the one having its hodograph origin located at F, where the line of origins crosses the line Q_1Q_2 in the hodograph plane. This trajectory ellipse will have the line Q_1Q_2 as its diameter since the terminal velocities are now pointing in the opposite directions. The departure path angle to achieve this particular trajectory of a normal group is, as seen from the hodograph,

$$\phi_{1II} = -\phi_{2II} = \frac{\pi}{2} - \frac{\psi}{2} \qquad (10.12)$$

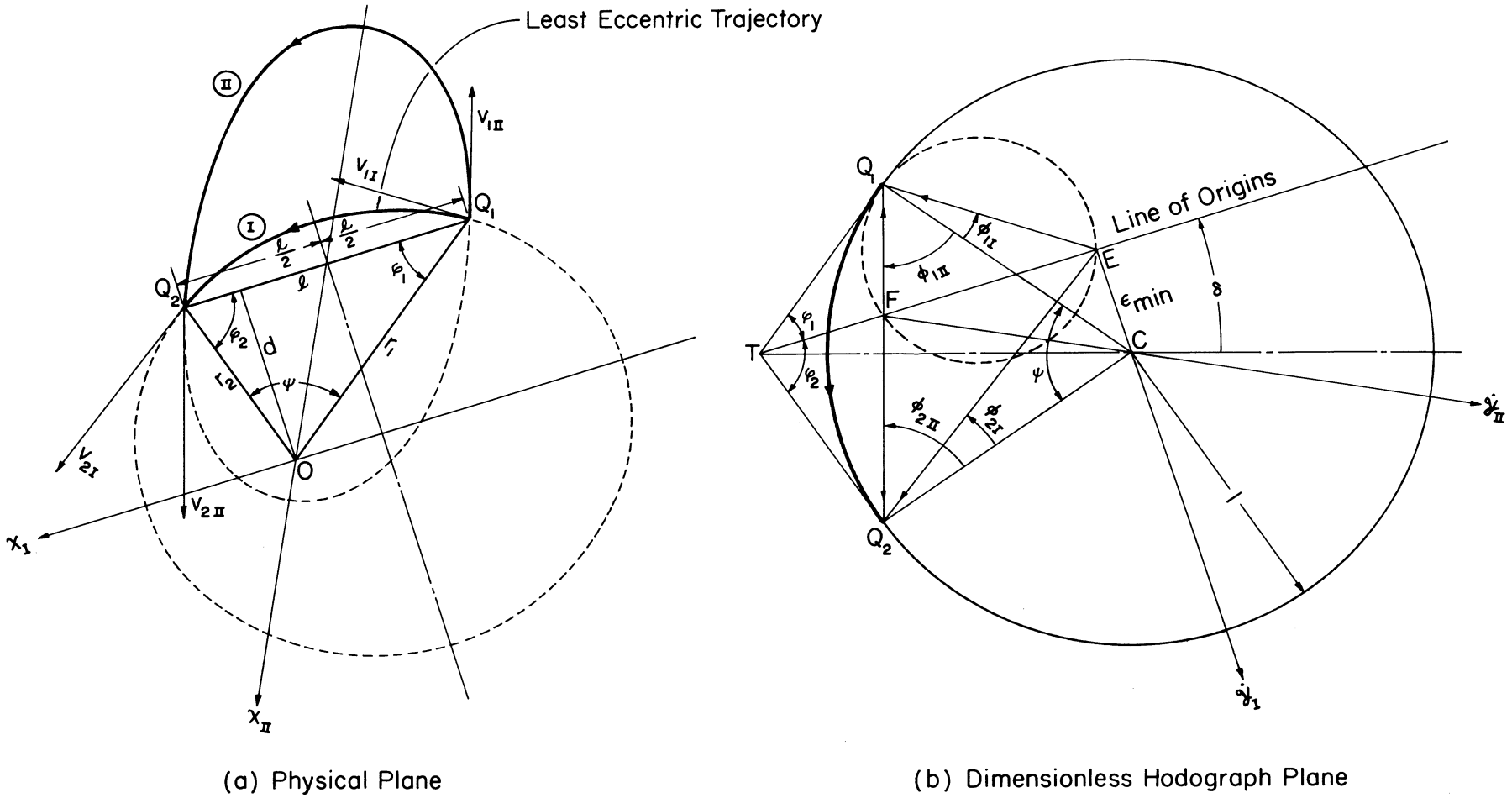

(a) Physical Plane

(b) Dimensionless Hodograph Plane

Figure II-9. The Least Eccentric Trajectory and Its Conjugate, Range < 180°.

The conjugate path angle, which is the one to achieve the least eccentric trajectory is then, according to Equations (9.16-1) and (10.12)

$$\phi_{1I} = -\phi_{1III} = \frac{1}{2}(\varphi_1 - \varphi_2) \tag{10.13}$$

The initial speed ratio λ_1 required for both trajectories and the resulting final speed ratio λ_2 may be easily found by noting that the speed ratios at the orbital points diametrically opposite on an elliptic orbit are connected by[10.2]

$$\lambda_1^2 + \lambda_2^2 = 1 \tag{10.14}$$

which, when combined with the general relation (8.1), yields

$$\lambda_1^2 = \frac{n}{n+1}, \quad \lambda_2^2 = \frac{1}{n+1} \tag{10.15}$$

The semimajor axis and the orbital energy of either trajectory are then given by

$$a = \frac{1}{2}(r_1 + r_2) \tag{10.16}$$

$$k = -\frac{\mu}{r_1 + r_2} \tag{10.17}$$

Thus the terminal speeds, the major axis, and the orbital energy of a least eccentric trajectory or its conjugate all depend on r_1 and r_2 only, and independent of the vertex angle ψ.

10.3 Other Trajectories

In addition to the few particular trajectories analyzed above there are some other ones which might be of interest. For example, associated with the point H_1, the intersection of the line of origins with the radius OQ_1 (or its extension, see Table II-6), the trajectory is one of horizontal departure, since the departure path angle is zero as

10.2 See Reference 9, p. 174.

indicated by the hodograph. Such a trajectory will have its apsidal axis coinciding with the initial terminal radius OQ_1 in the physical plane; and the point Q_1 will be its pericenter if $r_1 < r_2$, or apocenter if $r_1 > r_2$. Similarly, associated with the point H_2, where the line of origins crosses the radius OQ_2 (or its extension) the trajectory will have its final path angle equal to zero. Its apsidal axis will coincide with the final terminal radius OQ_2 and the point Q_2 will be its apocenter if $r_2 > r_1$ or pericenter if $r_2 < r_1$. In the latter case, if Q_2 is considered as the target point on a spherical surface, the trajectory will be cotangential with the surface, and is known in ballistics as the grazing trajectory. In reentry problems it represents the limiting trajectory for reentry to be effected. The principal elements of either the trajectory of horizontal departure or the grazing trajectory may be easily obtained from the hodograph.

Generally speaking, particular trajectories of interest depend on the particular problem at hand. Complete analysis of all these trajectories is impossible, and their treatment will be left to the separate studies of individual problems.

11. THE CASE OF 180 DEGREE RANGE

11.1 The Hodographic Representation and a General Survey

So far the analysis has been restricted to the case $\psi < \pi$ In the boundary case of $\psi = \pi$, the chordal and radial components of the terminal velocities all become parallel, the radical center T recedes to infinity, and the method of hodograph construction of Section 8.2 breaks down. However, the proof for the linear distribution of hodograph origins still stands. With the terminal points Q_1 and Q_2 located on the hodograph circle as usual, obviously the line of origins will be normal to the diameter $Q_1 Q_2$ as shown in Figure II-10b. The distance from the center of the hodograph circle to the line of origin is still given by $\overline{CE}$ according to Equation (8.4a) which reduces to

$$\overline{CE} = \frac{|1-n|}{1+n} \tag{11.1}$$

in the present case.

In the physical plane the base triangle degenerates into the line segment $Q_1 Q_2$, which becomes a focal chord; and the normal group and its complement now have the same range angle ψ. In fact, associated with a given chord $Q_1 Q_2$ all distinctions between a normal group and its complement disappear except in the direction of motion. For convenience, however, the same terminology will be retained here by referring to the group moving in the counterclockwise direction as normal, and the other its complement. The hodograph in Figure II-10b is drawn for the normal group, and the corresponding hodograph for its complement may be obtained by rotating Figure II-10b through 180° as usual. Following the general survey of Section 8.3 and with reference to Figure II-10, all realistic trajectories will have their origins lying in the

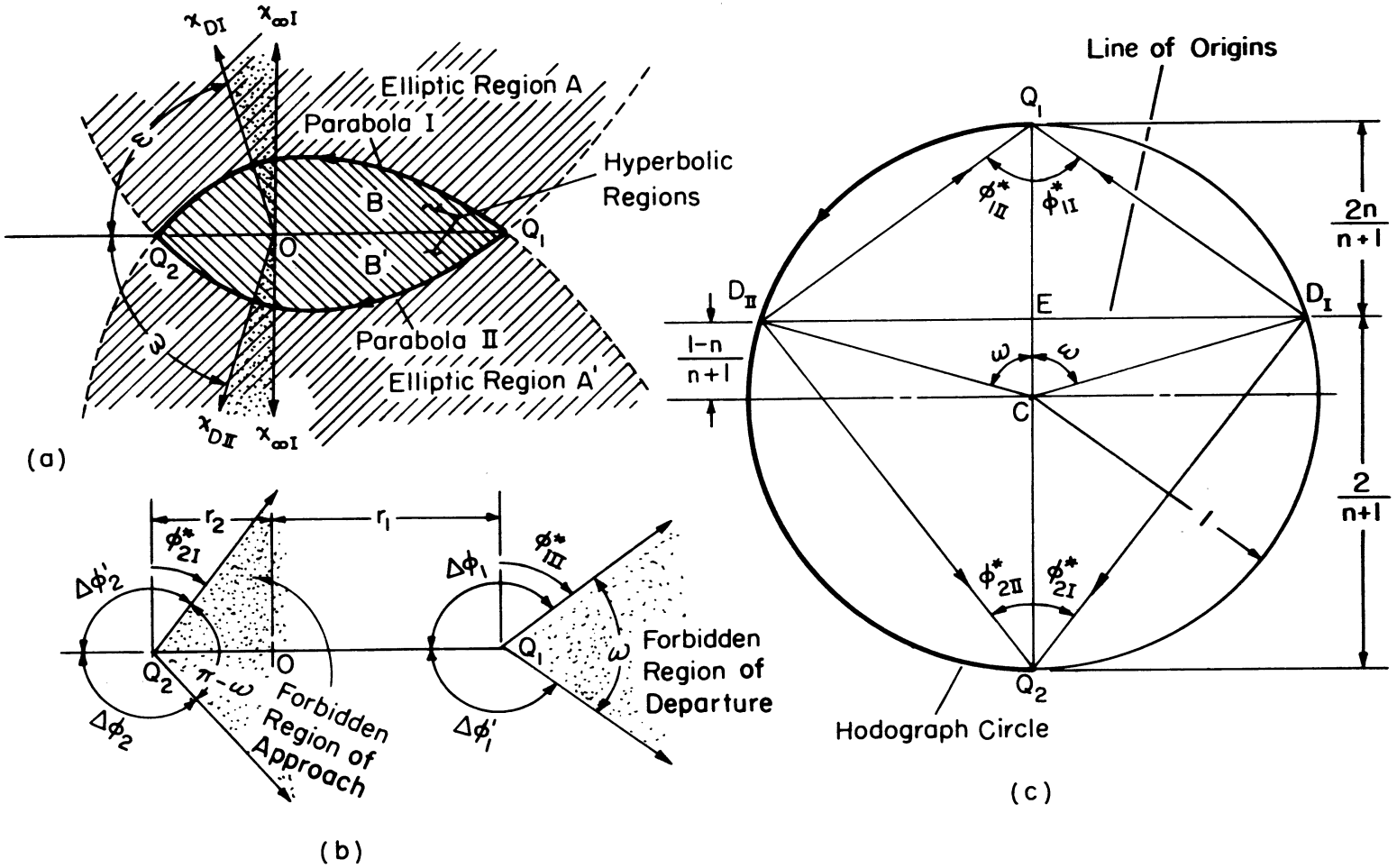

Figure II-10. System of Two-terminal Trajectories and Its Hodographic Representation, 180° Range.

TABLE II-7

POSSIBLE AND FORBIDDEN REGIONS OF DEPARTURE AND APPROACH ($\psi = \pi$)

Initial Terminal	Final Terminal
Limiting Directions of Departure	Limiting Directions of Approach
$(\phi_1)_{UL} = -(\phi_1')_{LL} = \frac{1}{2}(\pi-\omega)\ (= \phi^*_{1II})$	$(\phi_2)_{UL} = -(\phi_2')_{LL} = \frac{\pi}{2}$
$(\phi_1)_{LL} = -(\phi_1')_{UL} = -\frac{\pi}{2}$	$(\phi_2)_{LL} = -(\phi_2')_{UL} = -\frac{\omega}{2}\ (= \phi^*_{2I})$
Possible Regions of Departure	Possible Regions of Approach
$\Delta\phi_1 = \Delta\phi_1' = (\phi_1)_{UL} - (\phi_1)_{LL} = \pi - \frac{\omega}{2}$	$\Delta\phi_2 = \Delta\phi_2' = (\phi_2)_{UL} - (\phi_2)_{LL} = \frac{1}{2}(\pi+\omega)$
Total $\Delta\phi_1 + \Delta\phi_1' = 2\pi - \omega$	Total $\Delta\phi_2 + \Delta\phi_2' = \pi+\omega$
Forbidden Region of Departure	Forbidden Region of Approach
Included Angle $= \omega$	Included Angle $= \pi - \omega$

open interval from D_{II} via D_I to infinity. Furthermore, the symmetrical nature of the hodograph shows that the conjugate trajectory conics are now identical and symmetrically orientated with respect to the line $Q_1 Q_2$; and in fact the conjugate of a trajectory is the reflection of its complement about $Q_1 Q_2$. The inner forbidden region of departure and outer forbidden region of approach both vanish; the axes of the two limiting hyperbolas both coincide with the normal to the line $Q_1 Q_2$ at 0, but point in the opposite directions. The various regions and their included angles are shown in Figure II-10a and Table II-7. A typical conjugate pair and the corresponding hodograph are shown in Figures II-11 and II-12 for the elliptic and hyperbolic cases respectively; for the parabolic case, see Figure II-10.

11.2 The Characteristics of the Conjugate Trajectories and Their Principal Elements

Although the chordal and radial velocity components are no longer significant in dealing with the 180° range trajectories, the previously derived conjugate relations are preserved. Of course the constant in Equation (9-6) or (9.10) goes to infinity as ψ approaches π; however, the constant in each of the Equations (9-12) and (9-13) does approach a finite limit respectively. To see this we write the trigonometric identity

$$d \cdot \tan \frac{\psi}{2} = \frac{2r_1 r_2}{\ell} \sin^2 \frac{\psi}{2} \tag{11.2}$$

and find

$$\lim_{\psi \to \pi} d \cdot \tan \frac{\psi}{2} = \frac{2r_1 r_2}{r_1 + r_2} \tag{11.3}$$

Consequently the conjugate relations (9.12) and (9.13) reduce to

$$h_I h_{II} = \frac{2\mu r_1 r_2}{r_1 + r_2} \tag{11.4}$$

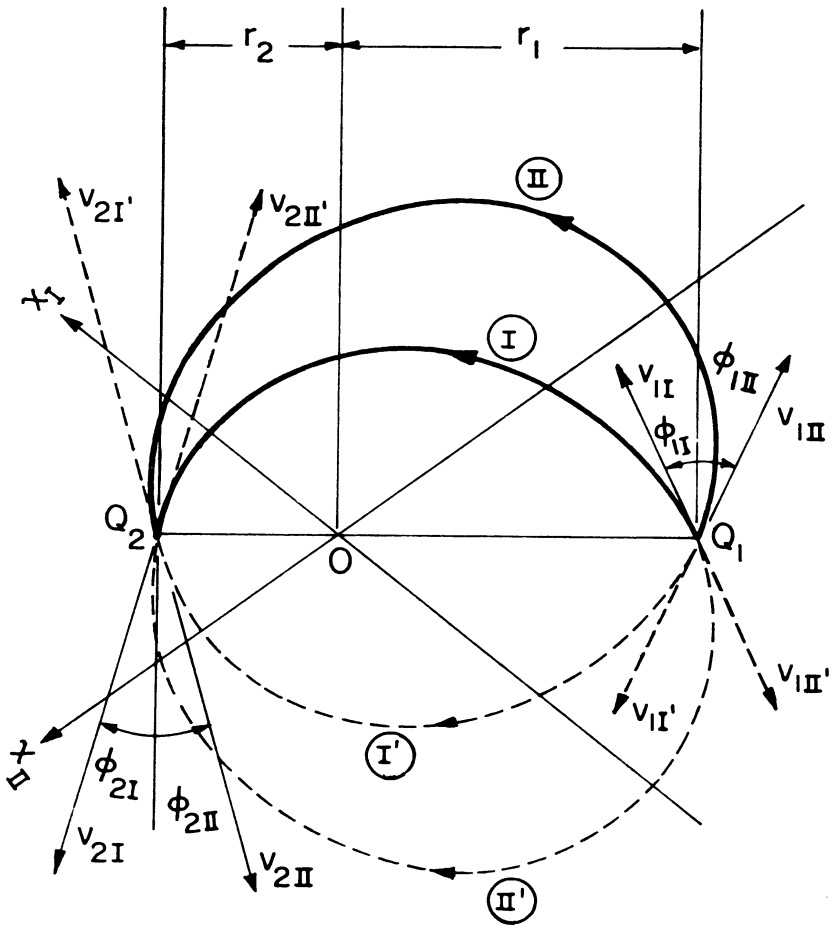

(a) Physical Plane

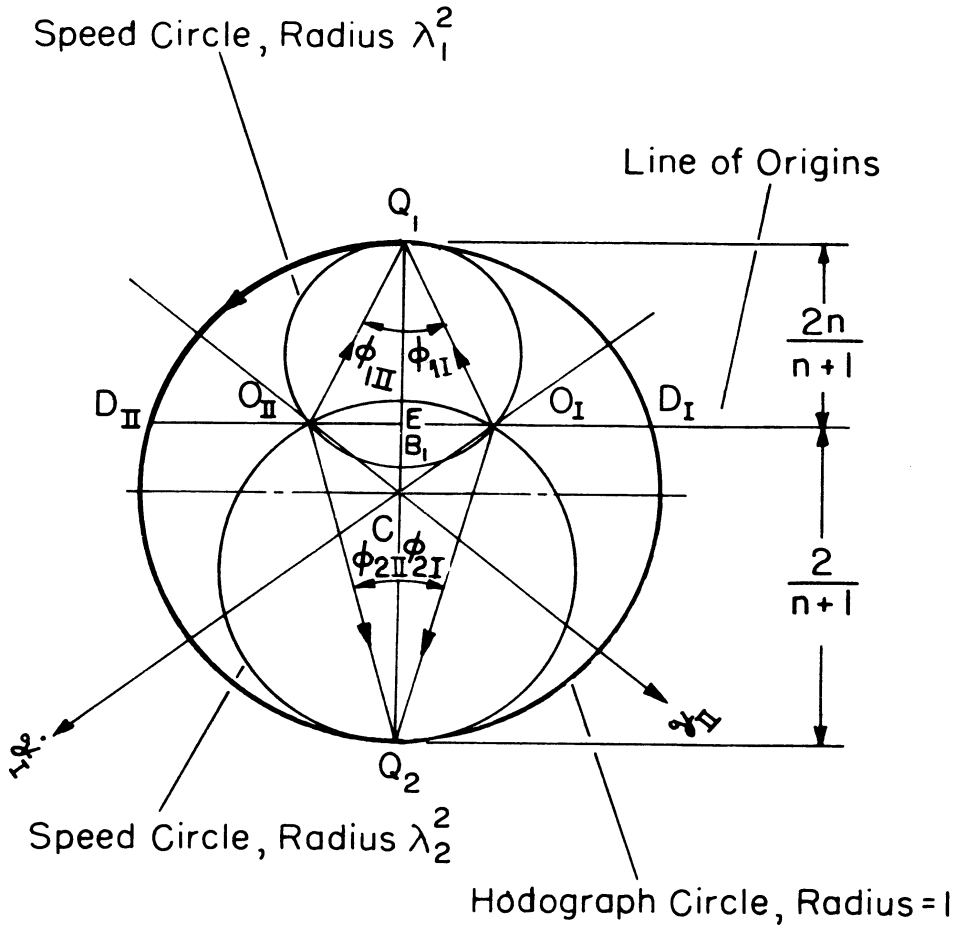

(b) Dimensionless Hodograph Plane

Figure II-11. The Conjugate Elliptic Trajectories, 180° Range.

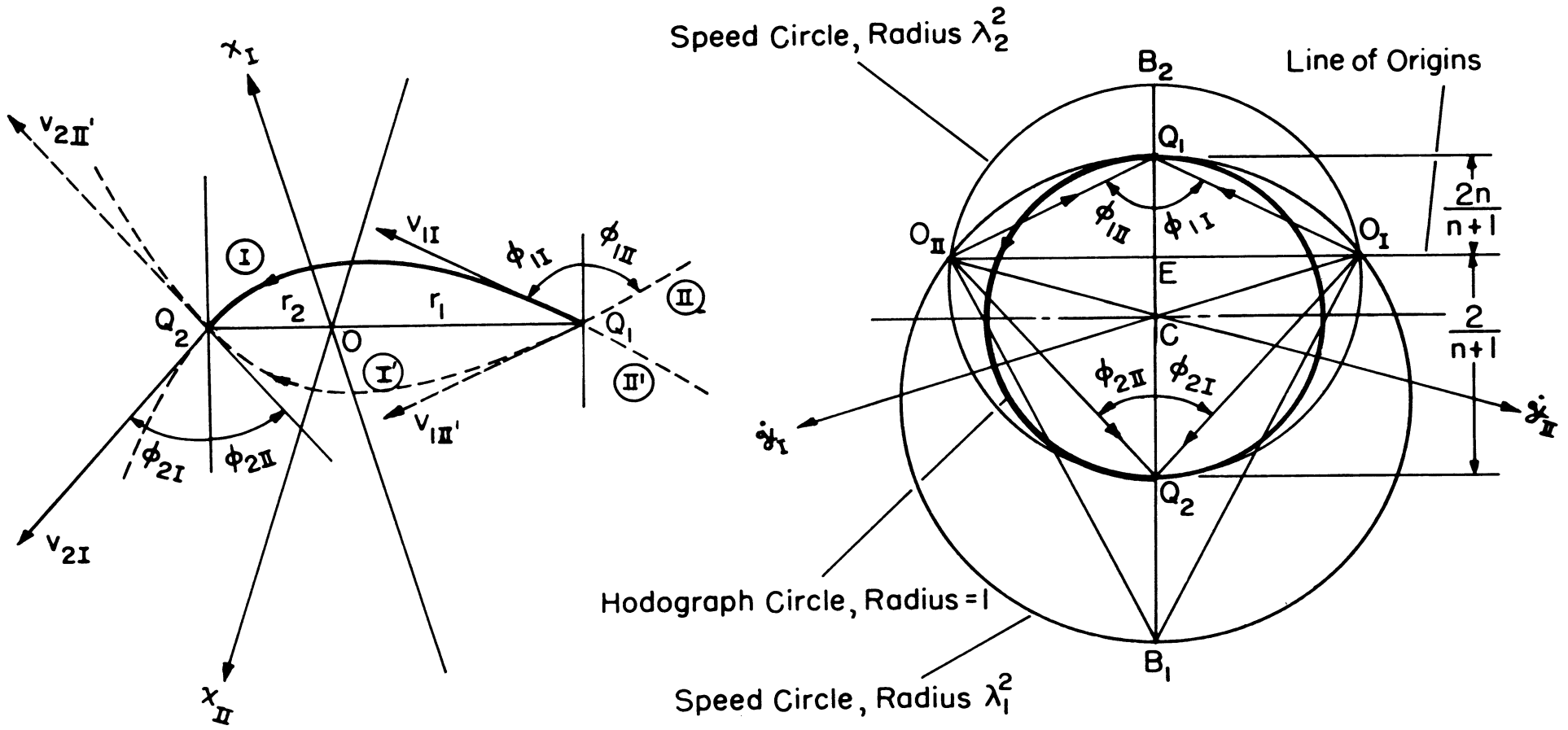

(a) Physical Plane

(b) Dimensionless Hodograph Plane

Figure II-12. The Conjugate Hyperbolic Trajectories, 180° Range.

$$\bar{r}_I \bar{r}_{II} = \frac{4 r_1^2 r_2^2}{(r_1 + r_2)^2} \tag{11.5}$$

for the present case. In fact, at this point we may go one step further; since, as pointed out earlier, the conjugate trajectories are now of identical conics, we have

$$h_I = h_{II} \quad , \quad \bar{r}_I = \bar{r}_{II} \tag{11.6}$$

which, when combined with Equations (11.4) and (11.5), give immediately the expressions for the angular momentum and the **semi-latus** rectum as shown in Table II-5 (column 3).

Noting that $\varphi_1 = \varphi_2 = 0$ when $\psi = \pi$, the conjugate relations (9.16) now becomes

$$\begin{aligned} \phi_{1I} + \phi_{1III} &= 0 \\ \phi_{2I} + \phi_{2II} &= 0 \end{aligned} \tag{11.7}$$

which are also evident from the symmetry of the present hodograph. To evaluate the terminal path angles we note from the hodograph that, in the right triangles $Q_1 O_I B_1$ and $Q_1 O_I E$ (Figures II-11, II-12),

$$\overline{Q_1 O_I} = 2\lambda_1^2 \cos \phi_{1I} \quad , \quad \overline{Q_1 O_I} \cos \phi_{1I} = \frac{2n}{n+1}$$

from which, by eliminating $Q_1 O_I$, we obtain

$$\cos \phi_{1I} = \frac{1}{\lambda_1} \sqrt{\frac{n}{n+1}} \tag{11.8}$$

And in view of Equation (11.7) we may write

$$(\phi_1) = \pm \cos^{-1}\left(\frac{1}{\lambda} \sqrt{\frac{n}{n+1}} \right) \tag{11.9}$$

A similar expression stands for the conjugate values of ϕ_2 . Note that the same results here may be obtained by setting $\psi = \pi$ in Equation (9.26a). This shows that the formulas (9.26a,b) originally deduced for the case $\psi=\pi$ hold also in the limiting case of $\psi = \pi$. Note here the special case of parabolic flight. The geometry of the hodograph, Figure II-10(c), shows that

$$|\phi_1^*| + |\phi_2^*| = \frac{\pi}{2} \tag{11.10}$$

for either group. That is, the terminal velocities in a 180° parabolic flight are normal to each other. Geometrically this implies that the two tangents at the ends of a focal chord of a parabola are orthogonal. This is in fact a geometrical property of a parabola.

Returning to the general case it is to be noted that, for a 180° flight between fixed terminals, although the initial speed may be arbitrary, its θ-component is not. This can be seen from the hodograph, Figures II-11, II-12, since

$$\lambda_{\theta 1}^2 = \frac{1}{2} \overline{Q_1 E} = \frac{n}{n+1} \tag{11.11}$$

which shows that $\lambda_{\theta 1}$ and consequently $V_{\theta 1}$ is fixed by the terminal distances alone, hence independent of the departure speed. The same is true for $V_{\theta 2}$.

Formulas for other trajectory elements may be likewise deduced from the hodograph geometry of Figures II-10 etc. or by using appropriate orbital relations. The results are summarized in column 3, Table II-5 and

the dependence of some of the principal trajectory elements on the distance ratio and the inital speed are shown graphically in Figures 14d and 15d. It is worth noting from Table II-5 that , for $\psi = \pi$, in addition to the θ-components of the terminal velocities, the angular momentum and latus rectum are also fixed by the terminal distances r_1 and r_2 alone, hence they are independent of the initial speed, or the particular choice of trajectory.

The criteria given in Table II-6 for the occurrence of apses on the trajectory still stand for the present case. However, it is to be noted that, as the present hodograph shows, the points H_1 and H_2 coincide at E . This indicates that at least one of the two apses will lie on the trajectory, and both will be on the trajectory when the origin is at E , corresponding to the minimum energy trajectory.

11.3 The Minimum Energy Trajectory and the Least Eccentric Trajectory

When $\psi = \pi$ the minimum energy trajectory and the least eccentric trajectory coincide, both have the point E as their hodograph origin (see Figure II-13). The trajectory is a half ellipse with its apsidal axis coinciding with Q_1Q_2 , and the trajectory conic is the well-known **Hohmann ellipse.** Thus a Hohmann's ellipse is not only the least energetic, but also the least eccentric, among all trajectories of common terminals with 180° range. From Equations (10.17) and (11.1) the orbital energy and the eccentricity of a Hohmann's ellipse are found to be

$$k^* \Big|_{\psi = \pi} = - \frac{\mu}{r_1+r_2} \tag{11.12}$$

and

$$\epsilon^* \Big|_{\psi = \pi} = \frac{|1-n|}{1+n} \tag{11.13}$$

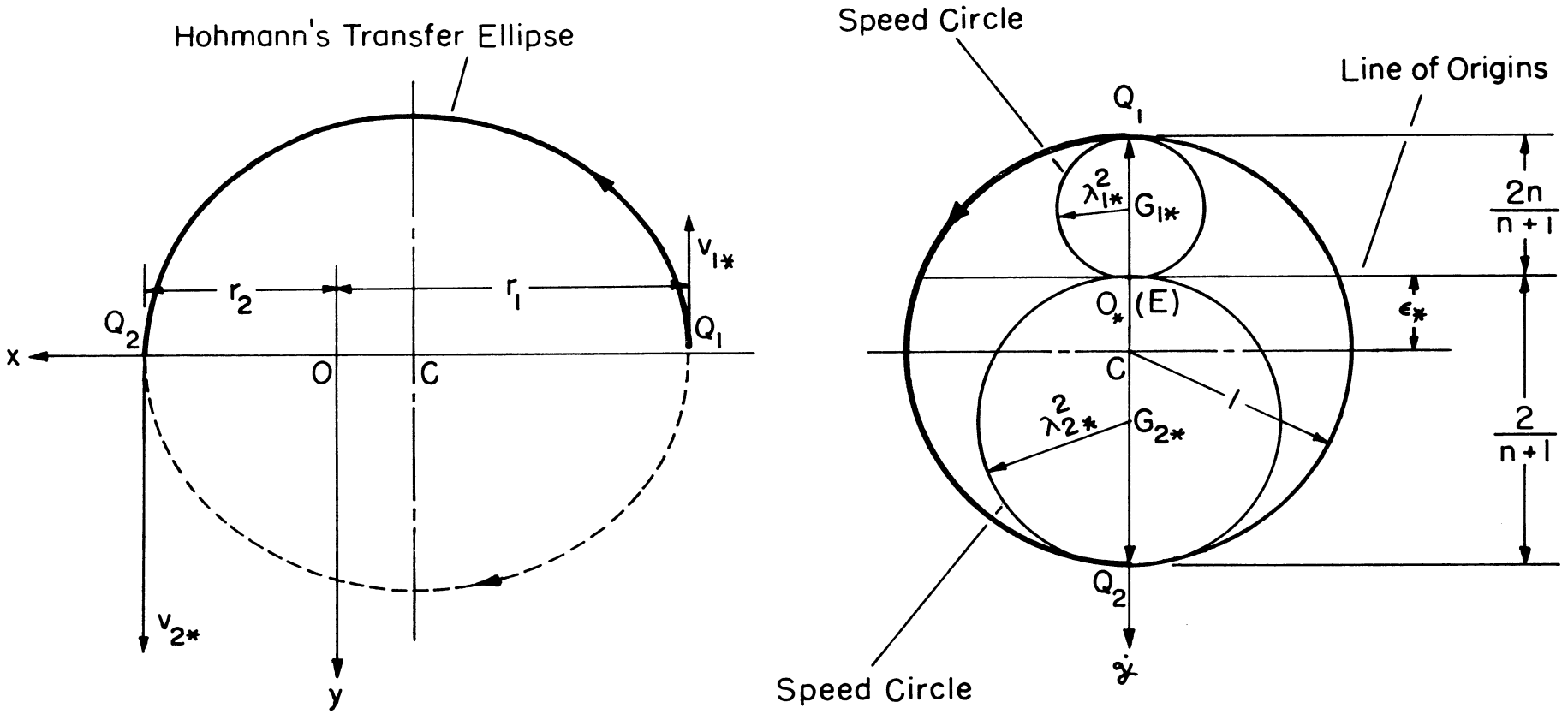

(a) Physical Plane

(b) Dimensionless Hodograph Plane

Figure II-13. The Minimum Energy and Least Eccentric Tranjectory, 180° Range.

Comparing these formulas with the corresponding general formulas (10.8) and (8.4a), we see that, if the terminal distances are fixed, but the range angle is allowed to vary, the energy of the Hohmann ellipse is in fact the greatest among all the minimum energy ones; while its eccentricity is the overall minimum in the entire trajectory system. Other elements of the Hohmann ellipse can be easily obtained from the hodograph as usual.

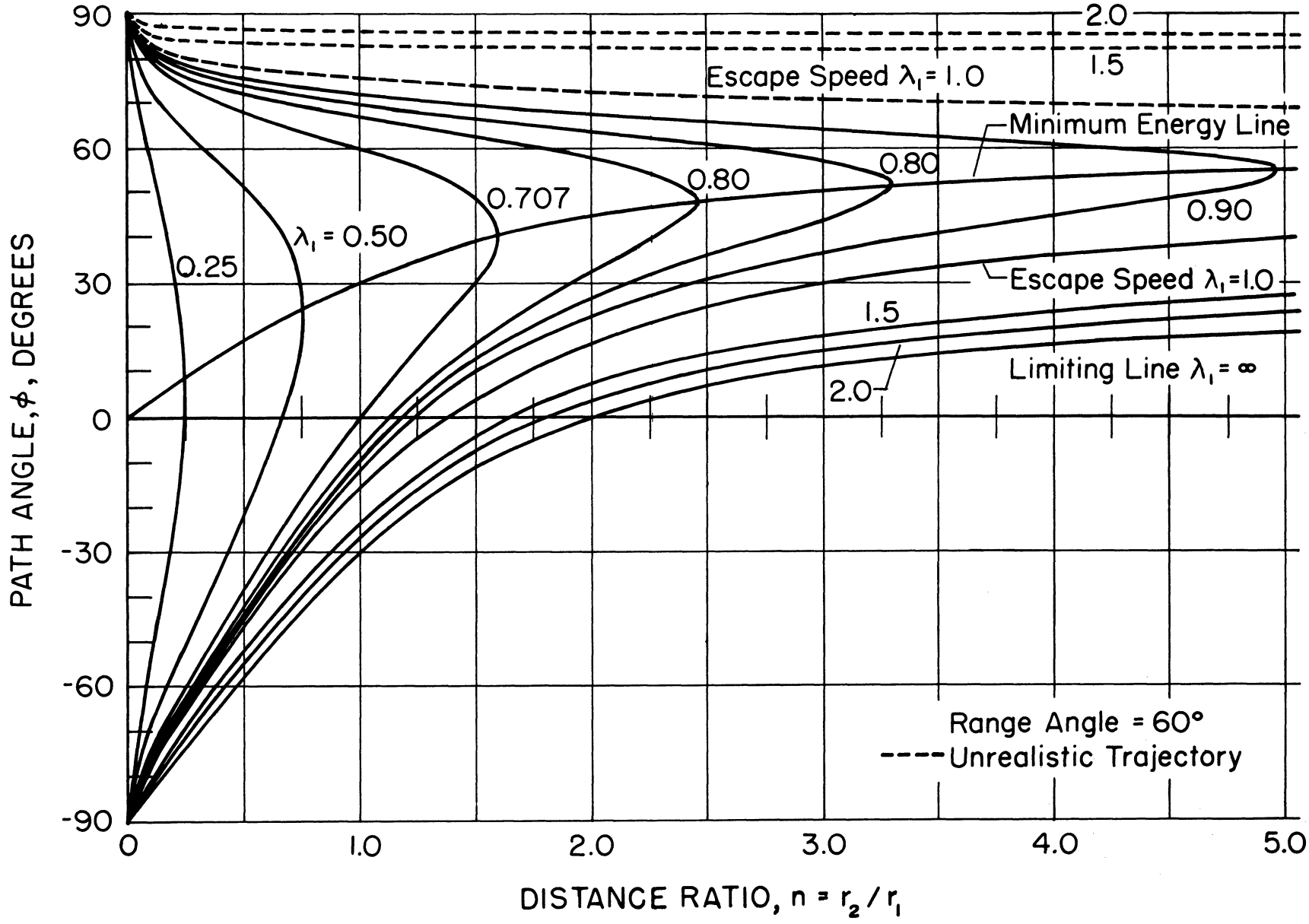

Figure II-14a. Variation of the Range-constrained Path Angle with Distance Ratio and Initial Speed ($\psi = 60°$).

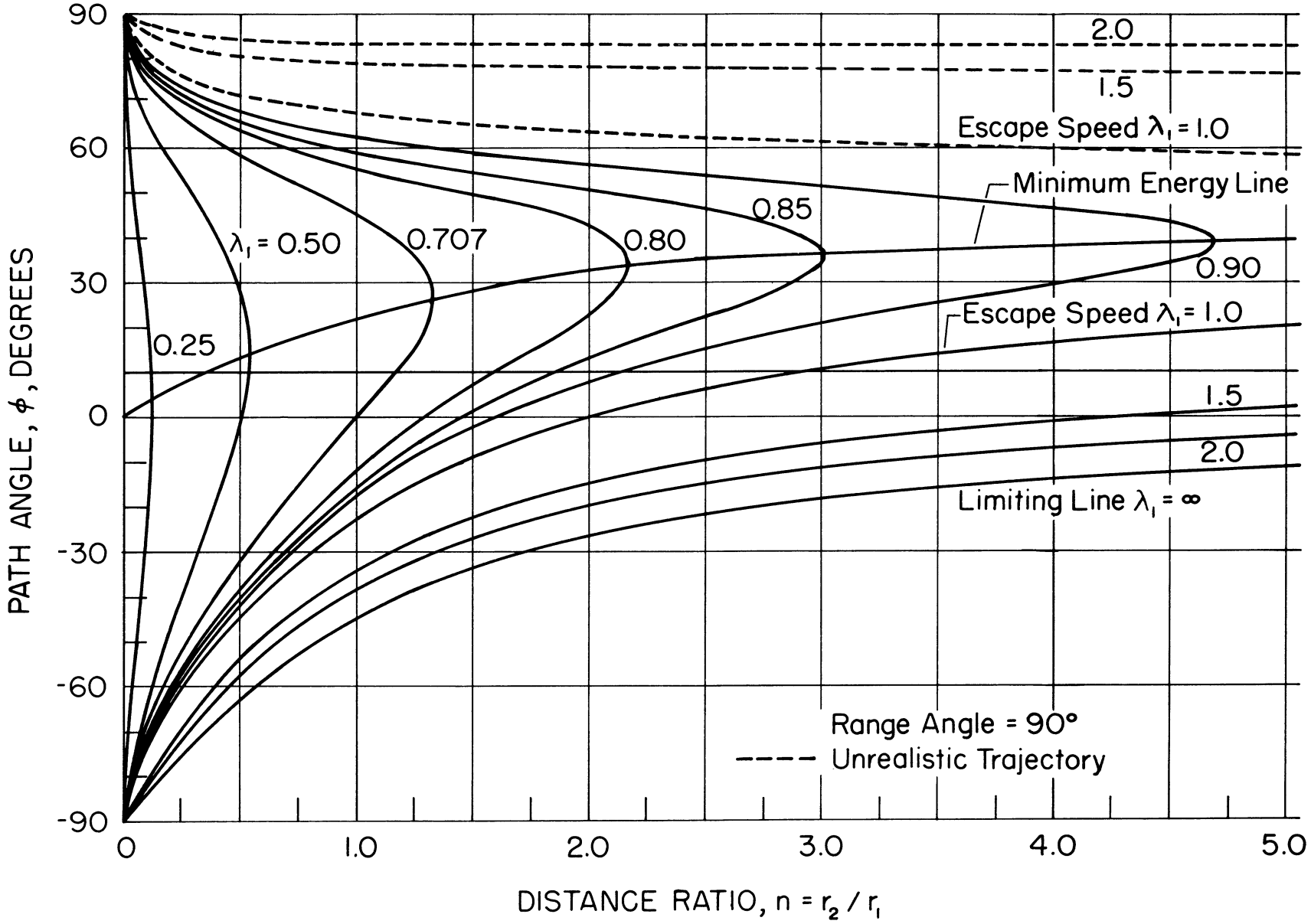

Figure II-14b. Variation of the Range-constrained Path Angle with Distance Ration and Initial Speed ($\psi = 90°$).

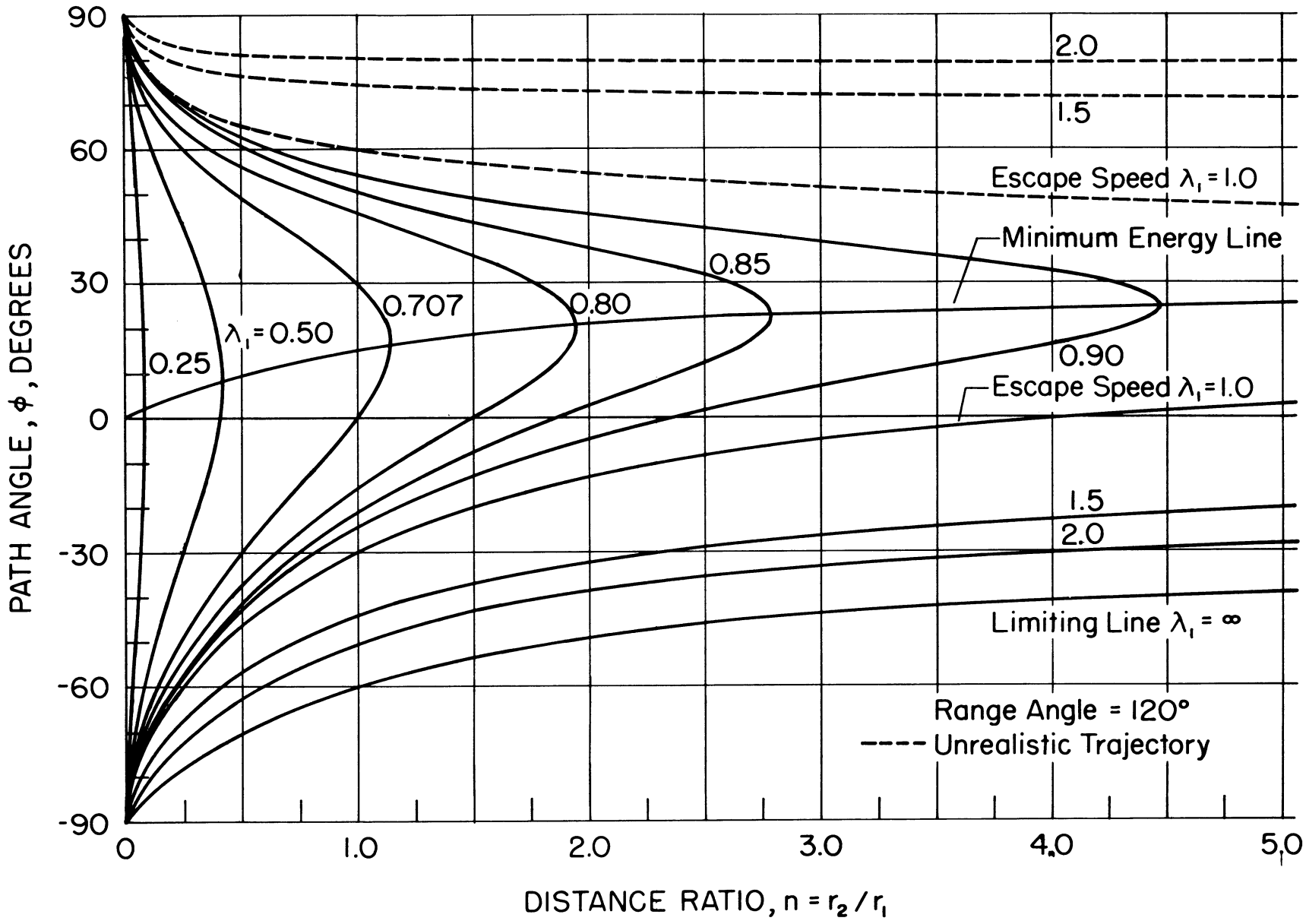

Figure II-14c. Variation of the Range-constrained Path Angle with Distance Ratio and Initial Speed ($\psi = 120°$).

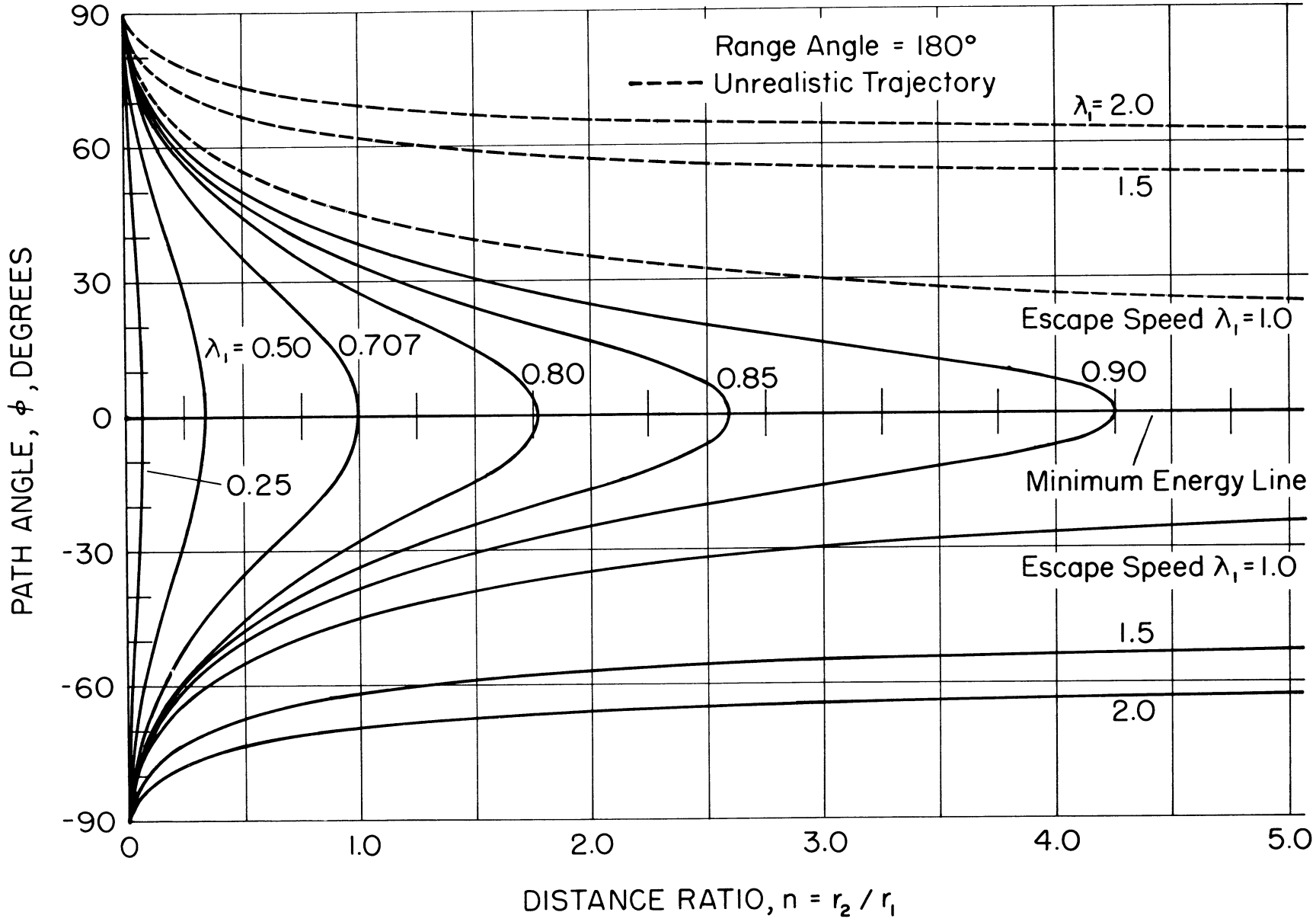

Figure II-14d. Variation of the Range-constrained Path Angle with Distance Ratio and Initial Speed ($\psi = 180°$).

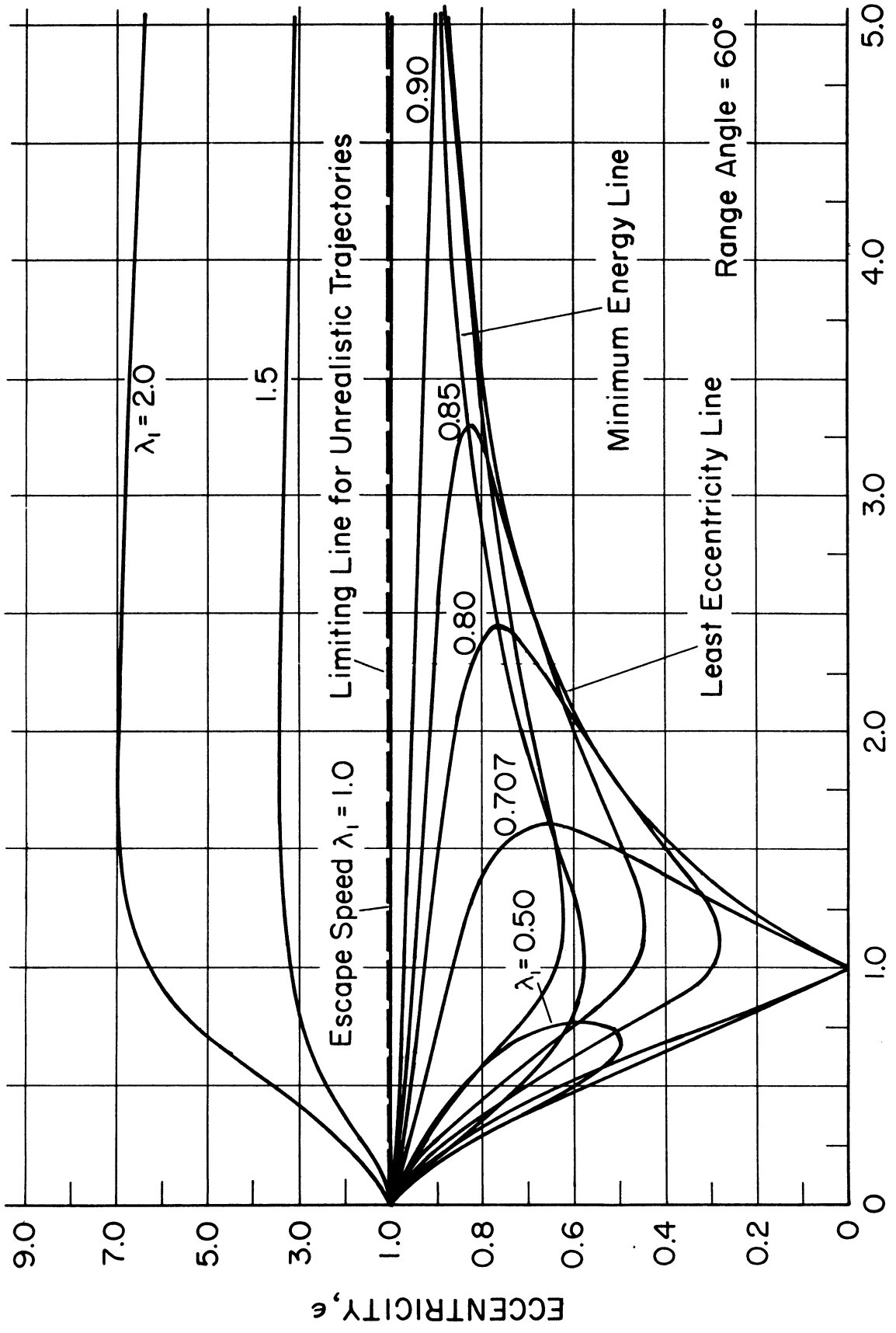

Figure II-15a. Variation of the Range-constrained Trajectory Eccentricity With Distance Ratio and Initial Speed ($\psi = 60°$).

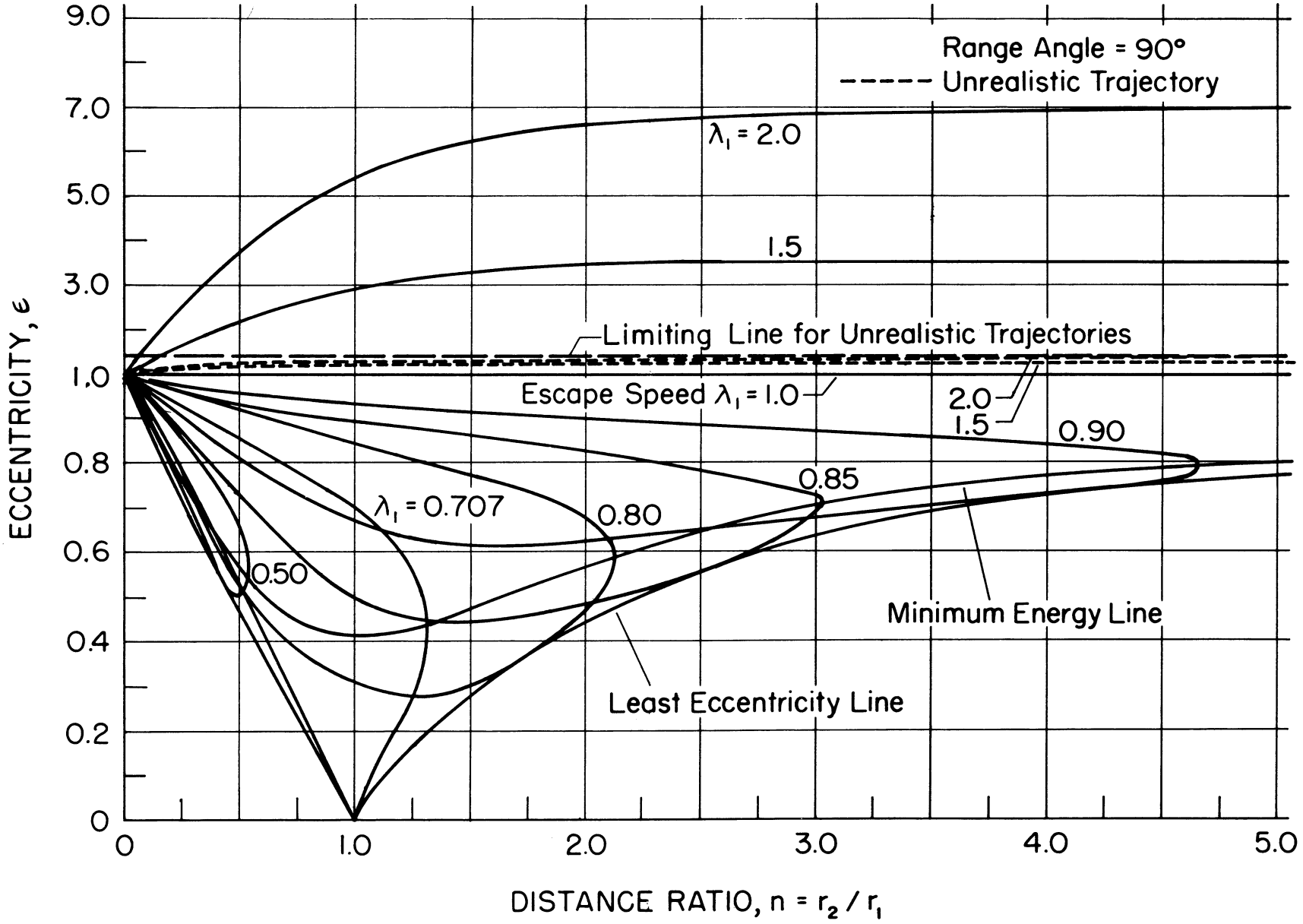

Figure II-15b. Variation of the Range-constrained Trajectory Eccentrici With Distance Ratio and Initial Speed ($\psi = 90°$).

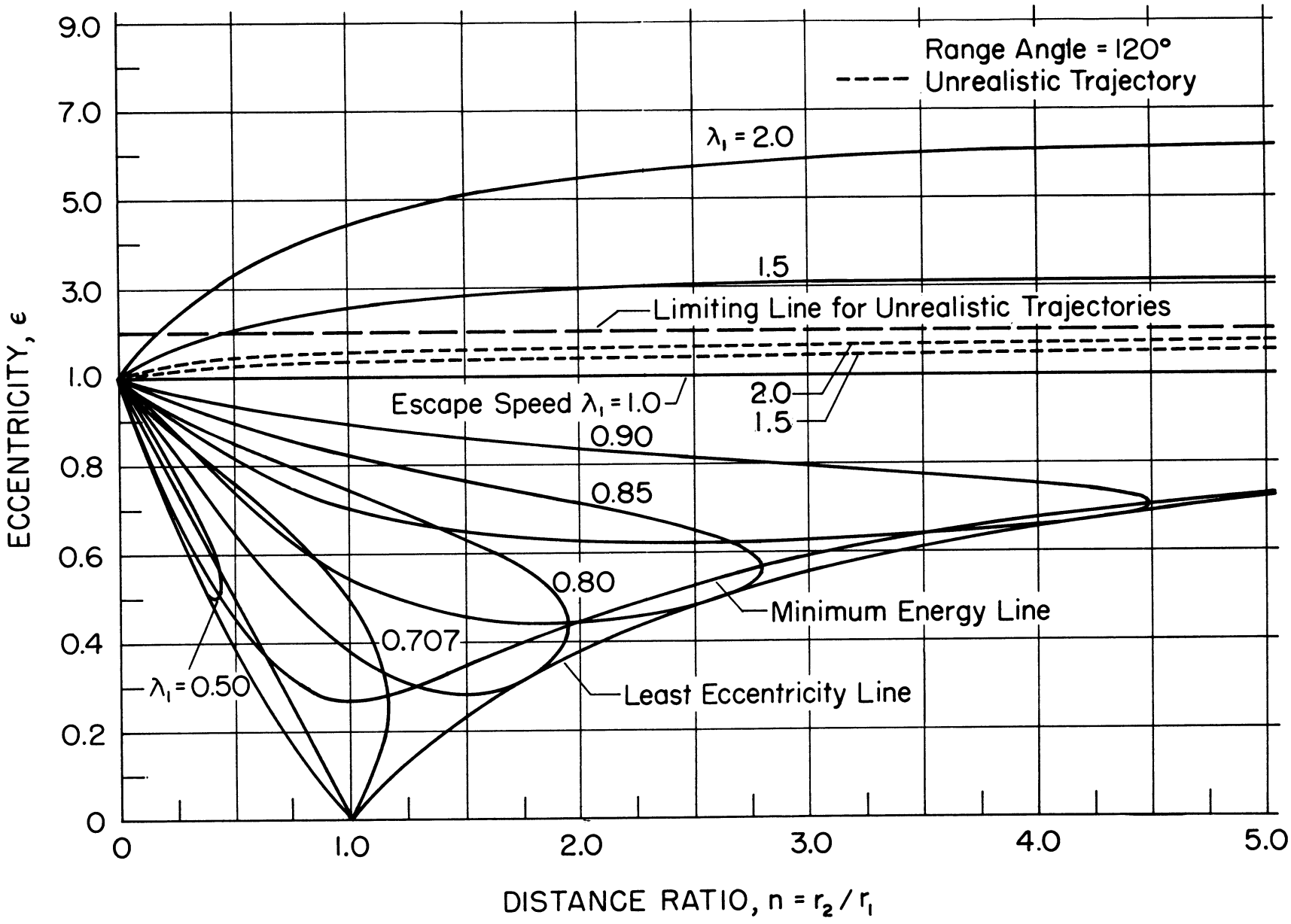

Figure II-15c. Variation of the Range-constrained Trajectory Eccentricity With Distance Ratio and Initial Speed ($\psi = 120°$).

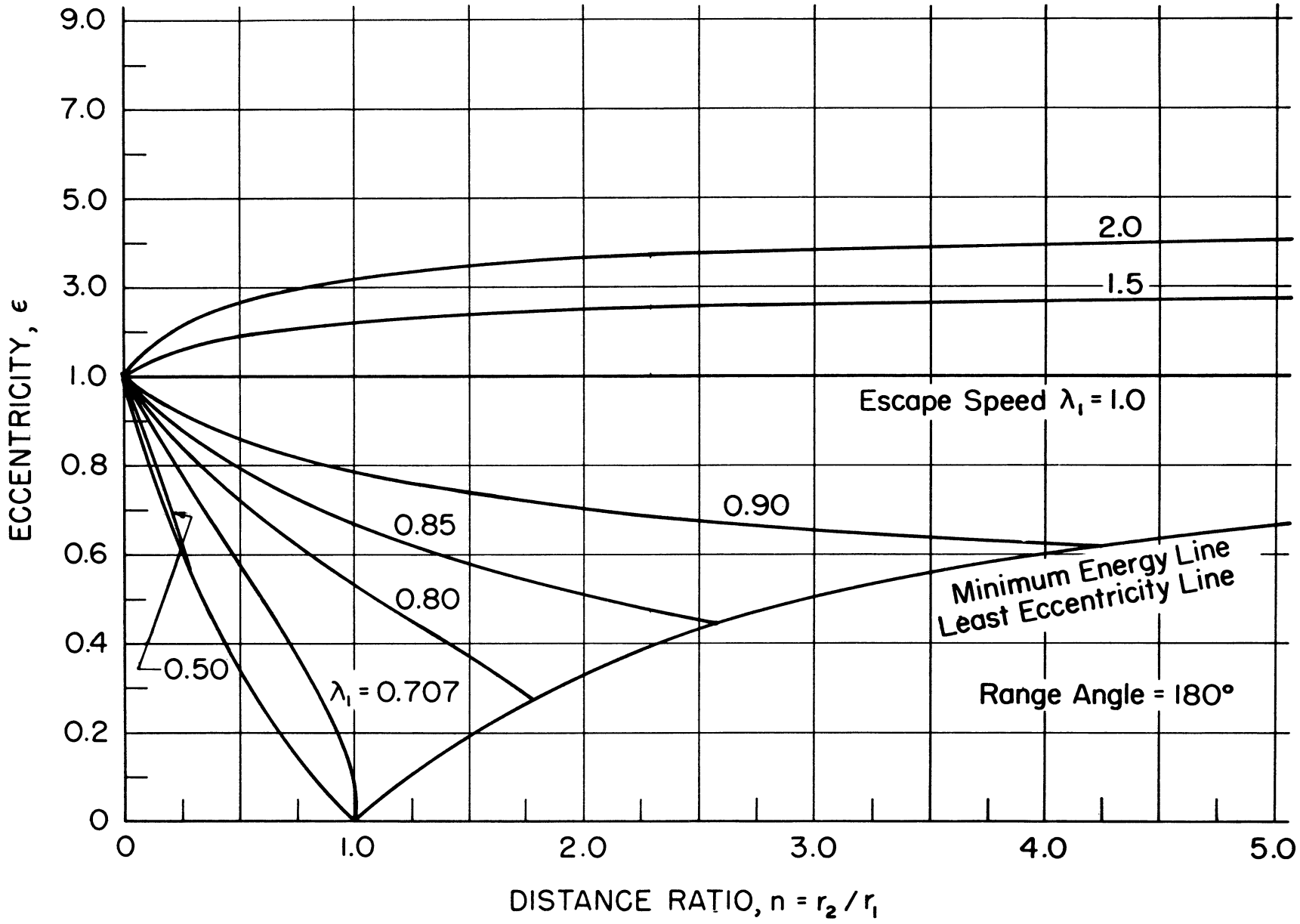

Figure II-15d. Variation of the Range-constrained Trajectory Eccentricity With Distance Ratio and Initial Speed ($\psi = 180°$).

12. SUMMARY OF FINDINGS

The main findings obtained in the present analysis may be summarized as follows:

12.1 General Conclusions on the Two-Terminal Trajectory System

(1) For a system of two-terminal trajectories of the same range angle, the locus of the hodograph origin in the dimensionless $\mathcal{x},\mathcal{y}$-plane is a straight line parallel to the line connecting the terminal points in the physical plane. This is true regardless of whether the range angle is less than, greater than or equal to π. (See Figures II-1b and II-10c)

(2) Of the infinitely many two-terminal trajectories associated with a given base triangle in a given field:

a. Only two are parabolic, and all the realistic trajectories, elliptic and hyperbolic, are confined in the region outside the base triangle and bounded between the branches of the parabolas extending from each terminal to infinity, with those of the normal group all above the chord or base (Q_1 Q_2) of the base triangle and the complementary group in the rest of the region (see Figure II-3a).

b. There exist an upper limit and a lower limit for the departure path angle in each group beyond which no such a trajectory is possible; consequently, there is a forbidden angular region for the directions of departure at the initial terminal. A similar situation exists for the directions of approach at the final terminal. The included angle of each region is determined by the geometry of the base triangle (see Figure II-3 and Table II-2).

c. The positive portions of the elliptic apsidal axes, and those of the hyperbolic apsidal axes are also confined in certain angular regions

bounded by the apsidal axes of the two parabolic trajectories and the two axes coinciding with the base altitude and the bisector of the vertex angle ψ of the base triangle respectively. The included angle of each region is also determined by the goemetry of the base triangle (see Figure II-3c and Table II-3).

d. Besides the well-known minimum speed, there exists a least elliptic eccentricity which the trajectory may attain, and an upper limit for the hyperbolic eccentricity of the complementary group (see Equations (8.4a) and (8.6)). There is no upper limit for the hyperbolic eccentricity of the normal group.

12.2 On the Conjugate Trajectories

For a pair of conjugate trajectories associated with a given base triangle and an arbitrary departure speed in a given field:

(1) The chordal and radial components of the terminal velocity of one trajectory are equal to the radial and chordal components of the terminal velocity of the other respectively (the reciprocal relation).

(2) The product of each conjugate pair of the following quantities is a constant:

i. The chordal component of the terminal velocity.

ii. The radial component of the terminal velocity.

iii. The angular momentum.

iv. The latus rectum.

Each constant depends on the vertex angle ψ and the base altitude d alone, hence independent of the departure speed, or the choice of the trajectory pair.

(3) The sum of the conjugate path angles at either terminal is a constant, equal to the base angle at that terminal.

12.3 On the Minimum Energy Trajectory

A minimum energy trajectory is characterized by the following features:

(1) The chordal and radial components of either terminal velocity are equal.

(2) The direction of motion at either terminal bisects any pair of conjugate directions at that terminal. This direction depends only on the base angle at that terminal (see Equation (10.4)).

(3) The chordal and radial components of the terminal velocity, the angular momentum, and the latus rectum are the geometrical mean of the conjugate pair of the corresponding quantities respectively associated with a base triangle of the same vertex angle ψ and base altitude d.

12.4 On the Least Eccentric Trajectory

A least eccentric trajectory is characterized by the following features:

(1) The apsidal axis of the trajectory ellipse is parallel to the chord Q_1Q_2.

(2) The terminal speed parameters, the major axis, and the orbital energy all depend on the terminal distances only, hence are independent of the range angle.

(3) The least eccentricity is proportional to the numerical difference between the terminal distances and inversely proportional to the length of the chord (see Equation (8.4a)).

12.5 On the Case of 180° Range (See also Section 12.6)

(1) The θ-components of the terminal velocities, the angular momentum and the latus rectum are all fixed by the terminal distances r_1

and r_2 alone, thus they are independent of the departure speed, hence the choice of trajectory.

(2) General conclusions of 12.1 apply to the present case. Of the forbidden regions, there exist only the outer one at the initial terminal and the inner one at the final terminal (a special case of 12.1(b)).

12.6 On the Hohmann Ellipse

(1) In a system of two-terminal trajectories of 180° range the Hohmann ellipse has both the minimum orbital energy and the least eccentricity.

(2) In a system of trajectories of two fixed terminal distances but varying range angle, the Hohmann ellipse has the overall least eccentricity, but the greatest minimum energy.

PART III

HODOGRAPH ANALYSIS OF THE OPTIMIZATION OF THE TRANSFER TRAJECTORIES BETWEEN TWO TERMINAL POINTS FOR MINIMUM INITIAL IMPULSE

13. INTRODUCTORY REMARKS

Following Part II the problem treated in this part is as follows: Consider a space vehicle, initially at the point Q_1 and having an initial velocity $\vec{V}_1$, to be transferred to a given point Q_2 by applying an instantaneous impulse at Q_1. The optimum transfer trajectory is defined as the one which requires the minimum impulse, which is equivalent to the minimum velocity increment at the initial terminal Q_1. Problems of this kind are often encountered in space flight whenever the primary objective is to impact a destination planet, or to intercept any target at a given point in space. Such problems have been previously treated by Battin[33] and Stark[39] and, in particular Stark's work was essentially an analysis in the hodograph plane. Numerical solutions have been found in both works when the space vehicle is initally on a circular orbit.

The present study is in general in line with Part II in which the family of all Keplerian trajectories between two fixed terminal points have been analyzed. For the optimization of such trajectories the geometrical approach in the hodograph plane by Stark will be used. However, the investigation will emphasize on the analytical behavior of such optimum equations rather than numerical details. Besides, the chordal and radial velocity coordinates will be used instead of the usual transversal and radial components employed by Stark. Such coordinates will facilitate the analytical treatment, and enable the previous findings in Part II to be readily utilized. In the following detailed treatment will be given to the two-dimensional analysis followed by some brief remarks on the three-dimensional case. Generalization of the present analysis to other problems of impulsive orbital change will also be introduced.

14. TWO-DIMENSIONAL ANALYSIS OF THE PROBLEM

14.1 Formulation of the Problem

As mentioned in Part II (Section 8.1) all transfer trajectories between two terminal points Q_1 and Q_2 lie in the plane of the base triangle OQ_1Q_2. Let us assume the initial velocity vector $\vec{V}_0$ also lies in the plane, then the problem is two-dimensional. Consider an arbitrary transfer trajectory from Q_1 to Q_2, and let $\vec{V}_1$ be the departure velocity at Q_1 along this trajectory (Figure III-1a). As before we will first restrict the vertex angle to be $0 < \psi < \pi$ so that the base triangle does not degenerate into a line segment. In such a case as shown in Section 9.1 the departure velocity $\vec{V}_1$ must satisfy Godal's compatibility condition[14.1]

$$V_C V_R = \frac{\mu}{d} \tan \frac{\psi}{2} \tag{14.1}$$

The velocity increment vector is then

$$\Delta \vec{V} = \vec{V}_1 - \vec{V}_0 \tag{14.2}$$

with its magnitude given by

$$|\Delta V|^2 = (V_C - V_{CO})^2 + (V_R - V_{RO})^2 - 2 (V_C - V_{CO})(V_R - V_{RO}) \cos\varphi_1 \tag{14.3}$$

which simplifies to

$$|\Delta V|^2 = V_C^2 + V_R^2 - 2N_O V_C - 2 M_O V_R + V_O^2 - 2 \cos \varphi_1 \tag{14.3a}$$

14.1 $V_{R1} = V_{R2}$ according to Equation (9.3), hence no subscript (1 or 2) is attached here and in the latter part unless the direction is to be particularly emphasized. See Section 9.1.

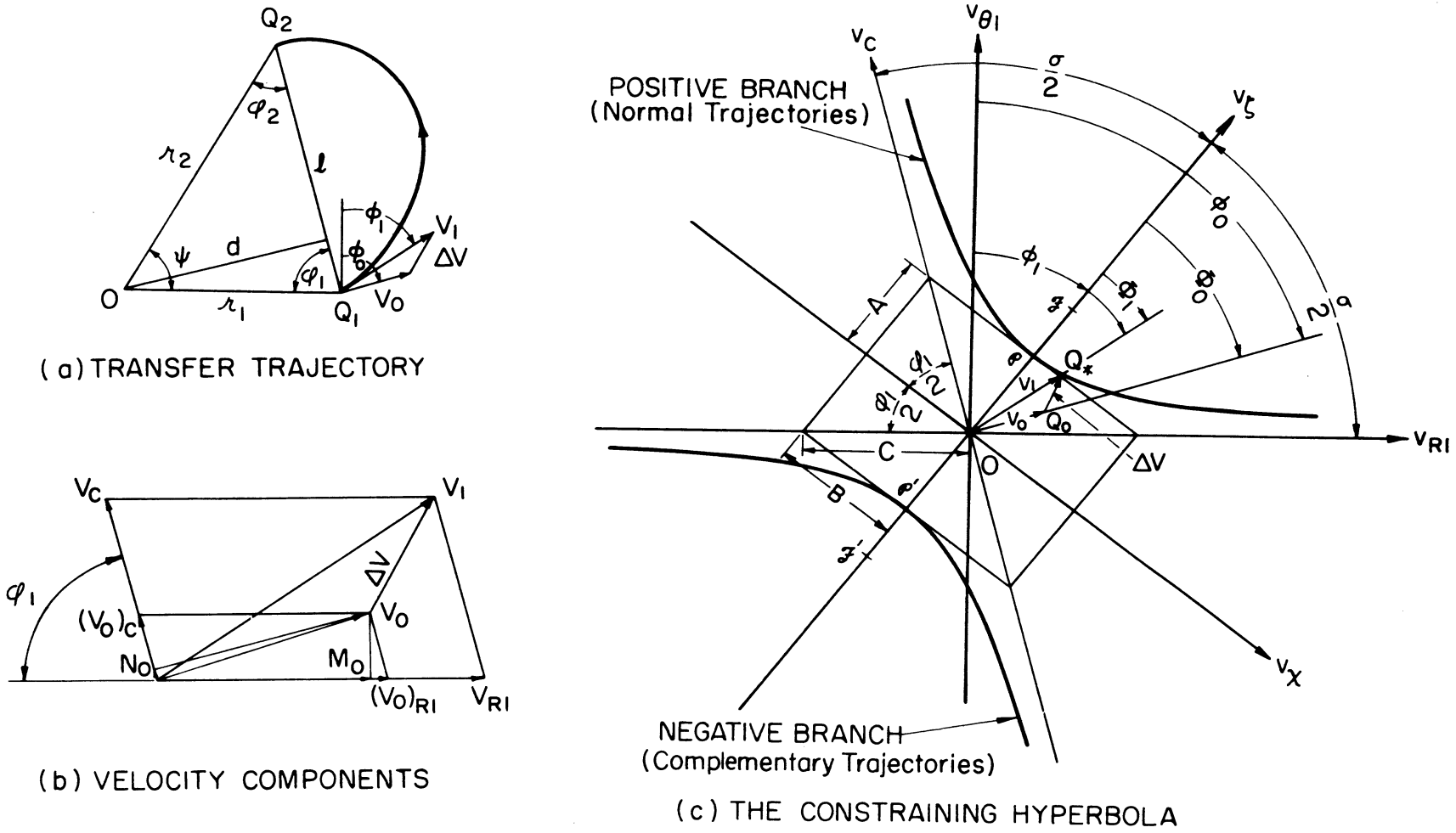

Figure III-1. The Transfer Trajectory and the Constraining Hyperbola in the Hodograph Plane

where

$$K \equiv \frac{\mu}{d} \tan \frac{\psi}{2} \tag{14.4}$$

$$M_0 = V_{R0} - V_{C0} \cos\varphi_1 \quad , \quad N_0 = V_{C0} - V_{R0} \cos\varphi_1 \tag{14.5}$$

Thus the problem is to minimize $|\Delta V|$ under the constraint Equation (14.1). It is to be noted that the parameters M_0 and N_0 here have the physical significance of being the orthogonal projections of the initial velocity vector $\vec{V}_0$ onto the V_{R1} - and V_c - axes respectively, as is obvious from the geometry of the velocity vectors shown in Figure III-1(b), (c).

14.2 The Constraining Hyperbola and the Orthogonality Condition

It is evident that the constraint equation (14.1) represents a hyperbola in the hodograph plane with the chordal and radial directions at Q_1 as its two asymptotic directions. Thus in order to insure that the trajectory will pass through the terminal point Q_2, the tip of the departure velocity vector $\vec{V}_1$ has to be constrained on this hyperbola, which in a given Newtonian gravity field is solely determined by the base triangle OQ_1Q_2. The problem is now reduced to finding the minimum distance from the tip Q_0 of the initial velocity vector $\vec{V}_0$ to the constraining hyperbola, and this requires the vector $\Delta\vec{V}$ to be normal to the hyperbola (Figure III-1(c)). This is the approach used by Stark[39] in which he employed the velocity coordinates V_θ and V_r to obtain an optimum equation by such an orthogonality consideration. In present coordinates this condition may be written

$$\frac{\Delta V_{C*} - \Delta V_{R*} \cos\varphi_1}{\Delta V_{R*} - \Delta V_{C*} \cos\varphi} = -\left(\frac{dV_R}{dV_C}\right)_* \tag{14.6}$$

where

$$\Delta V_{C*} \equiv V_{C*} - V_{CO}$$

$$\Delta V_{R*} \equiv V_{R*} - V_{RO} \tag{14.7}$$

and $(dV_R/dV_C)_*$ is to be evaluated along the constraining hyperbola. The subscript * here indicates the point on the constraining hyperbola at which the normal line passes through the point Q_O. Such a point will be referred to as the ortho-point corresponding to Q_O. From Equation (14.1) we have, at any point on the hyperbola,

$$\frac{dV_R}{dV_C} = - \frac{V_R}{V_C} \tag{14.8}$$

By substituting Equation (14.7) into Equation (14.6) and making use of Equation (14.8) the orthogonality condition becomes

$$V_{C*}^2 - N_O V_{C*} = V_{R*}^2 - M_O V_{R*} \tag{14.9}$$

Further eliminating V_{R*} from Equations (14.9) and (14.1) yields an equation in the single variable V_{C*} :

$$V_{C*}^4 - N_O V_{C*}^3 + K M_O V_{C*} - K^2 = 0 \tag{14.10-C}$$

The corresponding equation in V_{R*} is

$$V_{R*}^4 - M_O V_{R*}^3 + K N_O V_{R*} - K^2 = 0 \tag{14.10-R}$$

Both Equations (14.10-C) and (14.10-R) are of the fourth degree, and in fact they are of the same form. They will be referred to as the orthogonality quartics, and their solutions the orthogonality solutions. Either of

them can be solved in closed form by standard method of algebra, or by numerical approximations. With either of the unknown components V_{C*} or V_{R*} thus determined, the other component and the corresponding velocity increment $|\Delta V|$ can then be easily obtained from Equations (14.1) and (14.3a) and the principal elements of the transfer trajectory are then obtained from usual orbital relations. However, it is to be noted that the real solution of either Equation (14.10-C) or (14.10-R) is not unique since a quartic may give 4, 2 or no real solution. Furthermore, the orthogonality condition expressed by such a quartic is neither sufficient nor necessary for the optimum solution of the problem. It is merely a necessary condition for an interior extremem, and it may yield maxima, minima, or neither. And even if it gives a local minimum, it may not be the absolute one; and even if it is absolute, the resulting trajectory may be unrealistic[14.2] (see Section 8.1). Thus instead of going into numerical solutions the following vital questions are now posed:

(1) Under what condition will the orthogonality Equation (14.10-C) or (14.10-R) have a unique real solution, two, four or no real solutions?

(2) If multiple solutions exist, is there any simple rule for the selection of an absolute minimum?

(3) Under what condition will the resulting transfer trajectory be unrealistic? And if so, how to choose a realistic optimum trajectory for the problem?

These questions will be critically examined one by one in the sections that follow. Before proceeding to answering these questions, the dimensionless velocity parameter defined by

$$\nu \equiv V/V_{S1} \equiv V/\sqrt{\frac{\mu}{r_1}} \tag{14.11}$$

14.2 Called "false optimum" by Stark in[39].

TABLE III-1

PRINCIPAL FORMULAS IN THE NONDIMENSIONAL FORM
FOR TERMINAL-TO-TERMINAL OPTIMUM TRANSFER

Compatibility Condition	$v_C v_R = \kappa$	(14.1')
Velocity Increment	$\lvert\Delta v\rvert^2 = v_C^2+v_R^2 -2\eta_o v_C -2\mu_o v_R +v_o^2-2\kappa\cos\varphi_1$	(14.3')
The Orthogonality Equation		
in v_{C_*} , v_{R_*}	$v_{C_*}^2 - \eta_o v_{C_*} = v_{R_*}^2 - \mu_o v_{R_*}$	(14.9')
in v_{C_*}	$v_{C_*}^4 - \eta_o v_{C_*}^3 + \kappa\mu_o v_{C_*} - \kappa^2 = 0$	(14.10'-C)
in v_{R_*}	$v_{R_*}^4 - \mu_o v_{R_*}^3 + \kappa\eta_o v_{R_*} - \kappa^2 = 0$	(14.10'-R)
The Constant Product	$\kappa \equiv \tan\frac{\psi}{2}\csc\varphi_1$	(14.4)
The Orthogonal Projections of the Initial Velocity Vector	$\mu_o \equiv (v_R)_o - (v_C)_o\cos\varphi_1$ $\eta_o \equiv (v_C)_o - (v_R)_o\cos\varphi_1$	(14.5')

TABLE III-2

PRINCIPAL GEOMETRICAL ELEMENTS OF THE CONSTRAINING HYPERBOLA ($\nu_C\nu_R = \kappa$)

Element	Symbol	Formulas			Numbering
		In terms of κ, φ_1	In terms of ψ, φ_1	In terms of ψ, $n(\equiv r_2/r_1)$	
Included angle between the asymptotes	σ	$\pi - \varphi_1$	$\pi - \varphi_1$	$\sin^{-1}\left(\dfrac{2 \sin \frac{\psi}{2}}{\sqrt{(1 + \frac{1}{n})^2 \sec^2 \frac{\psi}{2} - \frac{4}{n}}}\right)$	(14.12)
Semi-transversal axis	A	$2\sqrt{\kappa} \sin \dfrac{\varphi_1}{2}$	$\sqrt{2 \tan \frac{\psi}{2} \tan \frac{\varphi_1}{2}}$	$\sqrt{\sec \frac{\psi}{2} \sqrt{(1 + \frac{1}{n})^2 \sec^2 \frac{\psi}{2} - \frac{4}{n}} - (1 + \frac{1}{n}) \sec^2 \frac{\psi}{2} + 2}$	(14.13)
Semi-conjugate axis	B	$2\sqrt{\kappa} \cos \dfrac{\varphi_1}{2}$	$\sqrt{2 \tan \frac{\psi}{2} \cot \frac{\varphi_1}{2}}$	$\sqrt{\sec \frac{\psi}{2} \sqrt{(1 + \frac{1}{n})^2 \sec^2 \frac{\psi}{2} - \frac{4}{n}} + (1 + \frac{1}{n}) \sec^2 \frac{\psi}{2} - 2}$	(14.14)
Center-to-focus distance	C	$2\sqrt{\kappa}$	$2\sqrt{\tan \frac{\psi}{2} \csc \varphi_1}$	$\sqrt{2 \sec \frac{\psi}{2} \sqrt{(1 + \frac{1}{n})^2 \sec^2 \frac{\psi}{2} - \frac{4}{n}}}$	(14.15)
Eccentricity	e	$\csc \dfrac{\varphi_1}{2}$	$\csc \dfrac{\varphi_1}{2}$	$\left\{\dfrac{2}{1 - \dfrac{(1 + \frac{1}{n}) - 2 \cos^2 \frac{\psi}{2}}{\sqrt{(1 + \frac{1}{n})^2 - \cos^2 \frac{\psi}{2}}}}\right\}^{1/2}$	(14.16)

will now be introduced, and the principal equations developed so far, be nondimensionalized as summarized in Table III-1.

Besides, formulas for the principal geometrical elements of the constraining hyperbola are presented in Table III-2. Some essential features of the constraining hyperbola worthy of noting are as follows.

(1) The conjugate and transversal axes of the hyperbola (v_χ, v_ζ -axes) are the bisectors of the interior and exterior angles at the initial terminal Q_1 of the base triangle respectively. The v_ζ -axis is in the direction of the minimum energy trajectory through the initial terminal according to Section 10.1 and may be called the minimum energy axis. The pair of directions (χ,ζ) together with the pair of the asymptotic directions (C, R_1) mentioned earlier and their respective normals to be introduced later constitute the most important reference directions of the present problem.

(2) The semi-transversal axis (A) of the constraining hyperbola is the minimum velocity satisfying the constraint, and therefore, the departure velocity along the minimum energy transfer trajectory as previously given by Equation (10.5) in Part II.

(3) Of the two branches of the hyperbola, the one on which $V_C > 0$, and $V_R > 0$ is the constraint for the normal trajectories, and the other one on which $V_C < 0$ and $V_R < 0$ is the constraint for the complementary trajectories. These two branches correspond to the two lines of origins in the nondimensional hodograph introduced in Part II (Figure II-1).

(4) Points on the hyperbola which are symmetrical with respect to its transversal axis correspond to a pair of conjugate trajectories, and will be called the conjugate points; points symmetrical with respect to the origin correspond to a pair of complementary trajectories, and will be called

the complementary points. Consequently, points symmetrical with respect to the conjugate axis correspond to a pair of trajectories one of which is the complementary of the conjugate of the other. Such a point pair and their corresponding trajectories will be called a complementary-conjugate pair for short.

For the convenience of later development the quadrants of the hodograph plane bounded by the symmetrical axes of the constraining hyperbola will be referred to as positive (+) or negative (-) according as it is on the positive or the negative side of the V_χ -axis; and high (H) or low (L) according as it is above or below the V_ζ -axis. The parts of the constraining hyperbola and all velocity vectors will also be so referred to according to the quadrant in which they lie. Such subdivisions are depicted in Figure III-2.

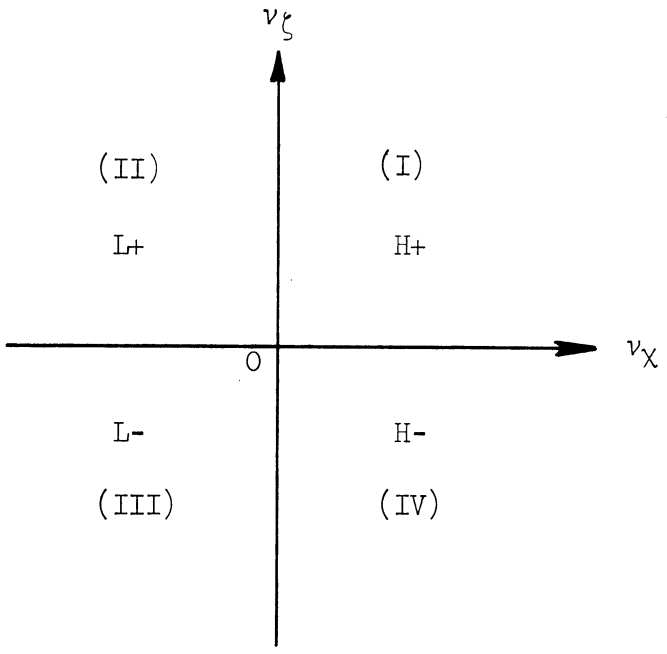

Figure III-2. Quadrants in the Hodograph Plane.

14.3 Criterion of the Nature of the Real Solutions and the Boundary Evolute

In order to examine the nature of the solutions of the orthogonality quartic, either the V_{*C} -equation (14.10-C) or the V_{*R} -equation (14.10-R) may be used since they are identical in form and have essentially the same discriminant. To fix the idea the following discussion will be based on the V_{*C} -equation. The discriminant for such a quartic is given by

$$\Delta \equiv I^3 - 27J^2 \tag{14.17}$$

where

$$\begin{aligned} I &\equiv \frac{1}{4}\ \kappa\ (m_o n_o - 4\kappa) \\ J &\equiv \frac{1}{16}\ \kappa^2 (m_o^2 - n_o^2) \end{aligned} \tag{14.18}$$

By using Burnside's criteria[23] together with Descartes' Rule of Signs we arrive at the conclusions in the first two columns of Table III-3, classifying the nature of the real roots. Since multiple roots of the equation give identical solutions, they will be considered as one solution. From such considerations we arrive at the further conclusions in column IV, Table III-3. The geometrical implication of such conclusions may be seen as follows.

With the expressions (14.17) and (14.18) the boundary condition $\Delta = 0$ may be written

$$4(m_o n_o - 4\kappa)^3 - 27\ \kappa(m_o^2 - n_o^2)^2 = 0 \tag{14.19}$$

Now introduce the polar coordinates (ν, Φ) for the velocity vector $\vec{\nu}$ and express the parameters m_o and n_o for the initial velocity vector as

$$\begin{aligned} m_o &= \nu_o \sin\ (\frac{\varphi_1}{2} + \Phi_o) \\ n_o &= \nu_o \sin\ (\frac{\varphi_1}{2} - \Phi_o) \end{aligned} \tag{14.20}$$

TABLE III-3

NATURE OF THE REAL ROOTS (ν_{C*} OR ν_{R*}) OF THE ORTHOGONALITY QUARTIC AND NUMBER OF REAL SOLUTIONS

(I)	(II)			(III)	(IV)		
	Real Roots				No of Real, Distinct Orthogonality Solutions		
		Number		Regions (see Fig. III-3)	Positive Solutions ($\nu_C > 0$, $\nu_R > 0$)	Negative Solutions ($\nu_C < 0$, $\nu_R < 0$)	TOTAL
Discriminant	Nature	Positive Roots	Negative Roots				
$\Delta < 0$	2 real roots, distinct	1	1	S_+ , S_-	1	1	2
$\Delta > 0$	4 real roots, all distinct	3	1	N_+	3	1	4
		1	3	N_-	1	3	4
$\Delta = 0$	4 real roots, not all distinct	3 (two equal)	1	H_+, L_+ branches	2	1	3
		3 (all equal)	1	cusp G	1	1	2
		1	3 (two equal)	H_-, L_- branches	1	2	3
		1	3 (all equal)	cusp G'	1	1	2

where Φ is the path angle referring to the minimum energy axis, which is related to the usual path angle ϕ by

$$\Phi = \phi - \frac{\varphi_1}{2} \tag{14.21}$$

By substituting these expressions into the boundary Equation (14.19) we obtain

$$[\bar{v}_o^2 (\cos 2\Phi_o - \cos\varphi_1) - 8\kappa]^3 - 54\kappa \bar{v}_o^4 \sin^2\varphi_1 \sin^2 2\Phi_o = 0 \tag{14.22}$$

where $\bar{v}_o$ is the magnitude of the initial vector $\vec{v}_o$, which satisfies the boundary condition. This equation may be transformed into the following standard form in the rectangular coordinates (v_χ, v_ζ)

$$(A\bar{v}_\zeta)^{2/3} - (B\bar{v}_\chi)^{2/3} = C^{4/3} \tag{14.23}$$

where the parameters A, B, and C have been given in Table III-3. From Equation (14.23) this boundary curve is recognized as one form of the Lamé curve,[30] which in the present case is the evolute of the constraining hyperbola. Some essential features of this curve are as follows (see Figure III-3):

(1) It is symmetrical with respect to both v_χ and v_ζ axes. Thus the boundary Lamé and the constraining hyperbola are co-axial.

(2) It is bounded between the v_c- and v_d-axes which are normal to the asymptotic directions of the constraining hyperbola (the radial and chordal directions) respectively.

(3) It has two portions, one on each side of the v_χ-axis, and each portion consists of two branches with a cusp (G, G') at its vertex given by the coordinates

$$(\bar{v}_o)_{G,G'} = 2\sqrt{\kappa} \csc \frac{\varphi_1}{2}, \quad \Phi_o = 0, \pi \tag{14.24}$$

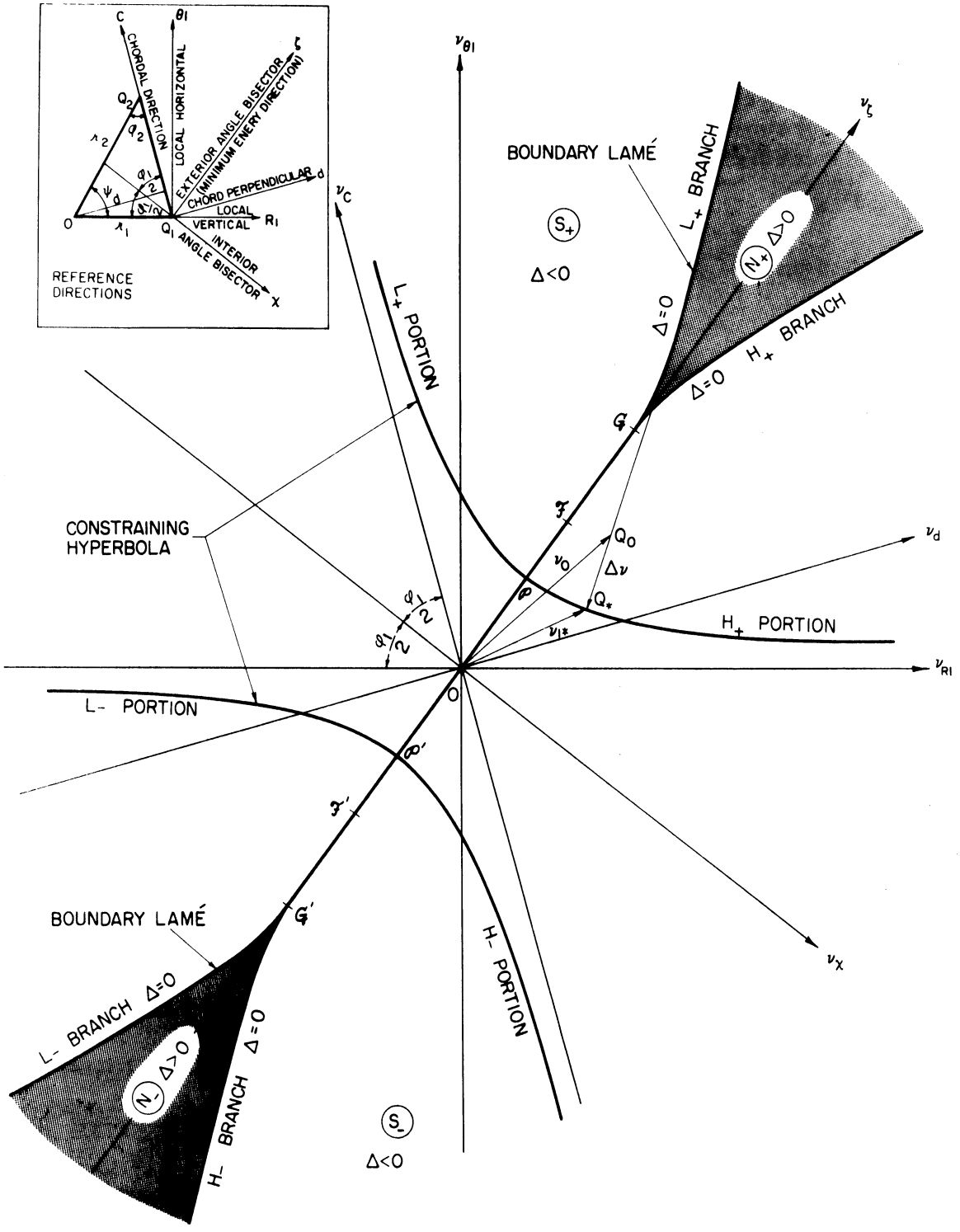

Figure III-3. Geometry of the Constraining Hyperbola and the Boundary Lamé

It is well-known that an evolute of a given curve is the envelope of all normals of this curve, or conversely, the given curve is the involute of its evolute. Since to find solutions of the orthogonality quartic according to a pair of given values of m_o and n_o is equivalent to drawing normals to the constraining hyperbola from a given point in the hodograph plane, naturally its evolute should form the boundary separating the regions in which different number of normals can be drawn. Directly from the concept of an evolute and the geometry of the hyperbola we see that

> All points of intersections of the different normals to the constraining hyperbola are in the regions beyond the boundary Lamé, and no two normals to the hyperbola can intersect in the region between the two portions of the boundary Lamé.

The latter region will be referred to as simple (S), while the former, non-simple (N). For convenience various portions of these regions, together with their boundaries, will be referred to as positive (+) or negative (-), and high (H) or low (L), according to the quadrant in which they are located, just as for the portions of the constraining hyperbola (Figure III-3).

With the foregoing understanding the conclusions previously derived from algebraic considerations may now be stated in geometrical terms as follows:

(1) Within the simple region one and only one normal can be drawn from a given point to each branch of the hyperbola.

(2) Within the non-simple region four distinct normals can be drawn from a given point, three to the nearer branch, and one to the farther branch.

(3) From any point on the boundary three distinct normals can be drawn : two to the nearer branch, and one to the farther branch except at the cusp, where only one normal can be drawn to each branch, both coinciding with the transversal axis.

Moreover, further examination of the geometry of a hyperbola shown that,

(4) The normals at points of the hyperbola in the same quadrant always intersect in the adjacent quadrant on the opposite side of the transversal axis of the hyperbola. (For example, two normals to the H+ part of the constraining hyperbola can meet only in the L+ portion of the N-region. This property is especially useful in the later treatment of the present problem; an analytical proof is given in Appendix C.)

Finally it is to be noted that for a given vertex angle ψ the distance of either cusp of the boundary Lamé from the origin, $(\bar{\nu}_o)_{G,G'}$ decreases with increasing φ_1 or n, and it has the limiting value

$$(\bar{\nu}_o)_{G,G'} \to \sqrt{2} \sec^2 \frac{\psi}{2} > \sqrt{2} \quad \text{when} \quad \varphi_1 \to \pi - \psi \ (n \to \infty) \qquad (14.25)$$

Thus multiple real solutions can occur only when the initial velocity or orbit is hyperbolic. Furthermore, owing to the presence of the asymptotic lines of the boundary Lamé, such a case cannot occur unless the initial velocity vector is directed above the local horizon but below its conjugate direction, the ν_d -axis. A necessary and sufficient condition for the occurrence of such multiple solutions may be precisely stated as follows:

$$\nu_o \geq \bar{\nu}_o \quad \text{and} \quad -\frac{\varphi_1}{2} < \Phi_o < +\frac{\varphi_1}{2} \qquad (14.26)$$

where $\bar{\nu}_o$ is given by Equation (14.22).

15. DETERMINATION OF THE OPTIMUM SOLUTION

15.1 The Absolute Minimum Solution and Its Determination

With the number of real and distinct solutions of the orthogonality quartic determined, the next task is to select the one for absolute minimum. For the time being let us disregard the question of unrealistic trajectory, and consider only the geometrical problem of determining the absolute minimum distance.[15.1] Such questions of maxima and minima can usually be settled by the second derivative test, and the absolute minimum determined by comparing the quantity to be minimized at these stationary points. However, it is simpler here to use a geometrical approach outlined below:

A. From the symmetrical nature of the hyperbola, it is evident that the minimum distance solution demands the optimum point on the constraining hyperbola to be in the same quadrant with the tip Q_o of the initial velocity vector. However, in view of the geometrical property of the hyperbola given by item (4) of the previous section, there is one and only one such a point on the constraining hyperbola in the same quadrant with the given point (see Figure III-4(1), (2), (3)) unless Q_o is on either of the symmetrical axes of the constraining hyperbola. This is true whether the point Q_o is in the simple or nonsimple region. Thus when Q_o is off the symmetrical axes, the choice is clear, and the absolute minimum distance solution is unique. Furthermore, directly from this co-quadrant requirement it can be inferred immediately that the trajectory corresponding to such a solution always belongs to the same group

---

15.1 The absolute minimum distance solution will be indicated by the subscript ** whenever it is to be distinguished from the orthogonality solution.

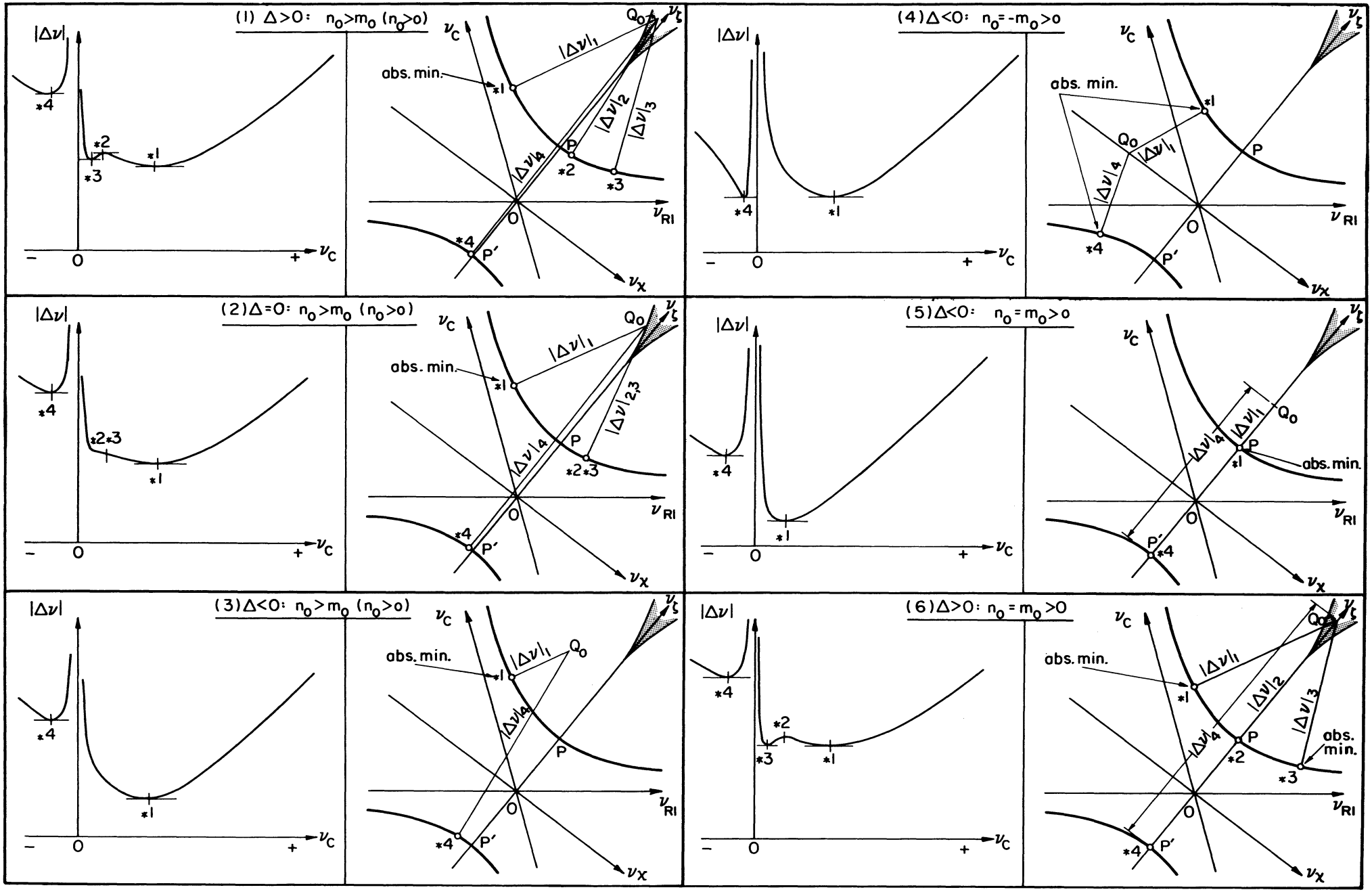

Figure III-4. Variation of $|\Delta\nu|$ and the Corresponding Geometry in the Hodograph Plane

TABLE III-4

THE REAL ROOTS OF THE ν_{C*}-EQUATION AND THE NATURE OF THE STATIONARY POINTS ON THE $|\Delta\nu|$-CURVE
(for the case $n > 0$ and $n_o \geq m_o$)

Designation of the root ν_{C*}	$\Delta > 0$		$\Delta = 0$				$\Delta < 0$	
			$I^2 + J^2 \neq 0$		$I = 0,\ J = 0$			
	sign of ν_{C*}	nature of $\|\Delta\nu\|$	sign of ν_{C*}	nature of $\|\Delta\nu\|$	sign of ν_{C*}	nature of $\|\Delta\nu\|$	sign of ν_{C*}	nature of $\|\Delta\nu\|$
1	+	min	+	min	+ (all equal)	min	+	min
2	+	max	+ (equal)	neither			—	—
3	+	min					—	—
4	-	min	-	min	-	min	-	min

(normal or complementary) and the same class (high or low) as the initial velocity vector.

B. In case Q_o lies on either of the symmetrical axes, then it is on the border of two adjacent quadrants. In such a case the minimum distance requirement is to have the optimum point in the half plane of these two quadrants; and thus two solutions are possible.

(1) If Q_o lies on the v_χ-axis, then the optimum point must be on the same side of the v_ζ-axis with Q_o. The geometry in the hodograph plane shows that Q_o is in the simple region and equidistant from both branches of the hyperbola. Thus there are two and only two normals which can be drawn from Q_o, one to each branch, and they are of equal length. Consequently both ortho-points may be admitted, and there are two solutions for absolute minimum distance. The two corresponding trajectories require the same amount of Δv, and their departure velocities also have the same magnitude. Obviously they constitute a complementary-conjugate pair, one belongs to the normal group, and the other, the complementary group. They will be either both high or both low according as the initial velocity vector is high or low. This situation is depicted in Figure III-4(4).

(2) If Q_o lies on the v_ζ-axis, then the optimum point must lie on the same side of the v_χ-axis. Now Q_o may be either in the simple region (S) or the non-simple region (N).

i Suppose Q_o is in the S-region, that is, it lies between two cusps, G and G', of the boundary Lame. Evidently the two and only two ortho-points now coincide with the vertices $\mathcal{P}$ and $\mathcal{P}'$ of the hyperbola, and there is only one on the same side of the v_χ-axis with Q_o.

Thus the absolute minimum solution is again unique, and the corresponding trajectory is the minimum energy one. It will belong to the same group as the initial velocity vector. This situation is depicted in Figure III-4(5).

ii. Suppose Q_o is in the N-region, that is, it lies on the parts of the v_ζ-axis which are beyond the cusp points of the boundary Lamé in either direction. Then according to property (3) given in the previous section, there are three normals on the branch of the hyperbola on the same side of the v_χ-axis. It is evident from the symmetry of the hyperbola that among the three ortho-points, which are on the branch nearer to the initial point Q_o, one coincides with the vertex, while the other two are of a conjugate pair, and equidistant from Q_o. The fourth ortho-point coincides with the other vertex. This situation is depicted in Figure III-4(6). Evidently, the fourth point should be rejected, and the choice will be between the point Q_{*2} and either of the points Q_{*1} and Q_{*3}. It can be shown that it is always the point Q_{*2} which is at a farther distance. (This can be proved either by considering the present case as the limiting case of case A when Q_o moves towards the v_ζ-axis, or by solving the orthogonality quartic with $\eta_o = \eta_o$, and comparing the distances since in this particular case the quartic admits a simple solution.) Consequently, both points Q_{*1} and Q_{*3} may be admitted, and there are two solutions giving the same amount of Δv. The two corresponding trajectories are conjugate to each other, requiring the same magnitude of departure velocity, and they are both of the same group as the initial velocity vector. It is interesting to note here that the minimum energy trajectory is no longer the optimum transfer

trajectory even though the initial velocity is in that direction; the two optimum directions are now inclined equally on either side of the minimum energy direction instead of lying along it.

iii. Finally when the point Q_o is at either cusp of the boundary Lamé, then both conjugate points coincide with the nearer vertex, and the minimum distance solution is again unique, and the corresponding trajectory is again a minimum energy trajectory. This is the same as case ii.

In conclusion,

(1) Whenever the point Q_o is not on the conjugate axis of the hyperbola nor on the part of its transversal axis beyong the cusps of its evolute, the absolute minimum distance solution is unique. The corresponding trajectory will belong to the same group and same class as the initial velocity vector.

(2) Whenever Q_o is on the conjugate axis of the constraining hyperbola there are two solutions with the same minimum distance. The corresponding trajectories are a complementary-conjugate pair of the same class as the initial velocity vector.

(3) Whenever Q_o is on the transversal axis of the constraining hyperbola beyond the cusp points of the boundary Lame, there are again two absolute minimum distance solutions. The corresponding trajectories are a conjugate pair of the same group as the initial velocity vector.

Based on such geometrical analysis we may now form the following "rules of thumb":

Rules - Geometric

(1) Always choose the optimum point which is in the same quadrant with the point Q_o whenever no ambiguity arises. (One and only one solution.)

(2) If ambiguity does arise such as when the point Q_o lies on either of the symmetrical axes of the constraining hyperbola, always choose the optimum point or points in the same half-plane with Q_o, and the ones off the minimum energy axis if they are present.

As shown above the geometrical rule for the selection of the absolute minimum solution is exceedingly simple. Such a geometrical analysis may in turn guide the selection of the appropriate root from the real solutions of the orthogonality quartic for an absolute minimum without calculating the magnitudes of the corresponding $\Delta\nu$'s. In view of the symmetry of the constraining hyperbola it is sufficient to consider all the possible cases when Q_o is in one certain quadrant, say the second, and center our attention on the variation of $|\Delta\nu|$ with one variable, say ν_{C*}, when Q_o is in this quadrant. The geometry of such cases are illustrated in Figure III-4(1) to (6), and the corresponding variation of $|\Delta\nu|$ with ν_{C*} and the nature of its stationary points as obtained from usual algebraic analysis are also graphically shown in Figure III-4 for each case, and are summarized in Table III-4 for reference.

It is to be noted that the present restriction of Q_o in quadrant II is equivalent to saying $\eta_o > m_o$ and $\eta_o > 0$ in the orthogonality quartic. Keeping this in mind and without going into algebraic details, an examination of the geometry of the hodograph plane shows that:

When $\mathcal{M}_o \neq \pm \eta_o$ (Q_o off the symmetrical axes), the optimum point in the hodograph plane always corresponds to the highest root ν_{C*1} of the orthogonality quartic (see Figure III-4 (1), (2), (3)).

When $\mathcal{M}_o = \eta_o$ (Q_o on ν_ζ-axis), the co-half-plane requirement from geometrical considerations indicates that the optimum root ν_{C**} must agree in sign with the initial value $\nu_{\zeta o}$. Thus, under the present assumption, only the positive roots need be considered. The hodograph shows that there may be either one or three such roots corresponding to the one or three orthopoints on the positive branch of the constraining hyperbola. In the former case the only positive root is necessarily the optimum one. In the latter case the geometry of the hodograph shows that the pair of optimum points correspond to the highest and the lowest roots respectively (see Figure III-4 (6)). Thus both roots may be chosen. It is to be noted that the prerequisite to have ν_{C**} agree in sign with $\nu_{\zeta o}$ hold in general whenever $\mathcal{M}_o \neq \eta_o$.

When $\mathcal{M}_o = -\eta_o$ (Q_o on ν_χ-axis), the two optimum points in the hodograph plane, one on each branch, correspond to the two and only two real roots of the quartic, one positive and one negative (see Figure III-4(4)). Thus again both roots may be chosen.

All the foregoing observations were made on the L_+ portion of the constraining hyperbola. The symmetry of the hyperbola with its conjugate axis shows that the same is true for the L- portion if we take the magnitude of the root algebraically. Thus same conclusions hold in the low-half plane where $\eta_o \geq \mathcal{M}_o$. In the high half plane, we have $\eta_o \leq \mathcal{M}_o$. By the symmetrical nature of the hyperbola with

its transversal axis, whatever is true for ν_C in the low plane is equally true for ν_R in the high half-plane. Or, in view of the reciprocal relation between ν_C and ν_R (Equation (14.1)) we may say that whatever is true for the largest ν_C (algebraic) in the low-half plane is equally true for the smallest ν_C (algebraic) in the high-half plane. Based on such observations we may form some algebraic rules of thumb as follows:

Rules - Algebraic

Consider the ν_{C*}-equation (14.10-C)

(1) If $\mathcal{M}_o \neq \pm \mathcal{N}_o$, always choose the root which agrees in sign with the initial value of $\nu_{\zeta o}$; and if more than one such root present, choose the largest one if $\mathcal{N}_o > \mathcal{M}_o$ and the smallest one if $\mathcal{N}_o < \mathcal{M}_o$ (one solution only).

(2) If $\mathcal{M}_o = \mathcal{N}_o$, choose both the largest and the smallest roots which agree in sign with $\nu_{\zeta o}$ (two solutions).

(3) If $\mathcal{M}_o = -\mathcal{N}_o$, only two real roots present, both may be chosen, (two solutions).

The magnitudes of roots are being considered algebraically. All rules (1) to (3) hold for the ν_{R*}-equation (14.10-R) if we interchange the words $\mathcal{M}_o$ and $\mathcal{N}_o$.

15.2 Lines of Constant Optimum Trajectory and Lines of Constant Velocity Increment

Before we take up the question of unrealistic trajectories, it is essential to note that when the tip Q_o of the initial velocity vector moves along a straight line normal to the constraining hyperbola, the absolute minimum point Q_{**} remains intact, and consequently the

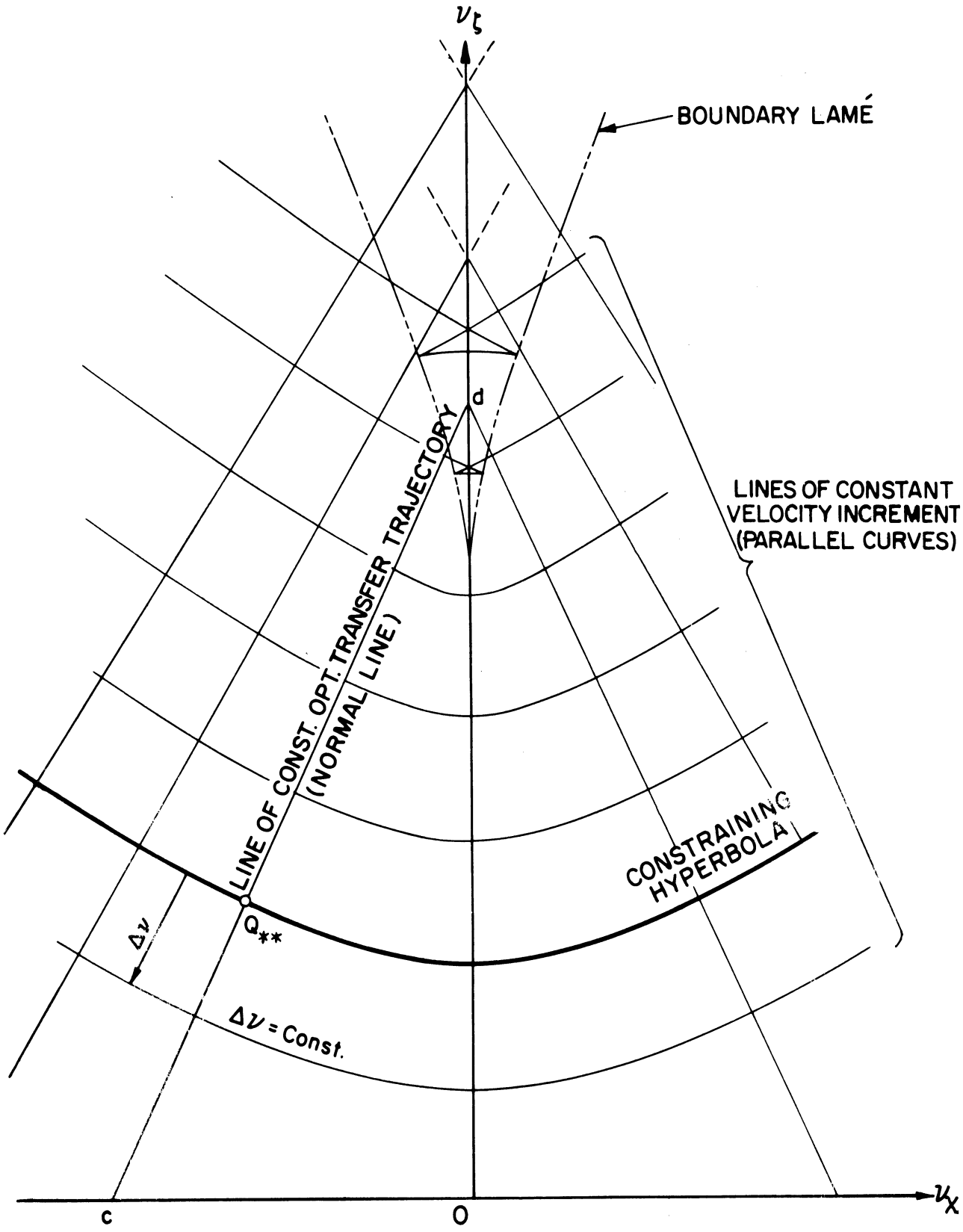

Figure III-5. Lines of Constant Optimum Transfer Trajectory and Lines of Constant Optimum Velocity-Increment

corresponding transfer trajectories are the same as long as Q_0 remains in the same quadrant. Such a trajectory will be the optimum trajectory for the present problem unless it is unrealistic. Thus the part of the normal line intercepted by the symmetrical axes of the constraining hyperbola (e.g., line cd in Figure III-5) may be regarded as a line of constant optimum trajectory. As soon as the normal line crosses either axis the absolute minimum point will shift to the other side of the axis and move along the constraining hyperbola resulting in a different trajectory for each point on the extended part of the normal line. It is to be noted that along a line of constant optimum trajectory the velocity-increment required varies from point to point depending on the position of Q_0 on this line, the farther Q_0 is from the constraining hyperbola, the larger the velocity-increment (absolute value) required.

In such a connection we may conceive that, when Q_0 moves along a curve running parallel to the constraining hyperbola, the amount of velocity increment required will remain the same while the optimum transfer trajectory changes from point to point. Thus such parallel curves may be regarded as lines of constant optimum velocity-increment. As known in geometry, all these parallel curves have the same normal lines and a common evolute. In the present case the boundary Lamé is this common evolute, and each of the parallel curves, including the constraining hyperbola is its involute. Thus the lines of constant optimum trajectory and the lines of constant velocity-increment are normal to each other, forming an orthogonal net in the hodograph plane. Such a net will be useful in developing hodographic charts for the present

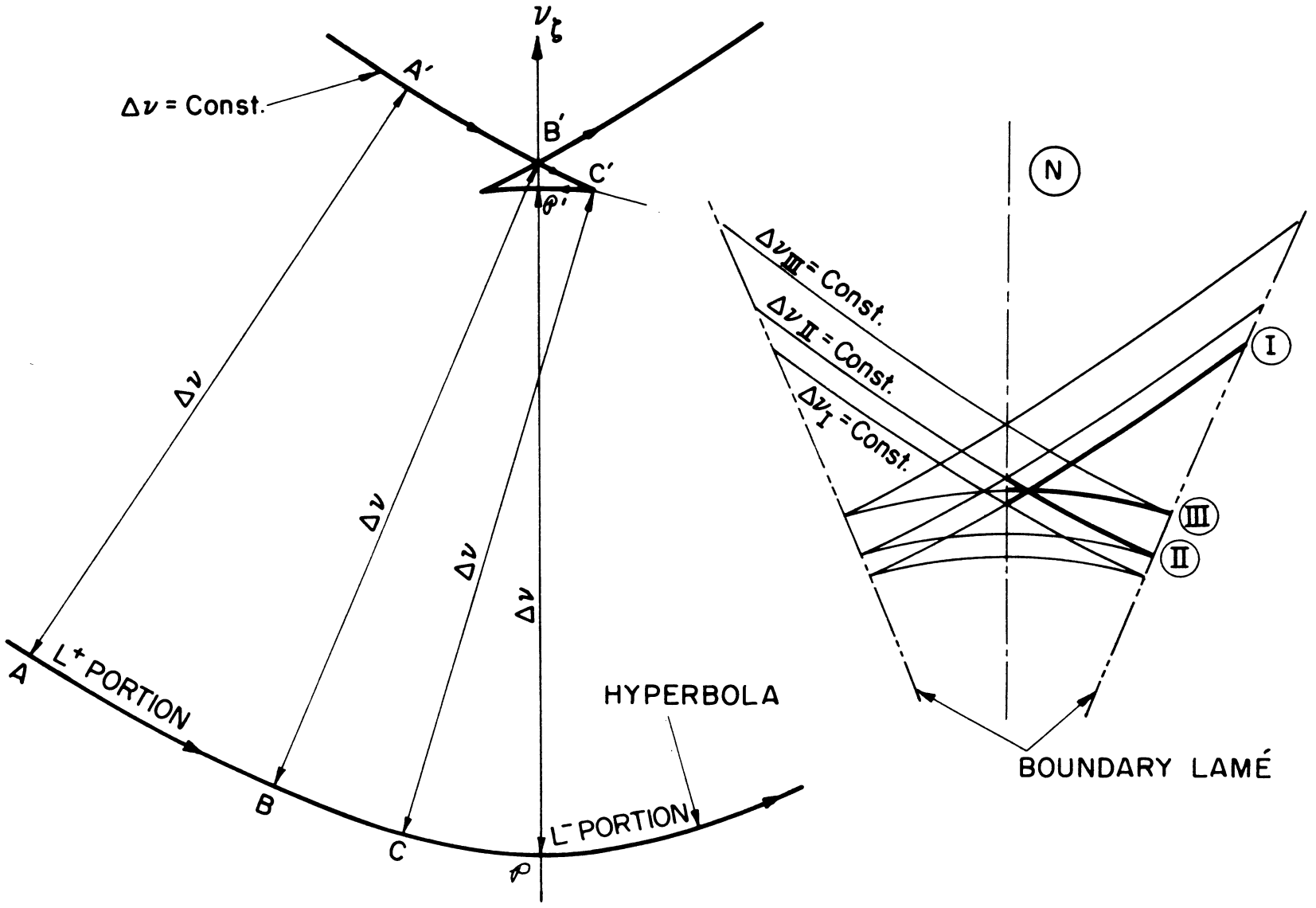

(a) Correspondence Between the Hyperbola and It's Parallel Curve.

(b) Three Parallel Curves Passing Through a Point in the Non-Simple Region.

Figure III-6. Geometry of the Parallel Curves

problem, which will be presented after the question of unrealistic trajectories has been cleared up. For the time being it is to be noted that such parallel curves though quite similar to the original curve (the constraining hyperbola) when they are close to it, may look radically different from it when they are farther from the hyperbola, especially when they enter the nonsimple region. The mathematic equation for the curves parallel to a hyperbola is in general of the eighth degree.(22) A few such typical curves are shown in Figure III-6.

15.3 The Critical Condition and the Unrealistic Trajectories

From the foregoing consideration of the lines of constant transfer trajectories it is evident that when the tip Q_o of the initial velocity vector moves along such a line which passes through a critical point ($\nu = \sqrt{2}$) on the constraining hyperbola, the absolute minimum distance solution will call for a parabolic trajectory. Such lines will be called the critical lines. Figure III-7 shows the four critical lines, one through each of the four critical points on the constraining hyperbola, forming a critical circuit a-b-a'-b'-a. These four critical points are given by the intersections of the hyperbola with the critical circle centered at the hodograph origin and having the radius $\sqrt{2}$. When Q_o moves along such a circuit, the trajectory corresponding to the absolute minimum distance solution will first be a parabola of the high class, and normal group when Q_o remains on ab; and as soon as it passes the point b, the trajectory will shift to its conjugate, and so forth.

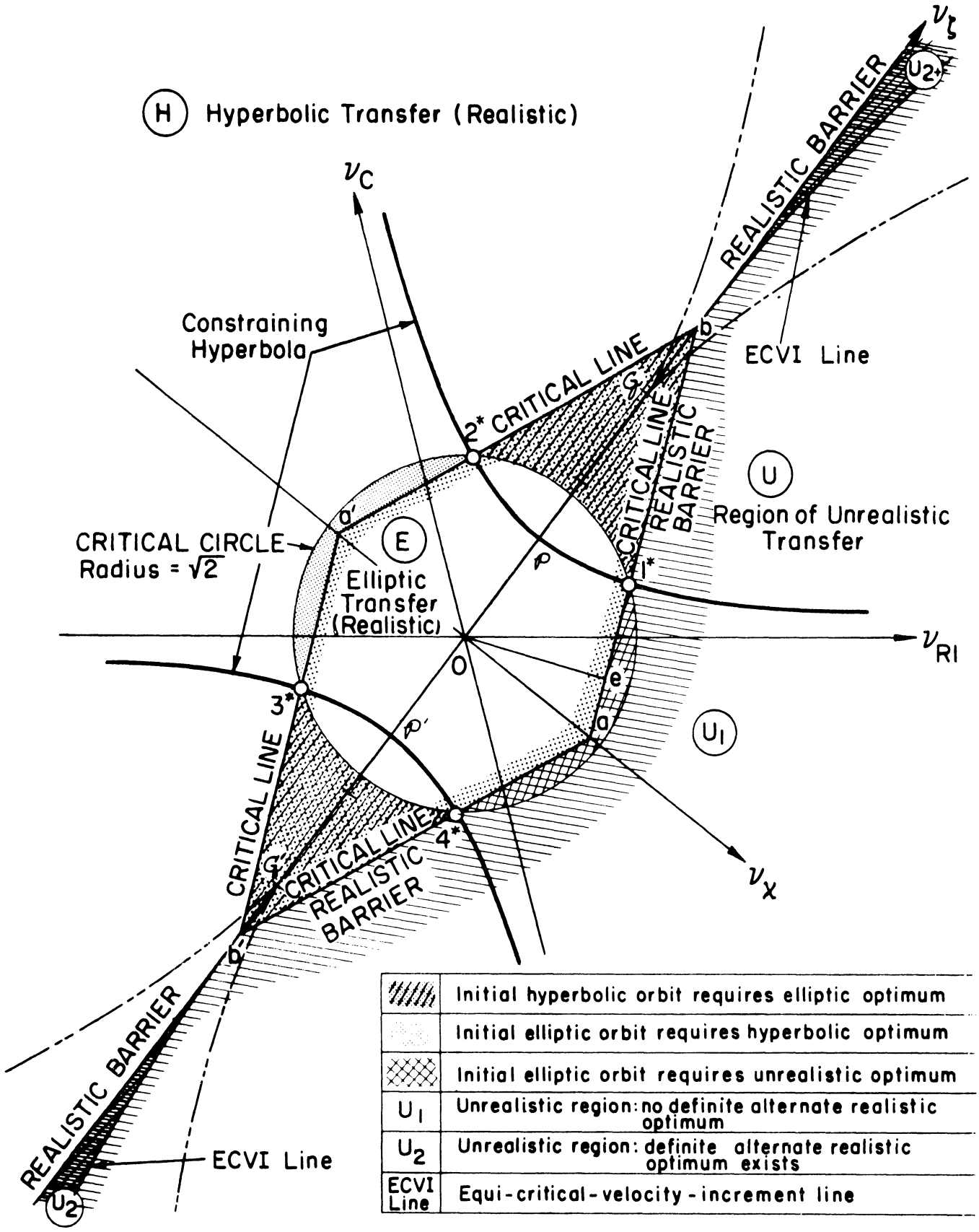

Figure III-7. Regions in the Hodograph Plane and the Nature of the Optimum Transfer Trajectory

As seen from the hodograph geometry, as long as Q_o is inside the rhomboid-shaped region bounded by the four critical lines, the corresponding absolute minimum point on the constraining hyperbola will remain inside the critical circle, consequently the transfer trajectory will be elliptic. This region will therefore be called the elliptic region. When Q_o is on the boundary of this rhomboid and beyond, the corresponding absolute minimum distance trajectory will first become parabolic and then hyperbolic. Thus the regions beyond the critical boundaries are hyperbolic regions. As shown in Section 8.3, a transfer trajectory between two fixed terminal points will be unrealistic only when it is parabolic or hyperbolic, and of the high class. Consequently the hyperbolic region on the high side is the region for unrealistic optimum transfer, and will be called the unrealistic region, while the hyperbolic region on the low side, and the elliptic region in between are regions for realistic optimum transfer, and will be called the realistic region. Thus the boundary b-a'-b separates the region for hyperbolic transfer from that for elliptic transfer, all realistic; while the boundary b'-a-b separates the elliptic realistic region from that of unrealistic transfer. Hence the two critical lines on the high side are in fact the barrier for a realistic optimum transfer, and will be referred to as the realistic barrier. Beyond the vertices b and b' of the rhomboid aba'b' the realistic and the unrealistic regions are further separated by the v_ζ-axis, which itself belongs to the realistic region. In short, the broken line b'-a-b and the part of v_ζ-axis beyond either b or b' form the entire realistic barrier which divides the whole hodograph plane into two main regions, the realistic region and the unrealistic region for the

optimum transfer. With such a partition established in the hodograph plane we may say that the absolute minimum distance solutions obtained in the preceding analysis is actually the optimum solution of the problem whenever the tip Q_o of the initial velocity vector lies in the realistic region. It ceases to be the optimum only when Q_o is beyond the realistic barrier, or on the boundary b'-a-b, excluding the two end points b and b'. The various regions in the hodograph plane are shown in Figure III-7, and further divisions of the unrealistic region will be presented in the next section.

It is interesting to note that the type of the optimum transfer trajectory, whether elliptic, parabolic, or hyperbolic does not necessarily agree with that of the initial velocity. The shaded region beyond the critical lines on the low side but within the critical circle is the region where the initial velocity is elliptic, but the optimum solution calls for a hyperbolic transfer. Similarly, the shaded region beyond the critical circle but within the rhomboid is the region where a hyperbolic initial velocity calls for an optimum elliptic transfer. It is also evident from the hodograph that even an elliptic initial velocity, if at sufficiently high path angle, may introduce an unrealistic optimum. The geometrical criterion for an unrealistic optimum transfer obtained so far will be analytically formulated as follows.

First, we note that there always exist such critical points, where $\nu = \sqrt{2}$, on the constraining hyperbola, since the minimum velocity along this hyperbola is always elliptic as is evident from Equation (14.13), Table III-2,

$$\nu_{min} = A = \sqrt{2 \tan \frac{\psi}{2} \tan \frac{\varphi_1}{2}} < \sqrt{2} \qquad (15.1)$$

since $\varphi_1 < \pi - \psi$.

The critical points are given by the intersection of the critical circle

$$\nu_\chi^2 + \nu_\zeta^2 = 2 \tag{15.2}$$

with the constraining hyperbola, whose equation in ν_χ , ν_ζ-coordinates is

$$\left(\frac{\nu_\zeta}{A}\right)^2 - \left(\frac{\nu_\chi}{B}\right)^2 = 1 \tag{15.3}$$

By solving Equations (15.2) and (15.3) and using formulas (14.13) and (14.14) the four critical points are found as follows:

	ν_χ^*	ν_ζ^*
1*	$+\sqrt{X^*}$	$+\sqrt{Y^*}$
2*	$-\sqrt{X^*}$	$+\sqrt{Y^*}$
3*	$-\sqrt{X^*}$	$-\sqrt{Y^*}$
4*	$+\sqrt{X^*}$	$-\sqrt{Y^*}$

(15.4)

where

$$X^* = 2 \sec \frac{\Psi}{2} \cos \frac{\varphi_1}{2} \cos \frac{1}{2}(\psi + \varphi_1)$$

$$Y^* = 2 \sec \frac{\psi}{2} \sin \frac{\varphi_1}{2} \sin \frac{1}{2}(\psi + \varphi_1) \tag{15.5}$$

The four points are numbered according to the quadrant they are in (see Figure III-7). The equation for the critical line through any of the critical points may be written

$$\nu_\zeta - \nu_\zeta^* = -(\nu_\chi - \nu_\chi^*) \left(\frac{d\nu_\chi}{d\nu_\zeta}\right)^* \tag{15.6}$$

where $(dv_\zeta/dv_\chi)^*$ is the slope of the constraining hyperbola at the critical point, and is given by

$$\left(\frac{dv_\zeta}{dv_\chi}\right)^* = \frac{v_\chi^*}{v_\zeta^*} \tan^2 \frac{\varphi_1}{2} \tag{15.7}$$

Substituting Equation (15.7) into Equation (15.6) and rearranging yields

$$v_\chi^* v_\zeta \sin^2 \frac{\varphi_1}{2} + v_\zeta^* v_\chi \cos^2 \frac{\varphi_1}{2} = v_\chi^* v_\zeta^* \tag{15.8}$$

which reduces to the polar form

$$v_o \left(v_\chi^* \cos \Phi \sin^2 \frac{\varphi_1}{2} + v_\zeta^* \sin \Phi \cos^2 \frac{\varphi_1}{2} \right) = v_\chi^* v_\zeta^* \tag{15.9}$$

by the coordinate transformation,

$$\begin{aligned} v_\chi &= v_o \sin \Phi_o \\ v_\zeta &= v_o \cos \Phi_o \end{aligned} \tag{15.10}$$

From Equation (15.9) and using Equations (15.4) and (15.5) we find the magnitude v_o^* of the initial velocity vector v_o on the critical boundary a-b-a'-b'-a as summarized below (where the usual subscripts H_+ etc. are used to indicate the quadrant where the tip of Q_o lies):

along a-b $(0 \le \Phi_o \le \frac{\pi}{2})$	$(v_o)^*_{H+} (C_1 \cos \Phi_o + C_2 \sin \Phi_o) = 1$	(15.11-1)
along b-a' $(-\frac{\pi}{2} \le \Phi_o \le 0)$	$(v_o)^*_{L+} (C_1 \cos \Phi_o - C_2 \sin \Phi_o) = 1$	(15.11-2)
along a'-b' $(-\pi \le \Phi_o \le -\frac{\pi}{2})$	$(v_o)^*_{L-} (C_1 \cos \Phi_o + C_2 \sin \Phi_o) = -1$	(15.11-3)
along b'-a $(\frac{\pi}{2} \le \Phi_o \le \pi)$	$(v_o)^*_{H-} (C_1 \cos \Phi_o - C_2 \sin \Phi_o) = -1$	(15.11-4)
$C_1 \equiv \sqrt{\frac{\sin^3 \frac{\varphi_1}{2} \cos \frac{\psi}{2}}{2 \sin \frac{1}{2}(\psi+\varphi_1)}}$, $C_2 \equiv \sqrt{\frac{\cos^3 \frac{\varphi_1}{2} \cos \frac{\psi}{2}}{2 \cos \frac{1}{2}(\psi+\varphi_1)}}$		(15.12)

Recalling that the realistic barrier is along a'-a-b, a criterion for unrealistic optimum transfer may now be stated as follows:

$$\begin{aligned} 0 < \Phi_o \leq \frac{\pi}{2} : \quad & v_o \geq (v_o^*)_{H+} \\ \frac{\pi}{2} \leq \Phi_o < \pi : \quad & v_o \geq (v_o^*)_{H-} \end{aligned} \tag{15.13}$$

Similarly, recalling that the realistic critical boundary is along b-a'-b', and that realistic hyperbolic transfer exists along the v_ζ-axis beyond b and b', a criterion for parabolic and hyperbolic optimum transfer is

$$\begin{aligned} -\frac{\pi}{2} \leq \Phi_o < 0 : \quad & v_o \geq (v_o^*)_{L+} \\ -\frac{\pi}{2} \geq \Phi_o > -\pi : \quad & v_o \geq (v_o^*)_{L-} \\ \Phi_o = 0, \pi : \quad & v_o \geq v_{b,b'} \end{aligned} \tag{15.14}$$

By setting $v_\chi = 0$ in Equation (15.8) and using formulas (15.4), (15.5) we find the distance from the origin to either corner point, b or b',

$$v_{b,b'} = \overline{Ob} = \sqrt{2 \sec \frac{\psi}{2} \csc^3 \frac{\varphi_1}{2} \sin \frac{1}{2}(\psi + \varphi_1)} \tag{15.15}$$

It can be shown by comparing Equation (15.15) with Equation (14.24) that,

$$v_{b,b'} > v_{G,G'}$$

That is, the corners of the elliptic region always extend into the non-simple regions. This should be expected since either point b or b' is an intersection of two normals to the constraining hyperbola. This situation implies that two realistic optimum solution exist in the elliptic region when the initial velocity is in the minimum energy direction,

and has the magnitude

$$v_{G,G'} < v_o < v_{b,b'}$$

As discussed before, the optimum solution in such a case does not give the minimum energy trajectory, but instead it gives a conjugate pair of two trajectories. And, within the present range of v_o they are both elliptic of course. The same situation exists when $v_o \geq v_{b,b'}$ except that the optimum trajectory is now hyperbolic, and the realistic optimum solution is unique since its conjugate becomes unrealistic.

Finally, as the hodograph shows, there is a minimum initial speed $(v_o^*)_{LL}$ below which neither a critical nor an unrealistic optimum can occur, for whatever the path angle may be. This is given by the length of the perpendicular drawn from the origin to any of the critical lines, e.g., the line segment oe in Figure III-7. From the trigonometry of the triangle oab, we find

$$(v_o^*)_{LL} = \overline{oe} = \sqrt{\frac{\sec\frac{\psi}{2}\sin(\psi+\varphi_1)}{\sin^3\frac{\varphi_1}{2}\cos\frac{1}{2}(\psi+\varphi_1)+\cos^3\frac{\varphi_1}{2}\sin\frac{1}{2}(\psi+\varphi_1)}} \qquad (15.16)$$

For example, if $\psi = 60°$, $\varphi_1 = 75°$ (corresponding to the transfer to a target point at the distance ratio $n = 1.366$) we have $(v_o^*)_{LL} = 1.22$. Besides, it is evident that unrealistic optimum cannot occur when the initial velocity vector is in the low half-plane ($\Phi_o \leq 0$).

15.4 Choice of the Realistic Optimum Transfer Trajectory

From the preceding analysis the absolute minimum solution of the orthogonality quartic is the optimum solution of the problem whenever the tip Q_o of the initial velocity vector is in the realistic region. However, whenever Q_o is outside this region, the absolute minimum

solution is an unrealistic optimum, from the physical point of view, and it remains to select a realistic optimum trajectory for the problem. Such a selection will depend on whether the point Q_o is in the simple or nonsimple region of the hodograph plane.

A. Suppose Q_o is in the simple region and off the v_χ-axis. Then the absolute minimum distance solution is unique. In such a case it is evident that the best choice will be the point on the constraining hyperbola sufficiently close to the critical point in the same quadrant with the initial point Q_o but still within the elliptic region. Thus, strictly speaking, there is no definite optimum solution for the problem in this case. The transfer trajectory so chosen will necessarily be highly eccentric, of the same class (high) and same group as the initial velocity vector. If Q_o is on the v_χ-axis, then the two critical points on the realistic barrier, one on each side of the v_χ-axis may be the reference points, and points close to either critical point may be chosen.

B. Suppose Q_o is in the non-simple region. We recall that in such a region three normals can be drawn from the point Q_o to the nearer branch of the constraining hyperbola. For definiteness let us assume Q_o is in the H+ portion of the region N (see Figure III-8). Then the three ortho-points on the constraining hyperbola will be distributed as follows:

Ortho-Point	Branch of the Constraining Hyperbola	Nature of the Solution
*1	H+	Min., absolute, unrealistic
*2	L+	Maximum
*3	L+	Min., local, realistic

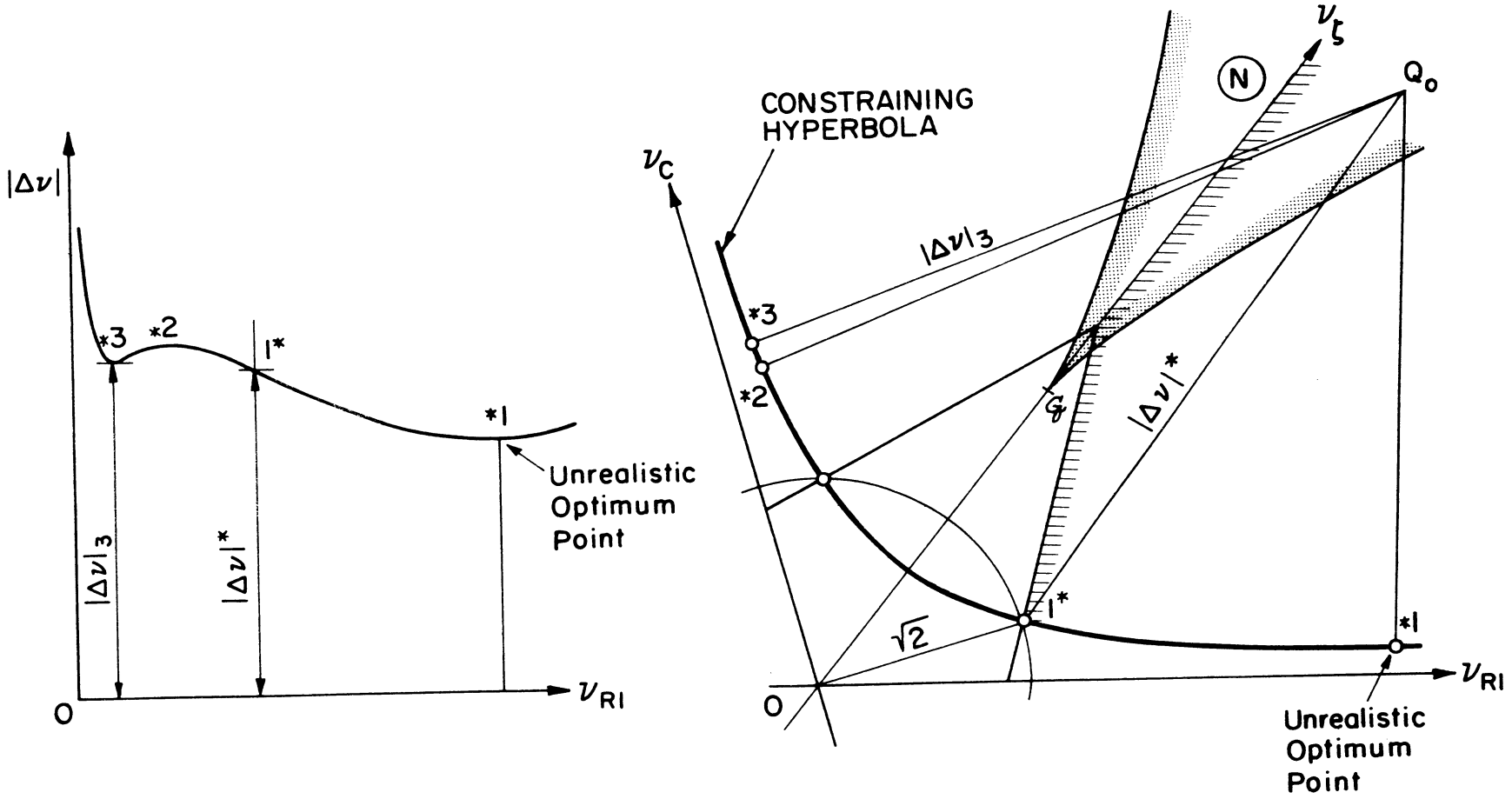

Figure III-8. Choice of the Realistic Optimum Trajectory: Initial Velocity Vector in the Unrealistic Region

Thus, besides the unrealistic minimum there is a second minimum for consideration, which is realistic. Let $|\Delta v|_3$ and $|\Delta v|^*$ be the velocity-increments required at the point 3 and the critical point under consideration (e.g. point 1* in Figure III-8) respectively. Then the choice will depend on the relative magnitudes of these two quantities.

(1) If $|\Delta v|_3 \leq |\Delta v|^*$, then the optimum trajectory is definite and unique, as given by the point *3.

(2) If $|\Delta v|_3 > |\Delta v|^*$, then some point close to the critical point but within the elliptic region should be chosen. This case is same as case A.

C. Suppose Q_0 is on the boundary Lamé, then the points *2 and *3 coincide, giving neither minimum nor maximum, leaving the unrealistic point *1 to be the only minimum solution. This case is again same as case A.

In making the foregoing comparison, the concept of constant velocity-increment introduced in Section 15.2 is helpful. It is to be noted that while such lines are curves parallel to the constraining hyperbola in the realistic region, they are concentric circles centered at the reference critical point in the unrealistic region, since in this latter region the velocity increment at the critical point is the standard for comparison. The point in the unrealistic region at which

$$|\Delta v|_3 = |\Delta v|^*$$

is then given by the intersection of such a circle with one of the parallel curves of the same constant $|\Delta v|$ as illustrated in Figure III-9. Of course only these intersections within the nonsimple region

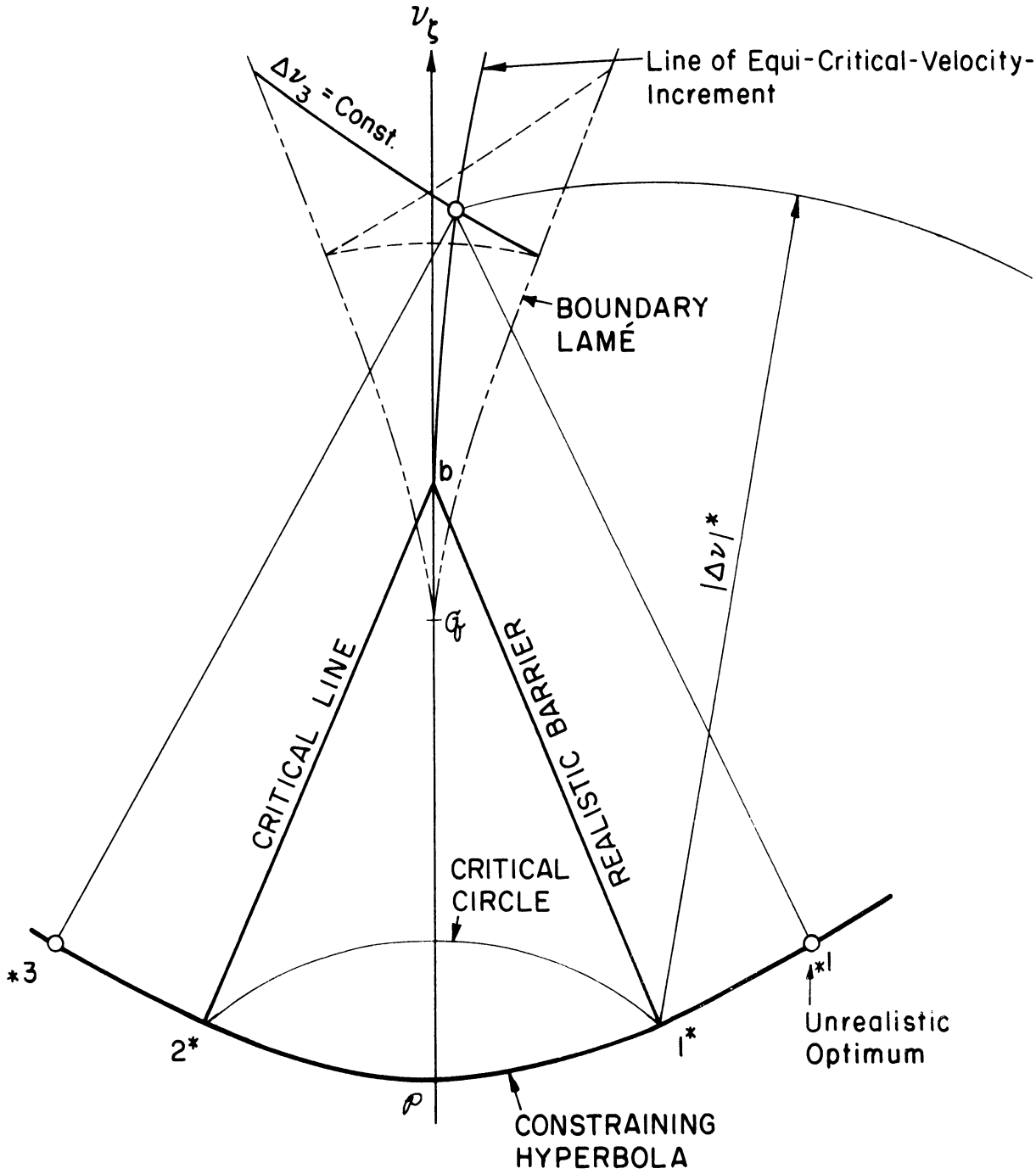

Figure III-9. Determination of the Boundary Point, $|\Delta v|_3 = |\Delta v|^*$

are of interest at present. The locus of all such points of intersections in the unrealistic region will be called the line of equi-critical-velocity-increment (E-C-V-I line for short), and there is one such line on either side of the $v\chi$-axis. As shown in Figure III-7 these two lines further divide the unrealistic region into the following subregions: the one bounded by each E-C-V-I line and the $v\zeta$-axis is the one in which we have $|\Delta v_3| < |\Delta v|^*$ and therefore the realistic optimum solution is definite and unique; and the one bounded between these two lines is the subregion in which either $|\Delta v_3| > |\Delta v|^*$ or Δv_3 does not exist, therefore the realistic optimum solution of the problem is indefinite. On the boundary $|\Delta v_3| = |\Delta v|^*$ the realistic optimum solution is also definite and unique. The latter region falls entirely within the non-simple region of course. From the geometry of the hodograph it can be inferred that, whenever a definite realistic optimum solution exists while the tip Q_o of the initial velocity vector is in the unrealistic region the optimum transfer trajectory will always be hyperbolic of the low class, since each E-C-V-I line terminates at the corners b and b' of the elliptic region respectively.

The foregoing analysis completes the discussion on the selection of the realistic optimum transfer trajectory for the problem. All the previous conclusions on such selections are summarized in Table III-5.

15.5 Effects of the Initial Velocity Vector on the Optimum Solution: Summary of Findings

As seen from the preceding analyses the optimum solution for the problem is determined by the geometry of the base triangle and the initial velocity vector. Based on the previous findings the effects of

TABLE III-5

REGIONS IN THE HODOGRAPH PLANE AND THE NATURE OF THE OPTIMUM TRANSFER TRAJECTORIES

Region				Number of Realistic Optimum Solutions	Nature of the Realistic Optimum Transfer Trajectory
Name	Designation	Description	Subregion		
Elliptic Region	(E)	Within the rhomboid aba'b'	Off v_x, v_ζ -axes	1	Elliptic
			On v_x-axis: between a and a'	2	Elliptic, complementary-conjugate pair
			On v_ζ-axis: between and at $\mathcal{Y}$ and $\mathcal{Y}'$	1	Elliptic, minimum energy
			On v_ζ-axis: between $\mathcal{Y}$ and b or $\mathcal{Y}'$ and b'	2	Elliptic, conjugate pair
Critical Line	b-a'-b'	Including end points b and b'		1	Parabolic
Hyperbolic Region	(H)	On the low side of the line b-a'-b' and the v_ζ-axis	Off v_x, v_ζ -axes	1	Hyperbolic
			On v_x-axis: beyond a'	2	Hyperbolic, complimentary-conjugate pair
Realistic Barrier	v_ζ-axis	Beyond b or b'		1	Hyperbolic
	Line b'-a-b	Excluding end points b and b'		Indefinite	Elliptic, highly eccentric, close to the unrealistic parabolic trajectory
Unrealistic Region	(U)	On the high side of the line b'-a-b and the v_ζ-axis	Between the two lines of equi-critical-velocity-increment (U_1)	Indefinite	Elliptic, highly eccentric, close to the unrealistic parabolic trajectory
			Between the v_ζ-axis and each line of equi-critical-velocity-increment (U_{2+}, U_{2-})	1	Hyperbolic

the initial velocity vector on the optimum solution for a given base triangle may be summarized as follows:

(1) Corresponding to every initial velocity vector $\vec{V}_o$ there exists at least one definite realistic optimum trajectory for the problem provided by the orthogonality quartic unless the tip of $\vec{V}_o$ exceeds the realistic barrier in the hodograph plane. Such a barrier is analytically defined by Equation (15.1, 4).

(2) If such a limit is not exceeded, the initial velocity vector is said to be in the realistic region, then the realistic optimem solution is unique whenever $\vec{V}_o$ is not directed along the bisector of either the interior or the exterior base angle at the initial terminal.

If this is the case, then the optimum trajectory will be of the same group and same class with the initial velocity vector $\vec{V}_o$. However, the type of the trajectory, whether elliptic, parabolic, or hyperbolic, does not necessarily agree with that of V_o, but is determined by the particular region in the hodograph plane in which its tip Q_o lies (see Table III-5 and Figure III-7).

(3) In a realistic region, if $\vec{V}_o$ is directed along the interior base angle bisector, then there are two optimum solutions for the problem, corresponding to a complementary-conjugate pair of trajectories of the same class with the initial velocity vector, and of the same type which is determined by the region in which the tip Q_o lies.

(4) The minimum energy direction of departure is along the exterior base angle bisector. If V_o is directed along this direction, then the optimum solution may be unique or not, depending on the

magnitude of V_o or the location of its tip, Q_o. Consider $\vec{V}_o$ in the positive half of the hodograph plane (the half-plane above the ν_χ-axis, see Figure III-7):

(a) When Q_o moves from the origin up to the cusp G of the boundary Lamè along the minimum energy direction such that $0 < V_o < V_G$ (where V_G is given by Equation (14.24)), the optimum solution is unique, the trajectory is elliptic, and of minimum energy, and the velocity-increment vector is to be directed along the minimum energy axis.

(b) When Q_o moves between the cusp G and the point b, where the boundary of the elliptic region meets the minimum energy axis such that $V_G < V_o < V_b$ (where V_b is given by Equation (15.15)), then there are two optimum solutions for the problem corresponding to a conjugate pair of trajectories of the same group with the initial velocity vector. They are both elliptic, but no longer of minimum energy, and the optimum directions for the velocity-increment vector deviate from the minimum energy direction with equal inclinations on either side of it even though the initial velocity vector is along that direction.

(c) When Q_o moves further along the minimum energy direction such that $V_o \geq V_b$ the realistic optimum is again unique. Like case (b) the optimum ΔV is no longer in the minimum energy direction, and the trajectory is no longer the minimum energy one. It is parabolic when $V_o = V_b$, and hyperbolic when $V_o > V_b$.

Situations similar to the foregoing three cases (a) to (c) exist when $\vec{V}_o$ is in the other half plane.

(5) Different initial velocity vectors may call for the same optimum transfer trajectory. This statement is necessarily true when

these velocity vectors all lie on the same normal line in the same quadrant in the realistic region.

(6) Similarly, different initial velocity vectors may call for the same amount of velocity increment. This statement is necessarily true when these velocity vectors all lie in the realistic region and on the curve parallel to the constraining hyperbola with the same common distance on either side of it.

(7) No unrealistic optimum will arise when the initial velocity is directed below the minimum energy direction regardless of its magnitude, or when its magnitude is below the lower critical limit $(V_o^*)_{LL}$ (given by Equation (15.16)) regardless of its direction.

(8) When the tip Q_o of the initial velocity vector exceeds the realistic barrier, it is said to be in the unrealistic region. In such a region a definite realistic optimum solution can be found only when Q_o is inside or on the boundary of the strip bounded by the v_ζ-axis and the line of equi-critical-velocity-increment (see Figure III-7). In such a subregion the realistic optimum trajectory is hyperbolic of the same group with the initial velocity vector, but of the low class. Outside this subregion no definite optimum solution can be found. The possible choice will be an elliptic one, of high eccentricity, close to the unrealistic parabolic trajectory given by the critical point or points nearer to Q_o .

16. HODOGRAPHIC REPRESENTATION OF THE TWO-DIMENSIONAL OPTIMUM TRANSFER

16.1 The Orthogonal Net in the Hodograph Plane and the Optimization Chart

As seen from the previous analysis the normal lines to the constraining hyperbola and its parallel curves form an orthogonal net in the hodograph plane. Such a net may be looked upon as the curvilinear coordinates of the initial velocity vector, and it forms naturally the basis for the development of the optimization chart for the present problem. A typical example of such a chart is shown in Figure III-10, which is constructed for the case of $\psi = 60°$ and $\varphi_1 = 75°$ corresponding to a transfer distance ratio of $n = 1.366$. As soon as the tip Q_o of the initial velocity vector is located on the chart, the optimum velocity increment vector and the optimum departure velocity vector can be readily determined by noting the normal line and the parallel curve passing through this initial point Q_o. In case an unrealistic optimum arises it can be seen at once from the chart, and in such a case a realistic optimum solution may also be obtained directly from the chart by noting the sub-region(U_1 or U_2 in Figure III-10) in which the point Q_o is located, and the rules given in Section 15.4. The type of the optimum transfer trajectory, elliptic, parabolic, or hyperbolic, will be indicated by the region in which the selected optimum point lies. To illustrate the use of this chart an example is given below:

Consider a transfer from an initially circular orbit to a target point in space at a distance ratio of $r_2 = 1.366\, r_1$, and with an angle of separation of 60°. By locating the initial point on the $v_{\theta 1}$-axis at $v_o = 1$, we find the optimum solution from the chart (Figure III-10) approximately as follows:

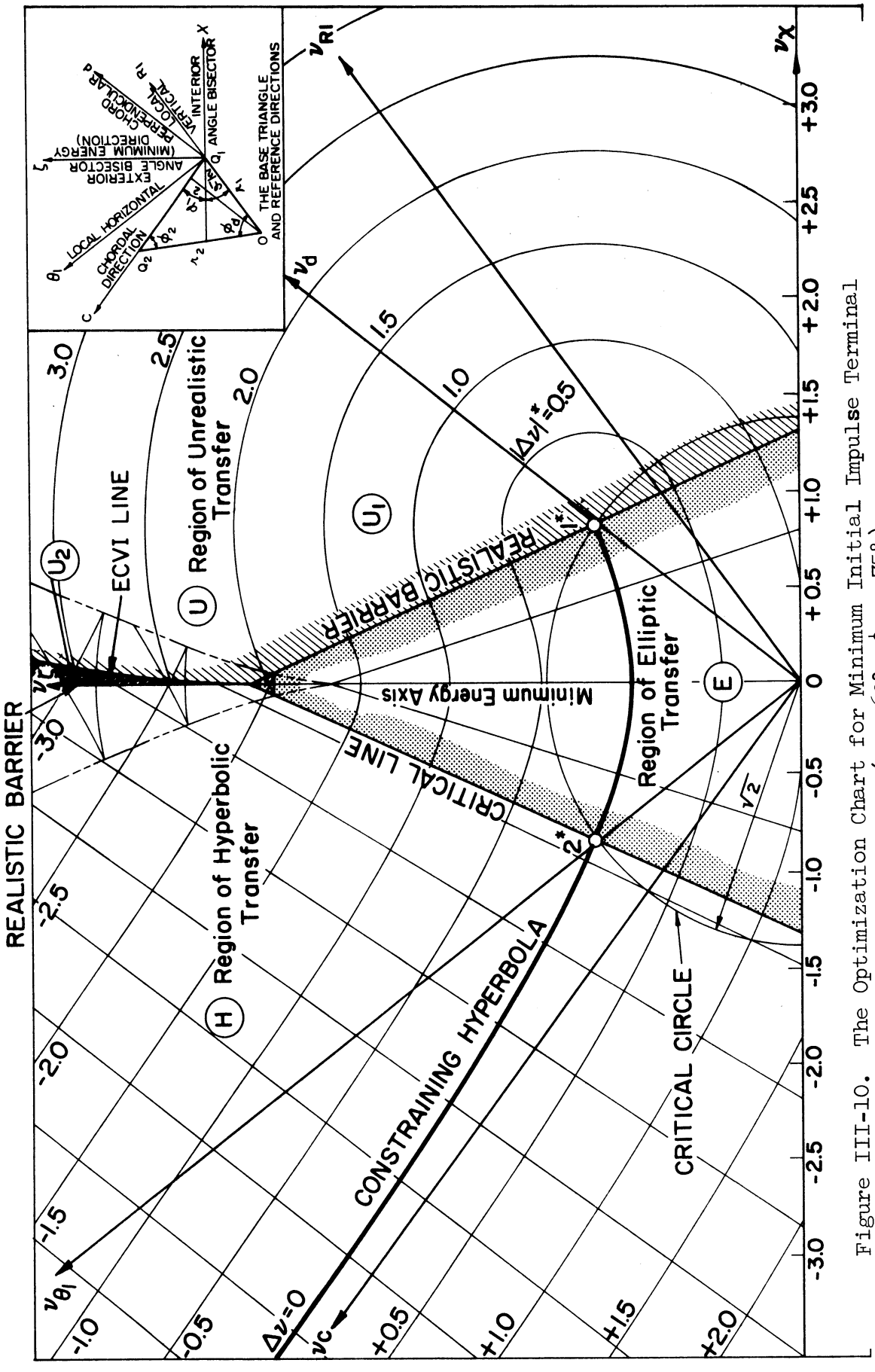

Figure III-10. The Optimization Chart for Minimum Initial Impulse Terminal to-Terminal Transfer ($\psi = 60°$, $\phi_1 = 75°$)

Velocity-increment $\Delta v = 0.26$ @ $\phi_\Delta = 54.5°$

Departure velocity $v = 1.16$ @ $\Phi = 10°$

The transfer trajectory is elliptic.

While such a chart yields immediately the optimum solution corresponding to a specified initial velocity vector, it does not give directly the principal elements of the transfer trajectory except its type. For such information the hodograph circle for the transfer trajectory should be constructed, and it will be presented in the next section. Finally it is to be noted that although such a chart is constructed on the basis of a hyperbolic constraint, it may well be applied when the departure velocity is constrained not on this hyperbola, but on any one of its parallel curves, since all of them have common normals and the same Lamé as their involute. The only change necessary is to shift the datum curve, on which $\Delta v = 0$, from the hyperbola to the new constraining curve and to make corresponding adjustment on the constant value of Δv on each of the parallel curves. Graphical techniques on the extensive use of such optimization charts, however, will not be elaborated here.

16.2 The Construction of the Transfer Hodograph

With the optimum departure velocity vector determined analytically or graphically, the hodograph for the transfer trajectory may be constructed by using the terminal relations given in Section 9.1 or Part II,

$$\vec{V}_{C1} = \vec{V}_{C2}\ ,\quad V_{R1} = V_{R2} \tag{9.3}$$

from which we see that once the hodograph image of the initial terminal Q_1 is determined, so is that of the final terminal Q_2. In fact the point Q_2 in the hodograph plane is also constrained on a hyperbola defined by

$$V_C V_R = -K \tag{16.1}$$

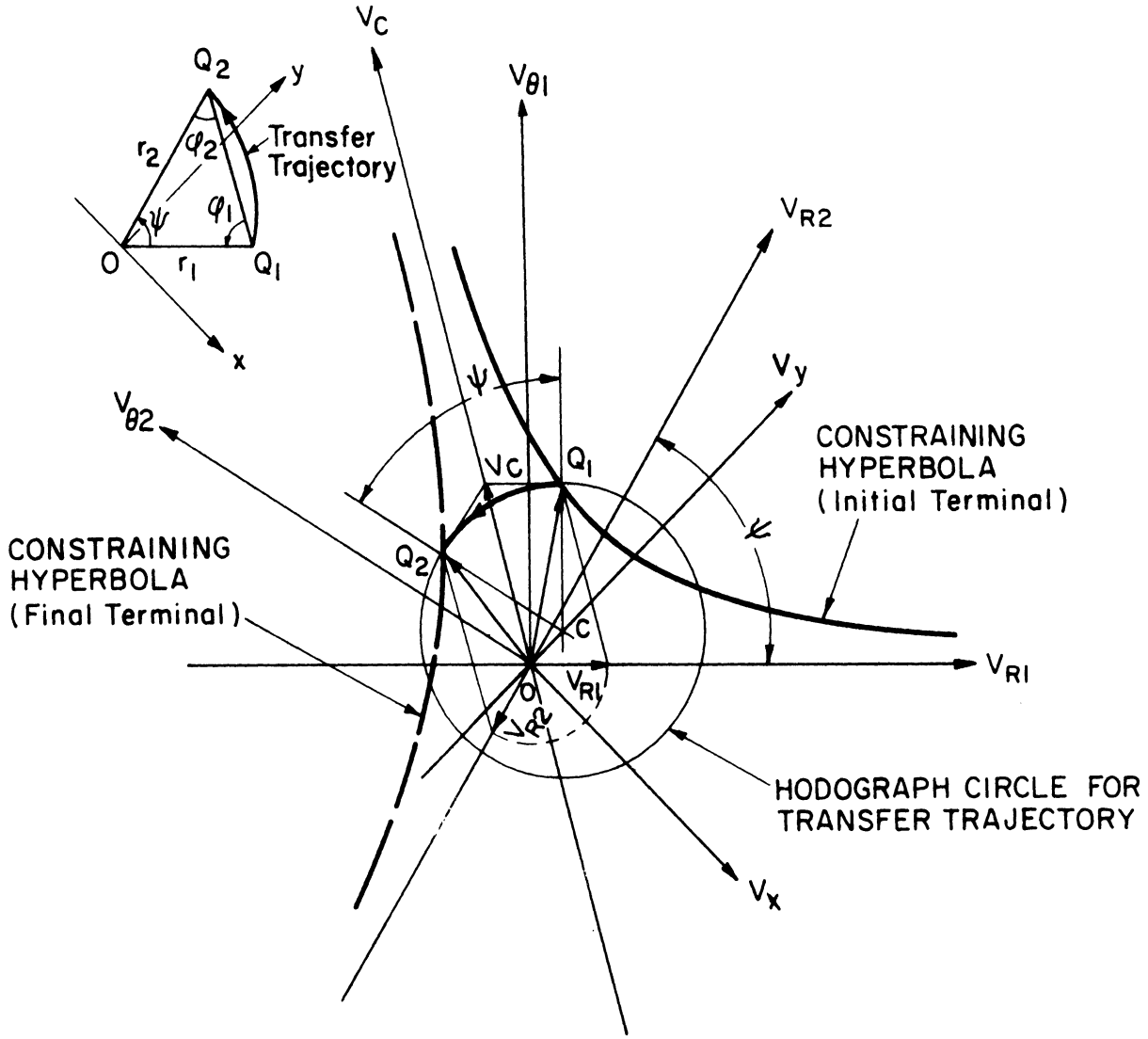

Figure III-11. Construction of the Transfer Hodograph in the $\vec{V}$-Plane

which is Godal's compatibility condition applied at the second terminal, the negative sign here signifies the fact that the vector $\vec{V}_{R2}$ is directed in the negative direction of the local vertical at Q_2 (see Figure II-4). However, the construction of this second constraint is not necessary since following Equation (9.3), the point Q_2 may be easily located in the hodograph plane by completing the two velocity parallelograms with the common side V_C and the other sides of equal length V_R lying along the directions of $\vec{r}_1$ and $\vec{r}_2$ respectively as shown in Figure III-11. With the two terminals on the transfer hodograph thus determined, the next step is to locate the center of the hodograph circle. According to the general correlation established in Section 3.1 of Part I this center must lie on the local horizontal line at each terminal. Thus by drawing the lines perpendicular to the local radial directions at Q_1 and Q_2 respectively we find their intersection at C, and by using C as center the hodograph circle can be drawn to pass through the points Q_1 and Q_2.[16.1] This completes the construction, and the circular arc between the points Q_1 and Q_2 extending a central angle ψ represents the transfer trajectory. The principal geometric as well as kinematic elements of the trajectory can then be determined from the hodograph according to the correlations given in Chapter 3.

16.3 The Hodograph of Optimum Transfer Trajectories in the $\vec{v}$ -Plane.

So far the analysis has been made exclusively in the $\vec{v}$ -plane. Such a hodograph, though nondimensionalized, is essentially different from the dimensionless hodograph in the $\vec{v}$ -plane introduced in Section 5.1.

16.1 Note here the vector $\vec{V}_2 - \vec{V}_1$ is in the direction of the bisector of the vertex angle ψ in the physical plane, see Section 4.1 of Part I.

To distinguish the two we will call them the $\vec{\nu}$ -hodograph and the $\vec{v}$ -hodograph respectively according to their planes. In a $\vec{\nu}$ -plane the velocity is nondimensionalized by dividing through by the circular speed at a fixed point, which is a constant in the problem. Thus the $\vec{\nu}$ -hodograph is in fact the same as the hodograph in the usual $\vec{V}$ -plane, except for the scale of plotting. However, in the $\vec{v}$ -plane the velocity is being divided through by the parameter μ/h which varies from one trajectory to another. Such a nondimensionalization has the advantage of reducing the hodograph of all Keplerian orbits into a unit circle, and it has been the basis for the analysis in Part II. Having made the analysis and representation of the present problem in the $\vec{\nu}$ -plane, it is appropriate to introduce here the hodographic representation of the same optimum solution of the problem in the $\vec{v}$ -plane.

According to Section 8.2, the locus of the hodograph origins in the $\vec{v}$ -plane is a straight line for all two-terminal trajectories of the same group. Thus, as pointed in Section 14.2, the two straight lines parallel to the chord of the base triangle shown in Figure II-1 are comparable to the two branches of the constraining hyperbola in the $\vec{\nu}$ -plane, one for each group. Thus while the tip of the departure velocity vector is constrained on the two branches of the hyperbola in the $\vec{\nu}$ -plane, the origin of the transfer hodograph is confined on these two straight lines in the $\vec{v}$ -plane. The portions of such a line on which the trajectories are high or low, realistic or unrealistic have been given in Section 8.3 (see Table II-1).

Consider a normal group. Let O be an arbitrary point on the straight line locus, and ρ its distance from the radical center T as shown in Figure III-12. Then by definition

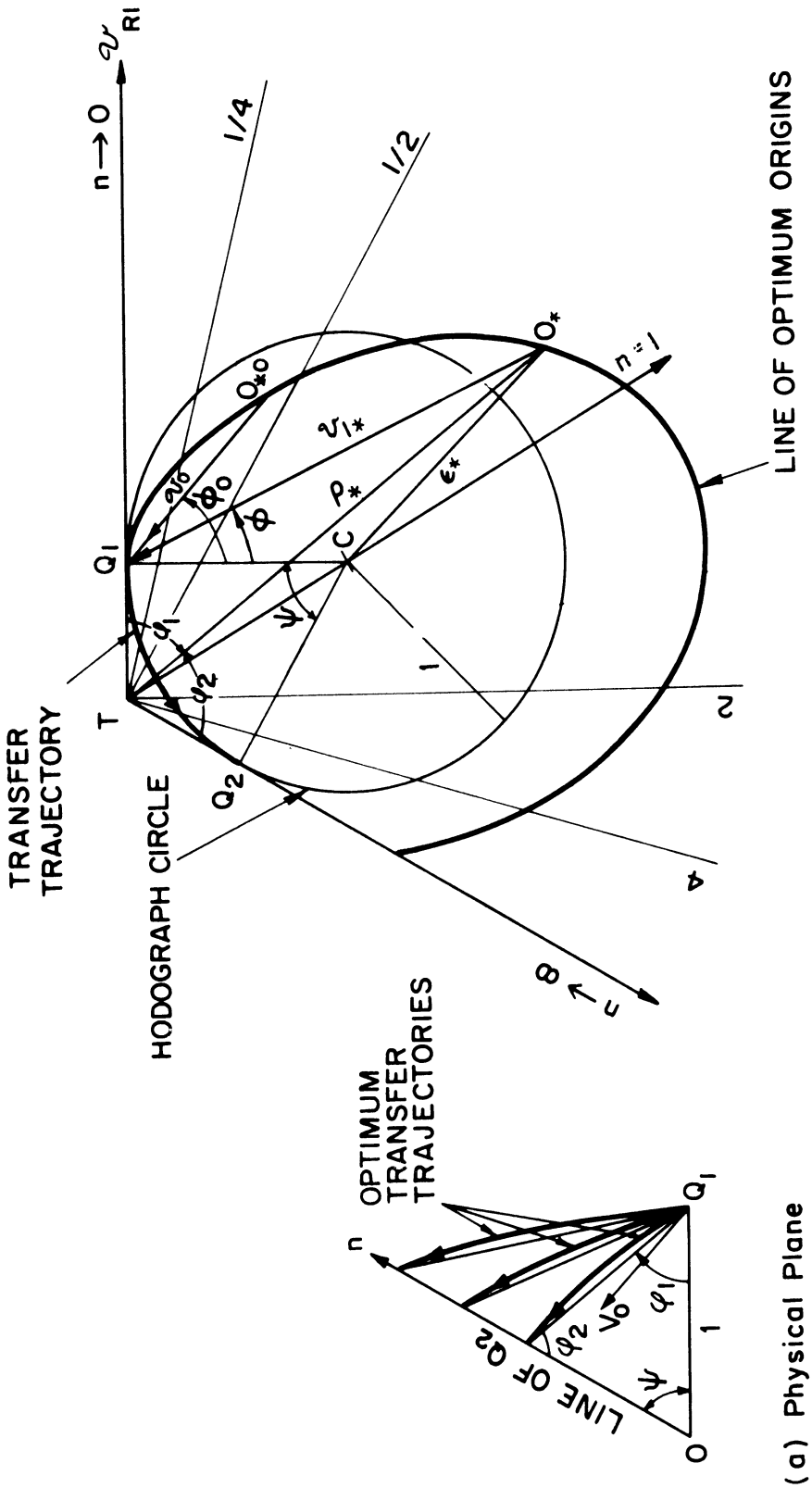

Figure III-12. Hodograph of Optimum Transfer Trajectories in the $\vec{v}$-Plane (ψ = Const.)

$$\rho = \frac{h}{\mu} V_C \tag{16.2}$$

Comparing this with the definition of ν given by Equation (14.11), and noting here,

$$h = V_C\, d = V_C\, r_1 \sin \varphi_1 \tag{16.3}$$

we find the relation

$$\rho = \nu_C^2 \sin \varphi_1 \tag{16.4}$$

Thus corresponding to each optimum value of ν_{C*} for a given base triangle and a given initial velocity vector there is a unique value of ρ_*, from which the origin $O*$ of the optimum transfer hodograph is determined. Such an origin will be called the optimum origin for the present problem, and the locus of such origins in the $\vec{v}$-plane, the line of optimum origins, or simply the $O*$-locus. A typical example of such a locus for a constant vertex angle ψ is shown in Figure III-12(b). By substituting Equation (16.4) into the orthogonality equation (14.10-C) we find the ρ_*-equation

$$(\rho_*^2 - \tan^2 \tfrac{\psi}{2})^2 = \rho_* \sin \varphi_1 \,(n_o \rho_* - m_o \tan \tfrac{\psi}{2})^2 \tag{16.5}$$

where m_o and n_o are given by

$$\begin{aligned} m_o &= \nu_o \sin \phi_o \\ n_o &= \nu_o \sin (\varphi_1 - \phi_o) \end{aligned} \tag{16.6}$$

according to Equations (14.20) and (14.21). For constant ψ such an equation may be looked upon as the polar equation of the ρ_*-vector with the angle φ_1 as the polar angle, and the directed tangent line $T Q_1$, its polar axis. It represents the $O*$-locus whenever the orthogonality Equation (14.10) yields a realistic optimum solution. Some essential featrues of the ρ_*-curves

are to be noted as follows:

(1) It is bounded between the two tangent lines at Q_1 and Q_2 on the hodograph circle since for a given vertex angle ψ the angle φ_1 can only vary between 0 and $\pi-\psi$.

(2) For a constant ψ each value of the angle φ_1 corresponds to a unique value of the distance ratio n. Thus the radial lines drawn from the radical center T are also the lines of constant n.

(3) The point Q_1 lies on the ρ_*-curve since the ρ_*-equation (16.5) is satisfied by $\varphi_1 = 0$ and $\rho_* = \tan\frac{\psi}{2}$ there[16.2].

(4) The origin of the initial orbit as given by the initial velocity vector $\vec{v}_o$ in the $\vec{v}$-plane lies on the ρ_*-curve, as its coordinates also satisfy the ρ_*-equation (16.5). The corresponding value of φ_1 and n at this point give the configuration of the base triangle such that the initial orbit passes through the final terminal Q_2, and thus itself may be regarded as the optimum transfer trajectory.

(5) The point where the ρ_*-curve intersects the hodograph circle is the critical point, and the portion of the curve beyond it is hyperbolic.

(6) From the critical point beyond, the ρ_*-curve will be unrealistic (corresponding to unrealistic optimum trajectories) if it is on the high side, otherwise it is realistic.

(7) When the ρ_*-curve is unrealistic, it ceases to represent the O_*-locus, and should be replaced by the arc of the hodograph circle from that point beyond, or modified according to its corresponding realistic

---

16.2 This is true only when r_1 is finite. The behavior of the ρ_*-curve when $\varphi_1 \to 0$ and $r_1 \to \infty$ will be discussed in Section 17.4.

optimum value of v_{C*} .

(8) The point where the O_* -locus meets the bounding line $T Q_2$ gives the optimum transfer trajectory from Q_1 to infinity. Such a transfer will be further discussed in Section 17.3.

Finally it is to be noted that the orthogonality principle does not directly apply in a $\vec{v}$ -plane since the initial orbit or velocity and the trajectory to be optimized are not represented by the same scale there. However, it has the advantage over the $\vec{\nu}$ - or $\vec{V}$ -hodograph in that it shows the totality of the optimum transfer trajectories for all possible configurations of the base triangle (given by the variable φ_1 or n) under a given vertex angle ψ and a prescribed initial velocity vector (see Figure III-12(a)). Furthermore, unlike the $\vec{\nu}$ -plane where a hodograph circle is to be drawn for each transfer trajectory, the $\vec{v}$ -hodograph enables one to use the same arc of the unit circle for all transfer trajectories between the fixed terminal points Q_1 and Q_2 , and from which all the principal geometrical as well as the kinematic elements of the transfer trajectory associated with a particular optimum origin can be readily determined according to the correlations presented in Chapters 3 and 5.

All the foregoing features are also true for the ρ_* -curve or the O_* -locus of the complementary group. Such a hodographic representation can be easily obtained by turning the corresponding hodograph for the normal group through 180° according to Section 8.2.

17. ANALYSIS OF SOME PARTICULAR CASES

So far the analysis has been restricted to $0 < \psi < \pi$, and r_1 and r_2 both considered finite. An examination of each of these extreme cases is now in order.

17.1 The Case $\psi = 0$

Physically this case corresponds to a vertical descent if $r_1 > r_2$ and a vertical ascent if $r_1 < r_2$. In either case the base triangle OQ_1Q_2 degenerates into a line segment with Q_1 and Q_2 on the same side of 0. The geometry in the physical plane and that in the hodograph plane for each case are shown in Figure III-13. The constraining hyperbola also degenerates in each case, and its principal elements are as follows:

	$r_1 > r_2$ $(n < 1)$	$r_1 < r_2$ $(n > 1)$
σ	π	0
A	0	$\sqrt{2(1 - \frac{1}{n})}$
B	$\sqrt{2(\frac{1}{n} - 1)}$	0
e	∞	1,

(17.1)

(a) Vertical Descent: $r_1 > r_2$ $(n < 1)$

The degenerate constraining hyperbola is a straight line parallel to the line OQ_1Q_2 in the physical plane. Consequently all normal lines are parallel to the local horizontal at Q_1 and Q_2, the orthogonal net

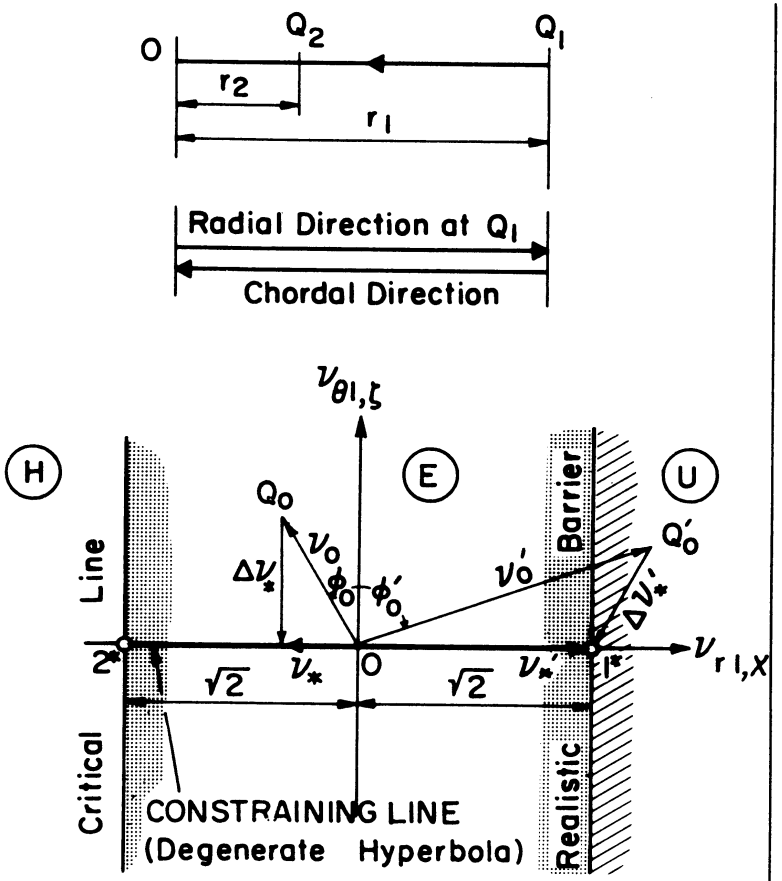

(a) $r_1 > r_2$ $(n>1)$

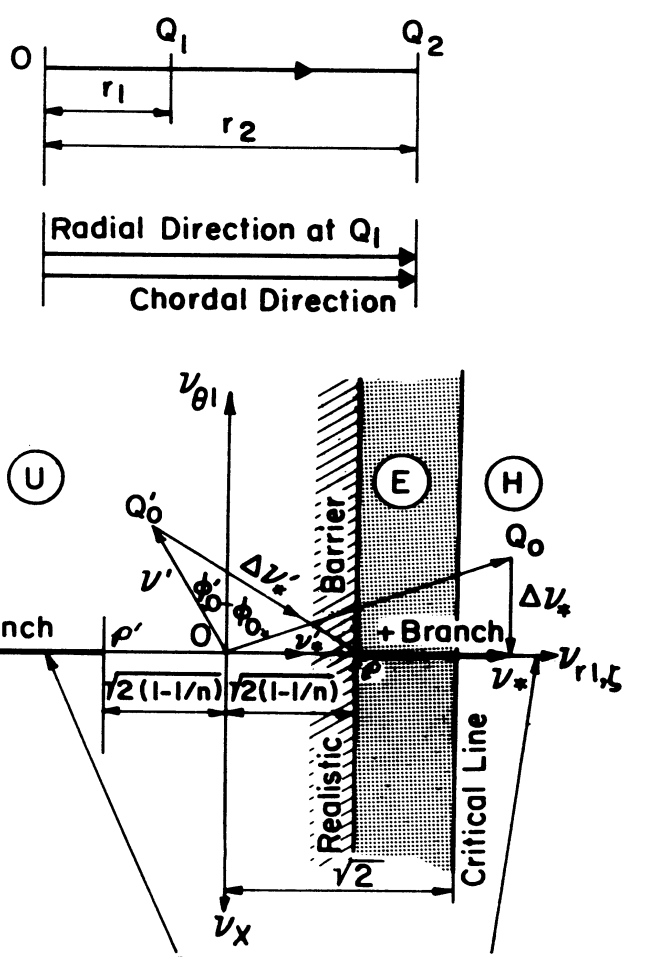

(b) $r_1 < r_2$ $(n>1)$

Figure III-13. Optimization of Vertical Transfer ($\psi = 0$)

becomes rectangular, and the transfer trajectory is a vertical straight line. The entire hodograph plane is divided into three main regions as usual: the hyperbolic region on the low side, the unrealistic region on the high side, and the elliptic region between them. However, it is to be noted that the usual closed elliptic region is now open since its sides are parallel. Furthermore, as a straight line trajectory is identical to its conjugate, as well as its complementary-conjugate, the optimum solution is unique everywhere in the realistic region even on the v_{r1},χ-axis.

The optimum solution of the problem is very simple in this particular case. As seen from the hodograph (Figure III-13) Q_o is in the realistic region whenever

$$v_o \sin \phi_o < \sqrt{2} \qquad (17.2\text{-}1a)$$

and the geometry of the hodograph gives readily the solution summarized in Table III-6, column a. As seen from the hodograph the optimum velocity-increment vector in this region is everywhere in the local horizontal direction. It is simply to nullify the horizontal component of the initial velocity if any - a fact which is evident from physical considerations. However, whenever

$$v_o \sin \phi_o \geq \sqrt{2} \qquad (17.2\text{-}2a)$$

Q_o is in the unrealistic region, the point on the v_{r1}-axis close to the critical point 1* but inside the elliptic region has to be chosen as discussed in Section 15.4. No second choice is possible at present since no evolute exists for a straight line and the hodograph plane is simple everywhere. Consequently, the optimum velocity increment vector is no longer in the normal direction, and in addition to nullifying the

TABLE III-6

OPTIMUM SOLUTIONS FOR VERTICAL TRANSFER ($\psi = 0$)

		(a)	(b)
		$r_1 < r_2$ $(n > 1)$ Vertical Descent	$r_1 > r_2$ $(n < 1)$ Vertical Ascent
REALISTIC REGION	Condition on v_o	$v_o \sin \phi_o < \sqrt{2}$ (17.2-1a)	$v_o \sin \phi_o \geq \sqrt{2(1 - \frac{1}{n})}$ (17.2-1b)
	<u>Velocity-Increment</u>		
	r-component $(\Delta v_r)_{opt.}$	$-v_o \cos \phi_o$	(17.3-1)
	θ-component $(\Delta v_\theta)_{opt.}$	0	
	<u>Departure Velocity</u>		
	r-component $(v_r)_{opt.}$	$v_o \sin \phi_o$	(17.4-1)
	θ-component $(v_\theta)_{opt.}$	0	
UNREALISTIC REGION	Condition on v_o	$v_o \sin \phi_o \geq \sqrt{2}$ (17.2-2a)	$v_o \sin \phi_o < \sqrt{2(1 - \frac{1}{n})}$ (17.2-2b)
	<u>Velocity-Increment</u> $(\Delta v)_{opt.}$	$\cong \Delta v^*$	$\cong (\Delta v)_P$
	r-component $(\Delta v_r)_{opt.}$	$\cong \sqrt{2} - v_o \sin \phi_o$ (17.3-2a)	$\cong \sqrt{2(1 - \frac{1}{n})} - v_o \sin \phi_o$ (17.3-2b)
	θ-component $(\Delta v_\theta)_{opt.}$	$- v_o \cos \phi_o$	$- v_o \cos \phi_o$
	<u>Departure Velocity</u>		
	r-component $(v_r)_{opt}$	$\cong \sqrt{2}$ (17.4-2a)	$\cong \sqrt{2(1 - \frac{1}{n})}$ (17.4-2b)
	θ-component $(v_\theta)_{opt.}$	0	0

horizontal component of the initial velocity, it has a vertical component opposed to that of the initial velocity so as to keep the resultant velocity below that for escape. The optimum solution in this case is indefinite, and, as seen from the geometry in the hodograph plane it may be written approximately as summarized in Table III-6, column b.

(b) Vertical Ascent: $r_1 < r_2$ $(n > 1)$

This case looks similar to the previous one, but there are some radical differences: 1) the constraining hyperbola degenerates into two semi-infinite lines along the radial axis instead of a single line as in case (a); and between the vertices $\mathcal{P}$ and $\mathcal{P}'$ of these two branches of the velocity constraint, there is a gap of length 2A where no normal lines to the constraint line can be drawn, and consequently the orthogonality principle cannot apply there; 2) trajectories of the complementary group are out of the question since in such a transfer all physically realistic trajectories must go in one direction only, that is, from Q_1 to Q_2 not through O. Thus the negative portion of the degenerate constraining hyperbola is meaningless. Consequently the straight line normal to the positive branch of the constraining line at its vertex $\mathcal{P}$ forms a realistic barrier instead of the usual critical line.[17.1] The geometry of the hodograph plane and various regions are shown in Figure III-13(b).

17.1 Note here in the region between the horizontal lines through $\mathcal{P}$ and $\mathcal{P}'$ there exists no optimum solution, realistic or unrealistic, and in the region to the left of the horizontal line through $\mathcal{P}'$ (not shown in Figure III-13) the unrealistic solution consists of elliptic trajectories in addition to the hyperbolic ones as encountered in the case of $\psi \neq 0$, owing to the consideration 2).

As seen from the hodograph, whenever

$$v_o \sin \phi_o \geq A \tag{17.2-1b}$$

Q_o is in the realistic region, the solution is definite and unique, and formulas are identical to those for case (a) in Table III-6. Whenever

$$v_o \sin \phi_o < A \tag{17.2-2b}$$

Q_o is in the unrealistic region, the orthogonality principle no longer applies. In such a case the vertex $\mathcal{P}$ should be chosen as the optimum point, giving

$$v_{opt.} = A = \sqrt{2(1 - \frac{1}{n})} \tag{17.4-2b}$$

which is the minimum departure velocity for such a transfer (see item (2) on the "Constraining Hyperbola", Section 14.2). Formulas for this optimum solution are summarized in Table III-6, column b.

17.2 The Case $\psi = \pi$

This case is of practical importance, and an analysis of all possible trajectories for such 180° transfers has been presented in Chapter 11, Part II. Like the previous case the base triangle degenerates again into a line segment but with the two terminal points on the opposite sides of O. The elements of the constraining hyperbola have the following limiting values according to Equations (14.12) to (14.16), Table III-2:

$$\begin{aligned} \sigma &\rightarrow \pi \\ A &\rightarrow \sqrt{\frac{2n}{n+1}} \\ B &\rightarrow \infty \\ e &\rightarrow \infty \end{aligned} \tag{17.5}$$

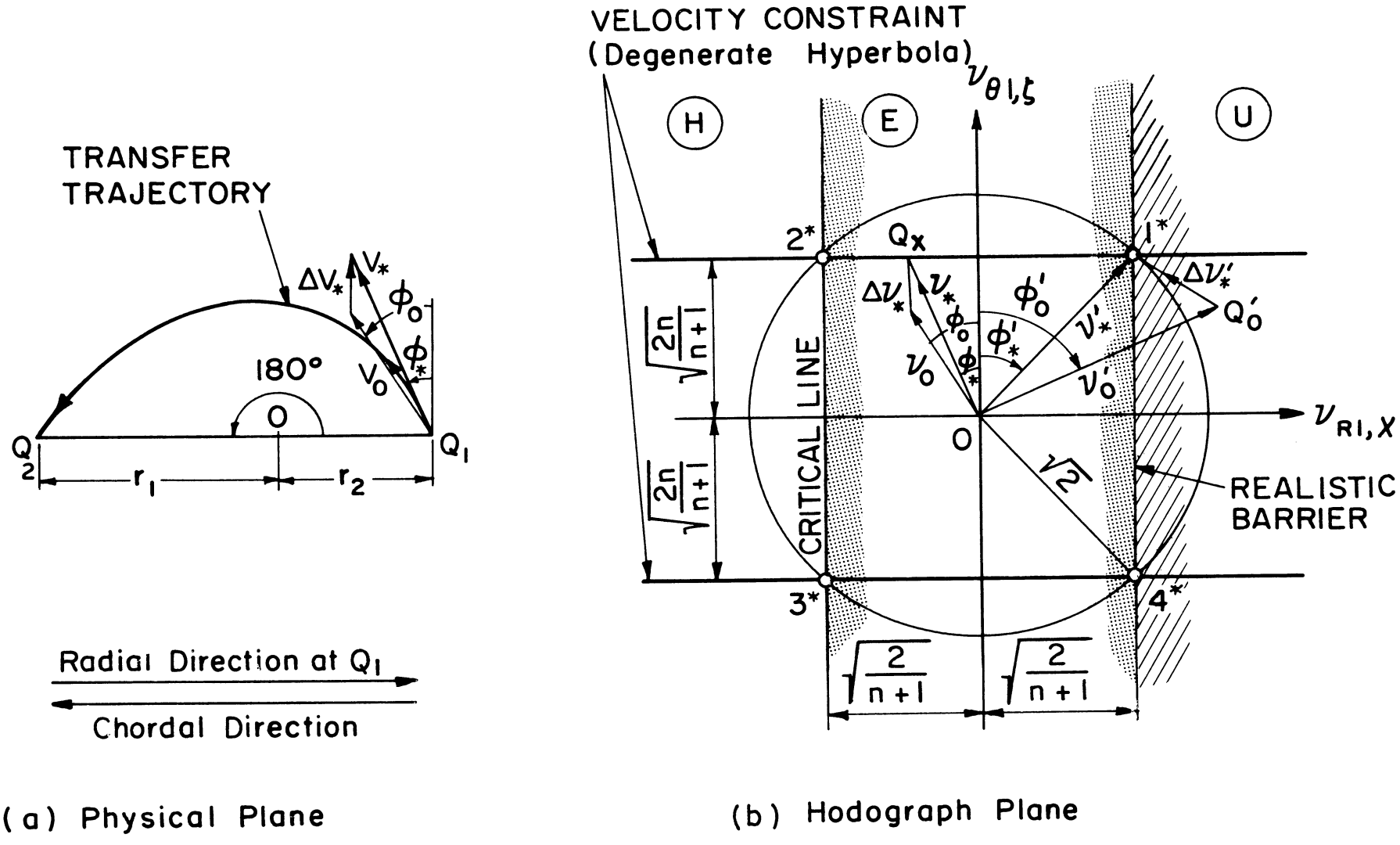

Figure III-14. Optimization of 180° Transfer ($\psi = \pi$)

Thus the constraining hyperbola degenerates into two straight lines parallel to the v_{r1}-axis at the distance $\pm A$. Consequently, all normal lines are again in the horizontal direction everywhere in the hodograph plane, the orthogonal net is again rectangular, and the plane is divided into the three regions, elliptic, hyperbolic, and unrealistic, by the two critical lines just as in the case $\psi = 0$, and $r_1 > r_2$. With the absence of the boundary Lamé the entire hodograph is again simple, and a definite and unique optimum solution exists everywhere in the realistic region except on the v_{r1}-axis along which a complementary-conjugate pair of optimum solutions exist. The geometry in the physical plane and that in the hodograph plane are shown in Figure III-14.

As seen from the hodograph, Q_o is in the realistic region whenever

$$v_o \sin \phi_o < \sqrt{\frac{2}{n+1}} \qquad (17.6\text{-}1)$$

and in this region the optimum direction of Δv is horizontal everywhere. The optimum solution can be readily obtained from the geometry of the hodograph, and is summarized in Table III-7, column 1.

Whenever

$$v_o \sin \phi_o \geq \sqrt{\frac{2}{n+1}} \qquad (17.6\text{-}2)$$

Q_o is in the unrealistic region. Since no non-simple region exists, the only choice for the optimum is then the one close to the nearer critical point, 1* or 4*, and remains in the elliptic region. The optimum solution is again indefinite, and may be written approximately as summarized in Table III-7, column 2.

TABLE III-7

OPTIMUM SOLUTIONS FOR 180° TRANSFER ($\psi = \pi$)

	(1) Realistic Region	(2) Unrealistic Region
Condition on $\vec{v}_o$	$v_o \sin\phi_o < \sqrt{\frac{2}{n+1}}$ (17.6-1)	$v_o \sin\phi_o \geq \sqrt{\frac{2}{n+1}}$ (17.6-2)
Velocity-Increment $(\Delta\vec{v})_{opt.}$		$\cong \Delta\vec{v}^*$
r-component $(\Delta v_r)_{opt.}$	0	$\cong \sqrt{\frac{2}{n+1}} - v_o \sin\phi_o$ (17.7-2)
θ-component $(\Delta v_\theta)_{opt.}$	$\pm \sqrt{\frac{2n}{n+1}} - v_o \cos\phi_o$ (17.7-1)	$\pm \sqrt{\frac{2n}{n+1}} - v_o \cos\phi_o$
Departure Velocity $(\vec{v})_{opt.}$		$\cong \vec{v}^*$ $(v^* = \sqrt{2})$
r-component $(v_r)_{opt.}$	$v_o \sin\phi_o$	$\cong \sqrt{\frac{2}{n+1}}$
θ-component $(v_\theta)_{opt.}$	$\pm \sqrt{\frac{2n}{n+1}}$ (17.8-1)	$\pm \sqrt{\frac{2n}{n+1}}$ (17.8-2)

NOTE: For the double sign: take the upper sign when $(v_\theta)_o > 0$ $(|\phi_o| < \frac{\pi}{2})$ (1 solution)

take the lower sign when $(v_\theta)_o < 0$ $(|\phi_o| > \frac{\pi}{2})$ (1 solution)

take both signs when $(v_\theta)_o = 0$ $(|\phi_o| = \frac{\pi}{2})$ (2 solutions)

With v_{1*} thus determined the hodograph for the transfer trajectory can be constructed in the $\vec{v}$-plane by noting that for a 180° trajectory we have

$$v_{\theta 1} : v_{\theta 2} = n : 1 \tag{17.9}$$

a consequence of Equation (2.2). Thus once the image point Q_1 is determined in the hodograph plane, so is the image point Q_2. Since the center of the hodograph circle is necessarily halfway between Q_1 and Q_2, the hodograph of the transfer trajectory is now completely determined, as shown in Figure III-15(a). It is interesting to note that, in a $\vec{v}$-plane the center of the hodograph circle for such transfer trajectories is constrained on a line also parallel to the v_{r1}-axis and at a distance $(1-n)/\sqrt{2n(n+1)}$ from it, which follows directly from Equations (17.5) and (17.9).

In the $\vec{v}$-plane the radical center T recedes to infinity, and all constant-n-lines become parallel according to Section 11.1 of Part II. Consequently, ρ_* also tends to infinity and the ρ_*-equation is no longer suitable for the description of the O_*-locus. In such a case the use of an alternate coordinate system is necessary. A convenient choice is a rectangular system with its axes coinciding with the directed lines TQ_1 and Q_2Q_1 in the $\vec{v}$-plane (which are in the local horizontal and vertical directions at Q_1 respectively). Let ρ_*' be the radius vector from the point Q_1 to the optimum origin O_*, then evidently, (see Figure III-15(b)).

$$\vec{\rho}_*' = - \vec{v}_{1*} \tag{17.10}$$

with their rectangular coordinates related

$$\begin{aligned} (\rho_*')_r &= - v_{r*} \\ (\rho_*')_\theta &= - v_{\theta *} \end{aligned} \tag{17.10a}$$

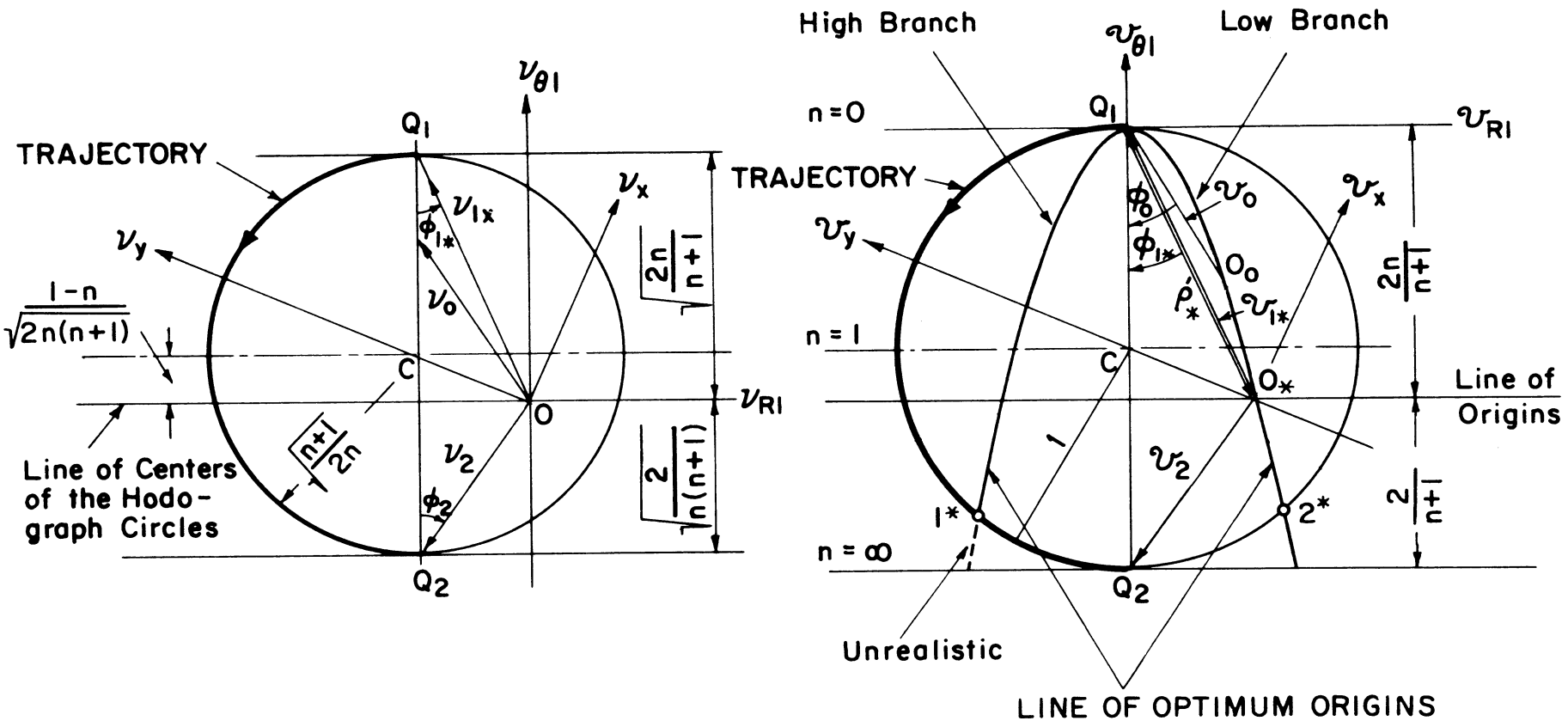

(a) The $\vec{\nu}$ – Hodograph

(b) The $\vec{v}$ – Hodograph

Figure III-15. The Optimum Trajectory Hodograph for 180° Transfer

Temporarily let us consider only the trajectories of the normal group, that is we restrict v_θ to be non-negative ($-\frac{\pi}{2} \leq \phi_o \leq \frac{\pi}{2}$) then directly from their definitions the components of v and $\vec{\nu}$ are related by

$$\begin{aligned} v_\theta &= \nu_\theta^2 \\ v_r &= \nu_r \nu_\theta \end{aligned} \tag{17.11}$$

It follows that

$$\frac{v_r^2}{v_\theta} = \nu_r^2 \tag{17.12}$$

But according to Equations (17.8-1) and (16.6) we have for realistic optimum,

$$\nu_{r*} = \nu_o \sin \phi_o \equiv \eta_o \tag{17.13}$$

Substituting Equation (17.13) in Equation (17.12) gives

$$v_{r*}^2 = m_o^2 v_{\theta*} \tag{17.14}$$

In terms of ρ'_r and ρ'_θ, this becomes

$$(\rho'_*)_r^2 = -m_o^2 (\rho'_*)_\theta \tag{17.15}$$

Thus the ρ'_*-equation is a parabola tangent to the ν_{r1}-axis at Q_1 and having the $v_{\theta 1}$-axis as its axis of symmetry (see Figure III-15(b)). Note that the line of optimum origins must pass through the initial point O_o determined by the initial velocity vector $\vec{v}_o$, according to Section 16.3. Thus the positive branch of this parabola corresponds to initial velocity vectors at negative path angles ($\phi_o < 0$) and will be designated as the low branch; while the negative branch corresponds to those at positive path angles ($\phi_o > 0$) and will be

designated as the high branch. The low branch therefore always gives a realistic optimum, and its portion beyond the hodograph circle is the hyperbolic portion. The high branch corresponds to a realistic optimum only up to the critical point, and beyond that the optimum origin will move closely around the circumference of the hodograph circle, but remain inside it.

It is to be noted that, when the initial velocity is directed in the local horizontal direction ($\phi_0 = 0$), the ρ'_*-parabola degenerates into the line Q_1Q_2, and all optimum transfer trajectories are realistic and elliptic. As is evident from both the $\vec{v}$-hodograph and the ν-hodograph, such an optimum transfer trajectory is always the Hohmann transfer ellipse (the minimum energy ellipse with the line Q_1Q_2 in the physical plane as its apsidal axis) independent of the magnitude of the initial velocity vector.

When the path angle of the initial velocity vector exceeds the limit $\pm \frac{\pi}{2}$, the optimum solution calls for a trajectory of the complementary group. The corresponding transfer hodograph can be easily obtained by rotating the present one for the normal group through 180° as usual (see Section 8.2).

17.3 The Case $r_2 \to \infty$ $(n \to \infty)$

When r_2 increases indefinitely while the angle ψ is fixed, the final terminal point Q_2 recedes to infinity along a given direction, and the problem becomes an escape from a given point Q_1 along a given asymptotic direction specified by ψ. The base triangle is now open with

$$\varphi_1 \to \pi - \psi \,, \quad \varphi_2 \to 0 \tag{17.16}$$

and the principal elements of the constraining hyperbola have the following limiting values

$$\begin{aligned} \sigma &\to \psi \\ A &\to \sqrt{2} \\ B &\to \sqrt{2}\tan\frac{\psi}{2} \\ e &\to \sec\frac{\psi}{2} \end{aligned} \tag{17.17}$$

Besides, the boundary Lamé has its cusps G and G' given by

$$v_{G,G'} \to \sqrt{2}\sec^2\frac{\psi}{2} \tag{17.18}$$

The geometry in the physical plane and that in the hodograph plane are shown in Figure III-16(a) and (b). The minimum velocity along the constraining hyperbola, as given by A, is the escape speed; thus all possible transfer trajectories are hyperbolic, or at least parabolic, a fact which is self evident. In the hodograph plane the critical circle now touches the constraining hyperbola at its vertices $\mathcal{P}$ and $\mathcal{P}'$, and the entire hodograph plane is divided into the realistic (all hyperbolic) and the unrealistic regions by the v_ζ-axis (see Figure III-16(b)).

It is to be noted that, although nonsimple regions exist in the hodograph plane for the present case, no realistic conjugate optimem solutions exist along the v_ζ-axis since no elliptic region exists, and the high half-plane is all unrealistic. Furthermore, a parabolic trajectory should not be admitted as a solution since it has no definite asymptotic direction as required by the problem. Thus whenever the tip Q_0 of the initial velocity vector lies between the points G and G' on the v_ζ-axis, a point on the constraining hyperbola in the realistic

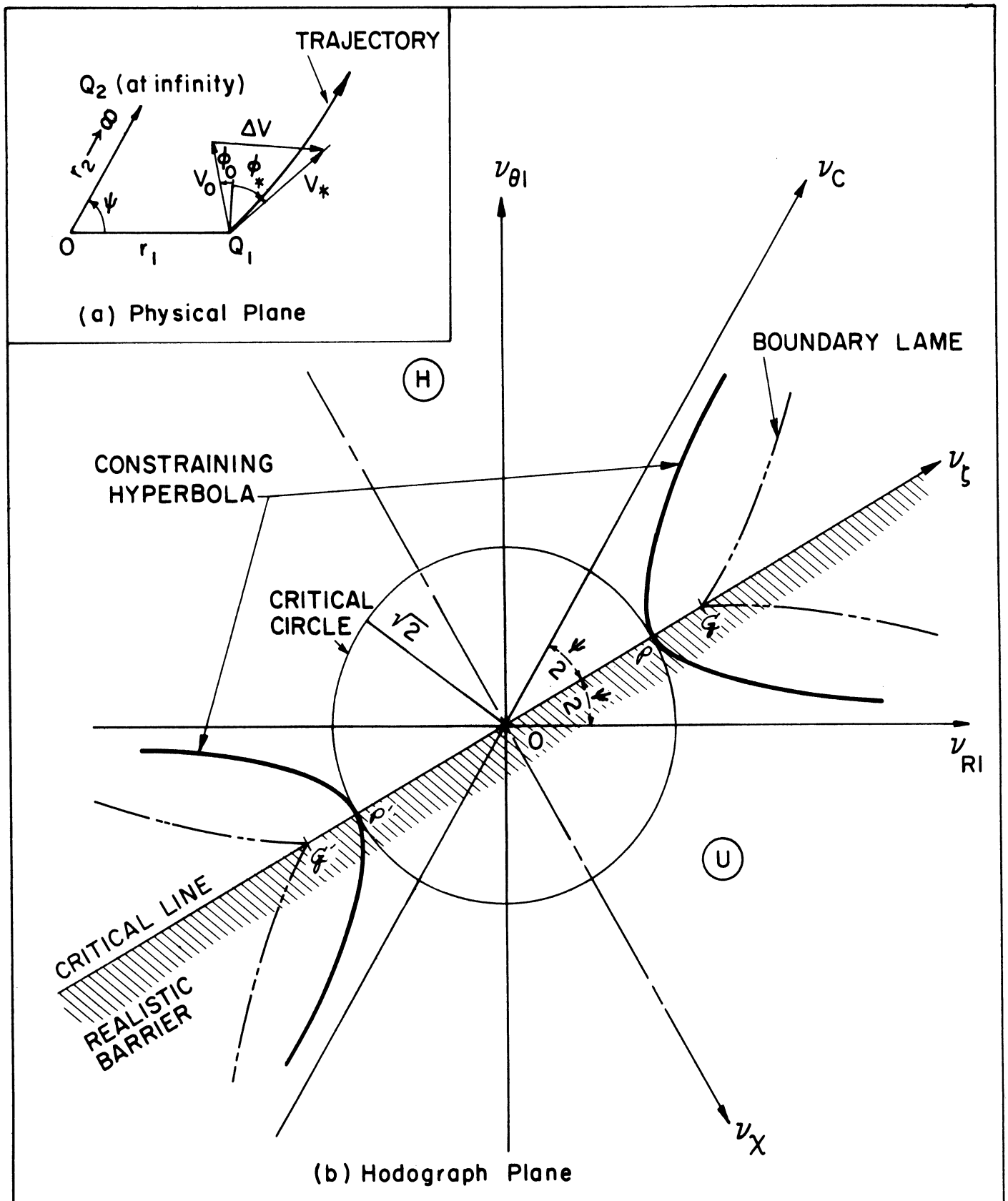

Figure III-16. Optimization of Transfer to Infinity ($r_2 \rightarrow \infty$)

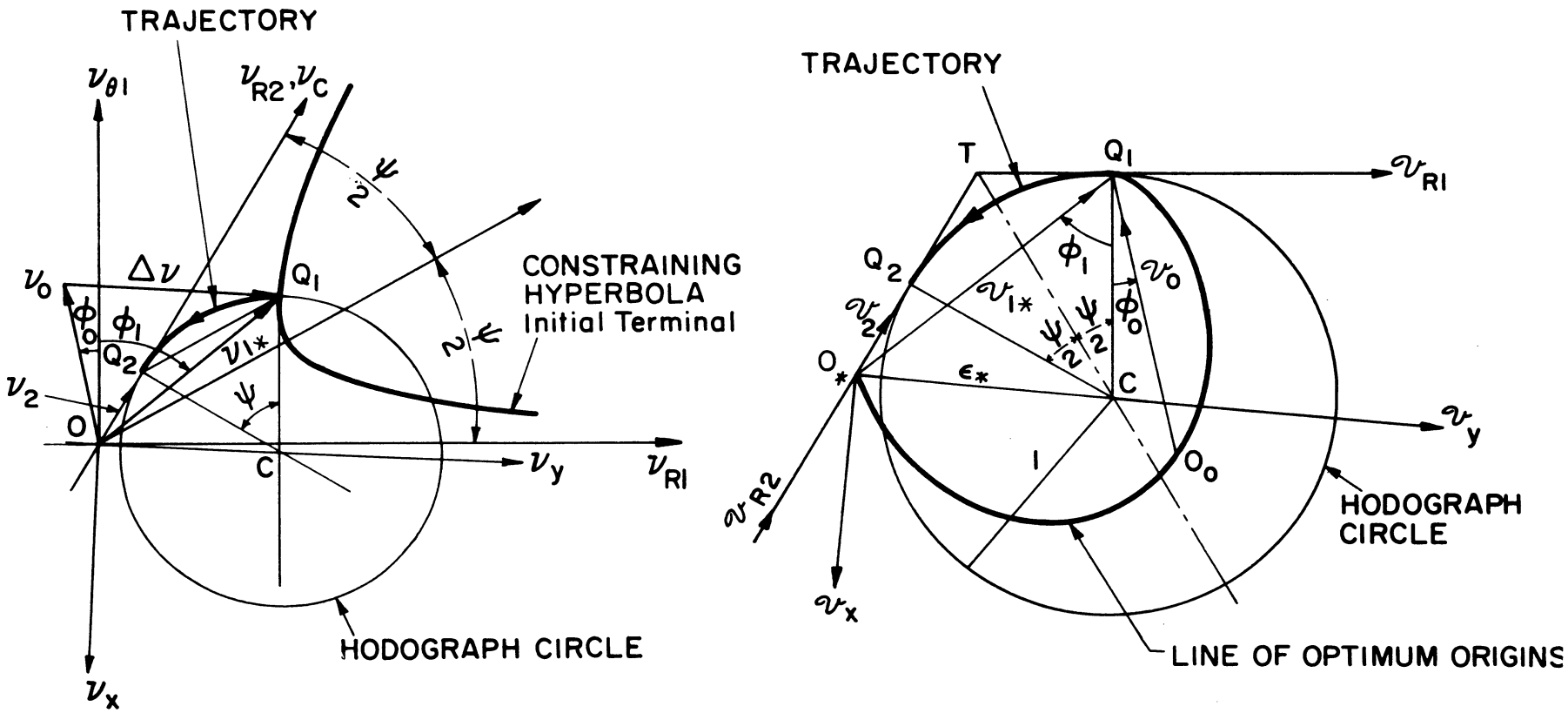

Figure III-17. The Optimum Trajectory Hodograph for Transfer to Infinity

region and close to the nearer critical point, $\mathcal{P}$ or $\mathcal{P}'$ is to be chosen as the optimum point. For points on the ν_ζ-axis beyond either G or G', of course hyperbolic realistic optimum solutions always exist. A simple criterion for realistic optimum transfer is then

$$
\begin{aligned}
&-\frac{1}{2}(\pi+\psi) < \phi_o < \frac{1}{2}(\pi-\psi) \quad (-\pi < \Phi_o < 0) \quad : \quad \text{any} \quad \nu_o \\
&\phi_o = \frac{1}{2}(\pm\pi-\psi) \quad (\phi = 0,-\pi) \quad : \quad \nu_o > \sqrt{2}\,\sec^2\frac{\psi}{2}
\end{aligned}
\tag{17.19}
$$

Note here that lines of equi-critical-velocity-increment exist in the unrealistic region, and whenever Q_o is in the unrealistic region a choice of an optimum solution should be made according to the rules presented in Section 15.4. The optimum solution corresponding to a given initial velocity vector cannot be readily written from the geometry in the $\vec{\nu}$-plane as was done in the previous particular cases. However, it is given by the point where the line of the optimum origins meets the line TQ in the $\vec{v}$-plane as shown in Figure III-17(b), and essential information concerning the transfer trajectory can be obtained from the $\vec{v}$-hodograph. For example, the eccentricity of the optimum trajectory is given by $\overline{O_*C}$, its apsidal axis by the line normal to $\overrightarrow{O_*C}$, and the residual velocity, the vector $\overrightarrow{O_*Q_2}$.

The $\vec{\nu}$-hodograph can be constructed as usual. In this case the point Q_2 in the hodograph plane can be easily located by drawing a straight line passing through Q_1 and parallel to the bisector of the angle ψ.[17.2] The point where this line meets the ν_{r1}-axis gives the point Q_2 required (see Figure III-17(a)). The hodograph circle will of course be tangent to the ν_{r1}-axis.

[17.2] See footnote 16.1, p. 172.

17.4 The Case $r_1 \to \infty$ $(n \to 0)$

When r_1 increases indefinitely while ψ remains fixed, the initial terminal Q_1 recedes to infinity along a given direction. With the presence of an initial velocity $\vec{V}_o$, the problem may be interpreted physically as changing an initial hyperbolic orbit with a residual velocity equal to $\vec{V}_o$ into a new hyperbolic orbit so as to reach the destination point from infinity along a given asymptotic direction specified by ψ. The base triangle now is again open with

$$\varphi_1 \to 0, \qquad \varphi_2 \to \pi - \psi \tag{17.20}$$

as shown in Figure III-18(a). Apparently, this case looks like the previous one with an interchange of the positions of Q_1 and Q_2. However, particular caution should be taken in that, while all the previous cases deal with the optimization at the initial terminal which is at a finite distance from the field center, the present optimization is at a point infinitely remote from it. The circular velocity V_{s1} at such a terminal tends to zero, and the nondimensionalization by dividing through with V_{s1} no longer applies. Instead, in the following analysis all velocities will be nondimensionalized with respect to the circular velocity V_{s2} at the final terminal Q_2, and the superscript ' will be used to designate such a nondimensionalization.

It is to be noted that the constant product K given by Godal's compatibility Equation (14.1) remains constant and nonzero, and after the present nondimensionalization it becomes

$$\kappa' = \tan \frac{\psi}{2} \csc \varphi_2 \tag{17.21}$$

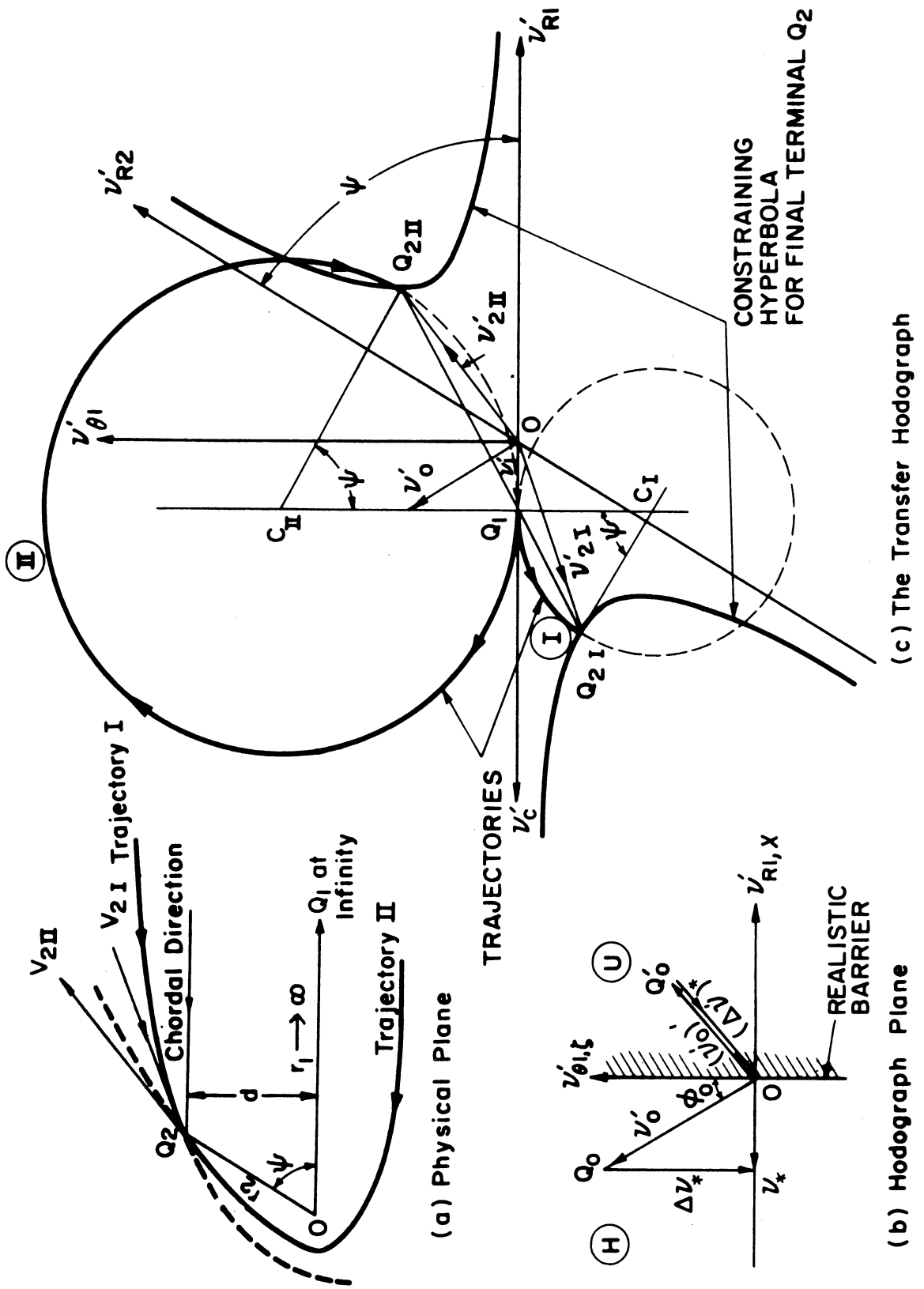

Figure III-18. Optimization of Transfer from Infinity ($r_1 \to \infty$)

Consequently the constraining hyperbola in the ν-plane is characterized by

$$\begin{aligned} \sigma &\rightarrow \pi \\ A' &\rightarrow 0 \\ B' &\rightarrow \sqrt{2}\sec\frac{\psi}{2} \\ e &\rightarrow \infty \end{aligned} \tag{17.22}$$

Thus the hyperbola degenerates again into a straight line parallel to the local radial direction at Q_1. All essential features of the geometry in the hodograph plane are the same as those in the case $\psi = 0$ and $r_1 > r_2$, except that the critical circle now shrinks to a point, the origin, since the critical velocity is zero at the terminal Q_1. Consequently no elliptic region exists in the hodograph plane and the entire plane is divided into the realistic (hyperbolic) and unrealistic regions by the $v_{\theta 1}$-axis along which the transfer is parabolic. Such a situation should be expected of course, since no elliptic trajectory can effect a transfer from infinite distance. For the same reason explained in the previous section, a parabolic trajectory should not be admitted as a solution; consequently the origin, which is the only critical point at present, must be excluded from the realistic region. It follows that Q_o is in the realistic region whenever $\phi_o < 0$ and $v_o > 0$. The geometry in the hodograph plane shows that the optimum velocity-increment vector is to be directed in the direction normal to v'_{R1}-axis everywhere in this region, and the optimum solution may be readily written as follows:

Velocity Increment

$$(\Delta'_{r1})_{opt.} = 0$$
$$(\Delta'_{\theta 1})_{opt.} = '_{o} \cos \phi_o \qquad (17.23)$$

Residual velocity along the transfer trajectory

$$('_{r1})_{opt.} = '_{o} \sin \phi_o$$
$$('_{\theta 1})_{opt.} = 0 \qquad (17.24)$$

When $\phi_o \geq 0$ and $\nu_o \geq 0$, Q_o is in the unrealistic region, and with the absence of the boundary Lamé the choice is simple. The indefinite solution is just

$$(\Delta')_{opt.} \cong \Delta'^{*} \qquad (17.25)$$

with the understanding that the optimum point so chosen should be close to the origin but in the realistic region, and the optimum solution is thus slightly hyperbolic.

Since no nonsimple region exists in the hodograph plane, the optimum solution obtained so far would be expected to be unique, especially in the realistic region off the $\nu_{Rl,\chi}$-axis. However, this is not the case. By following the optimum solution given by either Equations (17.23, 17.24 or 17.25) and using the usual orbital relations two complementary-conjugate trajectories will be found satisfying the given condition of the problem. It seems contradictory to the former assertions made in Section 15.5 concerning the uniqueness of such solutions. However, this apparent paradox may be explained by the fact that the constraining line here actually is the limiting position of both branches of the constraining hyperbola (one for each group of the transfer trajectories) as the radial distance r_1 tends to infinity. Consequently, every point on this constraining line may be regarded as consisting of

two coinciding points, one for each group, resulting in a complementary-conjugate pair of optimum solutions. Physically, this is understandable because the mere specifying the residual velocity vector of a hyperbolic orbit in addition to a finite orbital point does not completely specify the trajectory since it may approach this point along the same asymptotic direction on either side of its radius vector $\vec{r}_2$. To completely determine the trajectory the direction of its angular momentum vector must be specified. Thus for such a problem there are in general two solutions, and the choice will be the one whose angular momentum vector agrees in direction with that of the initial orbit.

The peculiar situation discussed above may be easily clarified by constructing the transfer trajectory hodograph. Before making such a construction, it is essential to note that while the point Q_1 in the hodograph plane is constrained on the ν'_{r1}-axis, the point Q_2 is constrained on another hyperbola given by Godal's compatibility condition for the terminal Q_2

$$\nu'_C \nu'_R = - \kappa' \tag{17.26}$$

which is not degenerate, since the chordal direction and the radius vector $\vec{r}_2$ intersect at an angle $\pi - \psi$ which is neither zero nor π . Thus with Q_1 determined from the optimum solution, the point Q_2 may be located in the hodograph plane by drawing the straight line through Q_1 and parallel to the bisector of the angle ψ and finding its intersection with the constraining hyperbola. In general, there are two such points of intersection, one on each branch of the hyperbola, giving two solutions of the problem. It is easy to see from the hodograph geometry that these two points (Q_{2I} and Q_{2II} in

Figure III-18(c)) are a complementary-conjugate pair since the line joining them is parallel to the transversal axis of the hyperbola. With the two possible points for Q_2 thus determined, the remaining construction is the same as that in Section 17.3. The resulting two transfer trajectories in the hodograph plane and the physical plane respectively are shown in Figure III-18(a) and (c).

Finally it is to be noted that the ρ_*-equation (16.5) does not hold for $r_1 \to \infty$ since it was formally derived on the basis of a finite r_1. Consequently the transfer trajectory in the $\vec{v}$-plane is not given by the point Q_1 as in the case of $\varphi_1 \to 0$ while r_1 remains finite. This is evident from physical considerations since the residual velocity for a hyperbolic trajectory does not vanish. In such a case we may express ρ_* alternately,

$$\rho_* = v_C'^2 \sin \varphi_2 \tag{17.27}$$

and obtain the ρ_*-equation in the form

$$(\rho_*^2 - \tan^2 \tfrac{\psi}{2})^2 = \rho_* \sin \varphi_2 (\mathcal{h}_o \rho_* - \mathcal{m}_o \tan \tfrac{\psi}{2})^2 \tag{17.28}$$

which has been nondimensionalized with respect to the final terminal instead of the initial terminal, and thus it holds regardless of r_1 being finite or infinite (but not for $r_2 \to \infty$). Recalling that for the present case we have

$$\varphi_2 \to \pi - \psi , \quad \varphi_1 \to 0 \tag{17.20}$$

and solving Equation (17.28) under these conditions, we find[17.3]

17.3 Negative roots have been rejected since they correspond to imaginary v_{C*}'s .

$$\rho_*\big|_{r_1\to\infty} = \tan\frac{\psi}{2} + \frac{1}{2}\dot{m}_o^2 \sin\psi \left(1 \pm \sqrt{1 + \frac{2}{\dot{m}_o^2}\sec^2\frac{\psi}{2}}\right) \qquad (17.29)$$

which gives a pair of solutions corresponding to the complementary-conjugate hodograph circles in the $\vec{v}$-plane. Note here by definition,

$$(v_1)_* = \frac{h_*}{\mu} V_* = \frac{\dot{m}_o h_*}{\sqrt{\mu r_2}} \qquad (17.30)$$

And in the $\vec{v}$-plane we have

$$\rho_*\big|_{r_1\to\infty} = \overline{TQ_1} + \overline{Q_1 O}_* = \tan\frac{\psi}{2} - v_{1*} \qquad (17.31)$$

Combining Equations (17.30) and (17.31) gives

$$\rho_*\big|_{r_1\to\infty} = \tan\frac{\psi}{2} - \frac{\dot{m}_o h_*}{\sqrt{\mu r_2}} \qquad (17.32)$$

Comparing Equations (17.29) and (17.32) yields immediately the pair of optimum angular momenta

$$(h_*)_{I,II} = -\frac{1}{2}\sqrt{\mu r_2}\,\dot{m}_o \sin\psi \left(1 \pm \sqrt{1 + \frac{2}{\dot{m}_o^2}\sec^2\frac{\psi}{2}}\right) \qquad (17.33)$$

That this is a complementary-conjugate pair can be verified by the fact that

$$(h_*)_I \cdot (h_*)_{II} = -\mu d \tan\frac{\psi}{2} \qquad (17.34)$$

in conformity with the characteristics of the conjugate trajectories presented in Section 9.2.

18. SOME GENERALIZATIONS

Based on the foregoing two-dimensional analysis, some generalizations may now be made.

18.1 The Orthogonality Principle and the Impulsive Change of Orbit

The orthogonality principle has been used by Stark without proof in his formulation of the optimum condition for the present terminal-to-terminal transfer problem[39]. It will be shown here that such a condition is generally applicable to the minimization of the initial velocity-increment for all problems of impulsive orbital changes.

In general, in a problem of this class the new orbit to be generated by an instantaneous finite impulse will be required to meet certain prescribed conditions which will in turn impose certain constraints on the new orbital velocity at the point where the impulse is to be applied. Mathematically such constraints may be expressed as

$$f_i(\vec{V}, \vec{V}_o, \vec{r}_o) = 0 \qquad i = 1 \ldots p \tag{18.1}$$

In a three-dimensional velocity space this system of equations will in general define a family of orbits or trajectories if the initial condition $(\vec{V}_C, \vec{r}_o)$ is specified and $p < 3$. If this is the case, then a choice of the optimum trajectory is possible, and for the minimum initial impulse problem the quantity to be minimized is $|\Delta V|$ which, in vector notation, may be written

$$|\Delta V|^2 = \vec{\Delta V} \cdot \vec{\Delta V} \tag{18.2}$$

With $\vec{V}_1$ constrained by Equations (18.1) a necessary condition for an interior extremum of $|\Delta V|$ is

$$d\,|\Delta V| = 0 \tag{18.3}$$

Recalling that $\vec{\Delta V} = \vec{V} - \vec{V}_o$ and here $\vec{V}_o$ is a constant vector, differentiating Equation (18.2) and using the condition (18.3) yields

$$\vec{\Delta V} \cdot \vec{dV} = 0 \tag{18.4}$$

where the vector $\vec{dV}$ is the vectorial element along the velocity constraint defined by Equations(18.1). By Equation (18.4) the two vectors $\vec{\Delta V}$ and $\vec{dV}$ are normal to each other. This formally establishes the orthogonality principle. As no particular form of the constraint is specified here, it is generally applicable to all impulsive change problems in which the instantaneous velocity-increment is to be minimized, and is not restricted to the present problem of terminal-to-terminal transfer.

Geometrically, if $p = 1$, the constraint Equation (83) may be viewed as a surface in the velocity space on which the tip of the new orbital velocity is constrained; and if $p = 2$, the constraint will in general be a space curve. In either case Equation (18.4) indicates that for an interior extremum of $|\Delta V|$, the velocity-increment vector is to be directed normal to the constraining surface or the constraining curve whichever applies. Such a general formulation and geometrical considerations are especially helpful in the treatment of such optimization problems for the three dimensional case.

18.2 The Three Dimensional Case of Terminal-to-Terminal Transfer

When the initial velocity vector or the initial orbit is not coplanar with the base triangle determined by the two fixed terminal points and the field center, the problem becomes three dimensional. In such a case, in addition to the usual terminal constraint for the in-plane component $\vec{V}_p$

of the terminal velocity $\vec{V}$,

$$f(\vec{V}_p) = 0 \tag{18.5-1}$$

we have an additional constraint for its out-plane component $\vec{V}_N$, namely

$$\vec{V}_N = 0 \tag{18.5-2}$$

Thus the condition is exceedingly simple in the 3-dimensional case of this particular problem, and, as previously presented, the constraint is still a hyperbola in the plane of the base triangle, except that the velocity-increment is now a vector lying in a plane normal to this hyperbola. This vector may be expressed as

$$\vec{\Delta V} = \vec{V}_p - \vec{V}_{po} - \vec{V}_{No} \tag{18.6}$$

where

$$\vec{V}_p = \vec{V} \tag{18.7}$$

in view of Equation (18.5-2), and the in-plane and out-plane components of the initial velocity are given by

$$V_{po} = V_o \cos\omega \quad , \quad V_{No} = V_o \sin\omega \tag{18.8}$$

where ω is the angle of inclination of $\vec{V}_o$ with respect to the base triangle plane, which is also the plane of the transfer trajectory. The geometry of such a 3-dimensional transfer is shown in Figure III-19. In

view of the constant component $-V_{NC}$ in Equation (18.6) the orthogonality

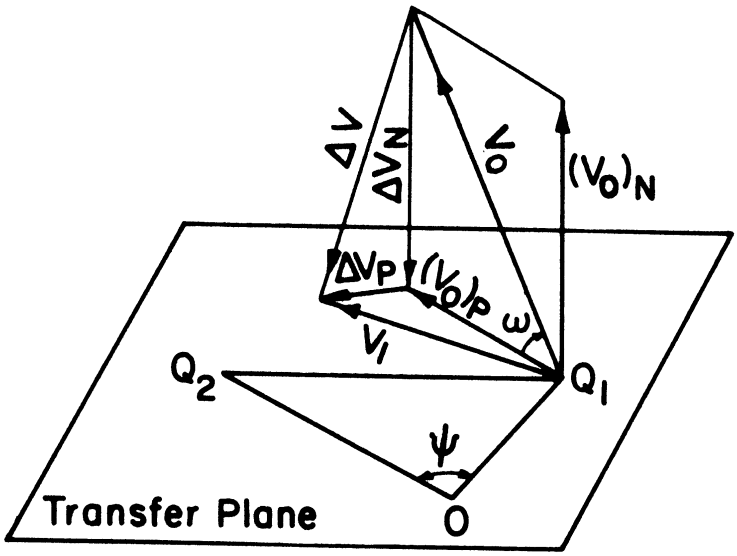

Figure III-19. Geometry of 3-Dimensional Terminal-to-Terminal Transfer.

condition (18.4) is equivalent to demanding the in-plane component $(\Delta V_p) = V_p - V_{po}$ to be normal to the constraining hyperbola. Thus all of the previous analysis for the two-dimensional case applies if we replace V_o by $V_o \cos\omega$, and ΔV by ΔV_p. Such a reduction of the three-dimensional case to the two-dimensional case has been mentioned in Starks work, and some numerical solutions have been found[39]. Thus no further disucssion is needed here. Finally it is worth to mention that the tilting of an initial velocity vector with respect to the plane of the base triangle may have the effect of changing the type of the optimum transfer trajectory as compared with the case when it is in the transfer plane. Thus an initial velocity vector may call for an hyperbolic transfer orbit when it lies in the transfer plane, but it is quite possible that the same velocity will call for an elliptic transfer trajectory if it is tilted up though at a greater expense of the initial impulse. Such a situation is evident from the optimization chart (Figure III-10).

18.3 Impulsive Orbital Change Problems with Hyperbolic Constraint

The previous two-dimensional analysis for the two-terminal-transfer problem was all based on the fact that the velocity constraint is represented in the hodograph plane by a hyperbola centered at the hodograph origin. However, it is interesting to note that such a hyperbolic constraint is not only present in this particular problem, but is often encountered in some other impulsive orbital change problems which are apparently unrelated. For example in the problem of re-entry at a specified path angle, the problem of impulsive rotation of the apsidal axis of an initial orbit, and so on, the formulation of the problem will in each case lead to some constraint which is represented by a hyperbola in the hodograph plane. For such a problem there always exists two asymptotic directions, say (ξ , η), in the hodograph plane, and by referring the velocity components to such directions the constraint can always be reduced to the standard form

$$v_\xi \, v_\eta = \text{const.} \tag{18.9}$$

which is comparable to Godal's compatibility condition for the two-terminal-transfer problem. Consquently, with such velocity coordinates, which are generally oblique, all basic formulations presented for the present transfer problem are directly applicable to such problems in general. The only differences will lie in the interpretation of the parameters involved (e.g. κ , σ etc. which will in general have different physical significance in different problems), but not in the form of these equations. For example, the application of the orthogonality principle to such a problem will always lead to the same form of quartic Equation (14.10-C) or (14.10-R) with the same boundary Lamé given by Equation (14.23). Thus not only the method of analysis, but also the general conclusions obtained here hold for all problems

of this class in general. Consequently the optimization chart developed for the present problem may also be used for the solution of other problems with proper interpretation of the parameters involved like ψ , φ , etc. Thus it is extremely interesting to see how these apparently diversified problems are interrelated through their common form of velocity constraint, and how they share the common characteristics of such solutions. However, owing to the limited scope and space of the present study, the analysis of other individual problems will not be attempted here.

FINAL REMARKS AND DISCUSSION

With the fundamentals and some of the applications of the hodograph method presented in Part I through Part III, a few remarks on the various aspects of this method together with some discussions may now be made.

As fully illustrated in these three parts, the orbital hodograph offers:

(1) A clear manifestation of the dynamic characteristics of the motion.

(2) A unified view of the three different types of Keplerian orbits.

(3) A geometrical approach in the velocity space to every dynamic problem of space flight.

(4) A direct path to the discovery of new theorems concerning the Keplerian motion by the highly suggestive nature of the hodograph geometry.

Based on these advantages the main applications of the hodograph method are:

(1) An analytical investigation of the characteristics of the motion and formulation of the orbital relations.

(2) A unified treatment of Keplerian motion, in general or in particular problems.

(3) A concise representation and simple treatment of the family of Keplerian orbits or trajectories consisting of either a finite or an infinite number of members (by using the dimensionless hodographs in the $\vec{v}$ -plane).

(4) A graphical determination of the orbital or trajectory elements.

As pointed out earlier in Part I the circularity of the Keplerian hodograph often renders a dynamic problem of the Keplerian motion readily solvable by simply applying elementary geometry in the hodograph plane.

This has been illustrated by the many examples provided in Parts I and II. However, it is to be noted that the hodograph geometry may become more involved when the problem becomes more complicated. This situation is illustrated by the optimization analysis presented in Part III in which a number of higher curves (like the boundary Lamé, the O^* -locus etc.) are encountered. Nevertheless, it can be said that, in comparison with the geometry in the physical space, the hodograph geometry usually is still simpler and offers a better view of the dynamic situation of the problem.

With the advantages and applications of the hodograph method thus reviewed, its limitation is also evident. Since the circular nature of the orbital hodograph, Hamiltonian or polar, is a direct consequence of Newton's inverse-square law of gravitation, and, as pointed out by Hamilton, "no other law of force would conduct the same result"(2), the present method can only be well applied to the Keplerian motion. Any deviation from the inverse-square law, or the presence of any other force, whether it comes from atmospheric drag, or the presence of a third gravitating body, or any other source, will upset Hamilton's Law of the Circular Hodograph and throw out all the simplicity of the present method. However, this does not mean the applicability of the hodograph method is restricted to the Keplerian motion only. Before discussing this point further a few areas amenable to immediate applications of the hodograph method within the realm of Keplerian motion will be cited first:

(1) A general treatment of the problems of impulsive orbital change.

The importance of this class of problems in space flight and a general scheme for its hodographic treatment have been outlined in Chapter 18, Part III. Under such a general treatment many problems of this class may be readily solved as particular cases; those of current interest are, e.g.,

a. Reentry at a specified direction

b. Reentry at a specified speed

c. Impulsive rotation of the orbital axis

d. Impulsive change of orbital eccentricity

and so on. For the optimum solution of these problems the essential procedures employed in the terminal-to-terminal transfer problems in Part III are applicable.

(2) The problem of multiple - impulse orbital transfer

The optimization problem treated in Part III may be categorized as a problem of single-impulse orbital transfer. The hodograph analysis of this rather simple but basic problem may serve as a stepping stone toward a better understanding of the more complicated problem of double-impulse orbital transfer, in which an octic optimum equation(15) is involved, and very little about it is analytically known. These basic analyses may finally lead to a hodographic treatment of the general problem of an N-impulse transfer. It is worth to mention that the hodograph method is particularly suitable for the treatment of such transfer problems in its capability of handling Keplerian conics in general without specifying the types of the initial and final orbits or those of the intermmediate trajectories if any.

(3) The Keplerian acceleration hodograph

An acceleration hodograph may be regarded as the hodograph of hodograph, and is a logical extension of the concept of the velocity hodograph. The Keplerian acceleration hodograph in an inertial frame has been shown by Altman(17) to be a form of Limacon[1] and an analytical study of the

---

[1] Strictly speaking, it is the graph of the square root of the gravitational acceleration which assumes the form of a Limacon in an inertial reference frame.

corresponding hodograph in a non-inertial frame comparable to the polar version of the orbital velocity hodograph may likely be made. Such a development may not be very necessary in the treatment of the Keplerian motion, since the inverse-square law of force, which is in direct proportion to the acceleration, is well manifested by the circular velocity hodograph. However, by using the Keplerian model the essential features of an acceleration hodograph and its relation with the velocity hodograph may be illustrated; and such a preliminary treatment may aid the development of the general acceleration hodograph which will be useful in dealing with Non-Keplerian motions to be discussed later.

(4) The Keplerian motion in a central repulsion field

The scope of the present study has been limited to the central gravity field. However, it is to be noted that Hamilton's law the circular hodograph holds also in a central repulsion field as long as it is governed by the inverse-square law. The same can be said about the polar hodograph. Thus all the fundamentals presented in Part I for a central gravity field equally apply to a central repulsion field with a change of sign of μ. As shown in Chapter 3 of Part I, the hodograph circle for a hyperbolic motion in fact consists of two parts: one for the motion in a central attraction field, and the other, a central repulsion field. Thus it is interesting to see that it takes both fields to complete the hodograph circle for the hyperbolic motion, and the hodographic study of such a motion in a central attraction field leads naturally to that in a central repulsion field. So far no direct application of such a hodograph in space flight problems can be seen since here we are concerned only with the gravity field, and very little work has been done on this subject[2]. However,

---

[2] See Section X of Reference (12).

it can be conceived that, by the joint use of the hodograph for a central repulsion field with that for a central attraction field, the geometry of motion in a complicated force field may be built up in analogy with the classical method of using sink and source to build up a flow field in aerodynamics. After all one never can tell that such a repulsion field will not be encountered in man's future space adventure. In any event the extension of the present hodograph method to include the Newtonian central repulsion field is simple and straight-forward.

The afore-mentioned areas do not exhaust all the possibilities of the application of the hodograph method within the frame of Keplerian motion. They serve merely to illustrate the typical areas in which the materials of the present development may be immediately applied. Before closing, a few remarks on the potentialities of the hodograph method for the analysis of the Non-Keplerian motions will be made.

Strictly speaking the Keplerian motion is a simple model for the motion of a vehicle in space flight, and all such actual motions are non-Keplerian. More specifically the non-Keplerian aspects are to be considered in the following classes of problems:

A. The presence of perturbing forces in addition to a Newtonian gravity field.

B. The presence of applied forces in addition to a Newtonian gravity field.

C. The presence of more than one Newtonian field center.

D. The presence of Non-Newtonian force fields.

In class A the perturbing forces here refer to the limited sense of being the uncontrolled ones like the aerodynamic force, the radiation pressure, and so on. Problems of this class are known as the classical

perturbation problems. When the perturbation is small, the perturbed motion, as suggested by Euler (1756), may be described by an osculating conic at each instant. Consequently the instantaneous corresponding hodograph is a circle of varying radius and varying origin-to-center distance, and lying in a plane of varying orientation in the velocity space, all being functions of time. Based on such concepts the fundamentals of the Keplerian hodograph may still be applied and the perturbed orbit may be well represented in the velocity space. By so doing a hodographic approach to the perturbed problem is provided in addition to the many classical technics employed in celestial mechanics.

The applied forces in class B refer to the controlled ones like the thrust of the propulsion system, and problems of powered space flight fall under this category. Class C constitutes the classical N-body problem, which has inspired astronomers and mathematicians for centuries; and class D broadens the present theoretical basis of space mechanics to include non-Newtonian fields and relativistic effects. So far problems of these three classes either have not been satisfactorially treated, or have barely been touched by the classical methods in celestial mechanics and astrodynamics, and a geometrical approach through the hodographic treatment may provide a new outlook on these problems and hold the key to their solutions. However, before the hodograph method can be successfully applied to these problems a much broader analytical foundation for hodograph transformation must first be firmly established. A recent research trend in this field indicates such a new theory is in the making[20, 21]. It seems the establishment of the hodograph transformation theory with the development of hodographs of higher orders is a reasonable direction for the future

research in this field, and such a new theory, aided by differential geometry, topology, and the related mathematics, may provide an effective treatment of some of the afore-mentioned classes of problems in space mechanics which has hitherto never been attained.

BIBLIOGRAPHY AND REFERENCES

Bibliography on the Orbital Hodograph

1. Mobius, A.F., Mechanik des Himmels, Gesammelte Werke, Vol. IV, pp. 36, 47, 1843.

2. Hamilton, Sir William R., The Hodograph, or a New Method of Expressing in Symbolical Language the Newtonian Law of Attraction, Proc. Roy. Irish Acad. Vol. III(1845-47), pp. 344-353 (read March 1847).

3. Hamilton, Sir William R., On a Theorem of Hodographic Isochronism, Proc. Roy. Irish Acad. Vol. III(1845-47), p. 417 (read March 1847).

4. Hamilton, Sir William R., On a Theorem of Anthohodographic Isochronism, Proc. Roy. Irish Acad. Vol. III(1945-47), p. 465 (read May 1847).

5. Hamilton, Sir William R., Elements of Quaternions, Vol. I, 1899, p. 99, Vol. II, 1901, pp. 29, 298-320 (art. 419), Longmans Green and Co. (second edition).

6. Boksenbom, A.S., Graphical Trajectory Analysis, NASA TN D-64, Dec. 1959.

7. Sun, F.T., A Special Hodograph for Orbital Motion, Proceedings 2nd International Symposium on Rockets and Astronautics, Tokyo, May 1960, (Yokendo Bunkyo-Ku, Tokyo, 1961, pp. 163-189).

8. Paul, E.W., The Hodograph and Ballistic Missile Trajectory Problems, Aerospace Eng., Feb. 1961.

9. Sun, F.T., Some Applications of the Special Hodograph for Orbital Motion, Proceedings of the 3rd International Symposium on Rockets and Astronautics Tokyo, August 1961, (Yokendo Bunkyo-Ku, Tokyo, 1962), pp. 381-396.

10. Altman, S.P., Orbital Transfer for Satellite, Proceedings of the Fourth Ballistic Missile and Space Technology Symposium on Rockets, Pergamon Press, New York, 1961, pp. 132-144.

11. Altman, S.P., and Pistiner, J.S., Hodograph Analysis of the Orbital Transfer Problem for Coplanar Non-Aligned Elliptical Orbits, ARS J. Vol. 31, No. 9, Sept. 1961.

12. Sun, F.T., On the Hodograph Method for Solution of Orbital Problems, Proceedings, XIIth International Astronautical Congress, Washington, D. C., Oct. 1961, (Academic Press, 1963). Vol. II, pp. 879-915).

13. Altman, S.P., and Pistiner, J.S., Polar Hodograph for Ballistic Missile Trajectories, ARS J. Vol. 31, No. 11, Nov. 1961.

14. Altman, S.P., and Pistiner, J.S., Hodograph Transformations and Mapping of the Orbital Conics, ARS J Vol. 32, No. 7, July 1962.

15. Altman, S.P., and Pistiner, J.S., Minimum Velocity Increment Solution for Two-Impulse Coplanar Orbital Transfer, AIAA J., Vol. I, No. 2, Feb. 1963.

16. Pesék, Rudolf, Invariant Two-Body Velocity Components and the Hodograph, AIAA J. Vol. 1, No. 7, p. 1676, July 1963.

17. United Aircraft Corporate Systems Center, Research Study on the Acceleration Hodograph and Its Application to Space Trajectory Analysis, NASA Report N64-11262, July 1963.

18. Altman, S.P., and Pistiner, J.S., Analysis of the Orbital Transfer Problem in Three-Dimensional Space, Progress in Astronautics and Aeronautics, Vol. 14, Academic Press, New York, 1964, pp. 627-654.

19. Sun, F.T., Hodograph Analysis of the Free-Flight Trajectories Between Two Arbitrary Terminal Points, NASA Report, CR-153, Jan. 1965.

20. Altman, S.P., Orbital Hodograph Transformation Theory, AIAA Paper 65-686, AIAA/Ion Astrodynamics Specialist Conference, Calif., Sept. 16-17, 1965.

21. Altman, S.P., The Hodographic Theory of Newtonian Mechanics,ASA/AAAS Special Astronautics Symposium, Dec. 1965.

Other References

22. Salmon, G., A Treatise on Conie Section, 6th Ed., Longmans, Green, and Co., 1879, pp. 337-338.

23. Burnside, W.S., and Panton, A.W., The Theory of Equations, Longmans, Green and Co., 7th Ed., 1912, pp. 144-145.

24. Moulton, F.R., An Introduction to Celestial Mechanics, MacMillan, New York, 1914 (2nd revised ed.).

25. Plummer, H.C., An Introductory Treatise on Dynamical Astronomy, Cambridge Univ. Press 1918, pp. 50-55.

26. Cranz, C, Lehrbuch der Ballistik, Band I,Springer, Berlin, 1925, pp. 27-33.

27. Hohmann, W., Die Erreichbarkeit Der Himmelskoeper, Oldenbourg Publ., Munich, 1925.

28. Johnson, R.A., Advanced Euclidean Geometry, Houghton Mifflin Co., 1929, p. 32.

29. Whittaker, E.T., A Treatise on the Analytical Dynamics of Particles and Rigid Bodies, Cambridge Univ. Press, 1937 (4th ed.).

30. Yates, R.C., Curves, Department of Mathematics, U.S. Military Academy, 1946, pp. 84-90, 155-158.

31. Barker, Clyde D., and Hart, Judson J., Maximum Range of a Projectile in a Vacuum, Am. J. Physics, Vol. 23, No. 5, May 1955.

32. Blitzer, L., and Hart, Judson J., Maximum Range of a Projectile in a Vacuum on a Spherical Earth, Am. J. Physics, Vol. 25, No. 1, Jan. 1957.

33. Battin, R.H., The Determination of Round-Trip Planetary Reconnaissance Trajectories, J. Aero-Space Sci., Vol. 26, No. 9, Sept. 1959, pp. 545-567.

34. Wheelon, A.D., Free-Flight of a Ballistic Missile, ARS J., Vol. 29, No. 12, Dec. 1959, pp. 915-926.

35. Sun, F.T., On the Dynamical Characteristics of Orbital Motion in a Central Gravity Field, Tsing Hua J. of Chinese Studies, Special No. 1 (Natural Science), Taiwan, China, Dec. 1959.

36. Sun, F.T., Launching Conditions and the Geometry of Orbits in a Central Gravity Field, Xth International Astronautical Congress, London 1959, Springer-Verlag, Wien 1960.

37. Godal, Th., Conditions of Compatibility of Terminal Positions and Velocities, Proceedings XIth International Astronautical Congress, Stockholm, 1960, Springer-Verlag, Vol. I, pp. 40-44.

38. Pistiner, J.S., Some Characteristics of the Planar Satellite Orbit, ARS J. Vol. 30, No. 3, March 1960.

39. Stark, H.M., Optimum Trajectories Between Two Terminals in Space, ARS J., Feb. 1961, pp. 261-263.

40. Bergonz, F.H., and others, Vehicle Kinematics and Sizing, Douglas Report SM 38513, Douglas Aircraft Co., Santa Monica, Calif., Feb. 1961.

41. Tsander, F.A., Problems of Flight by Jet Propulsion, Moscow, 1961 (translated from Russian and published by NASA, Washington, D.C., 9164), pp. 237-321.

42. Ehricke, K.A., Space Flight, Vols. I and II, Nostrad, New York, 1962.

43. Cronin, J.L., and Schwartz, R.E., Invariant Two-body Velocity Components, J. Aerospace Sci., 29, 1962, pp. 1384-85.

44. Deutsch, R., Orbital Dynamics of Space Vehicles, Prentice-Hall, 1963.

45. Pohle, F.V., Invariant Components of Motion in Inverse-square Field, AIAA J., Vol. 1, No. 4, April 1963.

APPENDICES

APPENDIX A

INTER-RELATIONS BETWEEN THE GEOMETRIC PARAMETERS AND THE DYNAMIC PARAMETERS OF THE KEPLERIAN ORBIT

TABLE A-1

CONVERSION OF GEOMETRIC PARAMETERS INTO DYNAMIC PARAMETERS

		k, h	λ, ϕ
Eccentricity	ϵ	$\sqrt{1 + \frac{2kh^2}{\mu^2}}$	$\sqrt{1-4\lambda^2(1-\lambda^2)\cos^2\phi}$
Semi-latus Rectum	$\bar{r}$	$\frac{h^2}{\mu}$	$2r\,\lambda^2\cos^2\phi$
Pericenter Radius	r_P	$-\frac{\mu}{2k}\left(1 - \sqrt{1 + \frac{2kh^2}{\mu^2}}\right)$	$\frac{r\left(1 - \sqrt{1-4\lambda^2(1-\lambda^2)\cos^2\phi}\right)}{2(1-\lambda^2)}$
Apocenter Radius	r_A	$\frac{\mu}{\lvert 2k\rvert}\left(1 + \sqrt{1 + \frac{2kh^2}{\mu^2}}\right)$	$\frac{r\left(1 + \sqrt{1-4\lambda^2(1-\lambda^2)\cos^2\phi}\right)}{2\lvert 1-\lambda^2\rvert}$
Semimajor or Semitransverse Axis	a	$\frac{\mu}{\lvert 2k\rvert}$	$\frac{r}{2\lvert 1-\lambda^2\rvert}$
Semiminor or Semiconjugate Axis	b	$\frac{h}{\sqrt{2\lvert k\rvert}}$	$\frac{r\,\lambda\cos\phi}{\sqrt{\lvert 1-\lambda^2\rvert}}$
Center-Focus Distance	c	$\frac{\mu}{\lvert 2k\rvert}\sqrt{1 + \frac{2kh^2}{\mu^2}}$	$\frac{r}{2\lvert 1-\lambda^2\rvert}\sqrt{1-4\lambda^2(1-\lambda^2)\cos^2\phi}$

TABLE A-2

CONVERSION OF DYNAMIC PARAMETERS INTO GEOMETRIC PARAMETERS

		$\bar{r}$, ϵ	a, ϵ	a, $\bar{r}$
Velocity at any Orbital Point (r,θ)	V	$\sqrt{\mu(\frac{2}{r} + \frac{\epsilon^2-1}{\bar{r}})} = \sqrt{\frac{\mu}{\bar{r}}(1+2\epsilon\cos\theta+\epsilon^2)}$	$\sqrt{\mu(\frac{2}{r} \mp \frac{1}{a})} = \sqrt{\frac{\mu}{a}\frac{1+2\epsilon\cos\theta+\epsilon^2}{\lvert 1-\epsilon^2\rvert}}$	$\sqrt{\mu(\frac{2}{r} \mp \frac{1}{a})}$
	V_θ	$\frac{1}{r}\sqrt{\mu\bar{r}} = \sqrt{\frac{\mu}{\bar{r}}}(1+\epsilon\cos\theta)$	$\frac{1}{r}\sqrt{\mu a\lvert 1-\epsilon^2\rvert} = \sqrt{\frac{\mu}{a\lvert 1-\epsilon^2\rvert}}(1+\epsilon\cos\theta)$	$\sqrt{\mu\bar{r}/r}$
	V_r	$\sqrt{\mu(\frac{2}{r} - \frac{\bar{r}}{r^2} + \frac{\epsilon^2-1}{\bar{r}})} = \sqrt{\frac{\mu}{\bar{r}}}\epsilon\sin\theta$	$\sqrt{\mu(\frac{2}{r} \mp \frac{a(1-\epsilon^2)}{r^2} \mp \frac{1}{a})} = \sqrt{\frac{\mu}{a\lvert 1-\epsilon^2\rvert}}\epsilon\sin\theta$	$\mu(\frac{2}{r} - \frac{\bar{r}}{r^2} \mp \frac{1}{a})$
	ϕ	$\tan^{-1}\frac{\epsilon\cos\theta}{1+\epsilon\cos\theta}$	$\tan^{-1}\frac{\epsilon\sin\theta}{1+\epsilon\cos\theta}$	$\cos^{-1}\sqrt{\frac{\bar{r}/r}{2 \mp \frac{\bar{r}}{a}}}$
Velocity at Pericenter $V_r = 0$, $\phi = 0$	V_P	$\sqrt{\frac{\mu}{\bar{r}}(1+\epsilon)}$	$\sqrt{\frac{\mu(1+\epsilon)}{a\lvert 1-\epsilon\rvert}}$	$\sqrt{\frac{\mu}{\bar{r}}(1 + \sqrt{1 \mp \frac{\bar{r}}{a}})}$
Velocity at Apocenter $V_r = 0$, $\phi = 0$ (Elliptic Orbit)	V_A	$\sqrt{\frac{\mu}{\bar{r}}(1-\epsilon)}$	$\sqrt{\frac{\mu}{a}\frac{1-\epsilon}{1+\epsilon}}$	$\sqrt{\frac{\mu}{\bar{r}}(1 - \sqrt{1 - \frac{\bar{r}}{a}})}$
Velocity at Ends of Latus Rectum $r = \bar{r}$, $\theta = \frac{\pi}{2}$	$V_{M,M'}$	$\sqrt{\frac{\mu}{\bar{r}}(1+\epsilon^2)}$	$\sqrt{\frac{\mu}{a}\frac{1+\epsilon^2}{1-\epsilon^2}}$	$\sqrt{\mu(\frac{2}{r} \mp \frac{1}{a})}$
	$\phi_{M,M'}$	$\tan^{-1}\epsilon$	$\tan^{-1}\epsilon$	$\tan^{-1}\sqrt{1 \mp \frac{\bar{r}}{a}}$
Velocity at Ends of Minor Axis (Elliptic Orbit) $r = a$, $\theta = \cos^{-1}(-\epsilon)$	$V_{N,N'}$	$\sqrt{\frac{\mu}{\bar{r}}(1-\epsilon^2)}$	$\sqrt{\frac{\mu}{a}}$	$\sqrt{\frac{\mu}{a}}$
	$\phi_{N,N'}$	$\sin^{-1}\epsilon$	$\sin^{-1}\epsilon$	$\sin^{-1}\sqrt{1 \mp \frac{\bar{r}}{a}}$
Velocity at Infinity (Hyperbolic Orbit) $V_\theta = 0$, $\phi = \frac{\pi}{2}$	V_∞	$\sqrt{\frac{\mu}{\bar{r}}(\epsilon^2-1)}$	$\sqrt{\frac{\mu}{a}}$	$\sqrt{\frac{\mu}{a}}$
Local Speed Ratio	λ^2	$1 + \frac{1}{2}\frac{r}{\bar{r}}(\epsilon^2-1) = 1 + \frac{1}{2}\frac{\epsilon^2-1}{1+\epsilon\cos\theta}$	$1 \mp \frac{r}{2a} = 1 - \frac{1}{2}\frac{1-\epsilon^2}{1+\epsilon\cos\theta}$	$1 \mp \frac{r}{2a}$
	λ^2_P	$\frac{1}{2}(1+\epsilon)$	$\frac{1}{2}(1+\epsilon)$	$\frac{1}{2}(1 + \sqrt{1 \mp \frac{\bar{r}}{a}})$
	λ^2_A	$\frac{1}{2}(1-\epsilon)$	$\frac{1}{2}(1-\epsilon)$	$\frac{1}{2}(1 - \sqrt{1 - \frac{\bar{r}}{a}})$
	$\lambda^2_{M,M'}$	$\frac{1}{2}(1+\epsilon^2)$	$\frac{1}{2}(1+\epsilon^2)$	$1 \mp \frac{\bar{r}}{2a}$
	$\lambda^2_{N,N'}$	$\frac{1}{2}$	$\frac{1}{2}$	$\frac{1}{2}$
	λ^2_∞	∞	∞	∞
Orbital Energy	k	$\frac{\mu}{2\bar{r}}(\epsilon^2-1)$	$\mp\frac{\mu}{2a}$	$\mp\frac{\mu}{2a}$
Angular Momentum	h	$\sqrt{\mu\bar{r}}$	$\sqrt{\mu a\lvert 1-\epsilon^2\rvert}$	$\sqrt{\mu\bar{r}}$
Period (Elliptic Orbit)	τ	$\frac{2\pi}{\sqrt{\mu}}(\frac{\bar{r}}{1-\epsilon^2})^{3/2}$	$\frac{2\pi}{\sqrt{\mu}}a^{3/2}$	$\frac{2\pi}{\sqrt{\mu}}a^{3/2}$

NOTE: Wherever double sign appears in this table, the upper sign is used for the elliptic orbit; the lower sign, for the hyperbolic; either sign may be used for parabolic orbit

APPENDIX B

PROOFS OF SOME OF THE CORRELATION FORMULAS

1. Local circular speed (Rule H-5)

Formula

$$V_s = \overline{QT} \tag{3.7}$$

Proof We have from the geometry of the hodograph (Figure I-2a)

$$\overline{QT}^2 = \overline{CQ} \cdot \overline{SQ} \tag{B-1}$$

from the hodograph construction,

$$\overline{CQ} = \frac{\mu}{h}, \quad \overline{SQ} = V_\theta \tag{2.7, 3.3}$$

and from the Momentum Integral,

$$h = rV_\theta \tag{2.2}$$

Substituting Equations (2.7, 3.3) into Equation (B-1) and using Equation (2.2) gives

$$\overline{QT}^2 = \frac{\mu}{r} \tag{B-2}$$

that is

$$\overline{QT} = V_s \tag{3.7}$$

according to Equation (1.8)

2. Local speed parameter (Rule H-6)

Formula

$$\lambda^2 = \frac{\overline{BQ}}{2\overline{CQ}} \tag{3.8}$$

Proof We have from the hodograph geometry (Figure I-2a)

$$\overline{OQ}^2 = \overline{BQ} \cdot \overline{SQ} \tag{B-2}$$

from the hodograph construction,

$$\overline{OQ} = V \tag{3.1}$$

and from Rule (H-5)

$$\overline{QT}^2 = \overline{CQ} \cdot \overline{SQ} = V_s^2 \tag{B-3}$$

By using these three equations and recalling the definition of λ we find

$$\frac{\overline{BQ}}{2\overline{CQ}} = \frac{\overline{OQ}^2}{2\overline{CQ}\cdot\overline{SQ}} = \frac{\overline{OQ}^2}{2\overline{QT}^2} = \frac{V^2}{2V_s^2} = \lambda^2 \tag{3.8}$$

3. True anomaly (Rule P-2)

Formula

$$\theta = \measuredangle PCQ \tag{3.13}$$

Proof From the orbital relations (see Table A-2, Appendix A)

$$V_r = \sqrt{\frac{\mu}{r}}\, \epsilon \sin\theta \ , \quad V_\theta = \sqrt{\frac{\mu}{r}}\,(1 + \epsilon \cos\theta) \tag{B-4}$$

we have, along a given orbit,

$$dV_r = \sqrt{\frac{\mu}{r}}\, \epsilon \cos\theta \, d\theta \ , \quad dV_\theta = -\sqrt{\frac{\mu}{r}}\, \epsilon \sin\theta \, d\theta \tag{B-5}$$

Thus the slope of the polar hodograph with respect to $r\theta$-axis is given by

$$\frac{dV_r}{dV_\theta} = -\cot\theta$$

Consequently the slope of the radius CQ is $\tan\theta$ since $\overline{CQ}$ is normal to the hodograph circle. This proves Equation (3.13).

4. Elliptic Eccentric Anomaly - $\dot{R}, R\dot{\theta}$-Plane

Formula

$$\alpha = \measuredangle BCD \tag{5.6P}$$

Proof From the defining equation

$$\epsilon \cos\alpha = 1 - \frac{r}{a} \tag{5.5}$$

and the orbital relation (see Table A-2)

$$\lambda^2 = 1 - \frac{r}{2a} \qquad \text{(B-6)}$$

eliminating r/a gives

$$\epsilon \cos \alpha = 2\lambda^2 - 1 \qquad \text{(B-7)}$$

From the hodograph geometry and the correlation formula (3. 18) we have

$$\epsilon \cos \hat{BCD} = \overline{CB} = \overline{OB} - \overline{OC} = 2\lambda^2 - 1 \qquad \text{(B-8)}$$

Comparing Equations (B-7) and (B-8) gives Equation (5.6P).

5. Elliptic Eccentric Anomaly - $\dot{\mathscr{X}}, \dot{\mathscr{Y}}$ -Plane

Formula

$$\alpha = \sphericalangle PCD = \sphericalangle eCf \qquad \text{(5.6H, 5.6'H)}$$

Proof By construction: $\sphericalangle PCD = < oCb$

It follows that

$$\epsilon \cos \hat{PCD} = \epsilon \cos oCb = \overline{cb} = \overline{CB}$$

Similarly we have by construction,

$$\epsilon \cos \hat{eCf} = \overline{Ce} = \overline{CB}$$

But from the hodograph (see Figure I-8c) and using the correlation formula (3.8) we have

$$\overline{CB} = \overline{BQ} - \overline{CQ} = 2\lambda^2 - 1$$

Consequently,

$$\epsilon \cos \hat{PCD} = \epsilon \cos \hat{eCf} = 2\lambda^2 - 1 \qquad \text{(B-9)}$$

Comparing Equation (B-9) with Equation (B-7) gives Equation (5.6H, 5.6'H)

6. Hyperbolic Eccentric Anomaly - $\dot{\mathscr{R}}, \dot{\mathscr{A}}\dot{\Theta}$-Plane

Formula

$$\alpha = \sphericalangle BCD \qquad \text{(5.8P)}$$

Proof From the defining equation

$$\epsilon \sec \alpha = 1 + \frac{r}{a} \tag{5.7}$$

and the orbital relation (see Table A-2)

$$\lambda^2 = 1 + \frac{r}{2a} \tag{B-10}$$

eliminating r/a gives

$$\epsilon \sec \alpha = 2\lambda^2 - 1 \tag{B-11}$$

From the hodograph geometry and the correlation formula (3.18), we have

$$\epsilon \sec \hat{BCD} = \overline{CB} = \overline{OB} - \overline{OC} = 2\lambda^2 - 1 \tag{B-12}$$

Comparing Equation (B-11) and (B-12) gives Equation (5.8P)

7. Hyperbolic Eccentric Anomaly - $\dot{x},\dot{y}$-Plane

Formula

$$\alpha = \sphericalangle PCD \tag{5.8H}$$

Proof By construction: $\sphericalangle PCD = \sphericalangle OCb$

It follows that

$$\epsilon \sec \hat{PCD} = \epsilon \sec \hat{OCb} = \overline{Cb} = \overline{CB}$$

As the hodograph geometry shows, here again we have

$$\overline{CB} = \overline{BQ} - \overline{CQ} = 2\lambda^2 - 1$$

and consequently,

$$\epsilon \sec \hat{PCD} = 2\lambda^2 - 1 \tag{B-13}$$

Comparing Equation (B-13) with Equation (5.7) gives Equation (5.8H).

8. Time of Hyperbolic Flight - $\dot{R}, R\dot{\theta}$-Hodograph

Formula

$$\frac{t}{T} = \overline{Pd} - \ln \frac{\overline{M'H}}{\overline{HM}} \tag{5.15P}$$

Proof From the hodograph geometry we have

$$\overline{Pd} = \epsilon \tan \alpha \tag{B-14}$$

and

$$\overline{CH} = \overline{AC} \tan C\hat{A}H = \epsilon \tan \frac{\alpha}{2} \tag{B-15}$$

Thus

$$\overline{M'H} = \overline{M'C} + \overline{CH} = \epsilon(1 + \tan \frac{\alpha}{2})$$

$$\overline{HM} = \overline{CM} - \overline{CH} = \epsilon(1 - \tan \frac{\alpha}{2})$$

and

$$\frac{\overline{M'H}}{\overline{HM}} = \frac{1 + \tan \frac{\alpha}{2}}{1 - \tan \frac{\alpha}{2}} = \tan(\frac{\alpha}{2} + \frac{\pi}{4}) \tag{B-16}$$

Substituting Equations (B-14) and (B-16) into Kepler's equation for hyperbolic flight (5.12) we obtain Equation (5.15P).

The proof of the corresponding formula (5.15H) for $\dot{x},\dot{y}$ - hodograph is entirely similar, and is therefore omitted.

APPENDIX C

THE INTERSECTING PROPERTY OF THE NORMALS OF A HYPERBOLA

Statement of the Property

Two normal lines at two distinct points on a hyperbola in the same quadrant will always intersect in the adjacent quadrant on the opposite side of the transversal axis of the hyperbola.

An Analytical Proof

Let the equation of the hyperbola be given by the parametric equations

$$\begin{aligned} x &= B \tan \omega \\ y &= A \sec \omega \end{aligned} \qquad \text{(C-1)}$$

Consider two normal lines at the points $Q_1(\omega_1)$ and $Q_2(\omega_2)$ on the hyperbola, and let their point of intersection be $P(x_P, y_P)$. For definiteness let us assume

$$0 < \omega_1 < \omega_2 < \frac{\pi}{2} \qquad \text{(C-2)}$$

so that Q_1 and Q_2 are distinct and in the same quadrant I. Then we are required to show that the point P is in the quadrant II (see Figure C-1.)

Now the equation of the normal line at any point $Q(\omega)$ on the hyperbola may be written

$$B\,x \sec \omega + A\,y \tan \omega = C^2 \tan \omega \sec \omega \qquad \text{(C-3)}$$

where

$$C^2 = A^2 + B^2 \qquad \text{(C-4)}$$

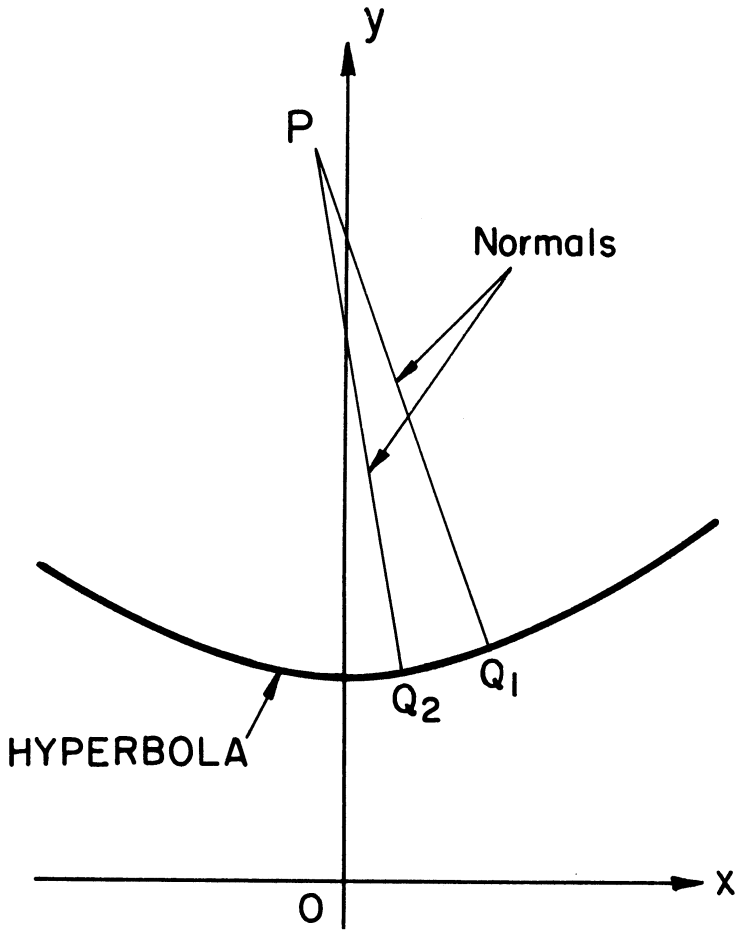

Figure C-1. Intersection of the Normal Lines to a Hyperbola

Thus for the point P we have

$$\begin{aligned} B\, x_p \sec \omega_1 + A\, y_p \tan \omega_1 &= C^2 \tan \omega_1 \sec \omega_1 \\ B\, x_p \sec \omega_2 + A\, y_p \tan \omega_2 &= C^2 \tan \omega_2 \sec \omega_2 \end{aligned} \tag{C-5}$$

Solving for x_P and y_P we find

$$x_p = \frac{C^2}{B} \tan \omega_1 \tan \omega_2 \frac{\cos \omega_2 - \cos \omega_1}{\sin \omega_2 - \sin \omega_1}$$

$$y_p = \frac{C^2}{A} \frac{\tan \omega_2 - \tan \omega_1}{\sin \omega_2 - \sin \omega_1} \tag{C-6}$$

from which we conclude under the assumption (C-2), that

$$x_p < 0 \ , \quad y_p > 0 \tag{C-7}$$

In other words, P is in the quadrant II.